ISBN 978-82-326-4606-7 (printed ver.)
ISBN 978-82-326-4607-4 (electronic ver.)
ISSN 1503-8181

Doctoral thesis
Ika Dewi Wijayanti

Doctoral theses at NTNU, 2020:129

Ika Dewi Wijayanti

Novel Zr- based AB_2 Laves type Alloys as Advanced Anodes for High Energy - High Power Metal Hydride Batteries

NTNU
Norwegian University of Science and Technology

Doctoral theses at NTNU, 2020:129

NTNU

NTNU
Norwegian University of Science and Technology
Thesis for the Degree of
Philosophiae Doctor
Faculty of Natural Sciences
Department of Materials Science and Engineering

NTNU
Norwegian University of Science and Technology

Ika Dewi Wijayanti

Novel Zr- based AB_2 Laves type Alloys as Advanced Anodes for High Energy - High Power Metal Hydride Batteries

Thesis for the Degree of Philosophiae Doctor

Trondheim, April 2020

Norwegian University of Science and Technology
Faculty of Natural Sciences
Department of Materials Science and Engineering

NTNU
Norwegian University of
Science and Technology

NTNU
Norwegian University of Science and Technology

Thesis for the Degree of Philosophiae Doctor

Faculty of Natural Sciences
Department of Materials Science and Engineering

ISBN 978-82-326-4606-7 (printed ver.)
ISBN 978-82-326-4607-4 (electronic ver.)
ISSN 1503-8181

Doctoral theses at NTNU, 2020:129

Printed by NTNU Grafisk senter

PREFACE

This doctoral thesis is written as a requirement to accomplish PhD degree and is based on the project of "Novel High Energy - High Power Metal Hydride Battery" which is collaboration work between the Department of Materials Science and Engineering of NTNU and the Department of Battery Technology of Institute for Energy Technology (IFE). The work was mainly carried out at the Department of Battery Technology of IFE. Parts of the studies were performed at the Department of Materials Science and Engineering of NTNU in collaboration with Master student Live Mølmen. Furthermore, the melt-spinning experiments were performed at CRNS-ICMCB Bordeaux in France in collaboration with A. Prof. Stéphane Gorsse.

This PhD project was conducted in the period from August 2016 to April 2020 and was supervised by Prof. Volodymyr Yartys and co-supervised by Prof. Hans Jørgen Roven. During by internship at BASF/Battery Materials–Ovonic, USA, I was supervised by Prof. Kwo Young,

Indonesia Endowment Fund for Education (LPDP) and Norwegian Research Centre on Zero Emission Energy Systems for Transport (MoZEES), Institute for Energy Technology and Norwegian University of Science and Technology provided partial financial support for the project.

ACKNOWLEDGEMENTS

First of all, I would like to thank Allah SWT. as my God Alhamdulillahirabbil'alaamiin for every part of happiness and sadness in my life, it has always been the most beautiful journey in my life to strengthen my soul.

A deepest gratitude to Prof. Volodymyr Yartys as my supervisors for helping me to pass through a PhD journey with 4 papers successfully published in the leading international journals. You always give me invaluable support to finish every single aspect in my PhD work, thus I always feel supervised by my own father.

A very special thanks to Dr. Suwarno. This PhD project would not happen without extraordinary help from Dr. Suwarno who is also my colleague in the Department of Mechanical Engineering Sepuluh November Institute of Technology (ITS) Surabaya. Dr. Suwarno deeply introduced and promoted me to Prof. Volodymyr Yartys so he accepted me as his PhD student. Indeed, encouragement from Dr. Suwarno to pursue my PhD made me encourage myself to gain my ability to complete this PhD project.

During my stay in NTNU Trondheim for about 8 months, Prof. Hans Jørgen Roven and Assoc. Prof. Fride Vullum Bruer were always available to solve all my problems related to the initial PhD requirements. In this case, Prof. Hans Jørgen Roven also has very high contribution to the experiments during the first semester in NTNU and preparation of the thesis writing. He gave me a very useful advice on how to conduct the experiments and to organize the thesis structure.

I owe many thanks to Master-student NTNU Live Mølmen (graduated in July 2019) for the incredible and fruitful collaboration on this project, for providing me plenty of her time to pick up my phone calls, to discuss everything about our problems and furthermore to find the solutions until the results come out.

Furthermore, I would personally like to thank to all the staff in Department of Materials Science and Engineering NTNU for their great assistance in technical and administrative

efforts. Especially a gratefulness to Prof. Tor Grande, Prof. Ragnhild Elizabeth Aune, Prof. Cristian Rosenkilde, Assoc. Prof. Ida Westermann, and Prof. Yanjun Li for sharing with me their priceless experience and knowledge during my first semester class at NTNU. Other than that, I would also like to thank to Pål Christian Skaret, Dr. Yingda Yu, Dr. Kristin Høydalsvik Wells, Dr. Dmitry Slizovskiy, Jonas Einan Gjøvik, Dr. Trygve Lindahl Schanche, Dr. Magnus Rotan, for giving me a great assistance during experimental laboratory work at NTNU. Special thanks go to Elin Synnøve Isaksen Kaasen, Hilde Martinsen Nordø, and Vidar Broholm for superb and friendly assistance in administrative work.

Most of the PhD works were performed at the Department of Ensys and Department of Battery Technology IFE with the help of many people: Dr. Martin Kirkeangen, Dr. Arne Lind, Dr. Hanne F. Andersen, Dr. Jan Petter Maehlen, Dr. Preben Joakim Svela Vie, Dr. Øystein Ulleberg, Dr. Ragnhild Hancke, Dr. Roman Denys, and Dr. Thomas Preston for helping me to experience PhD life at IFE. My sincere thanks also go to Dr. Nazia S. Nazer, Dr. Simona Palencsar, Dr. Magnus Helgerud Sørby, Marius Uv Nagell, Dr. Samson Yuxiu Lai, Ida Lereng, Dr. Gaute Svenningsen, and Marte Orderud Skare for providing me with precious support to conduct the experiments during my PhD work at IFE. Very special thanks to Linda Øro and Solveig Olstad for their valuable help to solve every single problem related to administrative work, also to Per Bang Jensen, Abelone Byrkjedal, and Rolf Jørgen Sødahl for a very kind help to solve my problem related to information and technology communications.

I thank my colleagues at NTNU for the uplifting discussions, sharing the experience during the course's studies and for all the fun we have at the beginning of my PhD time: Muh. Kurniawan, Fabian Imanasa Azof, David Dominikus Eide Brennhaugen, Yan Ma, Shubo Wang, Feng Lu, and Samuel Senanu. I am also grateful to all my Indonesian friends and Indonesian community in Trondheim and in Oslo, KMIT, PPIT, and UmiNOR.

Sincerely thanks to BASF Rochester Hills experts (Prof. Kwo Young, Taihei Ouchi, Dr. Jean Nei, Dr. Shuli Yan, Dr. Diana Wong, Shiuan Chang, Meng Xu, Hongkang Tian,

Pei Chen) who accepted me for the internship during the summer 2018 and guided my stay at BASF. I feel very honoured to have an extraordinary experience when working with a highly professional and friendly community at BASF. I enjoyed a kind hospitality and intense supervision during my stay allowing me to effectively execute my project work and have a full confidence in executing my tasks.

Last but not the least, I would like to thank my parents and my brother in Indonesia. My sincere thanks go to my husband Arif Hariyadi, my son Hylmi Fatih Adikara, and my daughter Alina Maryam Rahmadira for their eternal love and spiritual support during sometimes difficult time to finish this PhD journey.

CONTRIBUTIONS

This present work would never been completed without the help from:

- Dr. Roman Denys (IFE/Hystorsys AS) performed arc melting experiments and contributed to the studies of hydrogen storage properties for the alloys in all papers.
- Live Mølmen (Master of science, Department of Materials Science and Engineering, NTNU) performed rapid solidification, XRD, and SEM characterization presented in paper 2 and 3.
- Assoc. Prof. Stéphane Gorsse and Prof. Jean-Louis Bobet (University of Bordeaux, CNRS) provided rapid solidification facilities during the stay of Live Mølmen at the University of Bordeaux – the results are presented in paper 2 and in paper 3 (AES characterization).
- Dr. Matylda N. Guzik (Department of Physics, University of Oslo (UiO)) performed XRD characterization presented in papers 2, 3, and 4.
- Dr. Jean Nei and Prof. Kwo Young (BASF, USA) who supervised my access to the research laboratories of BASF/Ovonic during my internship to perform my research project.
- Dr. Suwarno (Department of Mechanical Engineering, Sepuluh Nopember Institute of Technology (ITS)) performed SEM characterizations and PCT measurements of the alloys (results are presented in paper 4).
- Dr. Mykhaylo Lototsky (University of the Western Cape) performed PCT modelling (results are presented in paper 4).

ABSTRACT

Metal hydrides have been developed during the last five decades and are used in various energy storage and conversion systems (heat pumps, cryocoolers, heat storage systems and rechargeable batteries). Among these applications, the use of metal hydrides as electrode materials is the most mature application with a huge worldwide market of commercial Nickel Metal Hydride (Ni-MH) batteries.

Laves phases, the largest group of intermetallic compounds, are able to reversibly absorb large amounts of hydrogen to form intermetallic hydrides and are recently becoming the most promising candidates for the negative electrodes in the metal hydride battery applications. This is because of their attractive electrochemical performance - high hydrogen storage and electrochemical capacities and successful operation in a high-power battery mode. Hydride-forming Laves type alloys most commonly crystallize with two types of structures, a C15 FCC $MgCu_2$ type and a C14 hexagonal $MgZn_2$ type which show complementary features of their H storage behaviours. Indeed, C14-predominated metal hydride alloys are more suitable for high-capacity and long-life time operation, while C15-predominated metal hydrides provide improved high-rate and low temperature performances. Therefore, optimizing the composition of C14/C15 Laves type alloys as H storage and battery electrode materials is the key to achieve optimum performance of the Ni-MH batteries.

This work was focused on the development of the metal hydride alloys as advanced anodes of Ni-MH batteries by achieving high electrochemical capacity, high rate dischargeability, fast activation, and excellent cyclic stability. To reach the goals, three major groups of the factors were considered as key ones helping to select advanced materials with the best performance including

(a) Selection and optimisation of the chemical composition and phase structural state;
(b) Control over the microstructural state of the alloys;
(c) Activation of the surface properties of the alloys allowing fast H exchange.

C14 and C15 Laves alloys were selected and their chemical composition has been optimized.

The selected rare-earth free compositions of these alloys can be easily modified to achieve the best electrochemical behaviours. Three different materials preparation techniques were applied to synthesize the studied alloys including arc melting and casting of the alloys, rapid solidification, and homogenisation annealing. Last group of optimization factors included creation of the active surfaces facilitating hydrogen uptake by the studied metal hydride alloys via metal-gas interactions and electrochemically. In order to achieve fast activation performance and to establish and to maintain the high rate dischargeability, the surface of the anodes of the Ni-MH batteries should be suitable for easy activation. In the present study, addition of a catalyser such as Lanthanum metal has been successfully chosen to improve the surface properties of the hydrogen storage alloys. Not only adding La, but also treating the metal hydride alloy in a hot KOH solution has proven to be efficient in achieving easy activation of the surface so that a fast activation performance was demonstrated.

The composition of the studied alloy can be described by a general formulae $AB_{2-x}La_{0.03}$ and belongs to the group of Laves type alloys, with $A=Ti_{0.15}Zr_{0.85}$; $B=Mn_{0.64–0.70}V_{0.11–0.12}Fe_{0.11–0.12}Ni_{1.097–1.2}$. The optimization of the composition was performed by adjusting the ratio between Zr and Ti in a range between 80/20 to 85/15 while the ratio between A (Ti+Zr) and B (Mn+V+Fe+Ni) components in the $AB_{2\pm x}$ alloys (x=0.05; 0.08; 0.1) was also optimized. The alloys compositions belong to the hypo-stoichiometric ($AB_{1.90}$, $AB_{1.95}$) and hyper-stoichiometric ($AB_{2.08}$) types alloys further to the stoichiometric $AB_{2.0}$ composition. Change of the B/A ratio allowed to optimize their hydrogen storage performance and behaviour as the advanced anodes of the metal hydrides batteries.

In the present work, a set of different characterisation techniques has been used to probe the studied alloys and their hydrides. These included testing of the phase-structural composition by X-Ray diffraction (XRD), characterisation of the microstructural state by Scanning Electron Microscopy (SEM) and Energy Dispersive Spectroscopy (EDS), investigation of hydrogen absorption–desorption properties and obtaining

thermodynamic characteristics of H_2 gas–solid reactions by studying Pressure-Composition-Temperature (PCT) diagrams and electrochemical charge-discharge performance, further to the Electron Impedance Spectroscopy (EIS) characterization.

As a result of the work, high discharge capacity approaching 500 mAh/g, good cycle stability, and good rate performance have been reached while offering affordable price of about 75 % cheaper than that for the commercial AB_5 alloys, by eliminating use of rare earth metals and cobalt, were successfully achieved through the development and optimization of the Zr- based multicomponent (Ti, Zr, Ni, Mn, Fe, V, La) AB_2 Laves type alloys.

PAPERS

1. A.A. Volodin, R.V. Denys, C. Wan, I.D. Wijayanti, S. Suwarno, B.P. Tarasov, V.E. Antonov, V.A. Yartys, Study of hydrogen storage and electrochemical properties of AB_2-type $Ti_{0.15}Zr_{0.85}La_{0.03}Ni_{1.2}Mn_{0.7}V_{0.12}Fe_{0.12}$ alloy, *Journal of Alloys and Compounds*, **793** (2019) 564-575. doi: 10.1016/j.jallcom.2019.03.134.

2. I.D. Wijayanti, L. Mølmen, R.V. Denys, J. Nei, S. Gorsse, K. Young, M.N. Guzik, V. Yartys, The electrochemical performance of melt-spun C14-Laves type Ti-Zr-based alloy, *International Journal of Hydrogen Energy*, **45** (2020) 1297-1303. doi: 10.1016/j.ijhydene.2019.02.093.

3. I.D. Wijayanti, L. Mølmen, R.V. Denys, J. Nei, S. Gorsse, M.N. Guzik, K. Young, V. Yartys, Studies of Zr-based C15 type metal hydride battery anode alloys prepared by rapid solidification, *Journal of Alloys and Compounds*, **804** (2019) 527-537. doi: 10.1016/j.jallcom.2019.06.324.

4. I.D. Wijayanti, R.V. Denys, S. Suwarno, A.A. Volodin, M.V. Lototsky, M.N. Guzik, J. Nei, K. Young, Hans J. Roven, V. Yartys, Hydrides of Laves type Ti-Zr alloys with enhanced H storage capacity as advanced metal hydride battery anodes, *Journal of Alloys and Compounds,* **828** (2020) 154354. doi: 1016/j.jallcom.2020.154354.

PRESENTATIONS

1. I.D. Wijayanti, A.A. Volodin, C. Wan, L. Mølmen, R.V. Denys, S. Gorsse, K. Young, H.J. Roven, V. Yartys, Effect of rapid solidification on the electrochemical performance of Zr-Ti Laves based alloys as a negative electrode of Nickel Metal Hydride Batteries, International Hydrogen and Fuel Cell conference, Trondheim, Norway, 14-15 May 2018. *Oral presentation*.

2. I.D. Wijayanti, L. Mølmen, R.V. Denys, S. Gorsse, J. Nei, M.N. Guzik, K. Young, V. Yartys, Studies of Zr-based C15 type metal hydride battery anode alloys prepared by rapid solidification, 16th International Symposium on Metal-Hydrogen Systems, Guangzhou, China, 28 October-2 November 2018. *Poster presentation*.

TABLE OF CONTENTS

Chapter 1

INTRODUCTION

1.1. Background and Motivation

Binary metal hydrides are chemical compounds of metals with hydrogen which reversibly store large amounts of hydrogen reaching high gravimetric and volumetric densities of accumulated H. Unfortunately, binary metal hydrides are either very stable (e.g., ZrH_2; decomposition temperature 600 °C) or unstable requiring very high pressures to be formed (NiH; 3 kBar H_2). That's why a discovery in 1950s of intermetallic hydrides was a real breakthrough. Indeed, their hydrogen storage capacities are as high as for the binary metal hydrides, but reversible hydrogen absorption and desorption to form/decompose these hydrides occur in the convenient temperature and hydrogen pressure ranges, often between 20 and 80 °C and 0.1–10 bar H_2,

Indeed, discovered in the 1950s of ZrNi-based ternary intermetallic hydride $ZrNiH_3$ showed that it has intermediate thermodynamic properties between the corresponding binary hydrides, ZrH_2 and NiH, while demonstrating a reversible hydrogen absorption and desorption in the temperature range 116-226 °C with equilibrium pressure of H_2 desorption being close to 0.1 bar H_2 at 226 °C [1].

Nevertheless, such favourable modification of the behaviours of ternary hydrides required significant improvements before becoming suitable for practical applications. Indeed, a discovery that metal hydrides are applicable to conveniently store hydrogen was announced in the late 1960s when intermetallic hydrides of the AB_5 composition with A = Rare Earth metal and B = Ni or Co, including $LaNi_5$, showed excellent performance as chemical reversible stores of hydrogen gas. In fact, an excellent performance of $LaNi_5H_{6.7}$ as a hydrogen storage material [2, 3] has been discovered by fortune during systematic studies of $SmCo_5$ as a high coercivity permanent magnet

material at Philips Research Labs in Eindhoven, Netherlands led by Prof. K.H.Jürgen Buschow [4].

It was observed that the coercivity of the $SmCo_5$ powders significantly decreased when storing the material in open air because of the chemical interaction with water vapour which released hydrogen gas in the following process:

$$2\ SmCo_5 + 3\ H_2O \rightarrow Sm_2O_3 + 10\ Co + 3H_2 \quad (1.1)$$

while in a subsequent step a formation of intermetallic hydride $SmCo_5H_{2.8}$ [2]

$$SmCo_5 + 1.4\ H_2 \rightarrow SmCo_5H_{2.8} \quad (1.2)$$

occurred, causing a decay in coercivity.

A nonmagnetic analogue of $SmCo_5$ was selected for the study of the hydrogenation process to understand the fundamental aspects of the interactions in the metal-hydrogen system by utilizing NMR, and $LaNi_5$ was the choice [5].

This resulted in a discovery of excellent features of H storage in $LaNi_5$ and its analogues as they are able to quickly, within just seconds, to form the hydrides when the metal alloy is exposed to hydrogen gas and to reversibly release H_2 when lowering the pressure in the system, while reaching high hydrogen per metal (H/M) ratios exceeding 1.0 and high volumetric H capacity surpassing a corresponding value for liquid hydrogen. Particularly attractive behaviours were found for $LaNi_5H_{6.7}$ as it was formed at pressures just slightly higher than atmospheric pressure ($P_{H_2\ absorption}/P_{H_2\ desorption}$ @ 20 °C of 1.83/1.36 atm H_2) and was able to provide stable and convenient for use hydrogen pressure during hydrogen absorption and desorption at equilibrium conditions [6].

As equilibrium pressure of hydrogen for $LaNi_5H_{6.7}$ is close to the atmospheric pressure, a natural proposal was to use $LaNi_5$ as a negative electrode and to charge it electrochemically with hydrogen when using an aqueous electrolyte. In 1976 by $LaNi_5$ was firstly charged with hydrogen in an aqueous KOH electrolyte showing

electrochemical capacity of 330-390 mAh/g corresponding to the composition $LaNi_5H_{5-6.7}$ [7-9].

Even though $LaNi_5$ was found to be unsuitable for practical use as an electrode in the Ni-Metal Hydride battery because of its quick corrosion degradation in KOH solution, changing of the composition by doping on both La and Ni sites resulted in a dramatic improvement of the cycling stability, which was related to the decreased stresses in the material because the doping reduced the lattice expansion during the hydrogenation and therefore reduced the corrosion, as it was related to the repeated large expansion and contraction of the metal lattice [8].

Already in the late 1980s, suitability of modified AB_5 alloys as metal hydride battery anodes of the Ni-MH battery allowed to develop a commercial product and to successfully introduce it to the market of rechargeable batteries. Further development went to the climax, when in the 2000s the first mass-produced hybrid vehicle Toyota Prius utilizing Ni-MH batteries became available at the worldwide arena.

Several features of the metal hydride batteries assure their successful use in hybrid vehicles. These features include: High safety; Affordable price; Simplicitly; High abuse tolerance; High endurance service life; Robustness – these are the factors which justified using these batteries in hybrid electric vehicles. Their replacement of Ni-Cd (Nickel Cadmium) batteries was simply achieved because of (a) the same chemistry of the cathode (nickel hydroxide) and of the electrochemical performance of the electrodes; (b) replacement of the toxic Cd-containing electrode materials by utilising safe in use and abundant elements components, while also reducing the materials costs.

At the same time, Ni-MH batteries are characterized by a relatively low gravitational energy density when comparing to the Lithium ion batteries [10]. To satisfy the market demand, better energy storage density characteristics of the Ni-MH batteries should be achieved. Thus, there is an urgent need to improve their performance.

Anode as the main component of the battery determines the performance characteristics of the Ni-MH batteries. In Ni-MH batteries, metal hydrides work as the anode electrode. To achieve excellent performance of Ni-MH batteries, one main direction is in optimizing properties of the anodes. Therefore, since their first invention many studies have been performed to develop advanced anode materials showing excellent performance, including fast activation behaviour, high reversible electrochemical capacity, and good cycle stability [6]. The selection of the suitable alloys composition and the appropriate processing routes for making metal hydrides should be tried to enhance the properties and to further improve the performance of the Ni-MH batteries [11].

Since their first invention, the improvement has been continuously performed for the AB_5 (A= Rare Earth Metal; B=Transition Metal) based alloys, when in 1980s there were discovered AB_5 alloys with compositions $MmNi_{3.55}Mn_{0.4}Al_{0.3}Co_{0.75}$ (Mm= mischmetal, containing rare-earth elements) which became commercialized. A maximum discharge capacity of about 320 mAh/g was achieved by utilizing these alloys. However, these alloys face a challenge of use of the high cost materials caused by a high content of the rare earth metals and cobalt.

Thus, it is important to develop alternative H storing alloys with high H storage and electrochemical capacity and lower price. Comparison of hydrogen storage properties of the different available hydrides is presented in Table 1.1. Magnesium hydride shows the largest storage of hydrogen, however, together with the unfortunate properties of poor hydriding/dehydriding kinetics at ambient temperatures and rapid degradation in alkaline solutions.

Similar hydrogen storage performance is also characteristic for the AB_2 type $ZrMn_{0.5}V_{0.5}Ni_{1.4}$-based intermetallic hydrides with appr. 1.5-1.8 wt.% H gravimetric capacity and an electrochemical discharge capacity of 315 mAh/g [12]. Here AB_2 represents a general stoichiometry of the Laves phases where A site stands for the metallic elements with larger atomic radii having a strong affinity to hydrogen (an early transition or rare earth metal), for example is Ti, Zr, La), while B site contains smaller

atoms with a weak hydrogen affinity, normally transition metals, such as Cr, Mn, Fe, Co, Ni, Cu [13-16].

Table 1.1. Comparison of hydrogen storage properties of the different hydrides

Alloys type	**Hydrides**	**Weight content of H in hydride (wt.% H)**	**Electrochemical capacity (mAh/g)**	**References**
AB_5	$LaNi_5H_6$	1.3	348	[17]
AB_2	$Ti_{1.5}Zr_{5.5}V_{2.5}Ni_{7.5}H_{2.2}$	1.59	359	[18]
Mg metal	MgH_2	7.7	2063	[19]
A_2B	Mg_2NiH_4	3.6	964	[20]
BCC	$V_{0.9}Ti_{0.1}H_2$	3.8	1018	[21]

AB_2 type alloys form hydride with reversible hydrogen storage capacities in the range 3-5.5 at.H / f.u. AB_2. The characteristics of some typical hydrides are listed in Table 1.2. Their maximum and reversible hydrogen storage capacity are directly related to the type of transition metal forming the intermetallic alloy. For the H content 3.6-3.8 at.H/f.u. AB_2 as in $ZrMn_2$ and $ZrCr_2$, their H storage capacity of 1.77-1.92 wt.% H is converted to the electrochemical capacity of 474-515 mAh/g. Such a value is superior as compared to the commercial AB_5 type alloys, with 320 mAh/g capacity justifying interest in studies of AB_2 hydrides and showing their applied potential.

Unfortunately, quite a number of ternary hydrides is not suitable for use as battery anodes in spite of their reasonable capacities in storage of gaseous hydrogen because they are either unstable at normal conditions applied in the MH battery - as $ZrFe_{1.98}Al_{0.02}H_{3.0}$ with hydrogen pressure required to reach its formation and composition being above 500 bar H_2 (see Table 1.2), or too stable as $ZrV_2H_{5.5}$ (see Table 1.2), making impossible hydrogen release during the electrochemical discharge of the anode.

The only way to bypass the problem is to prepare complex multicomponent compositions where the B components forming too stable ternary hydrides will be mixed with B components forming unstable and unsuitable for practical electrochemical applications hydrides. Examples include $ZrV_2H_{5.5}$ with B = V where excellent storage

capacity of 2.79 wt.% H cannot be electrochemically discharged and $ZrFe_{1.98}Al_{0.02}H_{3.}$ with B = Fe containing 1.47 wt.% H which is too unstable and cannot be formed by electrochemical charging. However, mixing B = V and Fe will create compositions of intermetallic alloys with intermediate properties which well suit to the task of building an efficient metal hydride anode. This latter approach has been successfully utilized in the present study. Such mixed hydrides should be designed to be able to easily absorb and desorb hydrogen when the hydrogen pressure in the rage of 0.1-5 atmosphere (room temperature) is applied in order to be practically utilized [22].

Table 1.2. Laves type intermetallic compounds with their hydrogen storage properties related to the weight content of hydrogen and equilibrium H_2 pressure of the formation/decomposition of their hydrides

Alloys type	**Hydrides**	**Weight content of H in hydride (wt.% H)**	**Electrochemical capacity (mAh/g)***	**P_{eq} (equilibrium pressure) (atm)**	**References**
$ZrFe_{1.98}Al_{0.02}$	$ZrFe_{1.98}Al_{0.02}H_{3.0}$	1.47	394	560	[23]
$ZrMn_2$	$ZrMn_2H_{3.6}$	1.77	474	0.1	[24]
$ZrCr_2$	$ZrCr_2H_{3.8}$	1.92	515	0.01	[25]
ZrV_2	$ZrV_2H_{5.5}$	2.79	748	$< 10^{-8}$ / 323 K	[26]

*The electrochemical capacity is calculated by using the following relationship: 1 wt.% H = 268 mAh/g.

Zr-based AB_2-type Laves phases are the preferential alloys for negative electrodes of Ni-MH batteries not only because of their superior hydrogen storage capacity but also because of their longer cycle life as compared to the AB_5 alloys [12, 27, 28]. Furthermore, from the applied prospective, activation properties and rate capacity of the alloys should be studied and optimized.

The alloy composition, bulk structure, and surface structure are the three aspects that determine the design of the metal hydride alloys for hydrogen storage applications. Table 1.1 shows the change of hydrogen storage characteristics of the alloys when the alloys composition was adjusted from intermetallic ternary hydrides to the multielement hydride alloys. Preparation methods of the alloys naturally become the main approach

to achieve optimum performance of the Ni-MH batteries [29]. In addition, the electrochemical behavior of the alloys depends on the crystal structure type of the alloys, microstructural properties, and chemical content of each element in the alloy. The most common method used to control the physical properties of hydrogen absorbing alloys is in using chemical substitution. It is important to investigate the substitution effect of various elements on hydrogen absorbing properties to achieve optimal alloy's design [30]. Therefore, in the present study the synthesis of the alloys with the most suitable composition and preparation technique will be in focus aimed at reaching the best electrochemical performance.

1.2. Problem statement

Zr-based AB_2 Laves alloys have attracted attention as a promising alternative to AB_5 H storage alloys because of their excellent hydrogen absorption ability. Indeed, C14 and C15 Laves type phases belong to the largest group of intermetallic compounds and are able to easily absorb large amounts of hydrogen when the appropriate chemical composition of the phases is selected. The variation of the composition of transition metals (La, Ni, Mn, V, Fe) in the Zr-based AB_2-type alloys leads to the significant changes of the hydrogen storage properties [31, 32]. Despite of the excellent discharge capacity obtained by adding transition metals (La, Ni, Mn, V, Fe) into Zr-based AB_2-type alloy, their activation behaviour, high rate discharge ability, discharge capacity, and cyclic stability of the alloys have a room for the significant improvements.

Excellent performance of the Nickel Metal Hydride (NiMH) batteries can be achieved by selecting and optimizing the chemical composition and phase structural state, controlling the microstructural state, and activating the surface properties by utilizing catalyzing additives. Further to these optimizations, different ways to prepare the alloys also play an important role in optimization of their properties in the hydrogen storage applications. With respect to the poor activation behavior of the AB_2 alloys, the surface treatment should also be considered aimed to shorten the activation cycling.

The objectives of this work are:

1. Develop novel, low-cost, high performance, and high energy-high power advanced metal hydride battery anodes;
2. Achieve discharge capacity of 500 mAh/g;
3. Extend the cycle life and stability of the battery anodes;
4. Enhance the corrosion resistance of the battery anodes;
5. Decrease the cost of the battery electrode alloys by at least 30%;
6. Reduce/eliminate use of the rare-earth metals.

1.3. Scope of the work

In line with reaching the objectives of the project, the scope of the present work is:

1. Synthesis of AB_2 Laves type battery anode materials with optimized chemical composition where their improved performance will be achieved by varying B/A ratios. The purpose is to study how the different B/A ratios affect the electrode properties and performance.
2. Synthesis of nanostructured battery anode materials by utilising rapid solidification. The aim is to study how the nano-structuring affects the electrode performance and to find optional quenching rates / wheel rotation speeds.
3. The phase composition and microstructural characterization of the studied alloys will be analysed by X-ray diffraction (XRD) and scanning electron microscopy (SEM) along with X-ray energy dispersive spectroscopy (EDS).
4. Hydrogen absorption and desorption characterization of the selected alloys will be assessed by using PCT Sievert's volumetric method.
5. Electrochemical characterization of charge-discharge processes at various current densities (including activation, rate, and cycling performance) will be performed in order to develop the alloys with desired performance at high-power discharge conditions.

6. Impedance spectroscopy characterization will be done for the studied electrodes as related to their history and chemical composition.
7. Auger spectroscopy characterization of the selected alloys will be performed.

1.4. Thesis structure

The structure of the thesis is the follows:

- Chapter 1 describes the background and motivation of the work, gives a problem statement, and presents the scope of the present work.
- Chapter 2 contains the literature review introducing the topic of rechargeable batteries in general and Ni-MH batteries in detail, including characteristics of Ni-MH batteries, thermodynamics vs. kinetics of electrochemical hydrogen storage, requirements for hydrogen storage and anode electrode alloys, and the development status of hydrogen storage alloys for Ni-MH batteries. Furthermore, a description of the rapid solidification as one of the nano-structuring techniques is also presented.
- Chapter 3 consists of the description of the used experimental methods, description of the materials preparation, experimental equipment used, and characterization methods applied.
- Chapter 4 includes discussion of the experimental results as related to reaching the objectives of this project in comparison with the available reference data.
- Chapter 5 presents the conclusions and summary of the results of the PhD thesis study.
- Appendixes contain four published papers and are presented at the end of the thesis. The articles present the main results of the PhD project and were published in 2018-2020 throughout the PhD fellowship time period.

Chapter II

LITERATURE REVIEW

2.1. Metal hydrides

Hydrogen is used as an ideal energy carrier for various future energy systems, including a power supply systems for automotive applications [33-36]. Hydrogen storage is one of the key challenges in developing future hydrogen economy using hydrogen as a synthetic fuel obtained by utilizing renewable energy [36, 37]. Hydrogen can be stored as a compressed gas, as liquid H_2, and in metal hydrides. Use of the first two techniques requires high energy consumption and is cost inefficient. Furthermore, first two technologies involve risk elements of their use as requiring application of high H_2 pressures and cryotemperatures. In contrast, metal hydrides offer important advantages allowing their use at low pressures and ambient temperature together with the easiness to realize heat management options involving use of hot and cold water and allowing to optimize metal hydride-based hydrogen storage systems [38]. The volumetric efficiency of hydrogen storage for metal hydrides is superior as compared to both compressed hydrogen and LH_2 storage [39, 40].

There are three different groups of metal hydrides, which are classified based on the type of bonding between the metal and hydrogen, which are realized in ionic, covalent, and metallic hydrides [33, 41]. The metallic bonding in the hydrides mostly having high thermal and electrical conductivities is formed by reaction of hydrogen with alloys containing transition metals belonging to 3-11 groups (IUPAC) of the Periodic Table together with rare earth metals, Zr, Ti, Mg. Metal hydrides are easily formed by direct interaction between the alloys and hydrogen gas proceeding in just seconds and allowing chemical storage of hydrogen which can be controlled by changes in hydrogen pressure and temperature. Furthermore, metals and alloys can be electrochemically charged with hydrogen to form metal hydrides and discharged generating electric current in aqueous electrolytes.

2.1.1. Thermodynamic and kinetic aspects of metal-H_2 gas interactions and electrochemical hydrogen storage properties

Thermodynamic and kinetic properties of the metal hydrides are their most important characteristics to determine the performance of the electrodes in the Ni-MH battery. To characterize the thermodynamics properties, a Pressure-Composition-Temperature (PCT) diagrams are measured allowing to determine the enthalpy and entropy of hydride formation for a set of particular metal hydride alloys. The kinetics properties are defined from the time dependent curves of the rates of hydrogen absorption and desorption which are directly related to the mechanism of H absorption/desorption via the values of the kinetics constants and reaction mechanisms. For the metal hydrides to fulfil the requirements for the metal hydride electrodes of the Ni-MH battery, the optimized kinetics of hydrogen absorption and desorption is required. When it comes to the thermodynamics, we assume that the stability of the metal hydride should fit the range of equilibrium pressures of hydrogen desorption and absorption between 0.1 and 1-5 bar H_2.

The absorption of hydrogen in metals to form metal hydrides proceeds via a mechanism shown in Fig. 2.1. The figure shows two stages of hydrogen absorption by the hydride-forming metals. The first stage of the interaction of H_2 with metal is chemisorption of its molecules at the surface of the metal (see Fig. 2.1. (a)). Physisorption of H_2 molecules at the surface of the material via van der Waals forces between the metal surface and H_2 molecules; (b) The second step is chemisorption, see Fig. 2.1, when H_2 molecules dissociate at the surface to form atomic H; (c) Atomic H diffuses into the bulk material to form α-solid solution; (d) Metal hydride is formed which is characterised by a presence of chemical bonds between the metal and hydrogen. These bonds are predominantly metallic bonds with some contribution from a covalent and ionic bonding [42, 43].

For the physisorption mechanism, its importance is higher for the materials with a higher specific surface area, or with a high porosity. Low enthalpy of adsorption/desorption

during the physisorption mechanism causes the hydrogen to be readily absorbed and desorbed resulting in a complete reversibility, fast kinetics, and very small amount of energy needed during the physisorption of hydrogen [44].

Interaction between metal and hydrogen eventually is accompanied by a phase transformation when the concentration of hydrogen in the metal bulk increases to form a β -hydride phase in which hydrogen atoms occupy interstitial positions in the crystal lattice (see Fig. 2.1. (b)).

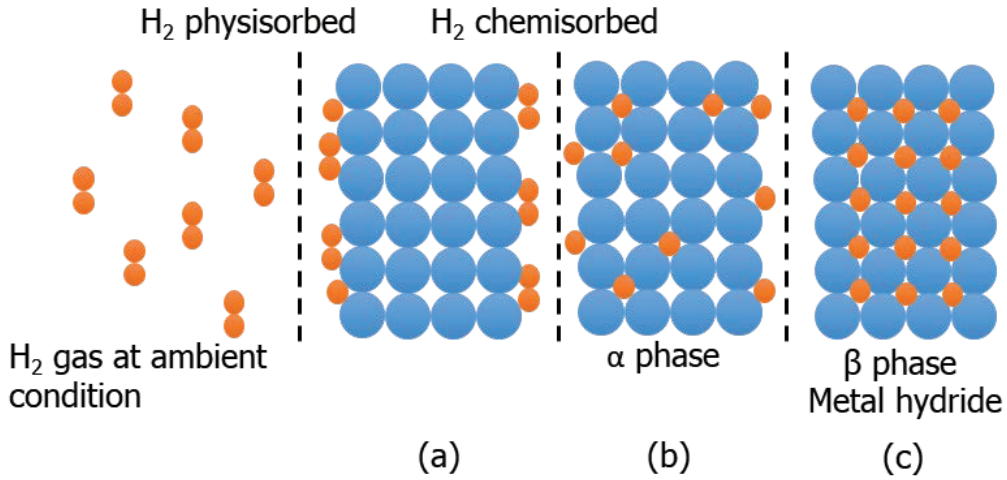

Fig. 2.1. Mechanism of hydrogen absorption by metals leading to the formation pf metal hydrides. Initial physisorption of hydrogen molecules on metal surfaces (a) is accompanied by a chemisorption wakening first and then breaking H-H bonds and forming atomic hydrogen; (b) Formation of the α-solid solution of H in metal; (c) Formation of β-hydride phase. Hydrogen atoms occupy interstitial sites in the metal lattice. Adapted from [42].

In order to be able to utilize the metal hydride alloys, a high hydrogen storage capacity and moderate hydride stability are needed [45]. Pressure composition temperature (PCT) diagrams allow to characterize the thermodynamics of the metal-hydrogen systems. Fig. 2.2 shows the typical curve PCT of metal hydride alloys with the X2 axis as the hydrogen content in the alloy indicating the electrochemical capacity corresponding to the gaseous H capacity, while the Y1 axis shows the equilibrium hydrogen gas pressure as related to the corresponding electrochemical potential of the alloy presented on the axis Y2.

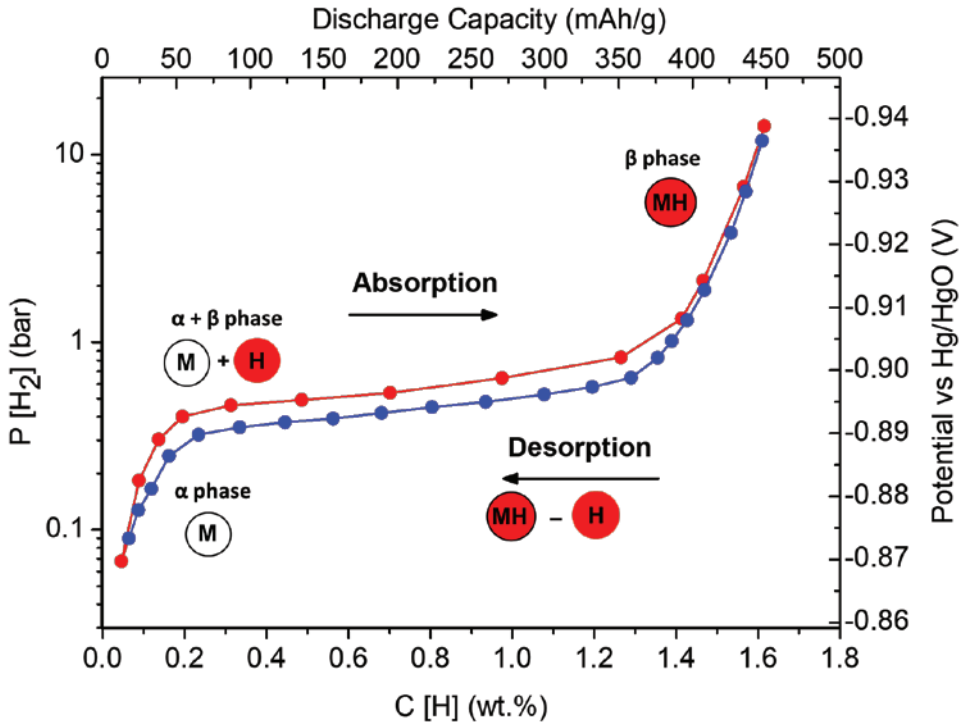

Fig. 2.2. Typical curve PCT built for a particular Metal-Hydrogen system. Solid red circle points show the absorption of hydrogen, while solid blue circle points show the desorption of hydrogen.

The PCT curve contains three different stages of the hydrogen absorption/desorption which are directly related to the different phase-structural transformations taking place in the metal hydride alloy. These include (a) formation of the α solid solution of H in metal; (b) two-phase region (α+β); and (c) formation of the homogeneous β hydride phase. At the beginning of hydrogen absorption, a pure α solid solution is formed with increasing of the H content following the pressure increase. As M-H interaction proceeds further and H_2 pressure increases, hydrogen atoms become accommodated in the interstitial sites of the crystal lattice of metal and β hydride phase is formed. This leads to the formation of the mixture of the α+β phases. As the overall concentration of hydrogen absorbed in the mixed phase increases, the amount of β phase also increases. Finally, when the available interstitial sites in metal hydride become filled with hydrogen atoms, the equilibrium pressure increases further indicating formation of the homogeneity range of the β hydride phase. Therefore, an ascending asymptotic part of

the curve of equilibrium hydrogen pressure appears. The hydrogen pressure in the plateau region of the PCT curve determines an interaction energy of the formation of the metal hydride [46]. The higher hydrogen pressure is required to form the metal hydride, the less stable hydride is formed.

The van't Hoff equation defines the thermodynamics of metal-hydrogen interaction with equilibrium hydrogen pressure in the metal-hydrogen system and absolute temperature being related to the changes in enthalpy and entropy during the hydrogen absorption or desorption:

$$ln\frac{P_{eq}}{P_{eq}^{0}} = -\frac{\Delta H}{RT} + \frac{\Delta S}{R}$$

where P_{eq}= the equilibrium pressure of metal hydride at temperature T,
P_{eq}^{0}= an ambient pressure 1 bar,
ΔH= the enthalpy change
ΔS= the entropy change
R= universal gas constant
T= the absolute temperature

It is easy to conclude that the enthalpy formation for the practically suitable metal hydrides should be in the range between 25 and 50 kJ/mol which can be converted to the equilibrium hydrogen pressure by using the above equation [47].

An example of PCT curves and van't Hoff plot for the present alloy is shown in Fig. 2.3. A PCT characterization was performed at three different temperatures, 293, 323, and 353 K. Please, note that ln(Peq) shows a linear relationship with 1/T, and the obtained line defines both ΔH and ΔS of the phase transformation on hydrogenation and on decomposition of the metal hydride.

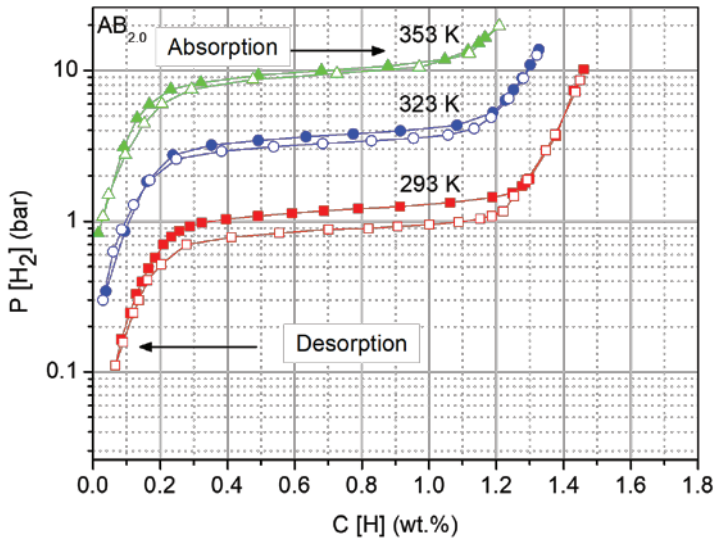

(a)

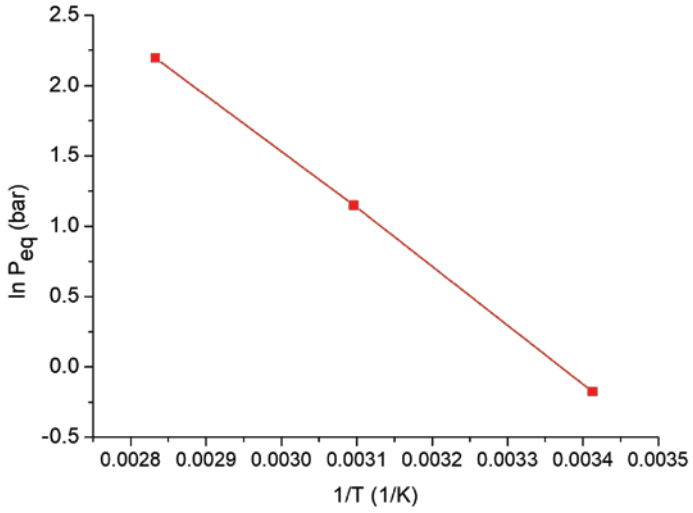

(b)

Fig. 2.3. PCT isotherms for the $AB_{2.0}$ alloy measured in this present work at three different temperatures (a) and a corresponding van't Hoff plot derived from the isotherms (b).

The pressure range between and 0.1 atm and 1 atm is considered as the most suitable pressure when selecting metal hydride battery anode materials, as the battery anode materials are tested in open electrochemical cells. As the equilibrium pressure of hydride formation is defined by van't Hoff plot in Fig 2.3. (b), the following equations show the

relationship between the electrochemical potential and equilibrium hydrogen pressure and between the storage capacity of gaseous hydrogen and electrochemical capacity of the hydride formed [22, 48]:

$$E = -0.9324 - 0.0291 \times \log PH_2 \ (vs. Hg/HgO,\ 20°C, 6\ mol\ KOH)$$

$$C\ (mAh/g) = 6 \times 26800 \frac{(H/M)_5 - (H/M)_{0.1}}{MW}$$

, where P_{H_2} = the desorption equilibrium pressure,

$(H/M)_5$ and $(H/M)_{0.1}$ = the hydrogen contents of metal hydride alloys at the pressure of 5 and 0.1 atm respectively,

M_W = the molecular weight of the hydrogen storage alloy.

2.1.2. Surface properties of metal hydrides: effect of oxides and catalysts

In order to reach high rate of charge, to improve the discharge performance at high current densities and to increase the cycle life, efficient metal hydrides are required which should have the particles easy permeable for hydrogen. Poor surface catalytic activity and high corrosion resistance in concentrated basic KOH solution are detrimental for the efficient high rate discharge performance and to the long cycle life of the electrode. Thus, surface properties of the anode electrode materials should be optimized. Further to the easy permeability for hydrogen, the surface should have a high catalytic activity in the process of electrochemical oxidation and reduction of hydrogen also showing a corrosion resistance in KOH electrolyte solution [49].

In the present study, Nickel, was used as a current collector and as a binder mixed with the metal hydride alloy. Further to the improvement of the electronic conductivity of the pressed anode electrodes Carbonyl Nickel could also show catalytic properties in electrochemical water splitting providing atomic hydrogen to the particles of the metal hydride alloy. This alloy was selected to have the particle size of 40-60 μm. The addition of Nickel also contributed to the improvement of the cyclic stability and corrosion

resistance of the studied alloys, helping to achieve efficient hydrogen diffusion and this reaching advanced discharge performance.

2.2. Introduction to Ni-MH batteries

For decades, fossil fuels dominated the energy demand for the society, particularly in transportation. As their availability is limited and will reach extinction in a foreseeable future, it is urgently necessary to develop alternative solutions, and renewable energy appears to be a sole viable alternative.

Further to the limitation in natural resources, the utilization of fossil energy caused pollution of environment which led to the increased CO_2 emissions and a greenhouse effect. As a result, the demand to a more extensive use of renewable energy trigged a broad introduction of electric vehicles (EV) which is rapidly growing year by year contributing to a preservation of a clean environment [45].

Renewable energy - wind, solar - because of its intermittent nature needs to be converted and stored before utilizing in electric vehicles. Rechargeable battery is one of the convenient solutions to realize reversible energy storage by converting the chemical energy into the electrical energy through reversible electrochemical oxidation/reduction (redox) reactions [50].

Various available types of rechargeable batteries include lead (Pb)-acid, nickel-cadmium (Ni-Cd), nickel-metal hydride (Ni-MH), and lithium (Li)-ion batteries [45]. Comparison of the efficiency of different rechargeable batteries types in terms of their usable gravimetric and volumetric energy densities is shown in Fig. 2.4. Lead acid and Ni-Cd battery systems have been used at early stages of the development in the EVs systems and now are gradually replace by more efficient rechargeable battery solutions.

Environmental concerns and low energy densities of the first two battery types caused a shift of the focus of the R&D to the Ni-MH and Li-ion batteries. Li-ion batteries have the energy density as 180 Wh/kg which is superior as compared to the other battery types

(see Fig. 2.4.). Unfortunately, their high cost and safety concerns remain the challenge for the EVs applications.

Considering the drawbacks of various mentioned types of rechargeable batteries, Ni-MH battery has begun to be considered as the preferred type of rechargeable batteries with a number of outstanding applied features [49]:

- High energy density;
- Excellent high rate performance and high achieved power densities;
- Safe performance during charge and discharge, including tolerance to the abusive overcharge and over-discharge;
- Excellent thermal tolerance;
- Environmental compatibility and recyclable use of the battery components;
- Maintenance free operation;
- Absence of poisonous components;
- Absence of electrolyte consumption during charge/discharge cycling [39, 51].

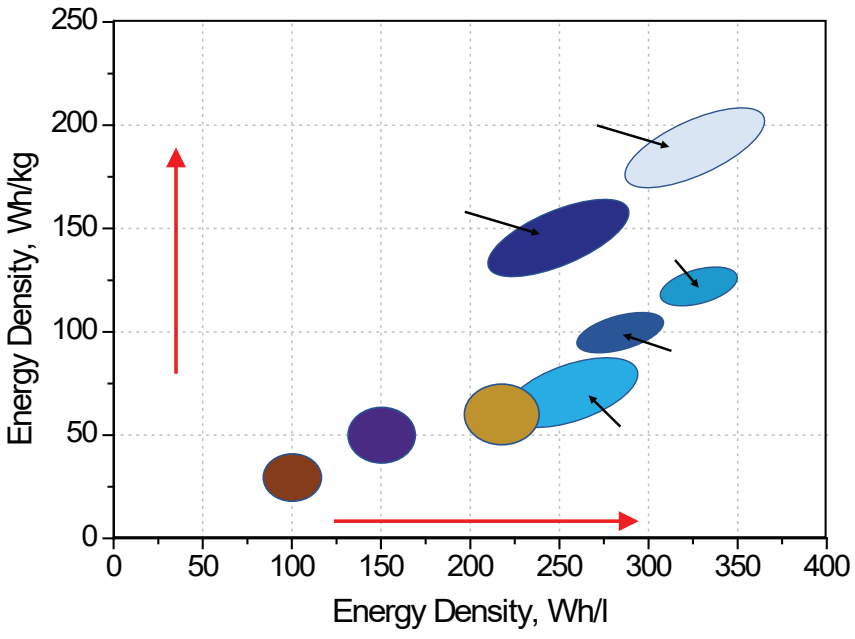

Fig. 2.4. Comparison of gravimetric and volumetric energy densities for the various types of the rechargeable batteries. Adapted from [52].

2.2.1. Working principle of the Ni-MH batteries

Ni-MH battery consists of three major components: metal hydride (MH) alloy used as the negative electrode, $Ni(OH)_2$ used as the positive electrode, and 6 M KOH aqueous solution used as electrolyte.

Working principle of Ni-MH battery is shown in Fig. 2.5. During the charging, the electrons are flowing from the positive electrode (cathode) to the negative electrode (anode) and vice versa during the discharging process.

Battery performance involves alternating oxidation and reduction processes causing a flaw of electric current and transfer of electrons. During the oxidation taking place during the charging process (see the reaction below), the electrons are taken from the positive electrode in a process involving oxidation of Nickel hydroxide into the Nickel oxyhydroxide (NiOOH) which transforms Ni^{2+} into Ni^{3+}. The electrons in turn are used at a negative electrode during the reduction process when the water forms atomic hydrogen at the surface of the metal before the metal is converted to the metal hydride.

The **charging** process can be described as:

Negative electrode (Cathode) => reduction

$$M + H_2O + e^- \rightarrow MH + OH^- \quad (2.1)$$

Positive electrode (Anode) => oxidation

$$Ni(OH)_2 + OH^- - e^- \rightarrow NiOOH + H_2O, \quad (2.2)$$

where M is the hydrogen storage alloy and MH is the corresponding metal hydride containing adsorbed hydrogen. The process of the hydrogen adsorption, which occurs at the metal surface covered by a thin layer of metal oxide consists of physisorption of H which is followed by chemisorption of hydrogen in the metal lattice (see Section 2.1.1).

During the **discharge** process, the reactions run in the opposite directions and thus overall discharge reaction taking place at the electrode cab be described as follows:

Negative electrode (Anode) => oxidation

$$MH + OH^- - e^- \rightarrow M + H_2O \tag{2.3}$$

Positive electrode (Cathode) => reduction

$$NiOOH + H_2O + e^- \rightarrow Ni(OH)_2 + OH^- \tag{2.4}$$

A summary of charging-and discharging reactions presents a reversible process which can be described as:

$$M + Ni(OH)_2 \underset{Discharge}{\overset{Charge}{\rightleftarrows}} MH + NiOOH \tag{2.5}$$

with keeps stable the concentration of the electrolyte and quantity of water during the charging and discharging process causing good overall performance of Ni-MH battery in hydrogen gas exchange, at low and high operation temperatures, while being resistant to the corrosion and swelling [53].

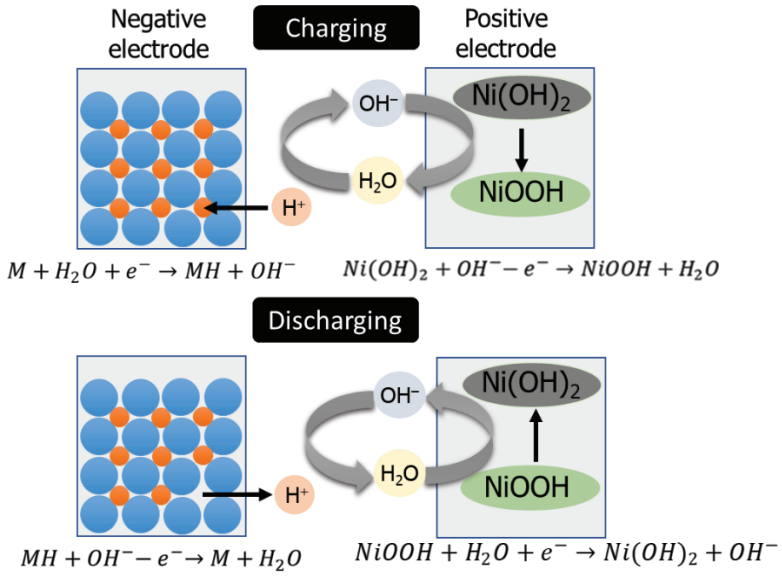

Fig. 2.5. Working principle of NiMH battery. Adapted from [54].

2.2.2. Mechanism of electrochemical charge-discharge to form metal hydrides

During the charge, the following reactions take place in the bulk of the alloys and at the interface between the electrode and electrolyte (see Fig. 2.6) [55]:

a) The diffusion of accumulated hydrogen from the bulk to the surface of the electrode, while a homogeneous distribution of hydrogen occurs in the metal hydride electrode being in equilibrium state,

b) The transformation of hydrogen atoms from adsorbed state to an absorbed state when diffusing from the surface of the alloy particles to the metal bulk:

$$H_{ads} \rightleftarrows H_{abs} \tag{2.6}$$

c) The reversible electrochemical reaction at the surface of the electrode can be described by the following equation and scheme:

$$H_2O + e^- \underset{Discharge}{\overset{Charge}{\rightleftarrows}} H + OH^- \quad (2.7)$$

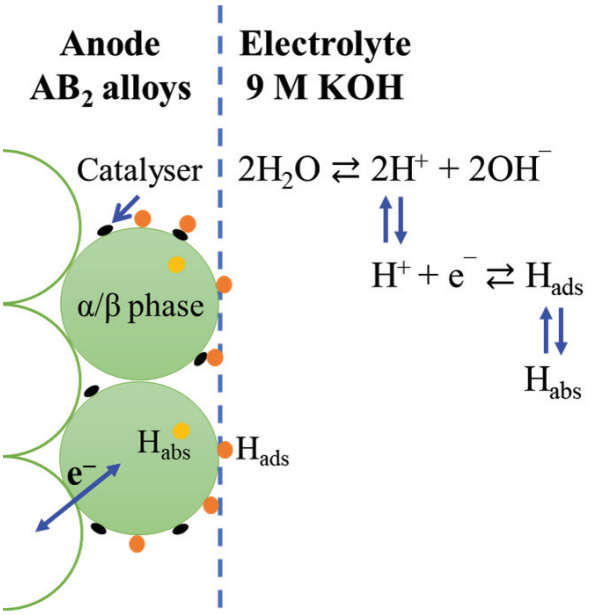

Fig. 2.6. Hydride formation/decomposition process occurring via electrochemical transformation. Adapted from [56].

2.2.3. Characteristics of Ni-MH battery

Fig. 2.7 shows the discharge rate performance of Ni-MH battery (AA size / 1 Ah) at different discharge current densities. At the highest applied current density of 4 C, approximately 80 % of discharge capacity can be maintained while a decrease in discharge capacity of about 20 % takes place. The discharge voltage gradually decreased during the discharge starting from appr. 1.3 V to 1. 1 V with the increase in the applied current density.

During the cycling, a capacity decay in battery performance occurs because of [22]:

a) Chemical changes in the active materials;
b) An increase of the internal ohmic resistance and polarization resistance;

c) A decrease of electrolyte amounts due to the side reactions of the chemical oxidation of the alloy's powder. Thus, to maintain a constant level of the electrolyte during charge/discharge cycles, a sealed Ni-MH battery is required.

The dependences between the discharge capacity and potential (vs. Hg/HgO) for the studied battery anode $AB_{1.95}$ alloy (see the figure caption for its detailed composition) are shown in Fig. 2.8 as related to the applied constant discharge current densities. The maximum discharge capacity decreases following an increase in the applied current densities because of the drowning of the flow of hydrogen atoms from inside of the hydride particles to the surface where their electrochemical oxidation takes place. In contrast, a more complete discharge can be achieved at smaller current densities as H diffusion from the core of the hydride particles to their surface is aligned with the oxidation rate,

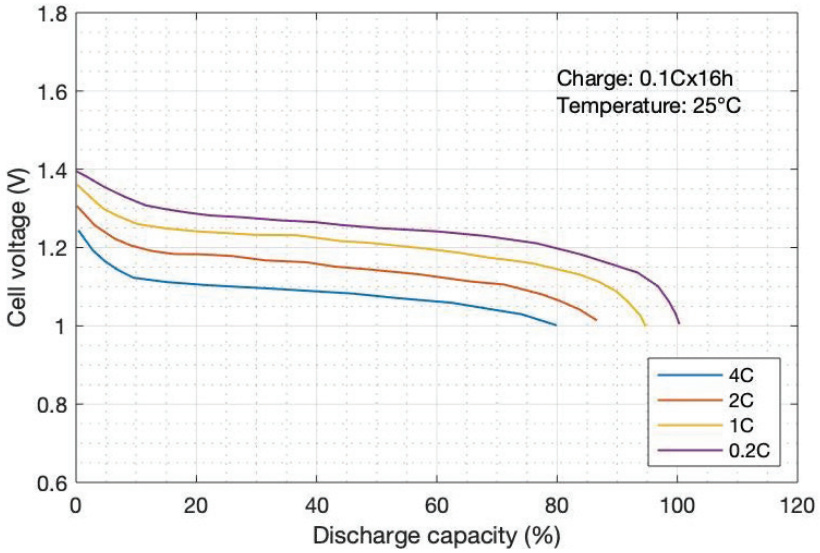

Fig. 2.7. Discharge rate performance of Ni-MH battery (AA size / 1 Ah) at different discharge current densities. Adapted from [57] .

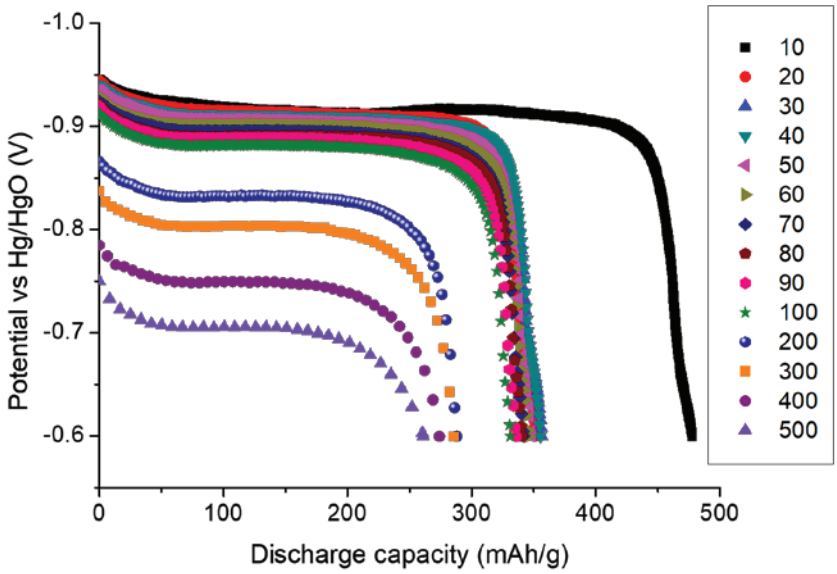

Fig. 2.8. Discharge capacity vs. potential (vs. Hg/HgO) curve of the $AB_{1.95}$ alloy with variation of discharge current density. The numbers shown in the box is the applied current densities in mA/g.

2.2.4. Electrochemical impedance spectroscopy as a method to characterize the hydride electrodes

The characterization of the kinetics of surface electrochemical reactions occurring in the electrode can be done by performing Electrochemical Impedance Spectroscopy (EIS) studies [58-68]. A small sinusoidal signal perturbation in a wide frequency range is applied to investigate the response of the system producing the Nyquist plot [46, 69, 70]. The experimental Nyquist impedance data (see Fig. 2.9.(a)) is analysed by modelling the typical equivalent circuit commonly called Randles equivalent circuit (see Fig. 2.9.(b)) which contains a semicircle and a straight-line part. Indeed, a series connection between the charge transfer resistance (R_{ct}) and a Warburg impedance (Z_w) and a parallel connection with a double-layer capacitance (C_{dl}) are contained in the Randles equivalent circuit (see Fig.2.9. (b)).

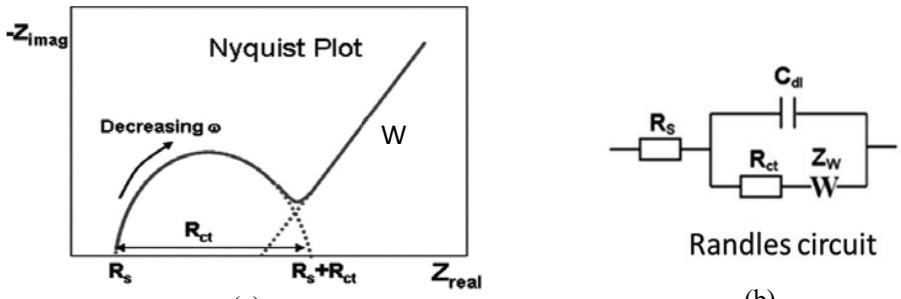

Fig. 2.9. Nyquist plot (a) and Randles circuit (b) containing charge transfer resistance and Warburg element (W). Adapted from [71, 72].

In present study, a standard Randles circuit is no longer suitable for the modelling of the Nyquist experimental data plot which was presented in the papers [73, 74] for the studied alloy due to its complex shape (see Fig. 2.10. (a)). Therefore, an original Randles circuit was modified by replacing the capacitance with a Constant Phase Element (CPE) and by moving the Warburg impedance connection forward, thus the Warburg impedance becomes separated from the charge transfer resistance connection contained in the equivalent circuit (see Fig. 2.10. (b)). This replacement is aimed to account for the surface inhomogeneity of the electrodes which is described as the depressed semicircle in the Nyquist plot. As a result, a much better fit of the EIS spectra is achieved. Further to this, a parallel circuit consisting of R and CPE is added and in series connected with a modified Randles circuit to achieve a more accurate modelling (see Fig. 2.10. (c)).

In the case of Nyquist plot of the studied alloy (Fig. 2.10. (a)), the first semicircle located in the high frequency region describes the contact resistance and capacitance between the current collector and the alloy particles ($R_{contact}$) and the second semicircle resided in the middle frequency region describes the charge transfer resistance (R_{ct}) and the capacitance of the electrode surface, while a straight-line laid in the low frequency is related to the Warburg element (W).

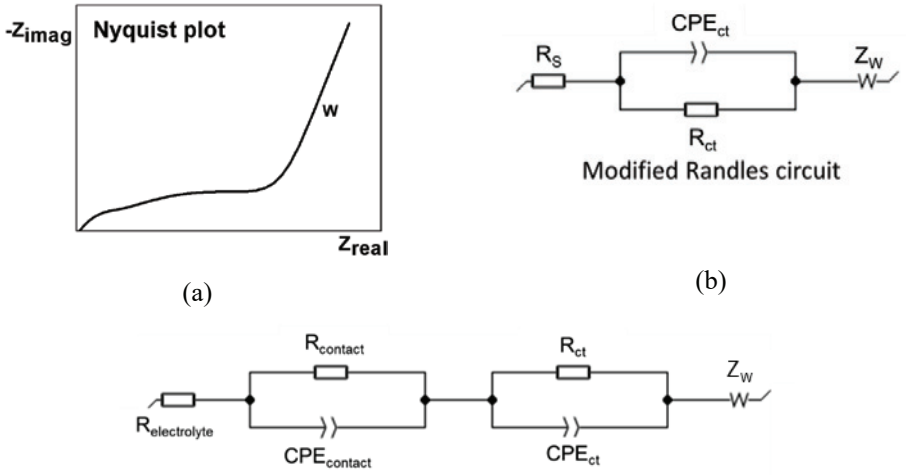

Fig. 2.10. Nyquist plot of present alloy (a) and a modified Randles circuit containing Constant Phase Elements (CPE) and individual Warburg element (W) connection (b).

By assuming that the process of hydrogen absorption by the metal hydride alloy is a semi-infinite diffusion type process, the diffusion of H atoms should follow the Fick's second law. In this case, the hydrogen concentration (electrolyte solution) in the cell is assumed not to change by the process in the electrode due to the small ratio of the electrode area as compared to the solution volume. Therefore, a simplified Fick's second law diffusion equation can be used to estimate the diffusion coefficient of H in the alloy by utilizing the following equation which is closely related to the Warburg element [75]:

$$D = \frac{R^2T^2}{2A^2n^4F^4C^2\sigma^2}$$

, where D= diffusion coefficient of hydrogen
R= ideal gas constant
T= absolute temperature
A= electroactive surface area per unit volume of electrode
N= number of electrons transferred
C= concentration of hydrogen ion
σ= Warburg impedance coefficient.

The above equation of the Warburg impedance is only valid if the diffusion layer has an infinite thickness. In this study, a presence of the semi-infinite boundary layer was assumed because of a small ratio of the electrode area to the solution volume and hydrogen supply to the metal surfaces [75].

The following equation is used to calculate the electroactive surface area (A), by assuming that the spherical alloy particles have the same size and are exposed to the electrolyte [66]:

$$A = \frac{3(1-\epsilon)}{r}$$

where ϵ= electrode porosity, assumed to be 0.3 [76]
r= radius of spherical particle (active alloy), 50 µm.

2.2.5. Comparison with other rechargeable batteries

The performance of the batteries is determined by their-specific energy (in Wh/kg) allowing to reach a specific vehicle range and a battery power (W/kg) allowing to control the vehicle acceleration during the peak power performance [53]. The comparison of some battery technologies for EV applications in terms of peak power vs. depth of discharge (DOD) is given in Fig. 2.11. Ni-MH battery produced by Ovonic Battery Company (OBC) shows the highest peak power of almost 250 W/kg while maintaining 80% DOD.

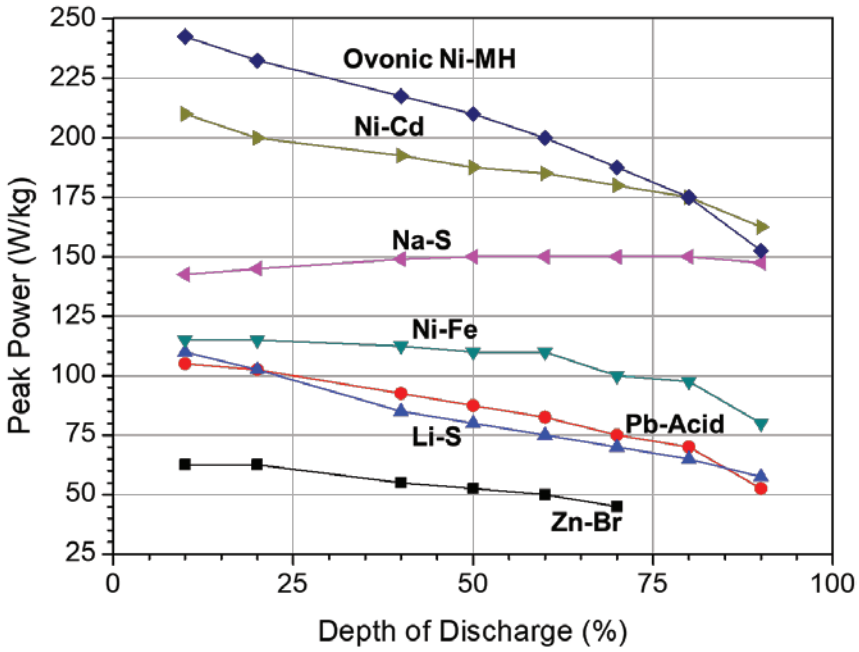

Fig. 2.11. Peak power vs. depth of discharge of some rechargeable batteries. Adapted from [77].

Compared to other rechargeable battery types, Ni-MH batteries have excellent characteristics in terms of specific energy, energy density, and operating temperatures. The safety and cost issues remain the challenge in the development of the Li-S, Ni-Cd, and Zn-Br batteries.

2.3. Development status of metal hydride alloys for Ni-MH batteries

Ni-MH batteries were invented in the 1980s and introduced into the market in the early 1990s resulting in the development of the mass produced commercially successful metal hydride battery anodes [45]. Nowadays, Ni-MH rechargeable batteries are within the most commercially successful power sources used in various consumer electronics, for stationary energy storage, and, most important, transportation appliances [78]. Toyota HEV Prius is a renowned example of a successful hybrid vehicle battery technology utilized in rechargeable Ni-MH batteries. According to Hong [79], the development of

commercial hydrogen storage electrode alloys for the metal hydride battery anodes is divided into three main intervals which are described in Table 2.2.

Table 2.1. Comparison of Ni-MH battery with other type of rechargeable batteries [80-84]

Properties	**Rechargeable battery type**						
	Ni-MH	**Ni-Cd**	**Na-S**	**Ni-Fe**	**Pb-Acid**	**Li-S**	**Zn-Br**
Nominal voltage, V	1.2	1.2	2	1.2	2.1	2.05	1.8
Specific energy, Wh/kg	60-120	40-60	150-240	19-25	35-40	500	34.4-54
Energy density, Wh/l	245	50-150	360	30	80-90	350	15.7-39
Cycle life, cycles	300-500	2000	2500	Repeated deep discharge does not reduce life significantly	< 350	1500	> 2000
Self-discharge, % per month	30	10	2-5	20-30	4-6	15	20
Operating temperature, °C	-20-60	-20-45	300-350	-40-46	-35-45	-40-60	20-50

As mentioned earlier, the performance of Ni-MH batteries is crucially dependent upon the properties of the metal hydrides alloys as the active materials of the negative electrodes. Many extensive studies have been conducted as related to the development of the hydrogen storage alloys for the electrochemical energy storage applications, including the rare earth-based AB_5-type alloys, the Ti- and Zr-based AB_2-type alloys, the Mg-based amorphous and nano-crystalline alloys, the rare-earth-Mg-Ni-based superlattice alloys, and Ti-V-based multicomponent multiphase alloys [45].

Table 2.2. Three main periods of the development of commercial hydrogen storage electrode alloys

Time	Alloys under development	Properties and challenges
1970s	AB- and AB_5-type alloys, including TiNi, TiFe, $LaNi_5$	Difficult to activate, short cycle life, low electrode capacity, affected by corrosion
	Conclusion: These alloys are not suitable for the commercial applications	
Early 1980s	Ti-Zr-based AB_2 alloys,	Capacity of 450 mAh/g at 25 mA/g current density, however, a cycle life needs to be improved
	The rare earth-based AB_5-type Ln–Ni–Co–Mn–Al alloys	Longer cycle life but smaller capacity
	Conclusion: These alloys have a potential for commercialization in the rechargeable Ni-MH batteries	
Late 1980s and early 1990s	AB_x-type multi-component alloys	Optimized performance as electrode materials by tailoring chemical composition of the alloys
	Conclusion: These alloys have a potential in improving their performances by achieving a higher electrochemical discharge capacity and longer cycle life	

2.3.1. Rare earth-based AB_5-type alloys

In the AB_5-type alloys, the A site consists of one or more rare-earth elements (La, Ce, Nd, Pr, Sm) were Mischmetal containing a natural mixture of rare earth metals (La-type Mm) is frequently used, while B site is composed by transition metals (Ni, Co, Mn, Fe), Al and/or Sn. AB_5 type allots possess a $CaCu_5$-type hexagonal structure (space group: *P6*/*mmm*) containing octahedral sites and three types of tetrahedral sites [17, 85]. In terms of hydrogen occupancy in the hydrides, H atoms prefer to occupy the tetrahedral sites, A_2B_2, AB_3, and B_4 (see Fig. 2.12) together with octahedral sites A_2B_4. One formula unit of $LaNi_5$ alloy can accommodate 6 hydrogen atoms to form the $LaNi_5H_6$ hydride which has electrochemical capacity of 372 mAh/g [2]. Unfortunately, a poor cyclic durability of $LaNi_5$ resulted in difficulties to accept it as a commercial battery anode material [86].

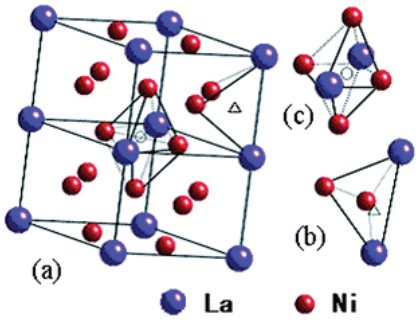

Fig. 2.12. Crystal structure of $LaNi_5$ alloy (a), the preferential for H atoms tetrahedral A_2B_2 sites (b), and octahedral sites A_2B_4 (c) [45].

By 1984, a breakthrough in improving the cyclic stability of $LaNi_5$ was achieved by partly replacing Ni atoms with Co leading to the commercialization of the Co-containing alloy [9]. This type of alloys showed capacities of 250-350 mAh/g depending on the choice and content of A and B components. In such alloys, the elements on the A site (La, Ce, Pr, and Nd) provide H storage and electrochemical capacities, whereas the elements on the B site control high catalytic activity (Ni), corrosion resistance (Fe), and high surface activity (Co, Mn, and Sn).

The most broadly utilized AB_5-type alloy composition for Ni-MH application is $MmNi_{3.55}Co_{0.75}Mn_{0.4}Al_{0.3}$ where Mm is a La-rich alloy with a composition $La_{0.62}Ce_{0.27}Pr_{0.03}Nd_{0.08}$ [87]. On reason for that is in a fact that this alloy contains less than 10 wt. % of Co which is the most expensive alloy component as its price accounts for nearly 40-50 % of the total cost of the raw materials used to prepare the alloy. Thus, a focus was put on the development of the low-Co or Co-free AB_5-type alloys by substituting Co with low-cost elements including Cu, Fe, Si, Cr, Sn, and Zn [88-94]. However, such a substitution negatively affected the alloys performance resulting in a lower discharge capacity and shorter cycle life due to the decreased content of Co.

Recent studies have been focused on the effect of the alloys preparation methods including annealing and rapid solidification on the performance of the low-Co or Co-free AB_5-type alloys by reaching an improvement in discharge capacities and the cycle life. Ma et al. reported that the increased discharge capacity - up to 309 mAh/g - and

improved (doubled) cycle stability occurred in the annealed at 1000° C/7 hours $MINi_{3.8}Co_{0.3}Mn_{0.3}Al_{0.4}Fe_{0.2}$ alloy [94]. At IFE, Weikang Hu, V.A. Yartys et al. studied Mg-containing Co-free AB_3-type La_2MgNi_9 alloy which was annealed at 900° C/6 hours yielding a discharge capacity of 360 mAh/g which was by 20 % higher than that for the commercial AB_5 alloy measured at the same conditions [95]. Based on the fact that AB_5-type alloys can only produce a capacity of about 300-360 mAh/g which is insufficient to satisfy the performance requirements of the commercialization of Ni-MH batteries, extensive studies are ongoing to develop advanced anode electrodes.

2.3.2. Mg-based amorphous and nanocrystalline alloys

The sufficiently high theoretical capacities of MgH_2 and Mg_2NiH_4 that reach 2200 mAh/g and 1080 mAh/g, respectively, and a low cost of the abundant raw materials resources allows to consider Mg-based alloys as a very promising candidate for use as hydrogen storage materials in the rechargeable Ni-MH batteries [96, 97]. Unfortunately, poor hydriding/dehydriding kinetics at ambient temperatures and rapid degradation in alkaline solutions restrained use of these materials in the Ni-MH batteries [98-101].

Many efforts to improve the Mg-based alloys included use of amorphous alloys [102], nano-crystallization [103, 104], alloying with other elements [105-107], all aimed to speed up the hydrogen diffusion process and the charge transfer reaction which establishes a high electrochemical capacity and improves resistance against corrosion in alkaline solutions [108]. However, a capacity degradation caused by the formation of $Mg(OH)_2$ hydroxide layer limits use of Mg-based alloys. Hence, new approaches are needed to prevent the oxidation/corrosion of Mg-containing materials.

2.3.3. Rare earth-Mg–Ni-based superlattice alloys

In the last decade, the rare earth-Mg–Ni-based (R-Mg–Ni-based) alloys have been developed and to become a promising next-generation negative electrode materials for high-energy and high-power Ni/MH batteries [45]. A modification of the alloys structures have been tried by introducing Mg into A side of $AB_{3.0\text{-}5.0}$-type rare-earth

based alloys eliminating the amorphization of the hydride phases and allowing to achieve a high reversible electrochemical capacity of 356 mAh/g [109]. Furthermore, Kohno et al found that a higher discharge capacity of 410 mAh/g was achieved for the $La_{0.7}Mg_{0.3}Ni_{2.8}Co_{0.5}$ alloy giving thus grounds to commercialize the R-Mg-Ni-based battery electrode materials for Ni-MH battery applications [110].

The introduction of Mg into the A site of $AB_{3.0\text{-}5.0}$-type rare-earth-based hydrogen storage alloys lead to the formation of the $(La,Mg)Ni_3$ phase with rhombohedral $PuNi_3$-type structure or the $(La,Mg)_2Ni_7$ phase with hexagonal Ce_2Ni_7-type structure [111]. These phases consist of the AB_5 unit ($CaCu_5$-type structure) and the AB_2 unit (Laves phase structure) which are rhombohedrally or hexagonally stacked with ratios of *n:1* along the *c*-axis direction as shown in Fig. 2.13.

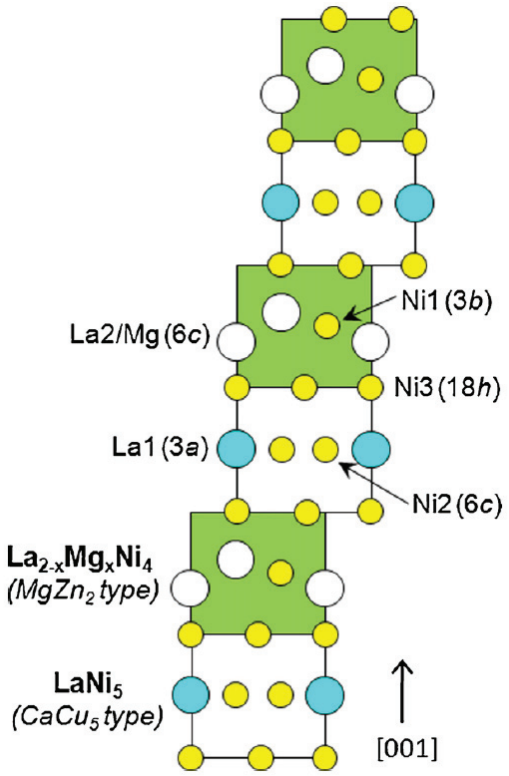

Fig. 2.13. Crystal structure of $La_{3-x}Mg_xNi_9$ compounds ($PuNi_3$ type) shown as a stacking of $LaNi_5$ ($CaCu_5$ type) and Laves type [112].

As we know, the composition and phase structure of the metal hydrides alloys determine their electrochemical performance. Thus, much efforts have recently been focused on achieving excellent properties of the rare earth-Mg–Ni-based (R-Mg–Ni-based) alloys by optimizing alloys composition [113], conditions of their homogenizing heat treatment [114], ball milling treatment [115], and surface treatment [116]. These measures will help to mitigate the negative influence of two major detrimental factors including the excessive self-pulverization of the alloy's particles and oxidation/corrosion of the alloys during the cycling eventually allowing to improve their electrochemical performance.

2.3.4. Ti- and Zr-based AB_2-type alloys

Intermetallic compounds of the AB_5 and AB_2 types have been successfully applied as negative electrode materials in Ni-MH batteries [55]. The hydrogen storage and electrochemical properties of the battery electrode materials are related to the type of the crystal structure of the intermetallic compounds [18, 117-122]. In the case of AB_5 type alloys, their hexagonal $CaCu_5$ type structure exhibits lower discharge capacities than AB_2 Laves type alloys [45].

To replace costly AB_5-type alloys, Ti- and Zr-based AB_2-type alloys have been developed as a new generation metal hydrides alloys for Ni-MH batteries applications [38, 79]. AB_2-type alloys have crystal structures of Laves type phases where A site with strong affinity for hydrogen (an early transition or rare earth metal) is surrounded by 16 other atoms, while B site with weak hydrogen affinity (last transition metals) contains smaller atoms surrounded by 12 neighbours [13-16]. Laves phases form topologically close packed structures with a geometrically ideal atomic radius ratio of $r_A/r_B \approx 1.225$ allowing the closest packing of the spheres [123, 124].

A combination of different types of A and B components (Fig. 2.14) leads to the formation of various structures. Kagome 6363 nets (A, B, C) are formed by smaller B atoms, whereas A_2B bucked nets (a, b, c) are formed by A and B atoms in a ratio 2/1 (see Fig. 2.14). 2-layer stacking of AcBc yields a C14 phase, while a 3-layer stacking of AcBaCb forms a C15 type phase.

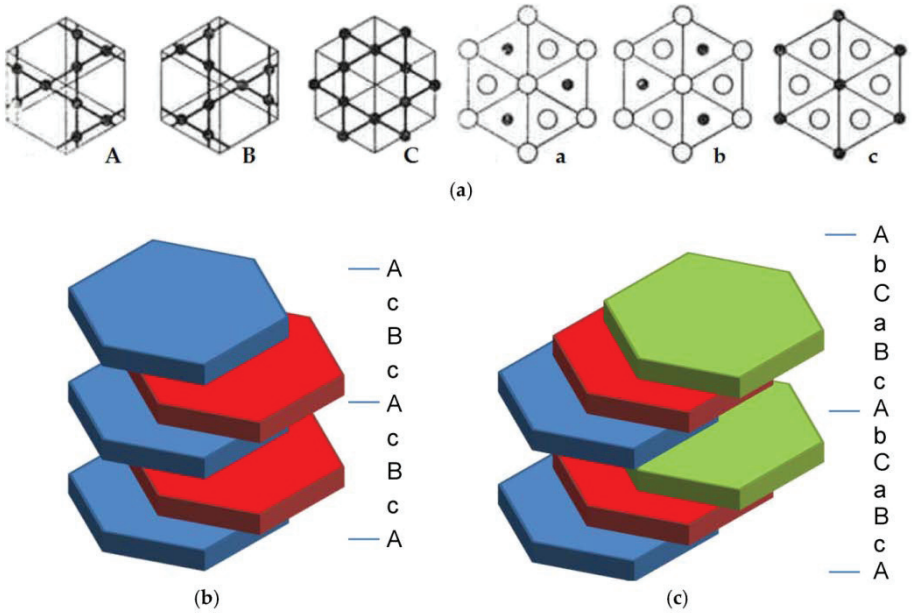

Fig. 2.14. A_2B buckled and flat Kagome 6363 nets formed by B-atoms only (a); stacking of the layers of C14 (b), and C15 (c) Laves phase structures. Adapted from [125].

For AB_2 Laves type compounds two types of structures are the most frequently formed, including an FCC C15 and a hexagonal C14 types. Their structures contain three different types of tetrahedral interstices, A_2B_2, AB_3 and B_4. The A_2B_2 cites are preferentially filled by hydrogen atoms in AB_2H_3 hydrides as shown by powder neutron diffraction studies [126].

Laves phase type structures are classified into three different structures which can absorb hydrogen including C14 hexagonal $MgZn_2$ (*$P6_3/mmc$*), C15 cubic $MgCu_2$ (*$Fd–3m$*), and C36 di-hexagonal $MgNi_2$ (*$P6_3/mmc$*) [124, 127-130] (see Fig. 2.15). The last one is rather seldom between the intermetallic structures. Furthermore, three types of interstitial sites in Laves phases are available to accommodate H atoms during the formation of the metal hydrides, A_2B_2, AB_3, and B_4 [13, 33, 125, 131]. However, not all these sites can be occupied at the same time as the sites with a common triangular face may not both accommodate hydrogen atoms into their centres. The distance between the centre of two

tetrahedral occupied by hydrogen sites sharing a triangular face is normally less than 1.6 Å, whereas the minimum distance between the individual H atoms is 2.0-2.2 Å [131].

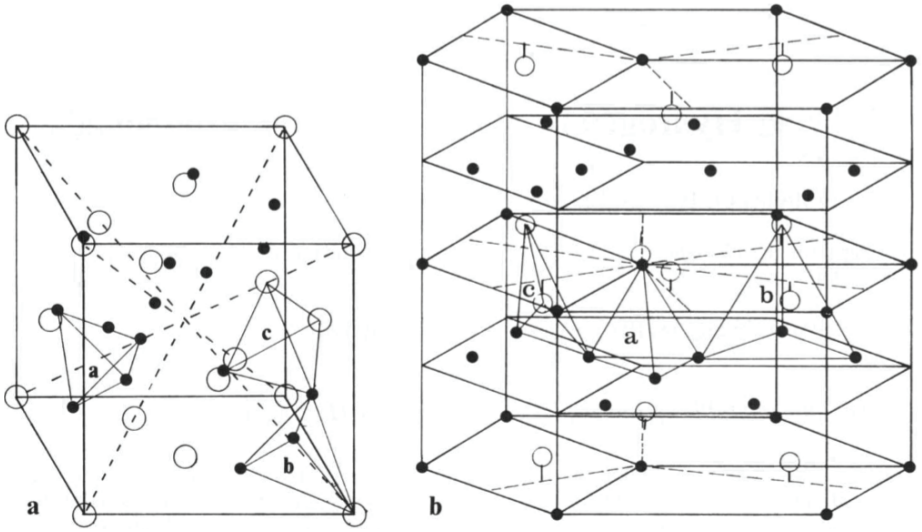

Fig. 2.15. Schematic drawings of cubic (a) and hexagonal (b) of Laves phase, open circle is A atom and black circle is B atom. The interstitial sites are shown as: (a) B_4 (b) AB_3 and (c) A_2B_2 sites. Adapted from [16, 132, 133].

Studies of AB_2-type alloys started by developing binary alloys, until the interest moved to the synthesis of the multielement metal hydrides alloys. Compared to the AB_5-type alloys, the multielement AB_2-type alloys show a better performance in achieving the higher discharge capacities being in the ranges from 370 to 450 mAh/g. As an example, the work by Ovshinsky revealed that $Ti_{0.55}Zr_{0.45}V_{0.36}Ni_{1.03}Cr_{0.3}Mn_{0.3}$ and $Zr_{0.57}Ti_{0.43}V_{0.36}Ni_{1.03}Cr_{0.3}Mn_{0.3}$ alloys achieved the discharge capacities of about 400 mAh/g at 0.25 C rate [53, 134].

Despite of the higher discharge electrochemical capacity, AB_2-type alloys suffer from the slow activation and low rate capabilities. Thus, in order to develop novel high-energy and high-power Ni-MH batteries by utilizing AB_2-type electrode alloys, considerable efforts related to the improvement of the performances are still required. Indeed, the present studies mainly concern to the alloys preparation methods in order to improve the properties and performance of the alloys in terms of discharge capacities, activation

performances, and cycle life stabilities. In our earlier reports, we presented the data confirming that that the optimization of the C14/C15 phase abundance can improve the overall electrochemical performance of the AB_2-type hydrogen storage electrode alloys [14, 135].

The C14 and C15 Laves phase behave differently when utilized as a negative electrode alloys of the batteries [14, 135-137]. C15 type alloys show excellent high rate dischargeability (HRD) performance and are easier to activate than C14 type alloys. In contrast, C14 type alloys are more appropriate for high capacity and long lifetime applications.

Feng and co-workers in their review paper concluded that a multiphase metal hydride alloy is preferable to achieve a better performance in the Ni-MH battery applications [55]. The use of non-stoichiometric compositions and multicomponent alloys can often improve the characteristics. As an example, multiphase AB_2 alloys, containing C14 and C15 Laves phases have their own specific roles, which allow to facilitate discharge capacities and to achieve improved activation performance, respectively. Thus, to achieve improved performance, the properties of multiphase metal hydrides alloys need to be optimized by adjusting the composition and by controlling the parameters of alloying.

2.3.5. Effect of alloying elements on the electrochemical behaviour, AB_2 alloys design concept

The interactions among the alloying elements in the MH system determine the properties of the alloys which are affected by the chemistry of the individual components [45, 46]. Table 2.3 shows the effect of individual selected elements on the electrochemical performance used for the synthesis of the studied AB_2 alloys based on the analysis of the reference data. In this present study, Ti, Zr, La, V, Mn, Fe, Ni components have been used as the contents of the C15 predominated alloys, whereas C14 predominated alloys are synthesized from Ti, Zr, V, Mn, Ni, Co, Cr, Al, Sn components.

Table 2.3. Effect of selected elements on the hydrogen storage and electrochemical properties of the studied AB_2 based metal hydrides

Elements	Preferable site		Individual properties	Ref
	A site	B site		
Ti	√	-	Complete solubility with Zr, when Ti is added into AB_2 alloy, hydrogen absorption capacity becomes smaller at the same H_2 pressure	[46, 126, 138, 139]
Zr	√	-	High electrocatalytic activity, improves, activation properties, mitigates oxidation, improve cycle life	[46, 140]
La	√	-	Improves the electrochemical activation behaviour	[46, 126, 141, 142]
V	√	√	When on B site in AB_2 alloy, improves hydrogen sorption capacity and kinetics	[46, 143-145]
Mn	-	√	As a catalyst, enhances the pulverization of the alloys, increases the mutual solubility of the other elements during solidification	[46, 54, 146]
Fe	-	√	Exhibits catalytic activity, improves activation performance	[46, 140, 147, 148]
Ni	-	√	High electrocatalytic activity, increases discharge capacity	[46, 54, 149, 150]
Co	-	√	Cycle life increases, exhibits catalytic activity, promotes incresed capacity at a relatively low discharge rate	[46, 54, 149]
Cr	-	√	Improves cycle life, enhances the corrosion resistance of the alloys	[46, 150]
Al	-	√	Increases the discharge voltage and significantly improves the high rate discharge capacities	[149, 151]
Sn	-	√	Improves cycle life and kinetics of hydrogen absorption and desorption	[152-154]

Metal hydrides alloys as the active materials for negative electrodes in Ni-MH batteries generally contain a multiple combination of different elements allowing them to operate in aggressive environment [49]. Moreover, all these materials have complex microstructures which are related to the technology used for their synthesis. By using multiphase and multielement alloys, hydrogen storage capacity, metal-to-hydrogen bond strength, acceptable catalytic activity and discharge kinetics, and sufficient

oxidation/corrosion resistance can all be optimized for the use of the alloys in Ni-MH batteries.

2.3.6. Effect of microstructure on the electrochemical behaviour

The electrochemical properties of a multicomponent metal hydrides alloys caused by the improvements are significantly affected by the alteration of a single-phase into the multiphase hydride forming materials [53, 155, 156]. Indeed, a multiphase hydride alloy consists of individual single-phase hydride forming materials and a second or even a third phase which are highly electrocatalytically active phases, and which are evenly distributed through the structure. Thus, the discharge performance of the multiphase hydride alloy shows improvements [56]. To produce such type of alloys, rapid solidification can be a viable option to apply, even though the uncertainty in morphological and microstructural variations caused by rapid solidification do not always lead to the improved performance.

Furthermore, the equilibrium microstructure composition can also be obtained by performing homogenisation annealing of the alloys [73, 95, 126, 157-165]. Obviously, the required time is much longer than the rapid solidification process.

2.4. Nano-structuring: Rapid Solidification

Nano-structuring is considered as a technique to improve the hydrogen storage performance of the materials by synthesizing them in a nanocrystalline state [166-178]. As a result of the nano-structuring, the number of grain boundaries increases thus increasing the diffusion rates of hydrogen atoms in the alloy. Furthermore, when the conditions of the rapid solidification are properly selected, this may lead to the minimization of the number of the secondary phases which do not contribute to the storage capacity and thus improve the overall H storage performance of the material. Hence, this results in the advanced performance at high rates of charge and discharge of the Ni-MH batteries [179, 180].

Rapid solidification is one of the nano-structuring techniques aimed to achieve in the materials where a molten metal or alloy are solidified very rapidly at rates of 10^6 K/s, at least at a rate of about 10^4 K/s (see Fig. 2.16) [181]. Rapid solidification affects the phase composition and structure of the solidified alloy. For the different compositions of the alloys, performing rapid solidification generates the differences in the phase composition, phase abundances, phase structures, morphology of the microstructures, and certainly affects the electrochemical performance of the melt spun alloys. All of these factors are simultaneously affected, and the mechanism of nano-structuring should be studied in order to perform optimization of the nanostructures.

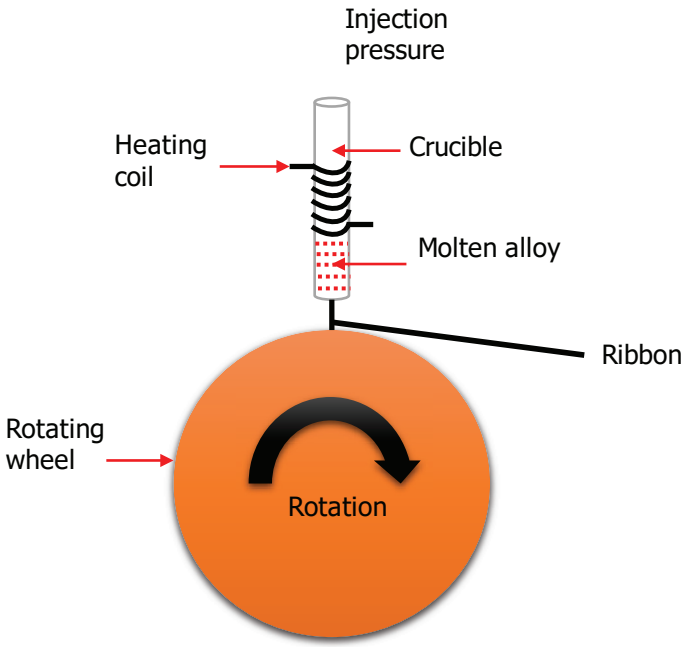

Fig. 2.16. Schematic of a melt-spinning apparatus.

To conclude, the rapid solidification generally affects the products [182] resulting in:

- Microstructure refinement;
- Extension of the range of solid solubility;
- Formation of metastable phases.

Rapid solidification can be classified into three categories: spinning, droplet solidification, and surface melting [183]. Melt spinning technique has been the most commonly used method since the 1970s allowing an accelerated progress of the rapid solidification technology to produce rapidly solidified ribbons with controlled shape and morphology [184]. In the case of the ejection of molten metal, the melt spinning process is distinguished as belonging to two different techniques, as free-flight melt spinning (FFMS), or a chill-block melt spinning (CBMS) if it is allowed to solidify against a cooled substrate [182, 185].

In this study, CBMS, or in short, melt spinning was used as a rapid solidification technique to process all alloys. The molten metal is heated by an induction coil until melting and is ejected from the nozzle on to the cold rotating Cu wheel to produce the melt-spun ribbon (see Fig. 2.16). Further to this, a pressurized gas flow is injected from the nozzle into the chamber to cool the melt [186].

Melt spinning has been performed to synthesize Zr- based Laves type alloys [169, 171, 172, 187]. It was observed that the refinements of the microstructure and grain sizes were achieved due to the rapid solidification. When using a slower speed of the wheel of the melt spinning setup, the more elongated ribbons were produced. Thus, more flakes are produced at higher wheel rotation speeds [181]. Besides that, thicker ribbons are in general expected to be produced at lower cooling rates as compared to the faster rotation speeds and quenching rates [188]. In addition to this, the change of the phase structures and the abundances of the C14 and C15 phases took place in line with the variation of the velocity of the wheel rotation. As a result, the performance of the ribbons also changed and was related to the conditions of the rapid solidification.

We performed melt spinning for different compositions of the alloys using variable speeds of the casting wheel/different quenching rates. The aim of the present study was to produce a nanostructured morphology of the alloys. We expected to achieve an improvement of the electrochemical performance of Zr-based AB_2 alloys by utilizing the melt spinning.

2.5. Requirements for metal hydride-based anode electrodes

The development of the batteries requires to achieve advanced performance of the electrode materials. As the active material of the electrodes, a hydrogen storage alloy has two major roles including being (a) electrochemical catalyst for the charge/discharge of hydrogen and (b) creating a reservoir storage for the absorbed hydrogen [79]. Hence to be a good hydride material for electrode application, Hong concluded that the required properties that must be fulfilled include:

- High reversible hydrogen storage capacity and suitable equilibrium hydrogen pressure,
- Easy activation,
- Good charge/absorption and discharge/desorption kinetics and efficiency,
- Low cost,
- Small hysteresis between charge-discharge isotherms,
- Excellent corrosion resistance in the KOH aqueous solution,
- Long cycle life.

Further to the above requirements, the specific properties of the metal hydrides used for the Ni-MH battery include [55]:

a) The desorption pressure of metal hydride should be between 0.1 and 1 atm at ambient temperature to ensure that the absorbed hydrogen can be easily desorbed while the hydride is stable against self-decomposition;
b) The equilibrium potential of metal hydride should be high enough (close to –0.9324 V against Hg/HgO) to reassure that a large amount of hydrogen can be completely released;
c) The enthalpy change of metal hydride formation should be between 25 and 50 kJ/mol H_2 [53] to achieve reversibility of the reaction and formation of the stable

M-H bonds, as if the M-H bonding is too stable, MH will not be able to electrochemically release hydrogen;

d) The oxidation and corrosion resistance of the metal hydride to the KOH solution should be sufficient to assure that the alloys can reach sufficient lifetime and cycle life;
e) The hydrogen diffusivity of metal hydride alloy should be high enough to ensure the hydrogen mass transport and charge transfer reactions efficiently take place.

Indeed, all the properties requirements to the metal hydride alloys are strongly influenced by the composition of the metal hydrides alloys. Therefore, the modifications to the alloy composition design, the structure, and control over the electrochemical process which takes place in the alloy, are required to achieve optimum performance of the Ni-MH battery [55]. Further to this, multiphase alloying and nano-structuring of electrode can be performed to improve the properties of the electrodes [53, 55, 134, 138, 189-199]. Thus, the present study is closely related to control and optimisation of these two kinds of properties aimed at the improvements of the metal hydrides alloys.

2.6. Summary of literature review and goals of the PhD project

Despite several decades have passed after the beginning of the research on use of metal hydrides as anode electrodes for the Ni-MH battery applications, further improvements in the performance of the electrode materials are still required and it is believed that such improvements can be reached by modifying their phase-structural composition and microstructure by achieving nano-structuring of the multielement alloys and by utilizing optimized techniques of their preparation.

The analysis of the reference data shows that by changing the composition of the hydrogen storage alloy, including the modification to the multicomponent compositions, or by adding electrocatalytic materials to facilitate the reaction of hydrogen uptake on charging and hydrogen evolution efficiency at the surface of the electrode, via adopting

the most efficient techniques of alloys preparation, an advanced performance of the Nickel Metal Hydride (NiMH) batteries can be achieved.

Earlier studies showed that AB_5-type alloys which were the first commercially used anode materials of the Ni-MH batteries (and still are) include the most broadly utilized composition of a multielement mischmetal-containing alloy $MmNi_{3.55}Co_{0.75}Mn_{0.4}Al_{0.3}$ with Mm = La-rich mischmetal and a composition $La_{0.62}Ce_{0.27}Pr_{0.03}Nd_{0.08}$. However, the limited discharge capacity range of AB_5 alloys which is about 300-360 mAh/g is a disadvantage caused by the fact that its $AB_5H_{5.0\text{-}6.0}$ hydride has a limited H storage capacity of around 1.3-1.4 wt.% H. Furthermore, the high price of raw materials in AB_5 alloys (rare earth metals and, also, cobalt) together with the limited availability of these raw materials put forward a task of replacing $MmNi_{3.55}Co_{0.75}Mn_{0.4}Al_{0.3}$alloy by alternative and improved anode electrode materials.

Other potentially interesting hydrogen storage materials are Mg-based hydrides. One example is Mg_2NiH_4 with an H storage capacity of 3.6 wt.% H and electrochemical capacity of 964 mAh/g. Unfortunately, Mg-containing hydrides are frequently too stable to allow hydrogen to be electrochemically discharged while another problem comes from their low corrosion stability in alkaline solutions resulting in oxidation of the alloys.

In contrast to the AB_5- and Mg-based hydrides, Laves type $AB_2H_{3\text{-}4}$ hydrides are able to reversibly store and release 1.8-1.9 wt.% H both during the metal-hydrogen interactions and also electrochemically when used as anode electrodes of the metal hydride batteries. Importantly, the properties of the hydrides can be optimized by optimizing composition on the A and B sites while the alloys show a reasonable stability in the electrolyte solution.

Thus, a very important R&D task on the way to develop better Ni-MH batteries is in a detailed study of the interrelation between the chemical and phase-structural composition of the alloys, particularly with respect to the formation of C14 and/or C15 intermetallics and ratio between C14 and C15, together with microstructural morphology of the alloys, as related to their electrochemical performance and their preparation

conditions. This area of research is not well studied, as this can be concluded from the analysis of the available reference data. One particular aspect of the research which should be particularly mentioned is an interrelation between the gaseous and electrochemical capacity in the metal-hydrogen system, being considered as an important tool to improve the electrochemical performance. Another interesting and important phenomenon which has not been sufficiently studied is establishing the rates of hydrogen diffusion in the materials as it defines their high-power performance at high applied current densities during their charge and discharge.

2.7. Goals of the PhD project study

The goal of the present work is to study how to achieve the advanced performance of the AB_2 type alloys as H storage materials and materials for the anode electrodes of the Ni-MH batteries with the objectives to reach increased discharge capacity, to achieve easy activation behaviour, increased cycle stability, high resistance to corrosion, increased hydrogen diffusion rates while arriving to the affordable price of the alloy as the electrode material.

These improvements include:

a) Selection and optimisation of the compositions of the advanced anodes decreasing/avoiding utilisation of expensive rare earth metals (which have a limited and controlled by China stock), which have an increased discharge capacity because of the high reversible storage capacity of the metal hydride alloys;
b) Improvement of the performance at high current densities and reaching an increased cycle life are aimed and will be achieved because of the use of multielement advanced anodes.

Nano-structuring and homogenizing treatments are selected as appropriate techniques to reach advanced electrode performance of the multielement AB_2 type alloys in order to achieve the favourable modification of the phase-structural composition together with

morphology of the alloys, thus enhancing their electrochemical performance as battery anodes.

The experimental work will involve several components, including:

- Preparation of the initial alloys by arc melting and annealing;
- Synthesis of nanostructured anode materials by rapid solidification. The purpose is to study how the nano-structuring is related to the electrode performance and to find optional compositions;
- The significant parts of the work will be phase structural and morphology and microstructure characterization. The microstructures will be studied using XRD and scanning (SEM) electron microscopy.
- Metal-hydrogen gas interactions will be studied by measuring the PCT diagrams of hydrogen absorption and desorption;
- Electrochemical characterization of charge-discharge at various power densities, using cycle life and impedance spectroscopy measurements will be done to relate the chemical composition of the electrodes, their microstructural state and electrochemical performance.

Particular focus of the work will be on:

- Study how the change of the element content in the $(Zr,Ti)(Ni,Mn,V,Fe)_{2\pm x}$ alloys will influence their H storage behaviours and their performance as metal hydride battery anodes. Select the alloys with optimized performance.

- Optimize B/A ratio in $AB_{2\pm x}$ type alloys on the properties and performance of the alloys in terms of their activation behaviours, rate performance, storage capacity of gaseous H, electrochemical discharge capacity of the anode electrodes, and hydrogen diffusion behaviours.

- Study of the effect of rapid solidification process on the phase structural composition and microstructural morphology of the multielement $AB_{2\pm x}$ type alloys. Study how

type of structure - C14 and C15 Laves type intermetallics - when rapidly solidified at variable wheel rotation speeds and quenching rates will affect their properties.

- Establish an interrelation between the microstructural and phase structural composition of the rapidly solidified alloys and their electrochemical performance, particularly with activation behaviours, rate performance, electrochemical discharge capacity, and hydrogen diffusion behaviours.

Chapter III

EXPERIMENTAL METHODS

The strategy of the experimental studies performed in the present PhD project is displayed in a scheme given in Fig. 3.1.

The materials were chosen for the detailed investigation of their electrochemical properties as metal hydride battery anodes and as H storage materials during the metal-hydrogen gas interactions. These alloys included 6 main components – Zirconium and Titanium as A components and Nickel, Manganese, Vanadium and Iron chosen as B components. Furthermore, small trace amount of Lanthanum was added as a catalyser. The atomic ratio between A components Zr and Ti was 85:15 and 80:20. The atomic ratio between the B components was fixed as 1.155:0.674:0.116:0.116 (Ni:Mn:V:Fe). Furthermore, Lanthanum additive was used at a trace level of 0.01-0.05 / (Zr+Ti) =1.

All alloys were prepared by arc melting in a protective Ar atmosphere and were modified by using various techniques.

Three major groups of factors were considered as being able to improve electrochemical and hydrogen storage performance of the alloys.

These include:

(a) Chemical composition of the alloys and their phase-structural state;
(b) Optimisation of the microstructure;
(c) Creating active towards hydrogenation surface of the alloys.

In more detail, choice of chemical composition is aimed at synthesis of Laves type alloys with ideal composition AB_2. Their composition could be changed to hypo-stoichiometric AB_{2-x} (e.g. $AB_{1.9}$) and hyper-stoichiometric AB_{2+x} (e.g. $AB_{2.08}$). These changes are accompanied by systematic variations of the thermodynamics of the metal-hydrogen

interaction and its kinetics, which we wish to optimize to suit the goal of using metal hydrides as Ni-MH battery anodes.

Furthermore, the phase structural state – formation of two Laves type structures of C14 and C15 types, will also depend on the stoichiometry of the studied alloys and their metallurgical state. Various types of such alloys were prepared and were tested as anode materials of the Ni-MH batteries.

Three different processing routes of the materials preparation were applied to the alloys including arc melting, rapid solidification, and homogenizing annealing.

When it comes to the preparation of the samples with active towards hydrogen surface, special activation treatments were performed including (a) adding of the catalyst materials to the composition of the parent alloys and (b) activation treatment of the powders of the parent alloys in a hot KOH solution.

A set of characterization techniques was used to probe the prepared alloys and to investigate their performance as anode electrodes of the MH batteries and hydrogen storage materials, including XRD, SEM, PCT, electrochemical charge-discharge experiments, and EIS. The conditions to prepare materials with advanced performance were established when this counts their high electrochemical capacity, high rate dischargeability, fast activation, and high cycle stability.

A flow chart of the detailed studies involving use of various experimental methods is presented in Fig 3.2. The figure shows the experimental techniques used to investigate two different types of alloys, C14 and C15 predominated alloys. Starting with the initial alloys prepared by arc melting process, parts of the alloy's ingots were used for their characterizations. This characterisation was performed for the as-cast alloys and for the alloys processed by rapid solidification with the melt spinner rotation wheel speeds selected at 5, 16.5, 33, and 100 Hz. The properties and performances of the resulting ribbons were then characterized in detail.

Similar to the C14 predominated alloys, the ingots of C15 alloys (hypo-stoichiometric, stoichiometric, and hyper-stoichiometric compositions) were characterized in as-cast state. Furthermore, hyper-stoichiometric C15 alloys were rapidly solidified using three-wheel rotation speeds of 5, 16.5, and 33 Hz. The obtained ribbons were further characterized. In addition, part of the hypo-stoichiometric and stoichiometric alloy ingots was annealed at 950° C for 24 hours. The annealed alloys were characterized by measuring the PCT isotherms of hydrogen absorption and desorption.

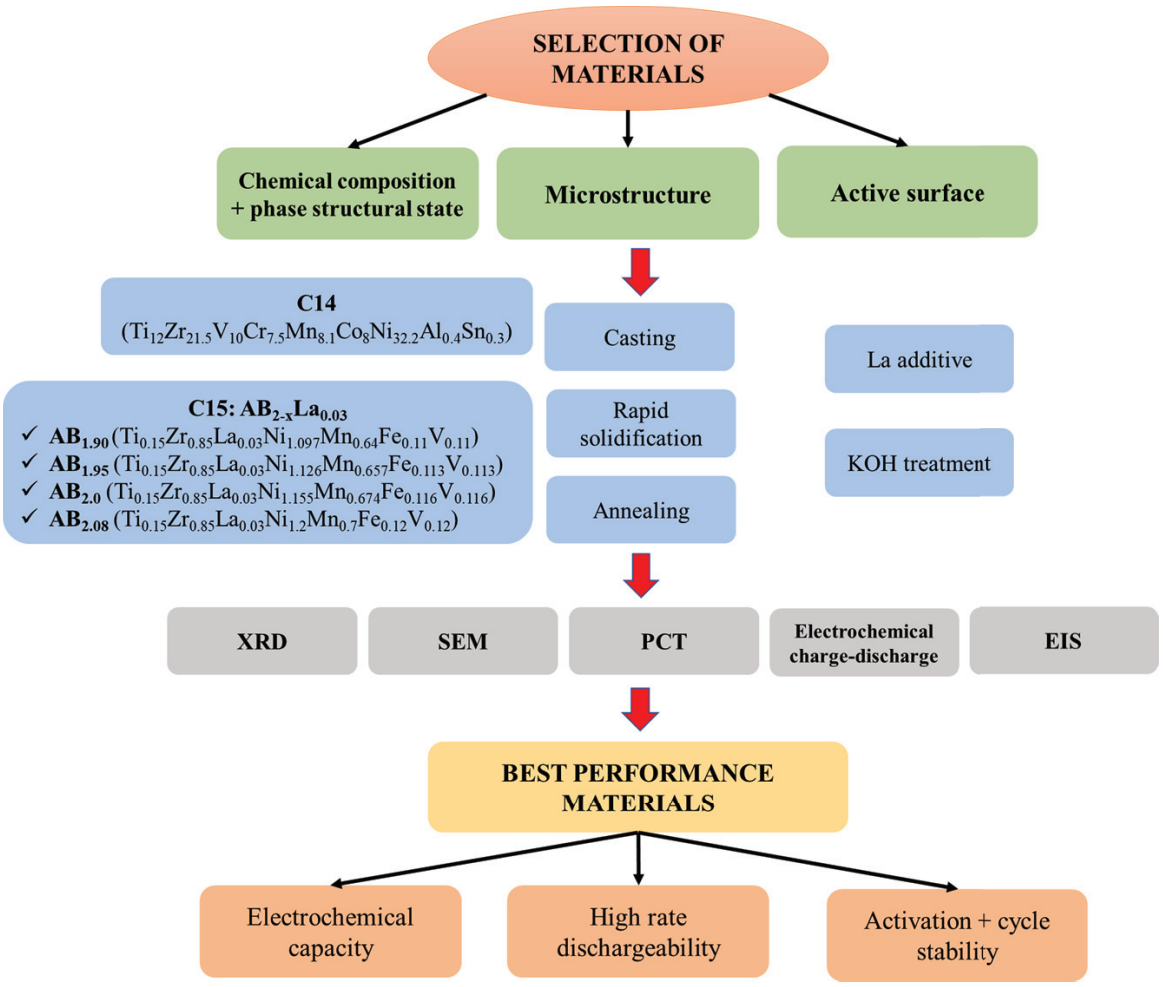

Fig. 3.1. Flow chart describing the performed experimental studies.

The sample preparation and applied characterization methods are described in detail in the following sections.

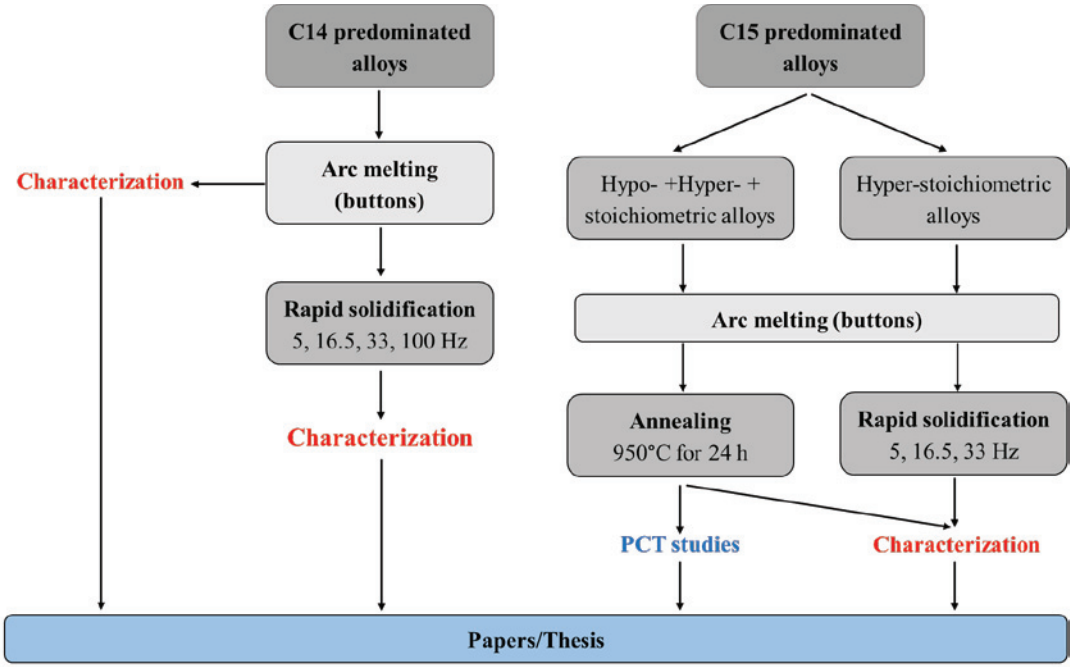

Fig. 3.2. Scheme presents the experimental methods applied in the present work. Characterization techniques include: XRD, SEM, Auger Electron Spectroscopy (AES), Electrochemical Impedance Spectroscopy (EIS), and measurements of the hydrogen absorption-desorption isotherms (PCT) using Sievert apparatus.

3.1. Materials preparation and alloys synthesis

In the present study, C14 and C15 predominated alloys were prepared by arc melting of the multi-component mixtures. The purity of the constituting elements was higher than 99.7% in each case.

Approximately 10 grams for each alloy were arc melted on a water-cooled copper hearth under argon atmosphere and re-melted three times to improve their homogeneity (see Fig. 3.3) using an Edmund Bühler AM/0.5 arc melter. Prior to the arc melting process, 3-4% excess of Mn as compared to the listed stoichiometry was added to the components used to prepare C14 and C15 predominated alloys, while 10% excess of Mn was added

to the rapidly solidified hyper-stoichiometric alloy to compensate for a higher rate of Mn evaporation.

Fig. 3.3. Edmund Bühler AM/0.5 arc melter.

The studied alloys included two types of alloys: (a) C14 alloy with the composition of $Ti_{12}Zr_{21.5}V_{10}Cr_{7.5}Mn_{8.1}Co_8Ni_{32.2}Al_{0.4}Sn_{0.3}$; (b) C15 alloys with composition $AB_{2-x}La_{0.03}$. In this latter case, three different compositions of C15 alloy were studied: stoichiometric $AB_{2.0}$ alloy, hyper-stoichiometric $AB_{2.08}$ alloy and two hypo-stoichiometric $AB_{1.9}$ and $AB_{1.95}$ alloys. Their compositions are presented in Table 3.1.

Table 3.1. Chemical compositions of the studied alloys $AB_{2-x}La_{0.03}$ (in atoms/$AB_{2-x}La_{0.03}$)

Alloys	Ti	Zr	La	Ni	Mn	V	Fe	B/A
$AB_{1.9}$	0.15	0.85	0.03	1.097	0.64	0.11	0.11	1.90
$AB_{1.95}$	0.15	0.85	0.03	1.126	0.657	0.113	0.113	1.95
$AB_{2.0}$	0.15	0.85	0.03	1.155	0.674	0.116	0.116	2.0
$AB_{2.08}$	0.15	0.85	0.03	1.2	0.7	0.112	0.112	2.08

3.1.1. Rapid solidification process of C14 and C15 predominated alloys

The rapid solidification process of the C14 predominated alloys was performed at National Centre for Scientific Research (CNRS, France) by using a SC Edmund Bühler setup, while C15 predominated alloys were rapidly solidified at NTNU (see Fig. 3.4). A scheme of the used melt spinning apparatus is shown in Fig. 2.16.

As mentioned earlier, the ingot of approximately 5 grams resulting from the arc melting was used as master alloys for the rapid solidification. The alloy pieces were placed into a boron nitride crucible (Fig. 3.4. (c)) located inside the melt spinner. Before the melting process, the chamber of the melt spinner has been evacuated under vacuum and flushed by Helium gas several time before filling the chamber to reach a pressure of 400 mBar He which was kept constant during the melt spinning, During the casting the distance between the wheel and the crucible with the melt was about 1.0 mm. Helium was used instead of Argon gas in order to reach a higher solidification rate as Helium gas has a higher heat conductivity as compared to that of Argon gas.

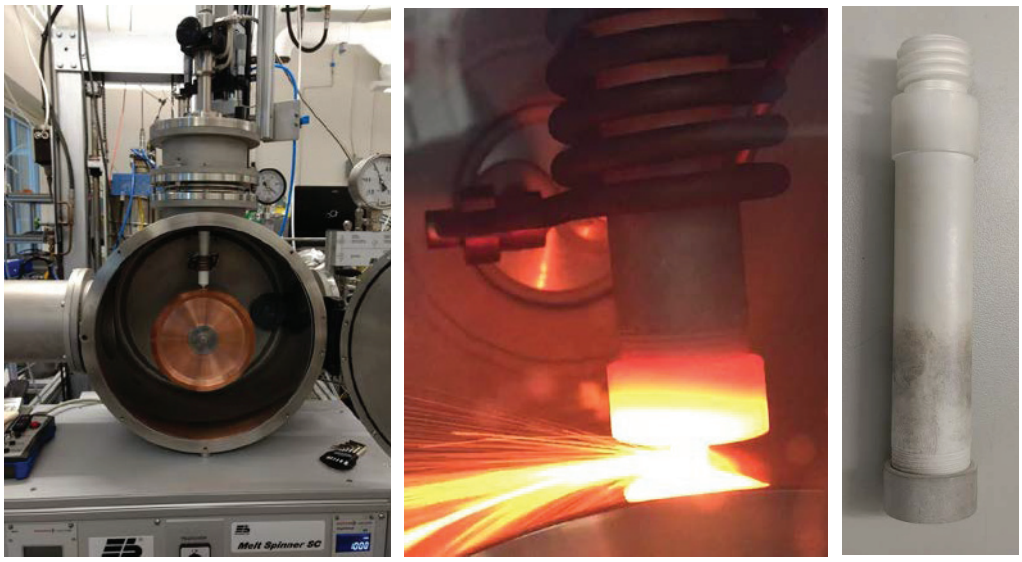

(a) (b) (c)

Fig. 3.4. SC Edmund Bühler melt spinner at NTNU (a); the rapid solidification process proceeds when molten metal is ejected from the crucible onto a rotating copper wheel (b); boron nitride crucible (c). Courtesy: Live Mølmen (b).

Prior to the casting process, the ingots were melted using an induction coil. The molten metal was then immediately ejected onto the copper rotating wheel with a diameter of 20 cm where the ribbons were produced. The wheel rotation speed was varied at 5, 16.5, 33, and 100 Hz (only applied for C14 predominated alloys) resulting in the variation of the ribbon dimensions – length and thickness (see Fig. 3.5).

3.1.2. Annealing of C15 predominated hypo-stoichiometric, stoichiometric, and hyper-stoichiometric alloys

The chemical compositions of C15 predominated alloys ($AB_{1.9}$, $AB_{1.95}$, $AB_{2.0}$, and $AB_{2.08}$) are shown in Table 3.1. The as-cast alloy ingot produced by the arc melting process was sealed in the stainless-steel sample tube holders filled with Argon gas and then transferred into an annealing furnace. The ingots of $AB_{2.08}$ alloy was subsequently annealed at 950 °C for 16 hours, whereas for $AB_{1.9}$, $AB_{1.95}$, and $AB_{2.0}$ alloys, annealing of

950 °C was applied for 24 hours. Afterwards, all the alloys were quenched into cold water (4 °C) which resulted in their homogenization.

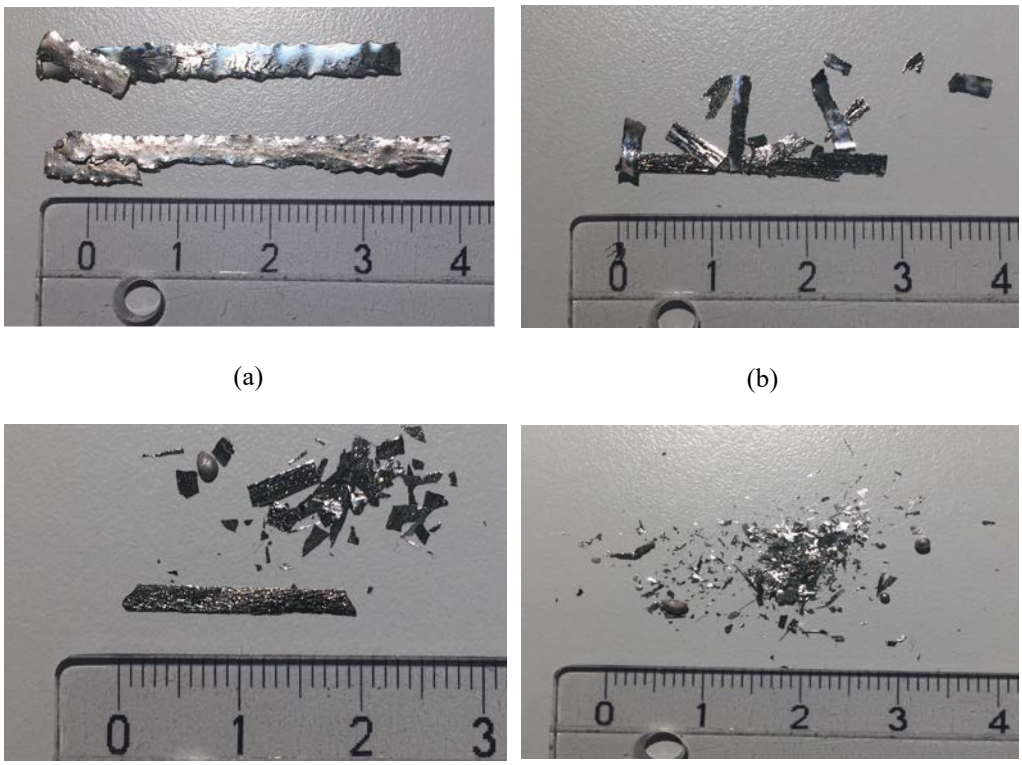

(a) (b)

(c) (d)

Fig. 3.5. The produced using a melt spinner with different wheel rotation speeds ribbons of C14 predominated alloys obtained at 5 (a), 16.5 (b), 33 (c), and 100 (d) Hz.

3.2. Hydrogenation studies and measurements of the PCT isotherms

Hydrogen storage performance of the alloys was characterized using a volumetric method and a Sieverts type apparatus shown in Fig. 3.6. The powdered samples, about 0.5–1 gram in mass, were inserted into a stainless-steel sample cell placed into a thermostated autoclave and activated in vacuum at 300 °C for 30 minutes. Alloys activation was done by performing several complete hydrogen absorption-desorption

cycles. The hydrogen absorption-desorption isotherms were measured after a completion of the alloy's activation and performed at 20, 50 and 80 °C (293, 323 and 353 K).

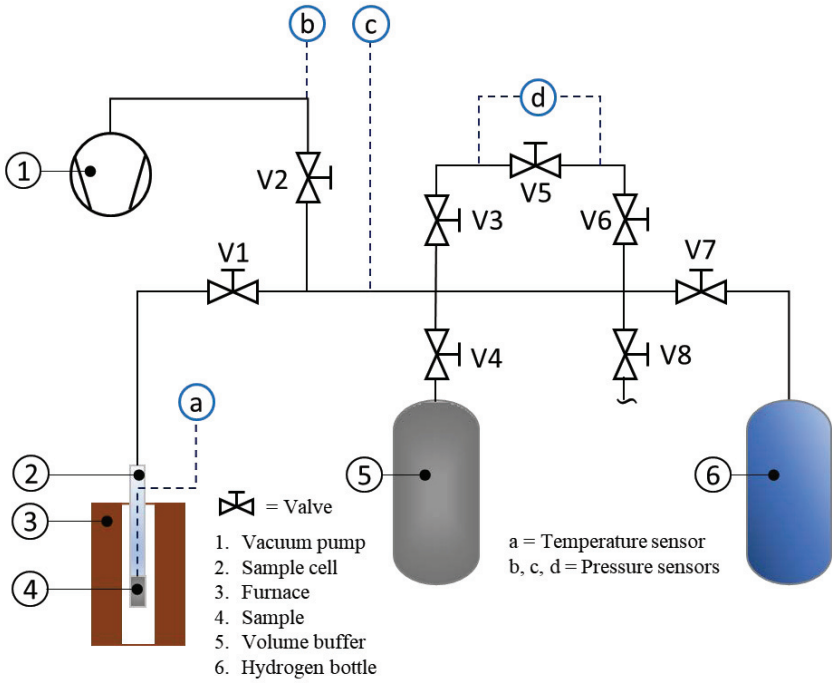

Fig. 3.6. Scheme of the PCT setup used for the measurements of the isotherms by Sievert's volumetric method.

3.1. Electrochemical measurements

3.3.1. Samples preparation

For the samples preparation, the ingot resulting from the arc melting process and the ribbon produced during the rapid solidification was crushed into the powders and sieved (see Fig. 3.7. (a)). The powder with the size of 40-60 μm was selected and mixed with a Carbonyl Nickel powder with a specific surface area of ~0.7 m^2/g in a weight ratio of 1:4 to assure a good conductivity of a MH anode (see Fig. 3.7. (b)). The mixture was then cold-pressed into a mould with a diameter of 10 mm under a pressure of 12 MPa for 5-6 minutes (see Fig. 3.7. (c)) to produce a 10 mm pellet which was further sandwiched between two nickel foams to secure good electrical conductivity at the anode

particularly after the activation performances of the electrodes resulting in their "breathing". Prior to this, the nickel foams (20-40 mm size) were spot welded to the two nickel strips with a size of approximately 5x10 and 5x100 mm respectively which were used as the contacts for the anode (see Fig. 3.7. (d)).

3.3.2. Measurements setup

A three-electrode measurement system consisted of a half-cell containing a MH alloy used as a working electrode, a sintered $Ni(OH)_2$/NiOOH plate obtained from a commercial supplier utilized as a counter electrode, and a mercury/mercury oxide (Hg/HgO) electrode as a reference electrode and was used to study the electrochemical performance of a MH anode. The electrochemical measurements were performed at room temperature using a LAND CT2001A Battery Tester in an open-to-air flooded cell configuration with the measurements done using a $Ni(OH)_2$/NiOOH counter electrode and a galvanostatic charge-discharge method (see Fig. 3.8).

Three features of the metal hydride anode including its activation behaviour, rate ability, and cycling stability were characterized for the selected alloys during the electrochemical testing. For studying the activation performance, 100 mA/g current density was applied to charge the electrodes for 5 hours, followed by a 30 minutes rest and further discharge of the electrodes. The same rate was applied until reaching a cut-off voltage of –0.7 V. Normally, 5-7 cycles are required to fully activate the electrodes. However, the cycling activation was extended if required to reach the full capacity of the electrodes. Further to the activation performance, to quickly and easily activate the alloy, KOH treatment was applied to the hyper-stoichiometric alloy by immersing the powder of 40-60 μm in size into a hot KOH solution which was kept at 90° C for 5 minutes. The powder was then rinsed using deionized water before preparing a pellet for the measurements.

(a)

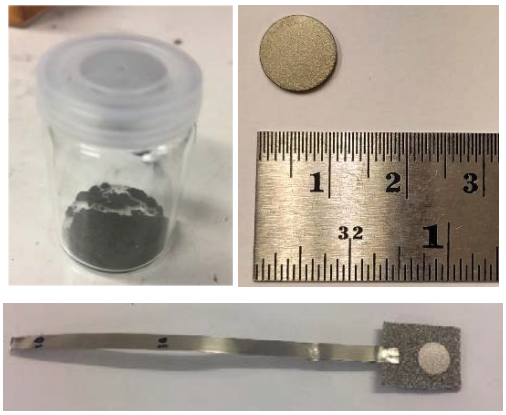

(b)

(c)

(d)

Fig. 3.7. Mortar (right) and sieve (left) (a), a powder (left), and a pressed 10 mm pellet (right), a sandwich structure of the nickel foam and the pellet prepared for the electrochemical tests (b), a press (c), and a welding apparatus (d).

Different current densities in the range of 10-500 mA/g were used to characterise the assembled Ni-MH battery anodes until reaching a cut-off voltage of –0.6 V. A capacity decrease was observed with increasing current densities. The flatter curve was indicative for a better rate performance of the alloys as battery anodes.

In terms of cycling stability performances, a current density of 300 mA/g was applied to charge and discharge the selected anodes for 500 cycles. The cycling stability was evaluated by a rate of capacity retention against the applied cycle number.

3.4. Electrochemical impedance spectroscopy (EIS) measurements

Electrochemical Impedance Spectroscopy (EIS) measurements were performed using SP-300-Potentiostat from Bio-Logic Science Instruments aimed to characterize the electrochemical behaviour of the metal hydride electrodes which included studies related to the kinetics of hydrogen diffusion in the electrodes and characterization of the surface reactions [200] (see Fig. 3.9). Galvanostatic Electrochemical Impedance Spectroscopy (GEIS) technique was applied in the present study by performing the measurements at 0.1 kHz ─ 0.5 mHz frequencies with the 10-mA current amplitude.

In order to determine the different components contributing to the overall resistance of the system containing electrode and electrolyte, EIS measurements were performed at high and at low frequencies [201] (see Fig. 3.10 (b)). Use of high frequency measurements allows to measure a lower in value contribution of the electrolyte resistance to the total resistance. In contrast, Warburg impedance is monitored in the low frequency range.

The activation treatment has been performed prior to the EIS studies of the MH anodes. By varying the State of Charge (SoC) or Depth of Discharge (DoD) on the Ni-MH battery anodes, a better understanding of their electrochemical performance has been achieved.

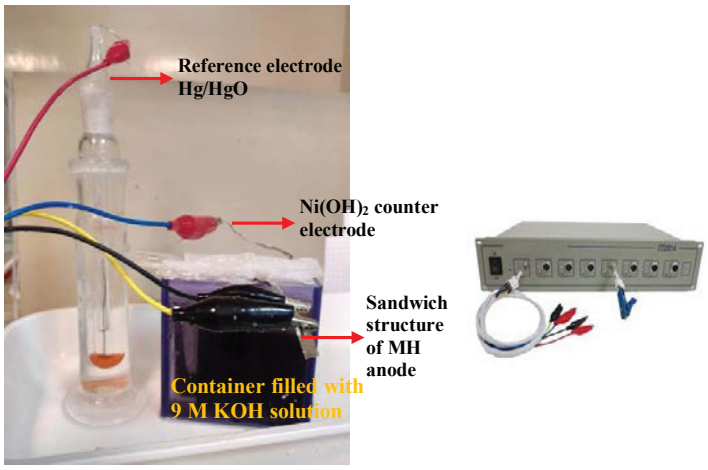

(a) (b)

Fig. 3.8. An experimental setup consisting a half-cell for the electrochemical testing built of a glass tube filled with Hg/HgO as a reference electrode, a container filled with 9 M KOH solution, a $Ni(OH)_2$ counter electrode, and a sandwich structure of MH anode (a) and a LAND CT2001A Battery Tester used in the present electrochemical study (b).

In the case of rapid solidification and annealing on the hyper-stoichiometric alloys, four different SoC of the electrodes were selected for the EIS studies, including SoC 0 (completely discharged anode), 30 %, 70 %, and 100 % (fully charged anode). All EIS measurements were carried out for the alloys after performing their activation and studies of the rate abilities.

The EIS characterization of the annealed hypo-stoichiometric and stoichiometric alloys was performed by studying the electrodes with 50 % SoC which went through a different number of cycles, namely after the cycling for 10, 100, 200, 300, 400, and 500 cycles.

The measurements of the EIS impedance plots resulted in spectra showing a complex shape (Fig. 3.10). These spectra were fitted with the equivalent model circuit by using EC-Lab® software of Bio-Logic Science Instruments. Such modelling resulted in excellent fit of the experimental data described by the Nyquist impedance plot. In order to reach the best fit of the experimental data, this data was deconvoluted into three constituent parts, describing contact resistance, charge resistance and Warburg straight line (see Fig. 3.11). A superposition of the individual components of the EIS spectra resulted in excellent agreement between the experimental data and the modelling results (see Fig. 3.11).

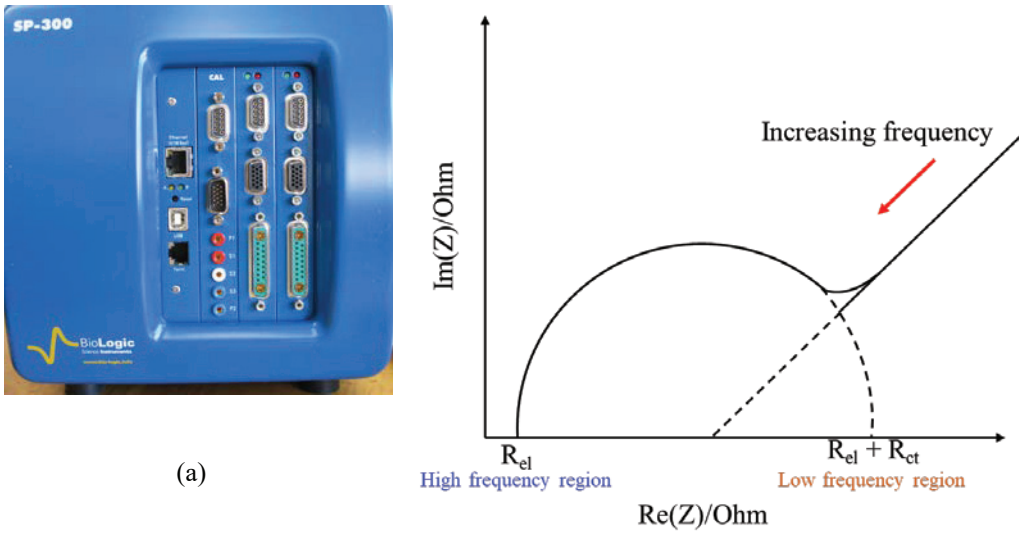

(a) (b)

Fig. 3.9. SP-300 – Potentiostat by Bio-Logic Science Instruments used for EIS characterization in the present study (a) and a complex plane impedance plot for modelling the Randles equivalent circuit. Increasing frequency of AC signal perturbation (high frequency region) causes the disappearance of the Warburg impedance (straight line). The Warburg impedance only exist in the low frequency region where the mass transfer is a limiting step. In contrast, the charge transfer as a limiting step only takes place in a high frequency region, where the electrolyte resistance (R_{el}) can be monitored (b).

The quality of EIS data fit and extent of success in deconvolution of the data were determined by the goodness of fit (χ^2) and Coefficient of determination (R^2) values. A goodness of fit (χ^2) value of less than one is confirms that the applied model provided an acceptable fitting of the experiments [202]. An excellent quality of the deconvolution was confirmed by the value of the Coefficient of determination (R^2) value of 0.99, which is close to 1. The higher the value of R^2 achieved, the better quality of the fit can be concluded.

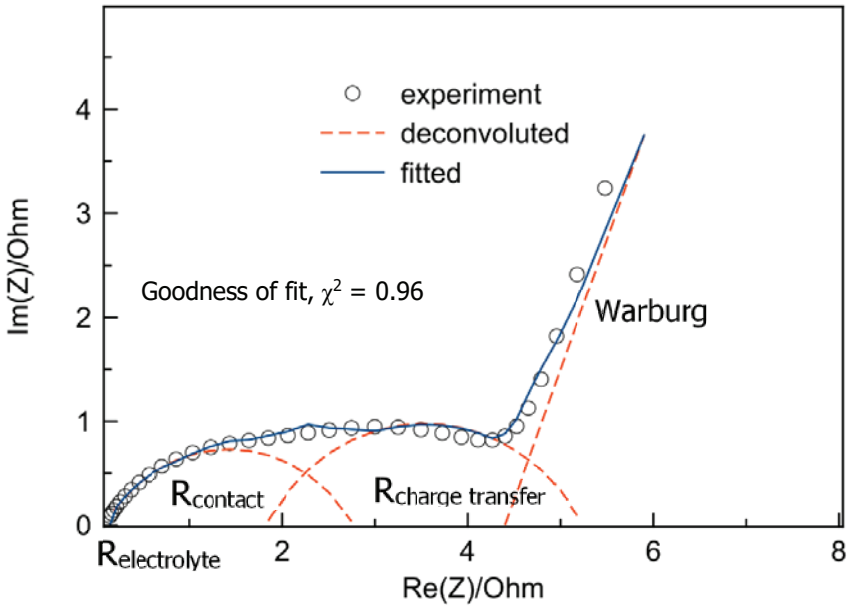

s

Fig. 3.10. The deconvolution of Nyquist impedance plot for 0% SOC of the electrode prepared from the as-cast alloy by using a superposition of equivalent circuits [73].

The equations to calculate the goodness of fit (χ^2) and Coefficient of determination (R^2) are presented below [203]. The coefficient of determination R^2 has a value between 0 and 1. A value of R^2 close to 1 indicates that most of the response variation of the data is explained by the different input values, whereas a value of R^2 near 0 indicates that a small share of the variation is explained by the different input values. In the present study, Coefficient of determination (R^2) value was 0.96 indicating that our deconvolution model can explains a reasonable value of 96 percent of the variation in the Nyquist plot impedance data [204].

$$\chi^2 = \sum_{i=1}^{n} \frac{|Z_{meas}\,(i) - Z_{model}\,(f_i, param)|^2}{SD_i^2}$$

where,

Z_{meas} (i) = measured impedance at f_i frequency
Z_{model} (f_i, param) = function of chosen model
f_i = frequency
param = model parameters: $R_{electrolyte}$, $R_{contact}$, $CPE_{contact}$, CPE_{ct}
SD_i = standard deviation

$$R^2 = 1 - \left\{ \sum_i \frac{(y_i - f_i)^2}{(y_i - \overline{y})^2} \right\}$$

where,

y_i = experimental data
f_i = calculated data
$\bar{y}$ = mean value of the experimental data

3.5. Characterization methods

In the present studies, the characterization methods of phase structural characterization methods included X-Ray diffraction (XRD), the microstructural characterization using SEM equipment, and Auger Electron Spectroscopy (AES) characterization.

3.5.1. Phase structural characterization

All studied alloys, including as-cast and melt-spun ribbons were mechanically crushed and ground to powders with the sizes below 40 μm to perform phase structural characterization by using X-Ray diffraction. In addition to this, Rietveld refinements were performed on the resulting XRD pattern using the GSAS suite of programs with the EXPGUI interface [205].

The different X-Ray diffractometers were used as a result of collaboration between the universities and research institutions and were utilized to characterize the phase structural composition of the MH anode alloys, including:

- A Siemens D500 BRAUN X-ray diffractometer with $CuK_{\alpha 1}$ radiation with a measurement range from 20° to 120°;
- A Bruker D8 Focus diffractometer with Cu-K_α radiation used for the measurements in the 2θ angle range of 10° to 90° and a step size of 0.00157°;

- A Rigaku MiniFlex 600 BenchTop X-Ray diffractometer with a CuK_{α} radiation (λ=1.5418 Å) having a flat plate geometry, with a measurement range from 20° to 80° and a step size of 0.01°;
- A monochromator-equipped Bruker D8 diffractometer (λ= $CuK_{\alpha 1}$ 1.5418 Å, step-size: 0.01975° 2θ, Bragg-Brentano geometry), with a measurement range from 10° to 120°.

3.5.2. Microstructural characterization

The as-cast and melt-spun ribbons alloys were embedded into SpeciFix Resin (Struers) and Epofix epoxy and polished, first using a mesh size range of 800-4000 SiC grinding paper, secondly with the diamond solution which has a particle size of 3 and 1 µm.

Similar to the phase structural characterization, the different equipment for SEM characterisation was used to characterize the microstructural structural of MH batteries anodes:

- A TESCAN VEGA II XMU SEM with OXFORD INCA X–Sight EDX Detector;
- A JEOL JSM6320F SEM equipped with EDS analysis;
- A LV-FE SEM of the Zeiss Supra 55VP type along with EDS analysis;
- A HITACHI FlexSEM 1000 VP-SEM equipped with EDS analysis.

Chapter IV

DISCUSSION

4.1. Effect of chemical composition - Zr/Ti ratio and selection of B – Mn, V, Fe, Ni - on the electrochemical performance

Constituent elements contributing to the chemical composition of the metal hydride alloy have their own role in influencing hydrogen storage performance. In this work the studied multicomponent Zr- AB_2 based Laves phase alloys contain 7 elements, including Ti, Zr, and a minor amount of La on the A site, and Mn, Ni, V, and Fe on the B site.

The selection of these particular elements on the A and B sites is based on our own in-house earlier performed research and on the analysis of the references data [31, 206, 207]. Maeda et al. [31] reported that 1% addition of La to $Ti_{0.24}Zr_{0.76}Ni_{1.2}Mn_{0.64}V_{0.14}Fe_{0.18}$ alloy improved the cyclic stability. Indeed, an investigation of a relationship between compositional changes and PCT properties in $(Ti,Zr)(Ni,Mn,X)_2$ (X=V, Cr, Fe) alloy showed that by adjusting the B/A ratio, Ti/Zr ratio, V and Ni concentration, an alloy with an excellent properties including a broad and flat plateau region with small hysteresis could be designed (Morii et al. [207]). Specifically, modifying the composition of $Ti_{0.2}Zr_{0.8}Ni_{1.3}Mn_{0.5}V_{0.2}$ alloy to $Ti_{0.24}Zr_{0.76}Ni_{1.155}Mn_{0.63}V_{0.1365}Fe_{0.1785}$ alloy resulted in a significant change of the slope and the width in a plateau region - from 0.71 to 0.14 and from 1.18 wt.% H to 1.45 wt.% H, respectively. At the same time, the hysteresis factor remained unchanged (0.07) during this modification.

As mentioned in a previous section, each element has several functions, including changes in the activation properties and cycle life (Zr), improved electrochemical activation behavior (La), enhanced catalytic activity in the hydrogen-involved redox reaction (Ni), improved surface activity to achieve fast hydrogen absorption-desorption

performance (Mn), increased hydrogen sorption capacity and kinetics (V), and increased corrosion resistance (Fe).

When it comes to the effect of titanium, it allows to achieve an important modification of the thermodynamic stability of the hydrides, without negatively affecting the storage capacity. This influence is based on the chemical similarity of Zr and Ti which allows to partially substitute Zr for Ti without change of the phase-structural composition of the alloys. As Ti is significantly smaller in size (1.46 Å) as compared to Zr (1.60 Å), this causes shrinking of the unit cells of the alloys and correspondingly destabilizes the formed hydrides (their enthalpy of formation decreases while equilibrium pressure of H_2 desorption increases following an increase of the content of Ti and a decrease in the content of Zr). This allows to finely tune stability of the hydrides by applying reasonably small changes in a ratio Zr/Ti. In our work, we used the alloys with atomic ratios Zr : Ti of 80/20 and 85/15.

The studied AB_2 type alloys consisted of C14 and C15 Laves phases as the main constituents. In such alloys, C15 phase favors an easy activation and provides excellent high-rate discharge ability (HRD) (ratio between the capacity at high discharge rate to that at a low discharge rate). In contrast, C14 phase brings a high capacity and a long cycle durability. Further to this, an appropriate composition ratio between C14 and C15 Laves phases contained in the metal hydride alloys allows to reach excellent performance of the Ni-MH battery anodes because of a synergy in the electrochemical performance of these two materials.

The modification of chemical composition of the metal hydride alloys can significantly affect the hydrogen storage properties of Ni-MH battery due to the change of the content of the phases in the alloys. The changing composition of Zr/Ti from 80/20 as in our earlier publication [126] to 85/15 in the present study resulted in some increase in the discharge capacity from 360 mAh/g to 370 mAh/g, respectively. Increased Ti content resulted in a decrease of the unit cell parameters and unit cell volume shrinking for the C15 type Laves phases which may cause a better performance at high current densities.

Importantly, by adjusting the B/A ratio to get hypo-stoichiometric (B/A<2), stoichiometric (B/A=2) or hyper-stoichiometric (B/A>2) alloys and by only allowing the change of ratio between the B and A components, caused extraordinary changes in hydrogen storage performance. A discharge capacity of 495 mAh/g has been achieved for the optimised chemical composition (hypo-stoichiometric with B/A of 1.95 while earlier studied hyper-stoichiometric alloy $AB_{2.08}$ showed a capacity of 370 mAh/g only. This favourable effect has been caused by changing the B/A ratio from hyper-stoichiometric to hypo-stoichiometric one (see Fig. 4.1.).

Change in the chemical composition also allows to optimize the ratio between C14 and C15 phases in the metal hydride alloys and can be achieved by changing the Zr/Ti ratio, ratio (Zr+Ti)/B, and by performing a rapid solidification process. As it can be seen from the Fig. 4.1., by applying quenching at 16.5 Hz to the as-cast C14 type alloy, results in an increase in maximum discharge capacity from 387 mAh/g to 435 mAh/g which could be associated with the change of composition of the Laves phases in the alloys. Indeed, performance of the RS at 16.5 Hz C15 type alloy caused an increase in the discharge capacity from 314 mAh/g to 414 mAh/g. On the other hand, electrochemical capacity dramatically dropped down to 195 mAh/g when using 33 Hz rapid solidification speed. Thus, the conditions of RS require optimization.

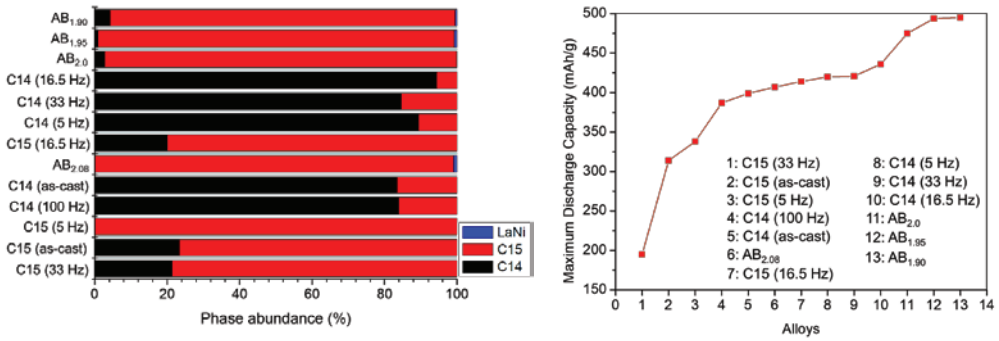

Fig. 4.1. The abundances of phase constituents - Laves phases (C14 and C15) and secondary phase LaNi (a) and maximum electrochemical discharge capacity (b) - in the studied alloys. The changes in the composition of C14 and C15 Laves phases of studied alloys with obtained maximum capacity as related to the electrochemical discharge capacity.

Furthermore, as shown in Fig. 4.1, the modification of the chemical composition on the alloys also affects the characteristics of gaseous hydrogen storage. Increasing B/A ratio from 1.9 to 1.95 resulted in an increase of the hydrogen storage capacity from approximately 1.55 wt.% H to 1.61 wt.% H respectively. However, when B/A ratio became 2.0, the hydrogen capacity decreased to 1.44 wt.% H. A further increase in hydrogen storage capacity - to 1.54 wt.% H - was retrieved as the B/A ratio was increased further to 2.08.

In the case of desorption pressure, the studied alloys showed that the formation of stable hydrides at ambient conditions with desorption pressure of 0.4-1 bar H_2 in the middle of the plateau pressures. From the PCT isotherms, a slight difference in enthalpies and entropies formation of the hydrides was observed by applying a modelling of the isotherms based on modified van't Hoff equation which resulted in the lowest ΔH and ΔS of –33.98 kJ/mol H_2 and –107.67 J/mol H_2 respectively for $AB_{1.9}$ alloy, followed by $AB_{2.08}$, $AB_{2.0}$, and $AB_{1.95}$ alloys for ΔH, while for ΔS the order changed to $AB_{1.95}$, $AB_{2.08}$, and $AB_{2.0}$ alloys Moreover, the critical temperature – quite low for all studied alloys - also continuously decreases from 386 K to 370 K and 366 K with increase of the B/A from 1.9 to 1.95 and 2.0, while the highest critical temperature - 393 K – was observed for B/A= 2.08 (see Table 4.1.).

Table 4.1. Chemical composition of the studied alloys with general formula of $AB_{2-x}La_{0.03}$ Laves type ($A=Ti_{0.15}Zr_{0.85}$; $B=Mn_{0.64–0.7}V_{0.11–0.12}Fe_{0.11–0.12}Ni_{1.097–1.2}$; x = -0.8, 0, 0.05 and 0.1) their properties related to PCI isotherms

Alloys type	**Ti**	**Zr**	**La**	**Ni**	**Mn**	**V**	**Fe**	**B/A**	**C_H max**	**P_d**	**$-\Delta H$**	**$-\Delta S$**	**T_C**
Hypo-stoichiometry	0.15	0.85	0.03	1.097	0.64	0.11	0.11	1.90	1.55	0.3	33.98	107.67	386
Hypo-stoichiometry	0.15	0.85	0.03	1.126	0.657	0.113	0.113	1.95	1.61	0.4	35.25	113.33	370
Stoichiometry	0.15	0.85	0.03	1.155	0.674	0.116	0.116	2.00	1.44	0.8	34.54	116.61	366
Hyper-stoichiometry	0.15	0.85	0.03	1.2	0.7	0.12	0.12	2.08	1.54	1	34	115	393

where,

C_H max= gaseous capacity (wt.% H)
P_d = equilibrium desorption pressure (bar)
$-\Delta H$= enthalpy change for hydride formation (kJ/mol H_2)

$-\Delta S$= entropy change for hydride formation (J/mol H_2 K)
T_C= critical temperature (K).

4.2. Effect of rapid solidification on microstructures of the alloys

It is a common knowledge that properties and performance of the hydrogen storage materials are strongly influenced by their microstructure. When this concerns H storage performance of the intermetallic alloys as materials for hydrogen storage, several aspects of the hydrogenation behavior of these intermetallics can be influenced by the microstructure and by nano-structuring, also by influencing the mechanism of hydrogen interaction with the metal matrix. Indeed, hydrogen molecules first dissociate at the metal surface into atomic hydrogen. Then atomic hydrogen diffuses along the grain boundaries before entering the bulk metal, diffusing into the bulk and forming the hydride. Nano-structuring creates large intergranular areas, where H diffusion proceeds faster than in the bulk material. Thus, supply of atomic hydrogen increases, and its efficient diffusion rate becomes higher. Furthermore, as diffusion inside the grains of the bulk material is slower, smaller alloy grains are faster converted into the metal hydride grains as they are quicker saturated by atomic H.

When it comes to the properties of the metal hydrides as the anodes of the metal hydride batteries, nano-structuring can also play an opposite role. The reason for that is in the fact that the ratio between the surface and the bulk is much higher for the nanostructured particles. Thus, their oxidation because of corrosion proceeds much faster leading to the decreased H capacity as the content of the non-oxidized bulk decreases. Thus, in terms of particle size, 40-60 μm particles were selected by our group as the optimal size of the metal alloy powders to perform an electrochemical study to achieve the best electrochemical performance. In such a case, a compromise between the fast diffusion and the limited in scale corrosion is reached as smaller grains are easily corroded and degrade quickly.

Zhang and co-workers reported that performing rapid solidification at a rate of 2 m/s on Ti-based ($Ti_{0.8}Zr_{0.2}Mn_{0.5}V_{0.5}Ni_{1.0}$) alloy resulted in a significant reduction of the grain size from approximately 12 μm for the as-cast alloy to 1.3 μm for the RS material. Indeed, with increasing the rapid solidification rate to 8 m/s, the grain size continuously refined to become 1 μm [175]. Such phenomena were accompanied by some increase in the discharge capacity from 308 mAh/g to approximately 316 mAh/g and 335 mAh/g proceeding in parallel with an increase in the rapid solidification rates from 2 m/s to 8 m/s causing a decrease in the grain size from 1.3 μm to 1 μm.

The melt-spinning of the $Zr_{0.9}Ti_{0.1}V_{1.7}$ alloy resulted in an improvement of its homogeneity when casted using a wheel speed of 40 m/s and was accompanied by a significant grain reduction from approximately 20 μm (as-cast alloy) to 0.5 μm (RS alloy; Zhang et al. [169]). Furthermore, maximum hydrogen absorption capacity significantly increased, by 1 wt. % H, as associated with improved homogeneity and grain refinement.

For the hydrogen storage alloys with a much lower melting point, La_2MgNi_9, rapid solidification resulted in an extraordinary reduction of the average grain size from 5 μm for the as-cast alloy to 75 nm and 10 nm for the RS alloys obtained at a wheel rotation speed of, respectively, 4.2 m/s and 10.5 m/s, as shown by our group, see Nwakwuo et al. [165]. Nano-structuring resulted in an improvement of the hydrogen storage performance of this alloy when comparing the properties of the melt-spun and as-cast La_2MgNi_9 alloys. Indeed, an increase of hydrogen capacity from 325 mAh/g to approximately 400 mAh/g was reached due to nano-structuring of the alloy.

In our recent studies of C14 and C15 predominated Zr/Ti-based Laves type alloys, we observed similar phenomena taking place during the rapid solidification process. Indeed, as shown in the data listed in Table 4.2, a significant reduction of the grain sizes took place for the RS alloys as compared to the as-cast C14 and C15 predominated alloys following a variation of the wheel rotation speed during the rapid solidification process. As an example, for the C14 type alloys the variation of the morphology of the microstructures was observed during the melt-spinning so an equiaxed grain structure

was formed at 5 Hz (≈6.3 m/s), dendritic structure was observed at 16.5 Hz (≈ to 21 m/s) and 33 Hz (≈ to 41 m/s), and finally the equiaxed grains with phase segregation at the gran boundaries were formed at 100 Hz (≈ to 62.8 m/s) quenching conditions (see Fig. 4.2.). Similarly, Shu at al. revealed that a plate-type lamellar microstructure was obtained for the as cast C14 type alloy while a more varied morphologies of the alloys were achieved after applying a rapid solidification process [171]. Starting from an initial as-cast C14 predominated alloy having a grain size with a length of approximately 15 μm and a width of 3-5 μm, performing RS at a 5 Hz wheel rotation speed resulted in the formation of uniaxial grains with an average grain size of 2 μm, see Fig. 4.2. At 16.5 Hz wheel rotation speed a dendritic morphology has been obtained with the arm length of approximately 3 μm and the arm spacing of 250 nm. Further increase in the speed of RS to 33 Hz, resulted in a formation of smaller dendrites reaching 2 μm in size with the arm spacing of 200 nm. Finally, at the highest quenching rate obtained at wheel speed of 100 Hz, an average size of the grains decreased to 900 nm (see Table 4.2.).

For the C15 type alloys, their rapid solidification resulted in decreasing of the grain sizes occurring for all 3 constituent phases (see Fig. 4.3.).

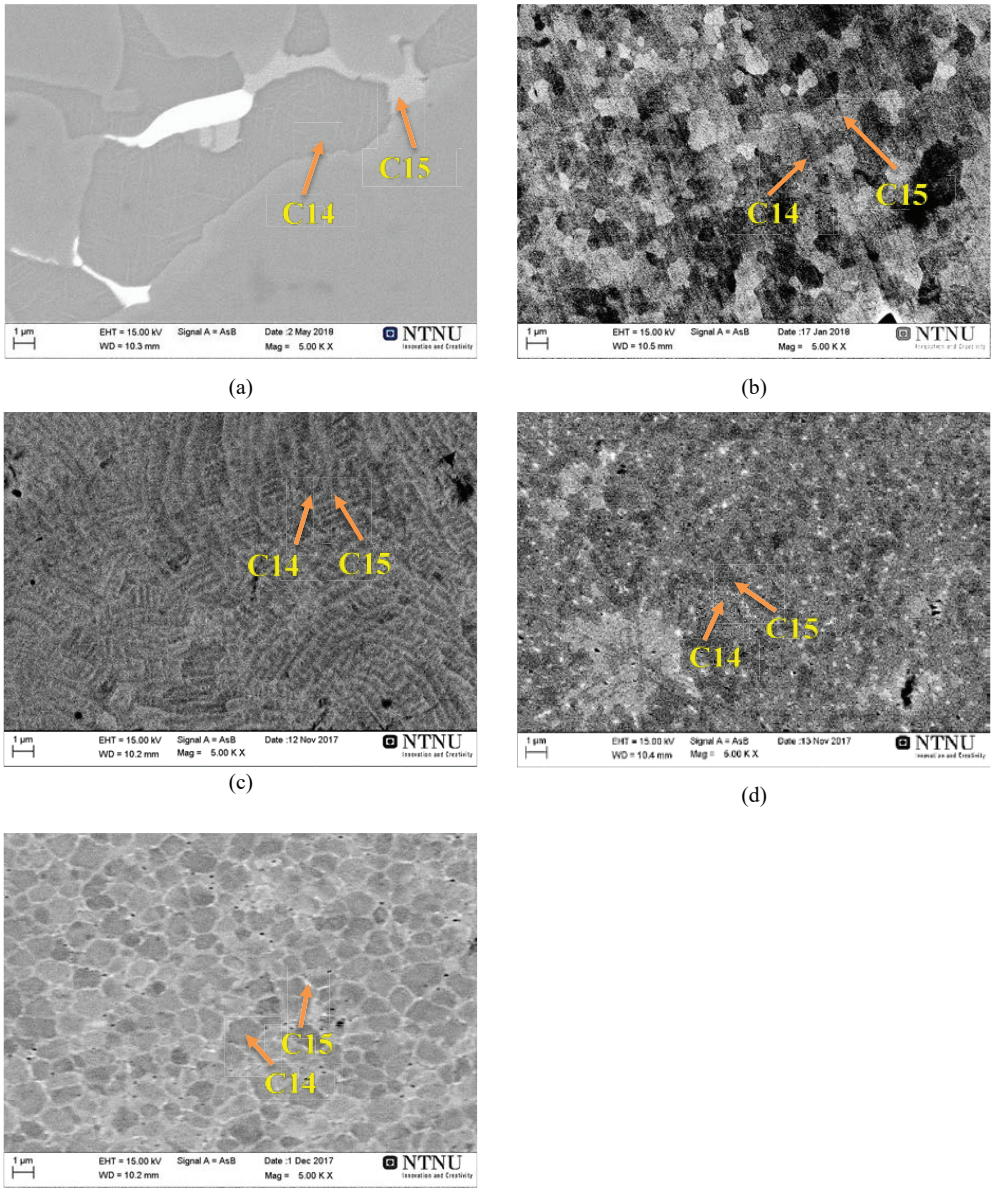

Fig 4.2. BSE SEM micrographs of as-cast (a) and melt-spun samples produced at different rotation speeds of 5 Hz (b), 16.5 Hz (c), 33 Hz (d), and 100 Hz (e). The decrease of the grain size of the melt-spun samples due to rapid solidification process contributed to the observed changes in morphology of the studied samples.

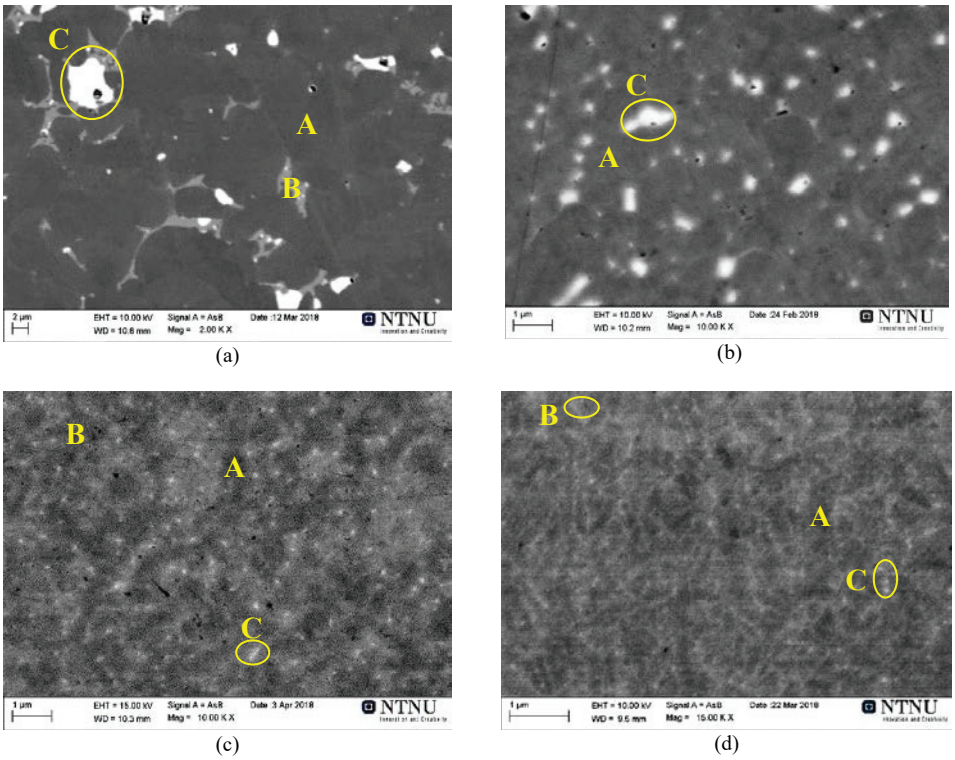

Fig 4.3. SEM BSE images of as-cast (a) and melt-spun samples obtained at variable rotation speeds of 5 Hz (b), 16.5 Hz (c), 33 Hz (d). 3 different phases are present including A: matrix phase (C15), B: secondary phase (C14), and C: La-rich phase. The grain refinement occurred in the melt-spun samples by achieving a decreasing grain size of the matrix phase from 3.5 μm for the as-cast down to 250 nm during the rapid solidification process.

Indeed, for the major C15 Laves phase the grain size decreased as follows; 3.5 μm → 500 nm → 300 nm → 250 nm; for the minor C14 phase this decrease at the same conditions was observed as 2 μm → 200 nm → 175 nm → 100 nm, and, finally, for the catalysing La-rich phase the changes were as follows - 2.9 μm → 375 nm → 250 nm → 70 nm. In each case the data are presented for the alloys prepared at the following conditions; as-cast alloy → RS / 5 Hz → RS / 16.5 Hz→ RS / 33 Hz of melt-spinning (see Table 4.2.).

Further to the changes in the grain size, regular variations were observed in the morphology of the white globular La-rich phase particles which became more evenly distributed in the melt-spun alloys obtained at 5 Hz and 16.5 Hz, whereas the dendrite

structure was formed from a supercooled liquid of C15 phase at 33 Hz of the wheel rotation speed. This can be associated with the fact that the major C15 phase became more homogeneous through the sample thus providing less nuclei sites for the solidification process.

In conclusion, Rapid Solidification process results in the refinement of the alloy grains, improves the homogeneity of the RS samples, and in the nano-structuring of the melt-spun alloys of both types resulting in the improvements of their hydrogen storage performance. The most pronounced increase in the H capacity for the C14 type alloy, appr. 10 %, was reached for the 16.5 Hz melt-spun, while as much as 32 % capacity increase was reached for the RS at 16.5 Hz melt-spun C15 type alloy.

Table 4.2. Interrelation between type of the Laves type alloy (C14/C15), their chemical composition, conditions of rapid solidification, morphology and size of the grains

Alloys and chemical composition			
C14 type alloys $Ti_{12}Zr_{21.5}V_{10}Cr_{7.5}Mn_{8.1}Co_8Ni_{32.2}Al_{0.4}Sn_{0.3}$		**C15 type alloys $Ti_{0.15}Zr_{0.85}La_{0.03}Ni_{1.2}Mn_{0.7}V_{0.12}Fe_{0.12}$**	
As-cast	Length of 15 µm and width of 3-5 µm	As-cast	3.5 µm
5 Hz	2 µm	5 Hz	500 nm (C15 phase), 200 nm (C14 phase), 375 nm (La-rich phase)
16.5 Hz	Dendrite size of approximately 3 µm with the arm spacing is 250 nm	16.5 Hz	300 nm (C15 phase), 175 nm (C14 phase), 250 nm (La-rich phase)
33 Hz	Dendrite reached 2 µm in size with the arm spacing is 200 nm	33 Hz	250 nm (C15 phase), 100 nm (C14 phase), 70 nm (La-rich phase)
100 Hz	900 nm	-	

4.3. Phase structural changes

A significant modification of the phase structure can be achieved by performing casting, rapid solidification, and annealing on the studied alloys (see Table 4.3). From Table 4.3. we conclude that:

(a) For C14 alloys, an increase in the wheel rotation speed resulted in the increase of the abundance of the C14 phase, indicating that the C14 phase is more likely formed at higher solidification rates as compared to the C15 phase [208].

Table 4.3. Crystallographic data and phase abundances for the studied alloys from the Rietveld GSAS refinements

Alloys	**Phase**	**Space group**	**Unit cell parameters, Å**				**Abundance (wt.%)**
			a	*b*	*c*	V, Å^3	
C14 as-cast	C15	$Fd\bar{3}m$	7.0037(3)	———	———	343.5(4)	16.5(1)
	C14	*P6₃/mmc*	4.9662(1)	———	8.0935(2)	172.9(1)	83.5(4)
C14 5 Hz	C15	$Fd\bar{3}m$	6.9888(1)	———	———	341.3(2)	10.7(4)
	C14	*P6₃/mmc*	4.9454(2)	———	8.0587(3)	170.7(1)	89.3(4)
C14 16.5 Hz	C15	$Fd\bar{3}m$	7.0106(6)	———	———	344.6(9)	5.7(3)
	C14	*P6₃/mmc*	4.9594(2)	———	8.0800(5)	172.1(2)	94.3(3)
C14 33 Hz	C15	$Fd\bar{3}m$	6.9945(6)	———	———	342.2(9)	15.4(2)
	C14	*P6₃/mmc*	4.9563(4)	———	8.0761(8)	171.8(4)	84.6(8)
C14 100 Hz	C15	$Fd\bar{3}m$	7.0173(6)	———	———	345.5(9)	16.2(3)
	C14	*P6₃/mmc*	4.9660(4)	———	8.0906(8)	172.8(4)	83.8(1)
C15 as-cast	C15	$Fd\bar{3}m$	7.0236(1)	———	———	346.5(2)	76.7(4)
	C14	*P6₃/mmc*	4.9848(3)	———	8.1516(9)	175.4(2)	23.3(2)
C15 5 Hz	C15	$Fd\bar{3}m$	7.0289(4)	———	———	347.3(7)	100
	C14	*P6₃/mmc*	———	———	———	———	———
C15 16.5 Hz	C15	$Fd\bar{3}m$	7.0391(8)	———	———	348.8(1)	80.0(3)
	C14	*P6₃/mmc*	4.9645(1)	———	8.1600(5)	174.2(2)	20.0(2)
C15 33 Hz	C15	$Fd\bar{3}m$	7.0156(8)	———	———	345.3(1)	78.7(3)
	C14	*P6₃/mmc*	4.9481(1)	———	8.1486(3)	172.8(1)	21.3(3)
$AB_{1.9}$	C15	$Fd\bar{3}m$	7.0374(6)	———	———	348.532(1)	95.2(1)
	C14	*P6₃/mmc*	4.9969(1)	———	8.1817(5)	176.920 (1)	4.3(1)
	LaNi*	*Cmcm*	3.902(7)	10.78(2)	4.385(8)	184.449(6)	0.5(6)
$AB_{1.95}$	C15	$Fd\bar{3}m$	7.0338(6)	———	———	348.004(9)	98.3(4)
	C14	*P6₃/mmc*	4.9834(4)	———	8.1053(1)	174.325(2)	0.9(1)
	LaNi	*Cmcm*	3.902(7)	10.78(2)	4.385(8)	184.449(6)	0.8(5)
$AB_{2.0}$	C15	$Fd\bar{3}m$	7.0235(7)	———	———	346.468(1)	97.2(1)
	C14	*P6₃/mmc*	4.9941(3)	———	8.1533(8)	176.111(2)	2.7(7)
	LaNi	*Cmcm*	3.902(7)	10.78(2)	4.385(8)	184.449(6)	0.1(5)
$AB_{2.08}$ (Ti/Zr= 15/85)	C15	$Fd\bar{3}m$	7.0235(1)	———	———	346.466(1)	99.1(1)
	LaNi	*Cmcm*	3.902(7)	10.78(2)	4.385(8)	184.449(6)	0.9(1)
$AB_{2.08}$ (Ti/Zr= 20/80)	C15	$Fd\bar{3}m$	7.0163(1)	———	———	345.41(1)	100

* Rietveld refinements of LaNi phase was done by using the reference data from [209].

(b) For C15 alloys, we observed that C14 phase as the main phase of the C14 alloy studied in our earlier work showed a decreased unit cell volume indicating the effect of increased Mn content in the C15 alloys. When 5 Hz rotation speed rapid solidification was applied, the abundance of the C15 phase increases. By increasing the rotation speed further to 16.5 and 33 Hz, the abundance of C15 phase decreases as compared to the 5 Hz speed allowing to assume that the C15 phase is more likely to be formed at lower solidification rates as compared to the C14 phase [210]. The largest unit cell volume for both C15 and C14 phases was observed for the 16.5 Hz melt-spun alloy, while for the 33 Hz melt-spun the opposite trend is observed.

(c) By increasing B/A stoichiometry in the alloys, the decrease of the lattice constants and the unit cell volumes occurred due to the larger atomic radii of the A site elements than that of the B elements. In this case, some B components occupy A sites which can cause the shrinkage of the lattice parameters [211].

(d) Increasing the stoichiometry (from $AB_{1.9}$ to $AB_{2.08}$) resulted in increasing the abundance of C15 phase and decreasing the abundance of the C14 phase which indicated achieving a better homogeneity.

4.4. Activation – Effect of La and KOH treatment

The activation behavior of metal hydride alloys as negative electrodes of Ni-MH batteries is a very important feature of the battery performance. Obviously, the faster activation performance can be reached, the better quality of the batteries is. Achieving a fast activation performance can be achieved by modifying the chemical composition to be alloys - by adding La which shows the catalytic influence by relaxing the conditions for activation [141, 212, 213] and by performing the treatment of the alloys in KOH solution [214-216]. The incorporation of just 2 at.% La into a C14 metal hydride alloy resulted in an enhancement of the activation performance by reaching 92 % HRD in the first cycle, whereas the alloy without addition of La required 6 cycles to reach the 92 % HRD as reported by Young et al. [141]. Sun et al. concluded that the addition of 5 % Lanthanum to a cubic C15 type $Zr(Cr_{0.4}Ni_{0.6})_2$ resulted in a full activation being reached

in the second charge-discharge cycle, even though a capacity was rather low, 240 mAh/g. Further to this, the hydrogen absorption by the La-added alloy has been greatly enhanced. In contrast, for the alloy without La addition it takes a very long time, as much as 88 h, to be well activated [213].

In agreement with these studies, our earlier publication revealed that the addition of 3% La to the $Ti_{0.2}Zr_{0.8}La_{0-0.05}Ni_{1.2}Mn_{0.7}V_{0.12}Fe_{0.12}$ alloy showed reaching a full discharge capacity in the fifth cycle with a maximum discharge capacity of 420 mAh/g and the capacity retention after 500 cycles of 63%. Quite opposite to that, the activation of La-free AB_2 (La_0) alloy was very slow and has not been completed during the first 10 cycles [126]. Therefore, 3 % La was selected as an optimum amount to be added to our studied alloys to improve the activation behavior while simultaneously reaching a high discharge capacity. The reason for the improved behaviour is in the fact that La forms the secondary phase LaNi due to the poor solubility in the Zr and Ti containing Laves phase metal hydride alloys. LaNi phase instantly absorbs a large amount of hydrogen during the activation performance forming $LaNiH_{3.6}$ [209] and contributes to a creating of a large surface area through pulverization during the hydrogen absorption and desorption process [217]. Thus, La plays an important role as a catalyser and a promoter improving the performance at high current densities during the charge and discharge process.

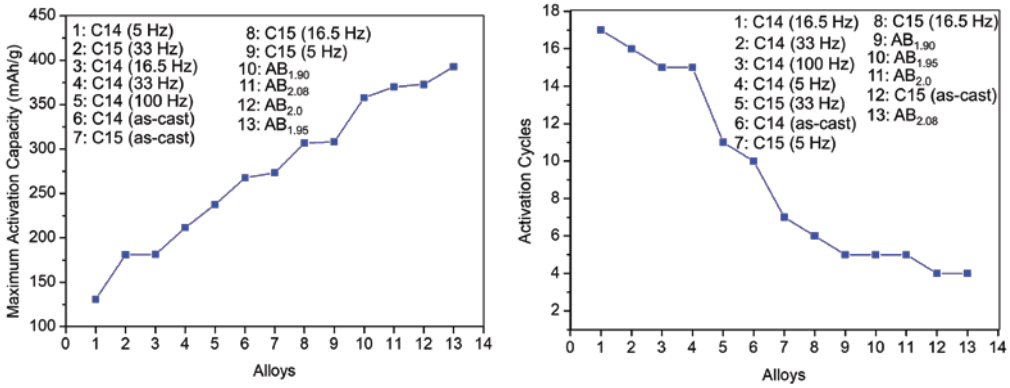

(a) (b)

Fig. 4.4. Maximum activation capacity of the studied alloys (a) and number of activation cycles required to activate the studied alloys.

When it comes to the performance of AB_2 alloys, several methods have been proposed to improve their poor activation behaviour by producing new fresh surfaces and by modifying/improving the existing metal surfaces [218]. In this study, the latter method was studied by treating the metal surface of the alloys in a hot KOH solution in order to produce the fresh and clean metal surface and furthermore to create the Ni- enriched regions caused by selective dissolution of the certain elements during the treatment [219].

In terms of KOH treatment, Choi et al. found that by immersing $Zr_{0.9}Ti_{0.1}Ni_{1.1}Co_{0.1}Mn_{0.6}V_{0.2}$ alloy electrodes into a boiling 6 M KOH solution for 2 hours, an easy activation has been immediately reached. Indeed, 320 mAh/g capacity was obtained already in the first cycle and reached the maximum value of 350 mAh/g after 20 cycles [214]. Furthermore, Tan et al. observed that with 80 min boiling of the $(Ti_{0.36}Zr_{0.64})$ $(V_{0.15}Ni_{0.58}Mn_{0.20}Cr_{0.07})_2$ alloy powder in a hot KOH solution, an increase of the discharge capacity reached a value of 390 mAh/g in the first cycle and the capacity subsequently exceeded 400 mAh/g after 2 cycles, while after 20 cycles the capacity remained almost unchanged [215]. Chen et al. concluded that the treatment by immersing $Mm(Ni–Mn–Co–Al)_5$ (Mm=Ce-rich mischmetal, La: 28.26 wt.%; Ce: 50.47 wt.%; Pr: 5.41 wt.%; Nd: 15.86 wt.%; other rare earths: 0.3 wt.%) alloys into a 6 M KOH+0.05 M KBH_4 solution at 70°C for 8 h successfully increased the capacity which was reached in the first cycle while the untreated electrode got only a 3 times smaller capacity. Indeed, ten cycles were needed to activate the untreated MH electrode, whereas the KOH/KBH_4-treated electrode was completely activated in the third cycle.

As can be seen from Fig. 4.5, an enhancement of the activation performance was achieved by immersing the $Ti_{0.15}Zr_{0.85}La_{0.03}Ni_{1.2}Mn_{0.70}V_{0.12}Fe_{0.12}$ alloy into a hot - 90° C - KOH for 5 minutes. An increase of maximum capacity from 300 mAh/g to 340 mAH/g has been achieved. Indeed, the formation of Ni- rich surface layers can be the reason of the increased capacity.

4.5. High power performance and the ways to improve it

In order to apply Ni-MH batteries in HEV applications, one of the major requirements is in reaching a satisfactory high-power performance, together with a high cycle stability and long calendar life further to a superior discharge capacity. For many of these properties a close interrelation between the electrochemical and mechanical properties of the alloy can be explored to optimize their performance as battery electrode materials [220]. Power performance is defined as the amount of energy that can be immediately transferred by a battery which is expressed by: P= V x I, where V is potential difference across the electrodes, measured in volts, while I is the current flow, measured in amperes. Obviously, intrinsic properties of the metal hydride alloys play the most important role in achieving their high performance in battery applications.

Ideally, an excellent electrochemical performance including high reversible hydrogen storage capacities, high electrochemical reaction rates, and high corrosion resistance in alkaline solution are highly desirable properties to be owned by hydrogen storage alloy as a negative electrode material for high power Ni-MH batteries. Improving power performance of battery also means improving the overall electrochemical performance of hydrogen storage alloys. Furthermore, much effort is directed to improve the power performance of Ni-MH batteries including chemical composition optimization, addition of catalyst materials, heat treatment, surface treatment, and nano-structuring [221].

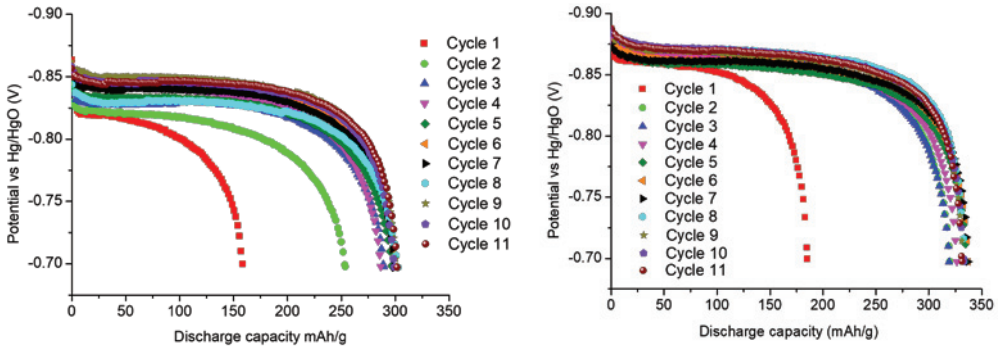

Fig. 4.5. Activation performance of as-cast (left) and KOH treated (right) $Ti_{0.15}Zr_{0.85}La_{0.03}Ni_{1.2}Mn_{0.70}V_{0.12}Fe_{0.12}$ alloys

In the present study, the development of the advanced metal hydride batteries by applying a significant improvement of the battery performances was conducted including nano-structuring by rapid solidification, chemical composition optimization by adjusting stoichiometry of the alloys, applying homogenizing annealing treatment, adding Carbonyl Nickel into the metal hydride pelleted alloys, adding 3 % Lanthanum into Zr- based AB_2 Laves type alloys, and selection of optimal particle size for the anode electrodes. Indeed, a high-power performance of the Ni-MH battery with the excellent activation performance approaching 400 mAh/g in 5 cycles, high discharge capacity reaching 500 mAh/g, and good rate performance maintaining approximately 61 % of the maximum capacity at 500 mA/g current density was successfully reached in these present studies.

4.6. Comparison of metal-gas and electrochemical interactions

Characterization of hydrogen storage capacity of the metal hydrides can be performed using two different types of measurements namely by electrochemical testing in alkaline solutions and by performing metal-hydrogen gas hydrogenation experiments using clean purified H_2. The difference in properties obtained through the two characterizations is normally observed due to the differences between the processes studied. Indeed, PCT characterizations are performed in equilibrium conditions, whereas electrochemical performances are probed in open cells. As a result, different hydrogen storage characteristics appear between the PCT diagram and the electrochemical charge-discharge curves including hydrogen storage capacity, the ranges of existence of the α-solid solution and β-hydride phase, the value plateau pressure in PCT diagram vs the value of potential in electrochemical curve, hysteresis in PCT diagram vs overpotential in electrochemical measurements. Therefore, the comparison of the hydrogen storage properties data of gaseous phase characterization vs. electrochemical performance of the alloys is important to be done.

Hydrogen storage capacity obtained in gaseous phase measurements is higher than that for the electrochemical performance. This phenomenon has been observed by Kong et al. [142]. A 1.69 wt. % H (≈ 452 mAh/g) was reached by addition of 1 at. % Nd into the $Ti_{14.6}Zr_{2.1}V_{44.1}Cr_{12.2}Mn_{6.9}Fe_{2.7}Co_{1.4}Ni_{15.7}Al_{0.3}$ alloy during studies of the metal-H_2 interactions [142]. A maximum discharge capacity of 360 mAh/g was obtained in electrochemical measurement of the alloy.

In the present study, the maximum electrochemical capacity obtained during the electrochemical measurement of hypo-stoichiometric ($AB_{1.9}$) alloy was about 495 mAh/g, which is much higher than obtained maximum gaseous capacity which was only 1.55 wt. % H (≈ 415 mAh/g). This result is consistent with observations by Young et al. [222] (see Fig. 4.6.). The obtained gaseous capacity of the $ZrV_{0.5}Ni_{4.0}$ alloy was much lower than electrochemical capacity.

These phenomena when the electrochemical capacity is larger than gaseous capacity indicate that the alloy has not reached maximum capacity due to the absence of excess H_2 pressure when in the electrochemical environment, thus the reduction in equilibrium hydrogen pressure when performing electrochemical experiments. Further to the Fig. 4.6., a shorter and flatter plateau pressure diagram in PCT measurement was observed compared to the voltage plateau when studying electrochemical capacity. Among other alloys, $AB_{1.9}$ alloy showed the smallest equilibrium pressure of H_2 which was 0.3 bar at 293 K resulting in the highest electrochemical capacity. Further studies are required to better understand the interrelation between the gaseous and electrochemical capacities and experiments in close electrochemical cells where excess hydrogen pressure can be applied will be very valuable. Such experiments are planned for the future continuation of this work.

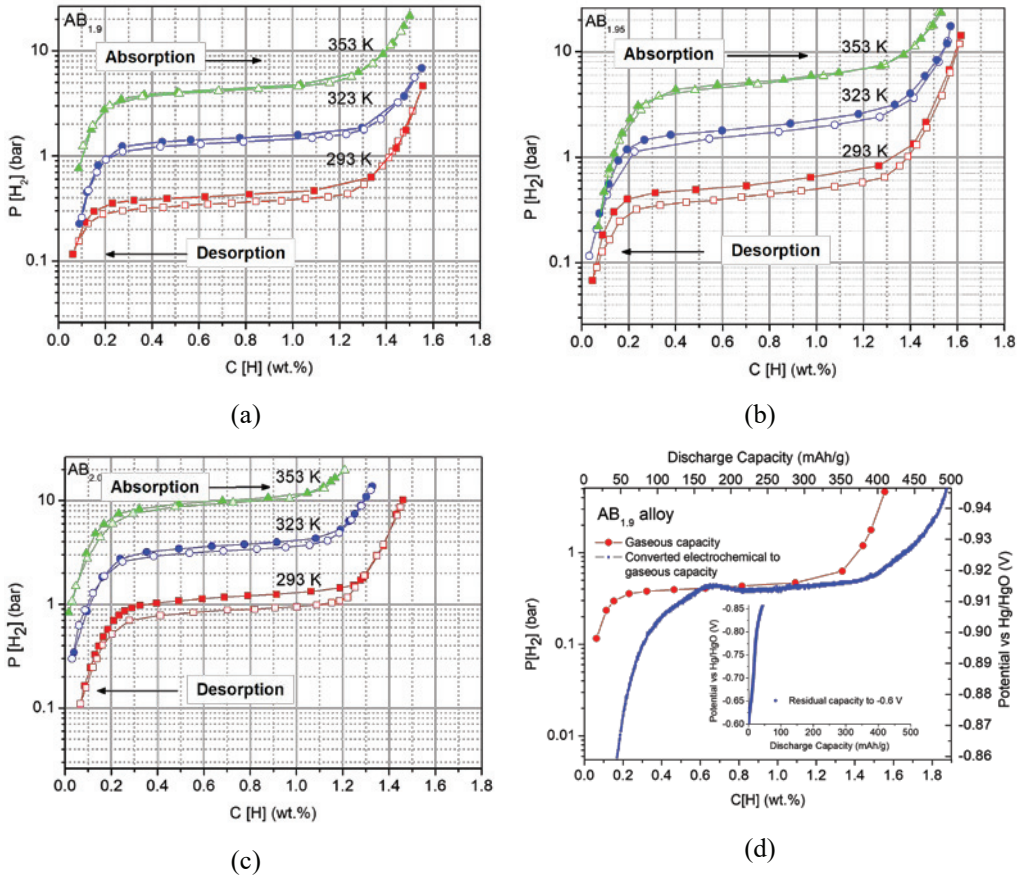

Fig. 4.6. PCT isotherms for $AB_{1.9}$ (a), $AB_{1.95}$ (b), $AB_{2.0}$ (c) alloys, and gaseous H storage capacity vs. electrochemical capacity for the $AB_{1.9}$ alloy, with electrochemical capacity in the voltage range between -0.85 and -0.6 V (cut-off voltage) shown in inset (d).

4.7. Improved cycle stability and corrosion resistance

Cycle stability during charge-discharge electrochemical performance testing is mainly affected by corrosion resistance of the metal hydride alloys working in alkaline solutions. Furthermore, pulverization, segregation and dissolution of some of the elements of the hydrogen storage alloys also lead to the worsening of the cycle life of Ni-MH battery anodes. Liu et al. reported that addition of chromium into the $Zr_{0.9}Ti_{0.1}Mn_{0.4}V_{0.2}Co_{0.1}Ni_{1.1}$ alloys improved the cycle life (500 cycles) by maintaining approximately 64 % of discharge capacity, which was 10 % better than that for the Cr-free alloy [223]. Furthermore, the hyper-stoichiometric $Zr_{0.9}Ti_{0.1}(Mn_{0.6}V_{0.2}Co_{0.1}Ni_{1.1})_{1.05}$ showed only

36% capacity loss which was much lower compared to the 57% capacity loss of the stoichiometric $Zr_{0.9}Ti_{0.1}(Mn_{0.6}V_{0.2}Co_{0.1}Ni_{1.1})_1$ alloy after 500 cycles. In addition, Wang et al. [224] concluded that when applying annealing at 1173 K / 20 h to the $La_{0.72}Nd_{0.08}Mg_{0.2}Ni_{3.4}Al_{0.1}$ alloy remarkably increased the discharge capacity retention from 56.6% for the as-cast alloy to 80.5% after performing 180 cycles. When it concerns the cycle life improvements caused by chemical composition modification, our earlier publication revealed that addition of 3 % La to $Ti_{0.2}Zr_{0.8}La_{0.03}Ni_{1.2}Mn_{0.7}V_{0.12}Fe_{0.12}$ alloy assisted in successfully maintaining 63 % discharge capacity which was just 52 % for the alloy without La addition (after 500 cycles) [126].

Performing the annealing at 1223 K for 16 hours on the $Ti_{0.15}Zr_{0.85}La_{0.03}Ni_{1.2}Mn_{0.70}V_{0.12}Fe_{0.12}$ alloy significantly improved the performance as 90 % of the discharge capacity was maintained which was just 80 % for the as-cast alloy (after 100 cycles). Moreover, changing Ti/Zr ratio from 20/80 to 15/85 resulted in increasing the maximum discharge capacity from 360 mAh/g to 420 mAh/g.

When changing the B/A ratio in the alloy from 1.9 to 1.95 and 2.0 resulted in a decrease of the capacity retention from 46.7% to 40.7% and then in an increase to 48.7% respectively, after performing 500 cycles. The better mechanical stability was observed for the $AB_{2.0}$ alloy caused by its smaller specific surface area thus its excessive pulverization can be prevented resulting in its better cyclic stability [225]. Further to this, the highest content of Ni in $AB_{2.0}$ reduced the corrosion rate of the alloy resulting in the highest capacity retention. Indeed, with changing the B/A ratio in the alloy to 2.08 [73, 126], an improved capacity retention was obtained as compared to the stoichiometric alloy (2.0). This phenomenon was caused by achieving a better mechanical stability during the cycle performance of the hyper-stoichiometric alloys due to a lower pulverization of the alloy.

4.8. Price advantage as compared with AB_5 alloys

In order to achieve commercialization of the battery electrode materials, a consideration of economic aspects in selecting the raw materials is mandatory to apply. In the last

decades, AB_5 type alloys have become the promising metal hydride alloys as possessing excellent properties including easy activation and reversible absorption and release hydrogen at room temperature [226]. However, a very high cost of Cobalt contained in the AB_5 alloy which almost takes up to about 40–50% of the total cost of the commercial $MmNi_{3.55}Co_{0.75}Mn_{0.4}Al_{0.3}$ alloys has motivated a research effort to reduce/eliminate Cobalt in the AB_5 alloys while maintaining the excellent storage capacity and cyclic stability [227]. The research efforts were focused at low-Co or Co-free AB_5-type alloys [228, 229]. As an alternative to the AB_5 alloys, AB_2 type Laves phase alloys can be considered as promising metal hydride alloys with superior properties both considering the prospective of their electrochemical performance and their cost as electrodes for the Ni-MH batteries. To compare the cost of the raw materials for the AB_2 type alloys, we analyzed and calculated the price of raw materials using the data from Sigma-Aldrich Corporation. Indeed, a cost reduction of 76.5 % can be achieved by selecting the AB_2 type alloys for the electrodes of Ni-MH batteries. This was one of the objectives of the present study - to reduce the cost of the alloys, thus this objective is reached by selecting Zr- based AB_2 Laves type alloys as negative electrodes of Ni-MH batteries.

Chapter V

CONCLUSIONS

This work was aimed at developing the materials for high energy-high power metal hydride batteries. The focus was on anode materials which are the key components in improving the batteries performance in total. The areas where the progress is required, and which were all addressed in the current study include:

- Increase of the electrochemical storage capacity;
- Replacement of the expensive and limited in natural resources rare earth metals by more affordable and more abundant zirconium and titanium;
- Increase of the cycle life;
- Improved activation performance of the alloys.

Our assumption was that a replacement of the rare earth and cobalt containing alloys by the alloys of zirconium and titanium with transition metals will offer a solution of the described problem.

We have selected AB_2 Laves type alloys as the materials providing the possibilities to reach the goals of the current research project. The performed studies included development of multicomponent Zr- based AB_2 Laves type alloys containing 7 elements - Ti, Zr, Ni, Mn, Fe, V, La - by optimizing their content in the alloys to achieve advanced performance of the anodes of the metal hydride batteries.

A high capacity, high power performance of the Ni-MH battery anodes with excellent activation performance and high discharge capacity reaching 495 mAh/g, and a good rate performance maintaining more than 60 % of the maximum capacity at 1 C discharge current density were successfully developed in this work while reaching activation of anode materials in just one cycle.

The optimization of their performance has been achieved by establishing an interrelation between the chemical composition of the alloys, their structure and microstructure, and electrochemical performance of the studied alloys which belong to the (Zr,Ti,La,Ni,Mn,Fe,V) system while the alloys composition was selected as $Zr_{0.80\text{-}0.85}Ti_{0.15\text{-}0.20}La_{0.01\text{-}0.05}(Ni_{1.097\text{-}1.2}Mn_{0.64\text{-}0.7}Fe_{0.11\text{-}0.12}V_{0.11\text{-}0.12})$.

Three various aspects related to the choice and optimization of the alloys were considered to optimize their performance, including:

(a) Changing the ratio between Zr and Ti;

(b) Changing the relative content of A and B components while aiming at the formation of the Laves type alloys;

(c) Use of catalyzing La additive to improve the performance of the alloys.

Optimized ratio between Zr and Ti

Changing the ratio between Zr and Ti from 85/15 to 80/20 resulted in a decrease of unit cell parameters leading to a shrinking of the volume of the unit cell by 0.6 % due to the replacement of a larger Zr atom (1.602 Å) by a smaller Ti atom (1.462 Å) in the crystal structure of the alloy. Similar volume decrease was observed for the $AB_{1.9}$, $AB_{1.95}$, and $AB_{2.0}$ alloys with 85/15 composition where an increase of the content of smaller in size B elements caused a shrinking of the volume of the unit cell by 0.6 %. Further to this, improvements of the activation performance were achieved by decreasing the ratio between Zr and Ti. However, this was followed by a decrease in maximum electrochemical capacity and gaseous capacity. Cycle stability also decreased by changing the content of Zr from 85 % to 80 %.

Ratio between A and B components

The change of the ratio between the Zr and Ti on the A site (Zr+Ti) and transition elements on the B site (Ni+Mn+Fe+V) ranging between $Zr_{0.80\text{-}0.85}Ti_{0.15\text{-}0.20}La_{0.01\text{-}0.05}(Ni_{1.097\text{-}1.2}Mn_{0.64\text{-}0.7}Fe_{0.11\text{-}0.12}V_{0.11\text{-}0.12})$ from 1.9, 1.95, 2.0, to 2.08 resulted in reaching a

maximum discharge capacity of 495 mAh/g for the hypo-stoichiometric alloys with optimised chemical composition B/A $AB_{1.90}$ and $AB_{1.95}$ = 1.95, which shows a significant improvement as compared to the behaviour of the earlier studied hyper-stoichiometric alloy with B/A=2.08 which showed a capacity of 370 mAh/g only (see Fig. 5.1).

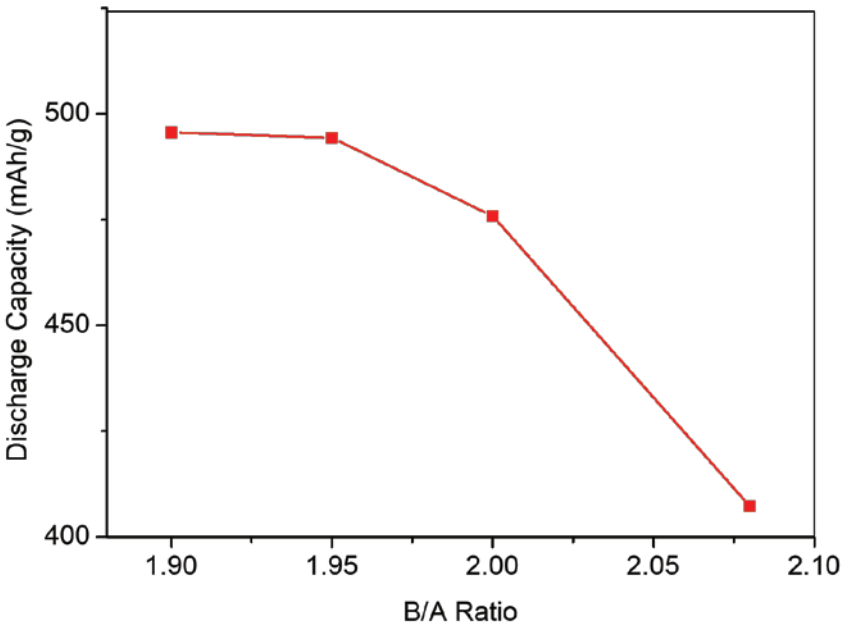

Fig. 5.1. Maximum electrochemical discharge capacity for the alloys with B/A ratio from 1.9, 1.95, 2.0, and 2.08. Increased B/A ratio resulted in a quick drop of the maximum discharge capacity of the alloys as compared to the alloys with optimum B content of $AB_{1.90}$ and $AB_{1.95}$.

Effect of catalyzing additive of lanthanum

Successful battery performance requires easy activation of the battery anode materials. Introduction of lanthanum into the alloys caused a significant improvement of the activation behavior, even at small content of lanthanum additive. Variable small additions of lanthanum metal were tried, 0.01; 0.03 to 0.05 at. La/f.u. $AB_{2\pm x}$ alloys. The addition of 3 % La to the alloys improves the activation behavior while simultaneously reaching a high discharge capacity as a result of the catalytic influence of La. Lanthanum, due to its poor solubility in the Zr and Ti containing Laves phases forms

globular particles of LaNi phase which are distributed along the grain boundaries and form a secondary intermetallic phase. LaNi absorb large amount of hydrogen during the activation forming $LaNiH_{3.6}$ thus inducing volume expansion which causes formation of cracks resulting in increase of the surface area through pulverization during the hydrogen absorption and desorption process proceeding during charge and discharge of the anode.

Structure- and microstructure-properties relationships

Choice of chemical composition of the alloys and their preparation techniques (as cast; annealed; rapidly solidified) resulted in a significant modification of their structure and microstructure, including:

(a) Formation of the C15 or C14 structures;

(b) Nano-structuring of the alloys.

(a) and (b) together allowed to control the electrochemical performance. Formation of a particular type of structure affects the metal hydride battery anode behavior as the contribution of Laves phases of two types C15 or C14 to the alloy's properties is different. Indeed, an excellent high rate dischargeability (HRD) and a faster activation performance were achieved for the alloys having C15 type alloys, while C14 type alloys show higher discharge capacities.

A modification of the morphology and the microstructures of the alloys was achieved by performing RS including:

(a) changes in a ratio between the main C15 and the secondary C14 phases by minimizing the amount of the secondary phases that do not contribute to the storage capacity

(b) a noticeable decrease in the grain size as compared to the as-cast alloys.

Modifications of the microstructure resulted in changing of the discharge capacity, activation properties, and high rate discharge performance as related to the metallurgical and phase-structural state of the alloys. The improvement of the rate performance and

increased diffusion of hydrogen were achieved for the melt-spun alloys. At the same time, more cycles were needed to activate the rapidly solidified alloys.

Electrochemical Impedance Spectroscopy studied showed that resistance of the alloys and the diffusion rates of hydrogen change as related to the chemical composition of the alloys and history of the anodes. Indeed, by applying rapid solidification process, Warburg element in the Nyquist impedance spectra dramatically decreased indicating increased rates of hydrogen diffusion. Furthermore, the best modelling of the EIS spectra was achieved by applying a model which used a superposition of 2 different components (resistance and constant phase element) with Warburg element in series connection. Indeed, by assuming that the diffusion in the metal hydride alloy is a semi-infinite linear diffusion, the calculation of hydrogen diffusion coefficient using the modified Fick's law can be reliably performed.

Cost factor

In terms of cost reduction, a significant cost decrease of more than 75 % can be achieved by selecting the Zr- based AB_2 Laves type alloys for the electrodes of Ni-MH batteries instead of Co- containing AB_5 alloys of rare earth metals. The cost reduction is reached by both avoiding using rare earth metals and cobalt as components of the alloys.

IN CONCLUSION,

advanced anodes for the high energy - high power performance metal hydride batteries with excellent activation performance, high discharge capacity approaching 500 mAh/g, good cycle stability, and good rate performance while offering an affordable price and eliminating use of rare earth metals and cobalt were successfully developed in the present studiy by developing and optimizing of Zr- based multicomponent (Ti, Zr, Ni, Mn, Fe, V, La) AB_2 Laves type alloys.

REFERENCES

[1] G.G. Libowitz, H.F. Hayes, T.R.P. Gibb, The system Zirconium–Nickel and Hydrogen, The Journal of Physical Chemistry, 62 (1958) 76-79.
[2] J.H.N. Van Vucht, F.A. Kuijpers, H.C.A.M. Bruning, Reversible room-temperature absorption of large quantities of hydrogen by intermetallic compounds, Philips Res. Rep., 25 (1970) 133-140.
[3] J. Willems, K. Buschow, From permanent magnets to rechargeable hydride electrodes, Journal of the Less Common Metals, 129 (1987) 13-30.
[4] K. Buschow, P. Naastepad, F. Westendorp, Preparation of $SmCo_5$ permanent magnets, Journal of Applied Physics, 40 (1969) 4029-4032.
[5] F.A. Kuijpers, RCo_5-H and related sytems, Philips Res. Repts. Suppl. , 2 (1973) 102.
[6] T. Sakai, K. Oguro, H. Miyamura, N. Kuriyama, A. Kato, H. Ishikawa, C. Iwakura, Some factors affecting the cycle life of $LaNi_5$-based alloy electrodes of hydrogen batteries, Journal of the Less Common Metals, 161 (1990) 193-202.
[7] G. Bronoel, J. Sarradin, M. Bonnemay, A. Percheron, J.C. Achard, L. Schlapbach, A new hydrogen storage electrode, International Journal of Hydrogen Energy, 1 (1976) 251-254.
[8] J.J.G.S.A. Willems, Metal hydride electrodes stability of $LaNi_5$-related compounds, in, Technische Hogeschool Eindhoven, 1984, pp. 100.
[9] J.J.G. Willems, Metal hydride electrodes stability of $LaNi_5$-related compounds, Philips J. Res., 39 (1984) 22.
[10] V. Yartys, D. Noreus, M. Latroche, Metal hydrides as negative electrode materials for Ni–MH batteries, Applied Physics A, 122 (2016).
[11] K.-h. Young, S. Yasuoka, Capacity Degradation Mechanisms in Nickel/Metal Hydride Batteries, Batteries, 2 (2016) 3.
[12] D.-M. Kim, K.-J. Jang, J.-Y. Lee, A review on the development of AB_2-type Zr-based Laves phase hydrogen storage alloys for Ni–MH rechargeable batteries in the Korea Advanced Institute of Science and Technology, Journal of Alloys and Compounds, 293-295 (1999) 583-592.
[13] F. Cuevas, J.-M. Joubert, M. Latroche, A. Percheron-Guégan, Intermetallic compounds as negative electrodes of Ni-MH batteries, Applied Physics A, 72 (2001) 225-238.
[14] K.-H. Young, J. Nei, C. Wan, R.V. Denys, V.A. Yartys, Comparison of C14-and C15-predomiated AB_2 metal hydride alloys for electrochemical applications, Batteries, 3 (2017) 22.
[15] J. Huot, E. Akiba, T. Ogura, Y. Ishido, Crystal structure, phase abundance and electrode performance of Laves phase compounds (Zr, A)$V_{0.5}N_{i1.1}Mn_{0.2}Fe_{0.2}$ (A ≡ Ti, Nb or Hf), Journal of Alloys and Compounds, 218 (1995) 101-109.
[16] G. Ivey Douglas, O. Northwood Derek, Storing Hydrogen in AB2 Laves-Type Compounds*, in: Zeitschrift für Physikalische Chemie, 1986, pp. 191.
[17] H.H. Van Mal, K. Buschow, A. Miedema, Hydrogen absorption in $LaNi_5$ and related compounds: Experimental observations and their explanation, Journal of the Less Common Metals, 35 (1974) 65-76.

[18] K. Young, T. Ouchi, M.A. Fetcenko, W. Mays, B. Reichman, Structural and electrochemical properties of $Ti_{1.5}Zr_{5.5}V_xNi_{10-x}$, International Journal of Hydrogen Energy, 34 (2009) 8695-8706.
[19] J.F. Stampfer Jr, C. Holley Jr, J. Suttle, The Magnesium-Hydrogen system, Journal of the American Chemical Society, 82 (1960) 3504-3508.
[20] J.J. Reilly, R.H. Wiswall, Reaction of hydrogen with alloys of Magnesium and Nickel and the formation of Mg_2NiH_4, Inorganic Chemistry, 7 (1968) 2254-2256.
[21] A. Kagawa, E. Ono, T. Kusakabe, Y. Sakamoto, Absorption of hydrogen by Vanadium-rich V-Ti-based alloys, Journal of the Less common Metals, 172-174 (1991) Part A: 64-70.
[22] M. Geng, J. Han, F. Feng, D.O. Northwood, Hydrogen-absorbing alloys for the Nickel–Metal Hydride battery, International Journal of Hydrogen Energy, 23 (1998) 1055-1060.
[23] V.A. Yartys, R.V. Denys, C.J. Webb, J.P. Mæhlen, E.M. Gray, T. Blach, O. Isnard, L.C. Barnsley, High pressure in situ diffraction studies of metal–hydrogen systems, Journal of Alloys and Compounds, 509 (2011) S817-S822.
[24] R. Van Essen, K. Buschow, Composition and hydrogen absorption of C14 type Zr-Mn compounds, Materials Research Bulletin, 15 (1980) 1149-1155.
[25] A. Pebler, E. Gulbransen, Equilibrium studies on the systems $ZrCr_2H_2$, ZrV_2H_2, and $ZrMo_2H_2$ between 0 and 900 C, Aime Met Soc Trans, 239 (1967).
[26] D. Shaltiel, I. Jacob, D. Davidov, Hydrogen absorption and desorption properties of AB_2 Laves-phase pseudobinary compounds, Journal of the Less Common Metals, 53 (1977) 117-131.
[27] S.K. Zhang, Q.D. Wang, Y.Q. Lei, G.L. Lü, L.X. Chen, F. Wu, The phase structure and electrochemical properties of the melt-spun alloy $Zr_{0.7}Ti_{0.3}Mn_{0.4}V_{0.4}Ni_{1.2}$, Journal of Alloys and Compounds, 330-332 (2002) 855-860.
[28] J.Y. Yu, Y.Q. Lei, C.P. Chen, J. Wu, Q.D. Wang, The electrochemical properties of hydrogen storage Zr-based Laves phase alloys, Journal of Alloys and Compounds, 231 (1995) 578-581.
[29] M. Tliha, C. Khaldi, S. Boussami, N. Fenineche, O. El-Kedim, H. Mathlouthi, J. Lamloumi, Kinetic and thermodynamic studies of hydrogen storage alloys as negative electrode materials for Ni/MH batteries: a review, Journal of Solid State Electrochemistry, 18 (2014) 577-593.
[30] M. Yoshida, E. Akiba, Hydrogen absorbing-desorbing properties and crystal structure of the Zr-Ti-Ni-Mn-V AB_2 Laves phase alloys, Journal of Alloys and Compounds, 224 (1995) 121-126.
[31] T. Maeda, T. Fuura, I. Matsumoto, Y. Kawakami, M. Masuda, Cyclic stability test of AB_2 type $(Ti, Zr)(Ni, Mn, V, Fe)_{2.18}$ for stationary hydrogen storage in water contaminated hydrogen, Journal of Alloys and Compounds, 580 (2013) S255-S258.
[32] M.Y. Song, D. Ahn, I. Kwon, R. Lee, H. Rim, Development of AB_2-type Zr–Ti–Mn–V–Ni–Fe hydride electrodes for Ni–MH secondary batteries, Journal of Alloys and Compounds, 298 (2000) 254-260.
[33] D.G. Ivey, D.O. Northwood, Storing energy in metal hydrides: A review of the physical metallurgy, Journal of Materials Science, 18 (1983) 321-347.

[34] A. Midilli, M. Ay, I. Dincer, M.A. Rosen, On hydrogen and hydrogen energy strategies, Renewable and Sustainable Energy Reviews, 9 (2005) 255-271.
[35] A. Züttel, A. Borgschulte, L. Schlapbach, Hydrogen as a Future Energy Carrier, Wiley, 2011.
[36] C.J. Winter, J. Nitsch, Hydrogen as an Energy Carrier: Technologies, Systems, Economy, Springer Berlin Heidelberg, 2012.
[37] P.P. Edwards, V.L. Kuznetsov, W.I.F. David, N.P. Brandon, Hydrogen and fuel cells: Towards a sustainable energy future, Energy Policy, 36 (2008) 4356-4362.
[38] K. Hong, The development of hydrogen storage electrode alloys for Nickel hydride batteries, Journal of Power Sources, 96 (2001) 85-89.
[39] H. Pan., J. Ma., C. Wang., C.P. Chen., Q.D. Wang., Effect of Co content on the kinetic properties of the $MINi_{4.3-x}Co_xAl_{0.7}$ hydride electrodes, Electrochimica Acta, 44 (1999) 11.
[40] K. Mazloomi, C. Gomes, Hydrogen as an energy carrier: Prospects and challenges, Renewable and Sustainable Energy Reviews, 16 (2012) 3024-3033.
[41] G. Piercy, The Physical and Chemical Behavior of Hydrogen in Metals, Canadian Institute of Mining and Metallurgy, Metallurgical Society of CIM Annual Volume Featuring" Hydrogen in Metals" and" Titanium", 17 (1978) 11-15.
[42] L. Schlapbach, Hydrogen-fuelled vehicles, Nature, 460 (2009) 809.
[43] J. Purewal, Hydrogen adsorption by alkali metal graphite intercalation compounds, in, California Institute of Technology, 2010.
[44] L.G. Scanlon, W.A. Feld, P.B. Balbuena, G. Sandi, X. Duan, K.A. Underwood, N. Hunter, J. Mack, M.A. Rottmayer, M. Tsao, Hydrogen storage based on physisorption, The Journal of Physical Chemistry B, 113 (2009) 4708-4717.
[45] Y. Liu, H. Pan, M. Gao, Q. Wang, Advanced hydrogen storage alloys for Ni-MH rechargeable batteries, Journal of Materials Chemistry, 21 (2011) 4743-4755.
[46] J. Kleperis, G. Wójcik, A. Czerwinski, J. Skowronski, M. Kopczyk, M. Beltowska-Brzezinska, Electrochemical behavior of metal hydrides, Journal of Solid State Electrochemistry, 5 (2001) 229-249.
[47] G. Sandrock, A panoramic overview of hydrogen storage alloys from a gas reaction point of view, Journal of Alloys and Compounds, 293 (1999) 877-888.
[48] C. Iwakura, M. Matsuoka, Application of hydrogen storage alloys to battery-related fields: Nickel-Hydrogen batteries, Progress in Batteries & Battery Materials, 10 (1991) 81-114.
[49] M.A. Fetcenko, S.R. Ovshinsky, B. Reichman, K. Young, C. Fierro, J. Koch, A. Zallen, W. Mays, T. Ouchi, Recent advances in Ni-MH battery technology, Journal of Power Sources, 165 (2007) 544-551.
[50] D. Linden, T. Reddy, Handbook of batteries, McGraw-Hill Education, 2001.
[51] M. Tliha, H. Mathlouthi, C. Khaldi, J. Lamloumi, A. Percheron-guegan, Electrochemical properties of the $LaNi_{3.55}Mn_{0.4}Al_{0.3}Co_{0.4}Fe_{0.35}$ hydrogen storage alloy, Journal of Power Sources, 160 (2006) 1391-1394.
[52] S. Abada, G. Marlair, A. Lecocq, M. Petit, V. Sauvant-Moynot, F. Huet, Safety focused modeling of Lithium-ion batteries: A review, Journal of Power Sources, 306 (2016) 178-192.

[53] S.R. Ovshinsky, M.A. Fetcenko, J. Ross, A Nickel Metal Hydride battery for electric vehicles, Science, 260 (1993) 176.
[54] F. Feng, M. Geng, D. Northwood, Electrochemical behaviour of intermetallic-based metal hydrides used in Ni-Metal Hydride (MH) batteries: A review, International Journal of Hydrogen Energy, 26 (2001) 725-734.
[55] F. Feng, M. Geng, D.O. Northwood, Electrochemical behaviour of intermetallic-based metal hydrides used in Ni/metal hydride (MH) batteries: a review, International Journal of Hydrogen Energy, 26 (2001) 725-734.
[56] P. Notten, P. Hokkeling, Double-phase hydride forming compounds: A new class of highly electrocatalytic materials, Journal of the Electrochemical Society, 138 (1991) 1877-1885.
[57] N. Furukawa, Development and commercialization of Nickel-Metal Hydride secondary batteries, Journal of Power Sources, 51 (1994) 45-59.
[58] X. Li, H. Dong, A. Zhang, Y. Wei, Electrochemical impedance and cyclic voltammetry characterization of a metal hydride electrode in alkaline electrolytes, Journal of Alloys and Compounds, 426 (2006) 93-96.
[59] W. Zhang, M.S. Kumar, S. Srinivasan, H.J. Ploehn, AC impedance studies on metal hydride electrodes, Journal of the Electrochemical Society, 142 (1995) 2935-2943.
[60] C. Wang, Kinetic behavior of metal hydride electrode by means of AC impedance, Journal of the Electrochemical Society, 145 (1998) 1801-1812.
[61] M.D. Levi, C. Wang, D. Aurbach, Two parallel diffusion paths model for interpretation of PITT and EIS responses from non-uniform intercalation electrodes, Journal of Electroanalytical Chemistry, 561 (2004) 1-11.
[62] R. De Levie, On the impedance of electrodes with rough interfaces, Journal of Electroanalytical Chemistry and Interfacial Electrochemistry, 261 (1989) 1-9.
[63] S.-J. Qiu, H.-L. Chu, Y. Zhang, D.-L. Sun, X.-Y. Song, L.-X. Sun, F. Xu, Electrochemical kinetics and its temperature dependence behaviors of $Ti_{0.17}Zr_{0.08}V_{0.35}Cr_{0.10}Ni_{0.30}$ alloy electrode, Journal of Alloys and Compounds, 471 (2009) 453-456.
[64] L.O. Valøen, A. Lasia, J.O. Jensen, R. Tunold, The electrochemical impedance of metal hydride electrodes, Electrochimica Acta, 47 (2002) 2871-2884.
[65] R. Cottis, S. Turgoose, N. International, Electrochemical impedance and noise, NACE International, Houston, TX, 1999.
[66] S. Malifarge, B. Delobel, C. Delacourt, Determination of tortuosity using impedance spectra analysis of symmetric cell, Journal of the Electrochemical Society, 164 (2017) E3329-E3334.
[67] X. Yuan, N. Xu, Determination of hydrogen diffusion coefficient in metal hydride electrode by modified Warburg impedance, Journal of Alloys and Compounds, 329 (2001) 115-120.
[68] X. Yuan, N. Xu, Comparative study on electrochemical techniques for determination of hydrogen diffusion coefficients in metal hydride electrodes, Journal of Applied Electrochemistry, 31 (2001) 1033-1039.
[69] N. Kuriyama, T. Sakai, H. Miyamura, I. Uehara, H. Ishikawa, Characterization of metal hydride electrodes by means of electrochemical impedance spectroscopy, Journal of Alloys and Compounds, 192 (1993) 161-163.

[70] L.O. Valøen, S. Sunde, R. Tunold, An impedance model for electrode processes in metal hydride electrodes, Journal of Alloys and Compounds, 253-254 (1997) 656-659.
[71] J.L. Hammond, N. Formisano, P. Estrela, S. Carrara, J. Tkac, Electrochemical biosensors and nanobiosensors, Essays in biochemistry, 60 (2016) 69-80.
[72] J.E.B. Randles, Kinetics of rapid electrode reactions, Discussions of the Faraday Society, 1 (1947) 11-19.
[73] A.A. Volodin, R.V. Denys, C. Wan, I.D. Wijayanti, B.P. Tarasov, V.E. Antonov, V.A. Yartys, Study of hydrogen storage and electrochemical properties of AB_2-type $Ti_{0.15}Zr_{0.85}La_{0.03}Ni_{1.2}Mn_{0.7}V_{0.12}Fe0_{.12}$ alloy, Journal of Alloys and Compounds, 793 (2019) 564-575.
[74] I.D. Wijayanti, L. Mølmen, R.V. Denys, J. Nei, S. Gorsse, M.N. Guzik, K. Young, V. Yartys, Studies of Zr-based C15 type metal hydride battery anode alloys prepared by rapid solidification, Journal of Alloys and Compounds, 804 (2019) 527-537.
[75] A. Bard, L. Faulkner, Electrochemical methods: Fundamentals and applications, John Wiley & Sons, Inc, 2001.
[76] P. De Vidts, J. Delgado, R.E. White, Mathematical modeling for the discharge of a metal hydride electrode, Journal of The Electrochemical Society, 142 (1995) 4006-4013.
[77] W. DeLuca, Paper presented at the 1991 annual automotive technology development contractors coordination meeting, Dearborn, Ml, 24 (1991).
[78] K.-H. Young, Research in Nickel-Metal Hydride batteries 2016, in, Multidisciplinary Digital Publishing Institute, 2016.
[79] K. Hong, The development of hydrogen storage alloys and the progress of Nickel hydride batteries, Journal of Alloys and Compounds, 321 (2001) 307-313.
[80] X. Xu, D. Zhou, X. Qin, K. Lin, F. Kang, B. Li, D. Shanmukaraj, T. Rojo, M. Armand, G. Wang, A room-temperature sodium–sulfur battery with high capacity and stable cycling performance, Nature Communications, 9 (2018) 3870.
[81] S. Hameer, J.L. van Niekerk, A review of large-scale electrical energy storage, International Journal of Energy Research, 39 (2015) 1179-1195.
[82] P. Breeze, Power system energy storage technologies, Academic Press, 2018.
[83] W.H. Zhu, Y. Zhu, Z. Davis, B.J. Tatarchuk, Energy efficiency and capacity retention of Ni–MH batteries for storage applications, Applied Energy, 106 (2013) 307-313.
[84] T.R. Crompton, Battery reference book, 3rd ed, Newnes, Boston, 2000.
[85] J.F. Lakner, F.S. Uribe, S.A. Steward, Hydrogen and Deuterium sorption by selected rare earth intermetallic compounds at pressures up to 1500 atm, Journal of the Less Common Metals, 72 (1980) 87-105.
[86] H.F. Bittner., C.C. Badcock., Electrochemical utilization of metal hydrides Journal of The Electrochemical Society: Reviews and news 130 (1983) 193C-198C.
[87] I. Råde, B.A. Andersson, Requirement for metals of electric vehicle batteries, Journal of Power Sources, 93 (2001) 55-71.
[88] T. Ozaki, H.-B. Yang, T. Iwaki, S. Tanase, T. Sakai, H. Fukunaga, N. Matsumoto, Y. Katayama, T. Tanaka, T. Kishimoto, M. Kuzuhara, Development of Mg-containing $MmNi_5$-based alloys for low-cost and high-power Ni–MH battery, Journal of Alloys and Compounds, 408-412 (2006) 294-300.

[89] W. Zhang, S. Han, J. Hao, Y. Li, T. Bai, J. Zhang, Study on kinetics and electrochemical properties of low-Co AB_5-type alloys for high-power Ni-MH battery, Electrochimica Acta, 54 (2009) 1383-1387.
[90] Z. Zhou, Y. Song, S. Cui, C. Huang, W. Qian, C. Lin, Y. Zhang, Y. Lin, Effect of annealing treatment on structure and electrochemical performance of quenched $MmNi_{4.2}Co_{0.3}Mn_{0.4}Al_{0.3}Mg_{0.03}$ hydrogen storage alloy, Journal of Alloys and Compounds, 501 (2010) 47-53.
[91] F. Meli, A. Züttel, L. Schlapbach, Electrochemical and surface properties of Iron-containing AB_5-type alloys, Journal of Alloys and Compounds, 231 (1995) 639-644.
[92] M. Geng, J. Han, F. Feng, D.O. Northwood, Charging/discharging stability of a metal hydride battery electrode, Journal of the Electrochemical Society, 146 (1999) 2371-2375.
[93] C. Iwakura, K. Ohkawa, H. Senoh, H. Inoue, A Co-free AB_5-type hydrogen storage slloy for Nickel-Metal Hydride batteries: $LmNi_{4.0}Al_{0.3}Si_{0.1}Fe_{0.6}$, Journal of the Electrochemical Society, 149 (2002) A462-A465.
[94] Z.-H. Ma, J.-F. Qiu, L.-X. Chen, Y.-Q. Lei, Effects of annealing on microstructure and electrochemical properties of the low Co-containing alloy $Ml(NiCoMnAlFe)_5$ for Ni-MH battery electrode, Journal of Power Sources, 125 (2004) 267-272.
[95] W.-K. Hu, R.V. Denys, C.C. Nwakwuo, T. Holm, J.P. Maehlen, J.K. Solberg, V.A. Yartys, Annealing effect on phase composition and electrochemical properties of the Co-free La_2MgNi_9 anode for Ni-Metal Hydride batteries, Electrochimica Acta, 96 (2013) 27-33.
[96] H. Huang, K. Huang, S. Liu, D. Chen, Microstructures and electrochemical properties of $Mg_{0.9}Ti_{0.1}Ni_{1-x}M_x$ (M=Co, Mn; x=0, 0.1, 0.2) hydrogen storage alloys, Powder Technology, 198 (2010) 144-148.
[97] P. Vermeulen, R. Niessen, P. Notten, Hydrogen storage in metastable $Mg_yTi_{(1-y)}$ thin films, Electrochemistry Communications, 8 (2006) 27-32.
[98] W. Liu, Y. Lei, D. Sun, J. Wu, Q. Wang, A study of the degradation of the electrochemical capacity of amorphous $Mg_{50}Ni_{50}$ alloy, Journal of Power Sources, 58 (1996) 243-247.
[99] N. Cui, B. Luan, H. Liu, S. Dou, Discharge behaviour of Mg_2Ni-type hydrogen-storage alloy electrodes in 6 M KOH solution by electrochemical impedance spectroscopy, Journal of power sources, 63 (1996) 209-214.
[100] H. Yuan, Q. Li, H. Song, Y. Wang, J. Liu, Electrochemical characteristics of Mg_2Ni-type alloys prepared by mechanical alloying, Journal of Alloys and Compounds, 353 (2003) 322-326.
[101] M. Anik, Electrochemical hydrogen storage capacities of Mg_2Ni and MgNi alloys synthesized by mechanical alloying, Journal of Alloys and Compounds, 491 (2010) 565-570.
[102] Y.-q. Lei, Y.-m. Wu, Q.-m. Yang, J. Wu, Q.-d. Wang, Electrochemical behaviour of some mechanically alloyed Mg-Ni-based amorphous: Hydrogen storage alloys, Zeitschrift für Physikalische Chemie, 183 (1994) 379-384.
[103] C. Iwakura, H. Inoue, S.G. Zhang, S. Nohara, Hydriding and electrochemical characteristics of a homogeneous amorphous Mg_2Ni-Ni composite, Journal of alloys and compounds, 270 (1998) 142-144.

[104] S. Nohara, N. Fujita, S.G. Zhang, H. Inoue, C. Iwakura, Electrochemical characteristics of a homogeneous amorphous alloy prepared by ball-milling Mg_2Ni with Ni, Journal of Alloys and Compounds, 267 (1998) 76-78.
[105] P. Notten, M. Ouwerkerk, H. Van Hal, D. Beelen, W. Keur, J. Zhou, H. Feil, High energy density strategies: From hydride-forming materials research to battery integration, Journal of Power Sources, 129 (2004) 45-54.
[106] R. Niessen, P. Notten, Electrochemical hydrogen storage characteristics of thin film MgX (X= Sc, Ti, V, Cr) compounds, Electrochemical and Solid-State Letters, 8 (2005) A534-A538.
[107] T. Kohno, M. Kanda, Effect of partial substitution on hydrogen storage properties of Mg_2Ni alloy, Journal of the Electrochemical Society, 144 (1997) 2384-2388.
[108] S. Bliznakov, N. Drenchev, B. Drenchev, P. Delchev, P. Solsona, T. Spassov, Electrochemical properties of nanocrystalline Mg_2Ni-type alloys prepared by mechanical alloying, Journal of Alloys and Compounds, 404 (2005) 682-686.
[109] J. Chen, N. Kuriyama, H. Takeshita, H. Tanaka, T. Sakai, M. Haruta, Hydrogen storage alloys with $PuNi_3$-type structure as metal hydride electrodes, Electrochemical and Solid-State Letters, 3 (2000) 249-252.
[110] T. Kohno, H. Yoshida, F. Kawashima, T. Inaba, I. Sakai, M. Yamamoto, M. Kanda, Hydrogen storage properties of new ternary system alloys: La_2MgNi_9, $La_5Mg_2N_{i23}$, La_3MgNi_{14}, Journal of Alloys and Compounds, 311 (2000) L5-L7.
[111] Y. Liu, Y. Cao, L. Huang, M. Gao, H. Pan, Rare earth–Mg–Ni-based hydrogen storage alloys as negative electrode materials for Ni/MH batteries, Journal of Alloys and Compounds, 509 (2011) 675-686.
[112] R.V. Denys, V.A. Yartys, Effect of magnesium on the crystal structure and thermodynamics of the $La_{3-x}Mg_xNi_9$ hydrides, Journal of Alloys and Compounds, 509 (2011) S540-S548.
[113] B. Liao, Y.Q. Lei, G.L. Lu, L.X. Chen, H.G. Pan, Q.D. Wang, The electrochemical properties of $La_xMg_{3-x}Ni_9$ (x=1.0–2.0) hydrogen storage alloys, Journal of Alloys and Compounds, 356-357 (2003) 746-749.
[114] H. Pan, Y. Liu, M. Gao, Y. Zhu, Y. Lei, Q. Wang, A study on the effect of annealing treatment on the electrochemical properties of $La_{0.67}Mg_{0.33}Ni_{2.5}Co_{0.5}$ alloy electrodes, International Journal of Hydrogen Energy, 28 (2003) 113-117.
[115] H.-L. Chu, S.-J. Qiu, L.-X. Sun, Y. Zhang, F. Xu, M. Zhu, W.-Y. Hu, Electrochemical hydrogen storage properties of $La_{0.7}Mg_{0.3}Ni_{3.5}$–$Ti_{0.17}Zr_{0.08}V_{0.35}Cr_{0.1}Ni_{0.3}$ composites, International Journal of Hydrogen Energy, 33 (2008) 755-761.
[116] L. Xiao, Y. Wang, Y. Liu, D. Song, L. Jiao, H. Yuan, Influence of surface treatments on microstructure and electrochemical properties of $La_{0.7}Mg_{0.3}Ni_{2.4}Co_{0.6}$ hydrogen-storage alloy, International Journal of Hydrogen Energy, 33 (2008) 3925-3929.
[117] K. Young, T. Ouchi, Y. Liu, B. Reichman, W. Mays, M. Fetcenko, Structural and electrochemical properties of $Ti_xZr_{7-x}Ni_{10}$, Journal of Alloys and Compounds, 480 (2009) 521-528.
[118] K. Young, J. Nei, D. Wong, L. Wang, Structural, hydrogen storage, and electrochemical properties of Laves phase-related body-centered-cubic solid solution

metal hydride alloys, International Journal of Hydrogen Energy, 39 (2014) 21489-21499.
[119] X. Song, Y. Chen, C. Sequeira, Y. Lei, Q. Wang, Z. Zhang, Microstructural evolution of body-centered cubic structure related Ti–Zr–Ni phases in non-stoichiometric Zr-based Zr–Ti–Mn–V–Ni hydride electrode alloys, Journal of Materials Research, 18 (2011) 37-44.
[120] H. Pan, Y. Zhu, M. Gao, Q. Wang, Investigation of the structural and electrochemical properties of superstoichiometric Ti-Zr-V-Mn-Cr-Ni hydrogen storage alloys, Journal of the Electrochemical Society, 149 (2002) A829-A833.
[121] K. Young, T. Ouchi, B. Huang, B. Reichman, M.A. Fetcenko, Effect of Molybdenum content on structural, gaseous storage, and electrochemical properties of C14-predominant AB_2 metal hydride alloys, Journal of Power Sources, 196 (2011) 8815-8821.
[122] S. Suwarno, J.K. Solberg, J.P. Maehlen, B. Krogh, V.A. Yartys, Influence of Cr on the hydrogen storage properties of Ti-rich Ti–V–Cr alloys, International Journal of Hydrogen Energy, 37 (2012) 7624-7628.
[123] A.R. Edwards, The lattice dimensions of the AB_2 Laves phases, Metallurgical Transactions, 3 (1972) 1365-1372.
[124] F. Stein, M. Palm, G. Sauthoff, Structure and stability of Laves phases: Part I. Critical assessment of factors controlling Laves phase stability, Intermetallics, 12 (2004) 713-720.
[125] K.-H. Young, J. Nei, C. Wan, R. Denys, V. Yartys, Comparison of C14- and C15-Predomiated AB2 Metal Hydride Alloys for Electrochemical Applications, Batteries, 3 (2017) 22.
[126] C. Wan, R. Denys, M. Lelis, D. Milčius, V. Yartys, Electrochemical studies and phase-structural characterization of a high-capacity La-doped AB_2 Laves type alloy and its hydride, Journal of Power Sources, 418 (2019) 193-201.
[127] C.T. Liu, J.H. Zhu, M.P. Brady, C.G. McKamey, L.M. Pike, Physical metallurgy and mechanical properties of transition-metal Laves phase alloys, Intermetallics, 8 (2000) 1119-1129.
[128] K.S. Kumar, P.M. Hazzledine, Polytypic transformations in Laves phases, Intermetallics, 12 (2004) 763-770.
[129] B. Mayer, H. Anton, E. Bott, M. Methfessel, J. Sticht, J. Harris, P.C. Schmidt, Ab-initio calculation of the elastic constants and thermal expansion coefficients of Laves phases, Intermetallics, 11 (2003) 23-32.
[130] N. Rusman, M. Dahari, A review on the current progress of metal hydrides material for solid-state hydrogen storage applications, International Journal of Hydrogen Energy, 41 (2016) 12108-12126.
[131] D.P. Shoemaker, C.B. Shoemaker, Concerning atomic sites and capacities for hydrogen absorption in the AB_2 Friauf-Laves phases, Journal of the Less Common Metals, 68 (1979) 43-58.
[132] J.B. Friauf, The crystal structure of Magnesium di-zincide, Physical Review, 29 (1927) 34-40.
[133] J.B. Friauf, The crystal structures of two intermetallic compounds, Journal of the American Chemical Society, 49 (1927) 3107-3114.

[134] S.R. Ovshinsky, M.A. Fetcenko, Development of high catalytic activity disordered hydrogen-storage alloys for electrochemical application in Nickel–Metal hydride batterie, Applied Physics A, 72 (2001) 239-244.
[135] K.-H. Young, J.M. Koch, C. Wan, R.V. Denys, V.A. Yartys, Cell performance comparison between C14-and C15-predomiated AB_2 metal hydride alloys, Batteries, 3 (2017) 29.
[136] K.-H. Young, S. Chang, X. Lin, C14 Laves phase metal hydride alloys for Ni-MH batteries applications, Batteries, 3 (2017) 27.
[137] J. Nei, K. Young, S. Salley, K. Ng, Determination of C14/C15 phase abundance in Laves phase alloys, Materials Chemistry and Physics, 136 (2012) 520-527.
[138] Y. Zhang, J. Li, T. Zhang, H. Kou, R. Hu, X. Xue, Hydrogen storage properties of non-stoichiometric $Zr_{0.9}Ti_xV_2$ melt-spun ribbons, Energy, 114 (2016) 1147-1154.
[139] A. Matsuyama, H. Mizutani, T. Kozuka, H. Inoue, Effect of Ti substitution on electrochemical properties of ZrNi alloy electrode for use in Nickel-Metal Hydride batteries, International Journal of Hydrogen Energy, 42 (2017) 22622-22627.
[140] E. Jankowska, M. Makowiecka, M. Jurczyk, Electrochemical performance of sealed Ni-MH batteries using nanocrystalline TiNi-type hydride electrodes, Renewable Energy, 33 (2008) 211-215.
[141] K. Young, D.F. Wong, T. Ouchi, B. Huang, B. Reichman, Effects of La-addition to the structure, hydrogen storage, and electrochemical properties of C14 metal hydride alloys, Electrochimica Acta, 174 (2015) 815-825.
[142] L. Kong, X. Li, K. Young, J. Nei, X. Liao, W. Li, Effects of rare-earth element additions to Laves phase-related body-centered-cubic solid solution metal hydride alloys: Thermodynamic and electrochemical properties, Journal of Alloys and Compounds, 737 (2018) 174-183.
[143] S. Banerjee, A. Kumar, C. Pillai, Improvement on the Hydrogen storage properties of $ZrFe_2$ Laves phase alloy by vanadium substitution, Intermetallics, 51 (2014) 30-36.
[144] K.-h. Young, D.F. Wong, J. Nei, Effects of Vanadium/Nickel contents in Laves phase-related body-centered-cubic solid solution metal hydride alloys, Batteries, 1 (2015) 34-53.
[145] K. Young, D. Wong, S. Yasuoka, J. Ishida, J. Nei, J. Koch, Different failure modes for V-containing and V-free AB_2 metal hydride alloys, Journal of Power Sources, 251 (2014) 170-177.
[146] K. Young, T. Ouchi, J. Koch, M.A. Fetcenko, The role of Mn in C14 Laves phase multi-component alloys for Ni-MH battery application, Journal of Alloys and Compounds, 477 (2009) 749-758.
[147] X.B. Yu, Z.X. Yang, S.L. Feng, Z. Wu, N.X. Xu, Influence of Fe addition on hydrogen storage characteristics of Ti–V-based alloy, International Journal of Hydrogen Energy, 31 (2006) 1176-1181.
[148] K. Young, T. Ouchi, B. Huang, B. Reichman, M.A. Fetcenko, The structure, hydrogen storage, and electrochemical properties of Fe-doped C14-predominating AB_2 Metal hydride alloys, International Journal of Hydrogen Energy, 36 (2011) 12296-12304.

[149] J.-K. Chang, D.-N.S. Shong, W.-T. Tsai, Effects of alloying elements and binder on the electrochemical behavior of metal hydride electrodes in Potassium hydroxide electrolyte, Journal of Solid State Electrochemistry, 7 (2003) 485-491.
[150] K. Young, T. Ouchi, J. Nei, T. Meng, Effects of Cr, Zr, V, Mn, Fe, and Co to the hydride properties of Laves phase-related body-centered-cubic solid solution alloys, Journal of Power Sources, 281 (2015) 164-172.
[151] Z. Li, H. Wang, L. Ouyang, J. Liu, M. Zhu, Reversible hydriding in $YFe_{2-x}Al_x$ (x= 0.3, 0.5, 0.7) intermetallic compounds, Journal of Alloys and Compounds, 689 (2016) 843-848.
[152] B.V. Ratnakumar, C. Witham, R.C. Bowman, A. Hightower, B. Fultz, Electrochemical Studies on $LaNi_{5-x}Sn_x$ metal hydride alloys, Journal of the Electrochemical Society, 143 (1996) 2578-2584.
[153] B.V. Ratnakumar, C. Witham, B. Fultz, G. Halpert, Electrochemical evaluation of La-Ni-Sn metal hydride alloys, Journal of the Electrochemical Society, 141 (1994) L89-L91.
[154] K. Young, M.A. Fetcenko, T. Ouchi, F. Li, J. Koch, Effect of Sn-substitution in C14 Laves phase alloys for Ni-MH battery application, Journal of Alloys and Compounds, 469 (2009) 406-416.
[155] M. Gutjahr, A new type of reversible negative electrode for alkaline storage batteries based on metal alloy hydrides, Power sources, 4 (1973) 79-91.
[156] K. Young, T. Ouchi, J. Yang, M.A. Fetcenko, Studies of off-stoichiometric AB_2 metal hydride alloy: Part 1. Structural characteristics, International Journal of Hydrogen Energy, 36 (2011) 11137-11145.
[157] Y. Zhu, H. Pan, M. Gao, Y. Liu, Q. Wang, A study on improving the cycling stability of $(Ti_{0.8}Zr_{0.2})(V_{0.533}Mn_{0.107}Cr_{0.16}Ni_{0.2})_4$ hydrogen storage electrode alloy by means of annealing treatment:: I. Effects on the structures, Journal of Alloys and Compounds, 347 (2002) 279-284.
[158] Y.L. Zhang, J.S. Li, T.B. Zhang, H.C. Kou, R. Hu, X.Y. Xue, Microstructural characterization and hydrogenation properties of non-stoichiometric $Zr_{0.9}Ti_xV_2$ alloys, International Journal of Hydrogen Energy, 39 (2014) 19637-19645.
[159] W.K. Zhang, C.A. Ma, X.G. Yang, Y.Q. Lei, Q.D. Wang, G.L. Lu, Influences of annealing heat treatment on phase structure and electrochemical properties of $Zr(MnVNi)_2$ hydrogen storage alloys, Journal of Alloys and Compounds, 293-295 (1999) 691-697.
[160] J. Nei, K. Young, R. Regmi, G. Lawes, S.O. Salley, K.Y.S. Ng, Gaseous phase hydrogen storage and electrochemical properties of Zr_8Ni_{21}, Zr_7Ni_{10}, Zr_9Ni_{11}, and ZrNi Metal hydride alloys, International Journal of Hydrogen Energy, 37 (2012) 16042-16055.
[161] W.-K. Hu, D.-M. Kim, S.-W. Jeon, J.-Y. Lee, Effect of annealing treatment on electrochemical properties of Mm-based hydrogen storage alloys for Ni-MH batteries, Journal of Alloys and Compounds, 270 (1998) 255-264.
[162] H.J. Chuang, S.S. Huang, C.Y. Ma, S.L.I. Chan, Effect of annealing heat treatment on an atomized AB_2 hydrogen storage alloy, Journal of Alloys and Compounds, 285 (1999) 284-291.

[163] Q.A. Zhang, Y.Q. Lei, X.G. Yang, K. Ren, Q.D. Wang, Annealing treatment of AB2-type hydrogen storage alloys: II. Electrochemical properties, Journal of Alloys and Compounds, 292 (1999) 241-246.
[164] Q.A. Zhang, Y.Q. Lei, X.G. Yang, K. Ren, Q.D. Wang, Annealing treatment of AB_2-type hydrogen storage alloys: I. Crystal structures, Journal of Alloys and Compounds, 292 (1999) 236-240.
[165] C.C. Nwakwuo, T. Holm, R.V. Denys, W. Hu, J.P. Maehlen, J.K. Solberg, V.A. Yartys, Effect of Magnesium content and quenching rate on the phase structure and composition of rapidly solidified La_2MgNi_9 metal hydride battery electrode alloy, Journal of Alloys and Compounds, 555 (2013) 201-208.
[166] A. Zaluska, L. Zaluski, J.O. Ström-Olsen, Structure, catalysis and atomic reactions on the nano-scale: A systematic approach to metal hydrides for hydrogen storage, Applied Physics A, 72 (2001) 157-165.
[167] A. Zaluska, L. Zaluski, J.O. Ström–Olsen, Nanocrystalline Magnesium for hydrogen storage, Journal of Alloys and Compounds, 288 (1999) 217-225.
[168] S.K. Zhang, K.Y. Shu, Y.Q. Lei, G.L. Lü, Q.D. Wang, Effect of solidification rate on the phase structure and electrochemical properties of alloy $Zr_{0.7}Ti_{0.3}(MnVNi)_2$, Journal of Alloys and Compounds, 352 (2003) 158-162.
[169] T. Zhang, Y. Zhang, J. Li, H. Kou, R. Hu, X. Xue, Microstructure and hydrogenation properties of a melt-spun non-stoichiometric Zr-based Laves phase alloy, Materials Characterization, 111 (2016) 53-59.
[170] Y.L. Zhang, J.S. Li, T.B. Zhang, R. Hu, X.Y. Xue, Microstructure and hydrogen storage properties of non-stoichiometric Zr–Ti–V Laves phase alloys, International Journal of Hydrogen Energy, 38 (2013) 14675-14684.
[171] K.Y. Shu, Y.Q. Lei, X.G. Yang, S.K. Zhang, G.L. Lü, H. Zhang, Q.D. Wang, Micro-crystalline C14 Laves phase in melt-spun AB_2 type Zr-based alloy, Journal of Alloys and Compounds, 311 (2000) 288-291.
[172] Y. Xiaoguang, S. Kangyin, Z. Xiaobin, L. Youngquan, W. Qidong, Electrode performances of melt-spinned AB_2 type Zr-based hydrogen storage alloys Transactions of Nonferrous Metals Society of China, 8 No 4 (1998) 4.
[173] Y.-h. Zhang, Y. Cai, C. Zhao, T.-t. Zhai, G.-f. Zhang, D.-l. Zhao, Electrochemical performances of the as-melt $La_{0.75-x}M_xMg_{0.25}Ni_{3.2}Co_{0.2}Al_{0.1}$ (M = Pr, Zr; x = 0, 0.2) alloys applied to Ni-Metal Hydride (MH) battery, International Journal of Hydrogen Energy, 37 (2012) 14590-14597.
[174] Y.-h. Zhang, W. Zhang, X.-p. Song, P.-l. Zhang, Y.-g. Zhu, Q. Yan, Effects of spinning rate on structures and electrochemical hydrogen storage performances of RE–Mg–Ni–Mn-based AB_2-type alloys, Transactions of Nonferrous Metals Society of China, 26 (2016) 3219-3231.
[175] Y.-H. Zhang, P. Li, X.-L. Wang, Y.-F. Lin, G.-q. Wang, The effects of rapid quenching on the electrochemical characteristics and microstructures of AB_2 Laves phase electrode alloys, Journal of Power Sources, 128 (2004) 90-96.
[176] Y.-h. Zhang, D.-l. Zhao, X.-p. Dong, Y. Qi, S.-h. Guo, X.-l. Wang, Effects of rapid quenching on structure and electrochemical characteristics of $La_{0.5}Ce_{0.2}Mg_{0.3}Co_{0.4}Ni_{2.6-x}Mnx$ (x=0–0.4) electrode alloys, Transactions of Nonferrous Metals Society of China, 19 (2009) 364-371.

[177] B. Liu, Q. Li, Z. Zhang, G. Mi, Q. Yuan, L. Wang, Crystallographic and electrochemical characteristics of $Ti_{45}Zr_{35}Ni_{13}Pd_7$ melt-spun alloys, International Journal of Hydrogen Energy, 34 (2009) 1890-1895.
[178] Y. Zhang, C. Zhao, T. Yang, H. Shang, C. Xu, D. Zhao, Comparative study of electrochemical performances of the as-melt $Mg_{20}Ni_{10-x}M_x$ (M=None, Cu, Co, Mn; x=0, 4) alloys applied to Ni-Metal Hydride (MH) battery, Journal of Alloys and Compounds, 555 (2013) 131-137.
[179] M. Fichtner, Properties of nanoscale metal hydrides, Nanotechnology, 20 (2009) 204009.
[180] C. Liu, F. Li, L.-P. Ma, H.-M. Cheng, Advanced materials for energy storage, Advanced Materials, 22 (2010) E28-E62.
[181] C. Suryanarayana, F. Froes, R. Rowe, Rapid solidification processing of Titanium alloys, International Materials Reviews, 36 (1991) 85-123.
[182] H. Liebermann, Rapidly solidified alloys made by chill block melt-spinning processes, Journal of Crystal Growth, 70 (1984) 497-506.
[183] M.S. El-Eskandarany, Mechanical alloying: Nanotechnology, materials science and powder metallurgy, Elsevier, 2015.
[184] C. Suryanarayana, A. Inoue, Bulk metallic glasses, CRC press, 2017.
[185] H. Jones, Splat cooling and metastable phases, Reports on Progress in Physics, 36 (1973) 1425.
[186] C. Suryanarayana, Non-equilibrium processing of materials, Elsevier, 1999.
[187] K. Shu, Y. Lei, X. Yang, G. Lin, Q. Wang, G. Lü, L. Chen, Effect of rapid solidification process on the alloy structure and electrode performance of $Zr(Ni_{0.55}V_{0.1}Mn_{0.3}Cr_{0.55})_{2.1}$, Journal of Alloys and Compounds, 293-295 (1999) 756-761.
[188] S. Suwarno, J.K. Solberg, J.P. Maehlen, B. Krogh, B.T. BØRresen, E. Ochoa-Fernandez, E. Rytter, M. Williams, R. Denys, V.A. Yartys, Microstructure and hydrogen storage properties of as-cast and rapidly solidified Ti-rich Ti–V alloys, Transactions of Nonferrous Metals Society of China, 22 (2012) 1831-1838.
[189] A. Anani, A. Visintin, K. Petrov, S. Srinivasan, J.J. Reilly, J.R. Johnson, R.B. Schwarz, P.B. Desch, Alloys for hydrogen storage in Nickel-Hydrogen and Nickel-Metal Hydride batteries, Journal of Power Sources, 47 (1994) 261-275.
[190] M. Tliha, C. Khaldi, S. Boussami, N. Fenineche, O. El-Kedim, H. Mathlouthi, J. Lamloumi, Kinetic and thermodynamic studies of hydrogen storage alloys as negative electrode materials for NiMH batteries: a review, J Solid State Electrochemistry, 18 (2014) 577-593.
[191] R.V. Denys, A.A. Poletaev, J.P. Maehlen, J.K. Solberg, B.P. Tarasov, V.A. Yartys, Nanostructured rapidly solidified $LaMg_{11}Ni$ alloy: II. In situ synchrotron X-ray diffraction studies of hydrogen absorption–desorption behaviours, International Journal of Hydrogen Energy, 37 (2012) 5710-5722.
[192] A.A. Poletaev, R.V. Denys, J.P. Maehlen, J.K. Solberg, B.P. Tarasov, V.A. Yartys, Nanostructured rapidly solidified $LaMg_{11}Ni$ alloy: Microstructure, crystal structure and hydrogenation properties, International Journal of Hydrogen Energy, 37 (2012) 3548-3557.
[193] V. Yartys, R. Denys, J.P. Maehlen, C.J. Webb, E.M. Gray, T. Blach, A.A. Poletaev, J.K. Solberg, O. Isnard, Nanostructured metal hydrides for hydrogen storage

studied by in situ synchrotron and neutron diffraction, MRS Online Proceedings Library Archive, 1262 (2010).
[194] Y. Wu, M.V. Lototsky, J.K. Solberg, V.A. Yartys, Microstructural evolution and improved hydrogenation–dehydrogenation kinetics of nanostructured melt-spun Mg–Ni–Mm alloys, Journal of Alloys and Compounds, 509 (2011) S640-S645.
[195] Z. Dehouche, R. Djaozandry, J. Huot, S. Boily, J. Goyette, T.K. Bose, R. Schulz, Influence of cycling on the thermodynamic and structure properties of nanocrystalline Magnesium-based hydride, Journal of Alloys and Compounds, 305 (2000) 264-271.
[196] H. Iba, E. Akiba, The relation between microstructure and hydrogen absorbing property in Laves phase-solid solution multiphase alloys, Journal of Alloys and Compounds, 231 (1995) 508-512.
[197] H. Miao, M. Gao, Y. Liu, Y. Lin, J. Wang, H. Pan, Microstructure and electrochemical properties of Ti–V-based multiphase hydrogen storage electrode alloys $Ti_{0.8}Zr_{0.2}V_{2.7}Mn_{0.5}Cr_{0.8-x}Ni_{1.25}Fe_x$ (x=0.0–0.8), International Journal of Hydrogen Energy, 32 (2007) 3947-3953.
[198] M.A. Fetcenko, S.R. Ovshinsky, K. Young, B. Reichman, C. Fierro, J. Koch, F. Martin, W. Mays, T. Ouchi, B. Sommers, A. Zallen, High catalytic activity disordered VTiZrNiCrCoMnAlSn hydrogen storage alloys for Nickel–Metal Hydride batteries, Journal of Alloys and Compounds, 330-332 (2002) 752-759.
[199] M. Bououdina, C. Lenain, L. Aymard, J.L. Soubeyroux, D. Fruchart, The effects of heat treatments on the microstructure and electrochemical properties of the $ZrCr_{0.7}Ni_{1.3}$ multiphase alloy, Journal of Alloys and Compounds, 327 (2001) 178-184.
[200] S. Cheng, J. Zhang, M. Zhao, C. Cao, Electrochemical impedance spectroscopy study of Ni-MH batteries, Journal of Alloys and Compounds, 293-295 (1999) 814-820.
[201] D. Pletcher, R. Greff, R. Peat, L. Peter, J. Robinson, Instrumental methods in electrochemistry, Elsevier, 2001.
[202] D. Hooper, J. Coughlan, M. Mullen, Structural equation modelling: Guidelines for determining model fit, Articles, (2008) 2.
[203] S.M. Ross, CHAPTER 12 - Linear Regression, in: S.M. Ross (Ed.) Introductory Statistics (Third Edition), Academic Press, Boston, 2010, pp. 537-604.
[204] G. Smith, Essential statistics, regression, and econometrics, Academic press, 2015.
[205] A.C. Larson, R. Von Dreele, General structure analysis system (GSAS) (Report LAUR 86-748), Los Alamos, New Mexico: Los Alamos National Laboratory, (2004).
[206] F.-J. Liu, S. Suda, G. Sandrock, Effects of Ni-substitution and F-treatment on the hydriding behaviors and microstructures of AB_2-compound (Ti, Zr)(Mn, Cr)$_2$, Journal of Alloys and Compounds, 232 (1996) 232-237.
[207] K. Morii, T. Shimizu, Hydriding characteristics in (Ti, Zr)(Ni, Mn, X)$_2$ alloys, Journal of Alloys and Compounds, 231 (1995) 524-527.
[208] H. Jones, Microstructure of rapidly solidified materials, Materials Science and Engineering, 65 (1984) 145-156.
[209] V. Burnasheva, V. Yartys, N. Fadeeva, S. Solovev, K. Semenenko, Neutron-diffraction study of $LaNiD_{3.7}$ Deuteride, Zhurnal Neorganicheskoi Khimii, 27 (1982) 1112-1116.

[210] F. Stein, M. Palm, G. Sauthoff, Structure and stability of Laves phases: Part II. Structure type variations in binary and ternary systems, Intermetallics, 13 (2005) 1056-1074.
[211] Y.L. Du, G. Chen, G.L. Chen, Optimization of Zr-based hydrogen storage alloys for Nickel-hydride batteries, Intermetallics, 13 (2005) 399-402.
[212] S.-J. Qiu, H.-L. Chu, J. Zhang, Y. Zhang, L.-X. Sun, F. Xu, D.-L. Sun, L.-Z. Ouyang, M. Zhu, J.P.E. Grolier, M. Frenkel, Effect of La partial substitution for Zr on the structural and electrochemical properties of $Ti_{0.17}Zr_{0.08-x}La_xV_{0.35}Cr_{0.1}Ni_{0.3}$ (x=0–0.04) electrode alloys, International Journal of Hydrogen Energy, 34 (2009) 7246-7252.
[213] D. Sun, J.M. Joubert, M. Latroche, A. Percheron-Guégan, Metallurgical state of Lanthanum and its effects on the activation behaviour of $Zr(Cr_{0.4}Ni_{0.6})_2$ hydride formation, Journal of Alloys and Compounds, 239 (1996) 193-197.
[214] W.K. Choi, K. Yamataka, S.G. Zhang, H. Inoue, C. Iwakura, Effects of surface treatment with boiling alkaline solution on electrochemical and physicochemical properties of the $Zr_{0.9}Ti_{0.1}Ni_{1.1}Co_{0.1}Mn_{0.6}V_{0.2}$ alloy electrode, Journal of The Electrochemical Society, 146 (1999) 46-48.
[215] S. Tan, Y. Shen, E. Onur Şahin, D. Noréus, T. Öztürk, Activation behavior of an AB_2 type metal hydride alloy for Ni-MH batteries, International Journal of Hydrogen Energy, 41 (2016) 9948-9953.
[216] W. Chen, Z. Tang, H. Guo, Z. Liu, C. Changpin, Q. Wang, Effects of surface treatment on performances of metal hydride electrodes and Ni-MH batteries, Journal of Power Sources, 74 (1998) 34-39.
[217] K. Young, B. Chao, D. Pawlik, H. Shen, Transmission electron microscope studies in the surface oxide on the La-containing AB_2 metal hydride alloy, Journal of Alloys and Compounds, 672 (2016) 356-365.
[218] E.O. ŞAHİN, Development of rare earth-free negative electrode materials for Ni-MH batteries, A thesis submitted to the Graduate School of Natural and Applied Sciences of Middle East Technical University, (2016) 94.
[219] X.P. Gao, W. Zhang, H.B. Yang, D.Y. Song, Y.S. Zhang, Z.X. Zhou, P.W. Shen, Electrochemical properties of the $Zr(V_{0.4}Ni_{0.6})_{2.4}$ hydrogen storage alloy electrode, Journal of Alloys and Compounds, 235 (1996) 225-231.
[220] P. Bäuerlein, C. Antonius, J. Löffler, J. Kümpers, Progress in high-power Nickel–Metal Hydride batteries, Journal of Power Sources, 176 (2008) 547-554.
[221] L. Ouyang, J. Huang, H. Wang, J. Liu, M. Zhu, Progress of hydrogen storage alloys for Ni-MH rechargeable power batteries in electric vehicles: A review, Materials Chemistry and Physics, 200 (2017) 164-178.
[222] K. Young, M. Young, S. Chang, B. Huang, Synergetic effects in electrochemical properties of $ZrV_xNi_{4.5-x}$ (x= 0.0, 0.1, 0.2, 0.3, 0.4, and 0.5) metal hydride alloys, Journal of Alloys and Compounds, 560 (2013) 33-41.
[223] B.H. Liu, Z.P. Li, R. Kitani, S. Suda, Improvement of electrochemical cyclic durability of Zr-based AB_2 alloy electrodes, Journal of Alloys and Compounds, 330-332 (2002) 825-830.
[224] B. Wang, Y. Chen, L. Wang, Y. Liu, Effect of annealing time on the structure and electrochemical properties of $La_{0.72}Nd_{0.08}Mg_{0.2}Ni_{3.4}Al_{0.1}$ hydrogen storage alloys, Journal of Alloys and Compounds, 541 (2012) 305-309.

[225] B.H. Liu, Z.P. Li, S. Suda, Electrochemical cycle life of Zr-based Laves phase alloys influenced by alloy stoichiometry and composition, Journal of The Electrochemical Society, 149 (2002) A537-A542.
[226] P. Li, X.-L. Wang, Y.-H. Zhang, J.-M. Wu, R. Li, X.-H. Qu, Research of low-Co AB_5 type rare-earth-based hydrogen storage alloy electrodes, Journal of Alloys and Compounds, 354 (2003) 310-314.
[227] W.-K. Hu, Studies on Cobalt-free AB_5-type hydrogen storage alloys, Journal of Alloys and Compounds, 289 (1999) 299-305.
[228] F. Meli, A. Züttel, L. Schlapbach, Electrochemical and surface properties of low cost, Cobalt-free $LaNi_5$-type hydrogen storage alloys, Journal of Alloys and Compounds, 202 (1993) 81-88.
[229] J.M. Cocciantelli, P. Bernard, S. Fernandez, J. Atkin, The influence of Co and various additives on the performance of $MmNi_{4.3-x}Mn_{0.33}Al_{0.4}Co_x$ hydrogen storage alloys and Ni-MH prismatic sealed cells, Journal of Alloys and Compounds, 253-254 (1997) 642-647.

APPENDIXES

PAPER I

PAPER I

Study of hydrogen storage and electrochemical properties of AB_2-type $Ti_{0.15}Zr_{0.85}La_{0.03}Ni_{1.2}Mn_{0.7}V_{0.12}Fe_{0.12}$ alloy

A.A. Volodin, R.V. Denys, C. Wan, I.D. Wijayanti, S. Suwarno, B.P. Tarasov, V.E. Antonov, V.A. Yartys

Journal of Alloys and Compounds, 793 (2019) 564-575.

Journal of Alloys and Compounds 793 (2019) 564–575

Contents lists available at ScienceDirect

Journal of Alloys and Compounds

journal homepage: http://www.elsevier.com/locate/jalcom

Study of hydrogen storage and electrochemical properties of AB_2-type $Ti_{0.15}Zr_{0.85}La_{0.03}Ni_{1.2}Mn_{0.7}V_{0.12}Fe_{0.12}$ alloy

Alexei A. Volodin [a, b], Roman V. Denys [b, c], ChuBin Wan [b, d], Ika Dewi Wijayanti [b, e, f], Suwarno [f], Boris P. Tarasov [a], Vladimir E. Antonov [g], Volodymyr A. Yartys [b, e, *]

[a] Institute of Problems of Chemical Physics RAS, Chernogolovka, 142432, Russia
[b] Institute for Energy Technology, P.O. Box 40, Kjeller, NO-2027, Norway
[c] HYSTORSYS AS, P.O. Box 45, Kjeller, NO-2027, Norway
[d] University of Science and Technology Beijing, 100083, China
[e] Norwegian University of Science and Technology, Trondheim, Norway
[f] Department of Mechanical Engineering, Sepuluh Nopember Institute of Technology (ITS), Surabaya, Indonesia
[g] Institute of Solid State Physics RAS, Chernogolovla, 142432, Russia

ARTICLE INFO

Article history:
Received 6 December 2018
Received in revised form
6 March 2019
Accepted 7 March 2019
Available online 9 March 2019

Keywords:
Hydrogen storage materials
AB_2 laves type intermetallics
Ni-MH batteries
Metal hydride anode
Hydrogen diffusion

ABSTRACT

A C15 AB_2 Laves-type $Ti_{0.15}Zr_{0.85}La_{0.03}Ni_{1.2}Mn_{0.7}V_{0.12}Fe_{0.12}$ alloy was prepared by arc melting and annealing. Phase-structural composition, microstructure, hydrogen absorption-desorption properties, thermodynamic and electrochemical performances were characterized by X-ray diffraction, scanning electron microscopy, hydrogen absorption-desorption measurements and electrochemical characterization and were related to the use of the alloys as metal hydride battery anodes.

The alloy contains a C15 FCC intermetallic compound as the main phase and a LaNi secondary phase as the minor constituent (~1 wt%).

During the electrochemical tests, the anode electrodes quickly, after just a few activation cycles, reached a maximum discharge capacity. This was related to the catalytic effect of the La-rich secondary phase which acted as a catalyst of hydrogen absorption-desorption.

Annealing resulted in increase of the maximum discharge capacity from 345 mAh/g for the as cast alloy to 370 mAh/g. Furthermore, the annealed alloy showed a better high rate dischargeability and a higher cyclic stability. After 100 cycles with 100% DOD at discharge current density of 1C, the discharge capacity of the annealed alloy was very high, at a level of 90% of the initial capacity.

The rates of hydrogen diffusion have been characterized by Potentiostatic Intermittent Titration Technique and Electrochemical Impedance Spectroscopy. With increasing an extent of transformation into the hydride, the H diffusion rate in the bulk of the alloy particles decreased. The maximum value of D_H measured by PITT for the annealed alloy was observed for the nearly fully discharged electrode, (SOC 2%).

1. Introduction

Currently, AB_5-, A_2B_7-, AB_3- and AB_2-type multicomponent metal hydride alloys are extensively studied as anodes of the Ni-MH batteries [1]. AB_2-type alloys in many aspects are advantageous as compared to the other alloys [2,3]. Due to the optimised design of the AB_2 alloys, during the hydrogen sorption-desorption the crystal lattice volume variations keep the cubic symmetry unchanged, thus reducing the strains and decreasing hysteresis between the pressures of hydrogen absorption and desorption and overpotential of charge and discharge for the metal hydride anode electrode. A smaller hysteresis assists in decreasing energy losses and in improving energy efficiency [4]. One example of AB_2 alloy with high H storage capacity is ZrV_2 intermetallic compound storing 4.8 at. H/f.u. (2.43 wt% H) at 1 bar H_2 [5]. However, at room temperature the formed hydride has a very low equilibrium pressure of hydrogen desorption of 10^{-8} bar and thus it cannot be used as a metal hydride anode material.

* Corresponding author. Institute for Energy Technology, P.O. Box 40, Kjeller, NO-2027, Norway.
E-mail address: volodymyr.yartys@ife.no (V.A. Yartys).

https://doi.org/10.1016/j.jallcom.2019.03.134
0925-8388/

The alloys with attractive electrochemical properties should have a pressure of hydrogen sorption-desorption below 1 bar at ambient conditions, allowing to reach a high reversible electrochemical capacity. Such pressures can be achieved by a proper selection of the chemical composition of the alloys.

One significant problem with the use of Zr- and Ti-based AB_2 alloys is in their difficult activation requiring a long activation process. Thus, improvement of the activation behaviors is a very important issue towards applications of metal hydrides as anode materials of the Ni-MH batteries.

Typically, battery anode AB_2-type alloys consist of Zr and Ti on the A site together with a variable combination of transition metals, including V, Cr, Mn, Ni and Fe on the B site [6]. Up till now, the effect of various additives on hydrogen absorption-desorption and electrochemical properties of the AB_2 alloys such as Titanium [7,8], Lanthanum [9], Yttrium [10,11], Cerium [12], Praseodymium [13], Neodymium [14], Nickel [15], Molybdenum [16,17], Zinc [18], Aluminum [19], Manganese [20], Vanadium [21], Iron [22,23], Silicon [24] has been extensively studied and documented in the reference publications.

Laves type AB_2 alloys predominantly crystallize with structures of two types, a C15 FCC $MgCu_2$ type and a C14 hexagonal $MgZn_2$ type [2]. Analysis of the available reference data leads to a conclusion that C14-predominated MH alloys are more suitable for high-capacity and long-life time applications, while C15-predominated MH alloys provide improved high-rate and low-temperature performances [2,3]. Therefore, many studies are aimed at optimizing the composition of C14/C15 Laves type alloys as H storage and battery electrode materials [25,26], and these works include the use of various mixtures of intermetallic compounds with different structures [27], and the development of activation methods [28] to increase the H storage capacity and to improve the hydrogenation-dehydrogenation kinetics. In addition, the sensitivity of AB_2 alloys to gaseous impurities should be addressed [29] together with improvement of their performance in metal-H_2 interactions at subzero temperatures (down to − 40 °C) [30].

In the present study we have prepared arc melted $Ti_{0.15}Zr_{0.85}La_{0.03}Ni_{1.2}Mn_{0.7}V_{0.12}Fe_{0.12}$ AB_2-type alloy and performed detailed studies of its phase composition and microstructure, including the effect of the annealing, on hydrogen absorption-desorption and electrochemical properties. The objective of the present work was to study electrochemical performance of the predominantly C15 type phase, which was obtained during the annealing. In addition, we used La as a catalyst to facilitate the process of electrochemical exchange. The obtained results are discussed in comparison with the available reference data.

The composition $Ti_{0.15}Zr_{0.85}La_{0.03}Ni_{1.2}Mn_{0.7}V_{0.12}Fe_{0.12}$ was selected based on our in-house research of AB_2-type alloys for their application as hydrogen storage materials. The studied alloy showed excellent hydrogen sorption properties (high reversible storage capacity, easy activation, fast kinetics and low hysteresis of isotherms of hydrogen absorption-desorption) which suggested that it could be very promising for its electrochemical applications as well.

As a starting point in the development of this composition we have used the data which was reported for the $Zr_{1-x}Ti_xNi_{1.3}Mn_{0.7-y}V_y$ alloys by Yoshida and Akiba [31]. They showed the use of a multicomponent substitution is an effective method to improve hydrogen storage properties of AB_2 alloys. Simultaneous substitution by Ti on Zr site and by V on the Mn site in a C15-type $ZrNi_{1.3}Mn_{0.7}$ phase alloy allowed to control the level of plateau pressures and to reduce hydrogen absorption/desorption hysteresis. As hysteresis leads to the energy loss during absorption/desorption cycle, in MH electrodes it causes voltage overpotential during the charging of the anode.

We have optimised composition of the alloys to obtain a flat and broad pressure plateau with a minimum value of hysteresis. Selection of optimised composition of our alloy allowed to reach the following benefits: proper choice of Ti/Zr ratio tuned the values of the plateau pressures; vanadium substitution reduced hysteresis while small addition of Fe resulted in flat plateaux and increased the values of the reversible H storage capacities.

2. Experimental

The $Ti_{0.15}Zr_{0.85}La_{0.03}Ni_{1.2}Mn_{0.7}V_{0.12}Fe_{0.12}$ alloy was prepared by arc melting of the starting elemental metals with a purity of not less than 99.7% in argon atmosphere. Manganese was taken in 4 wt% excess to compensate for its evaporation loss during the melting. As-cast alloy ingot was crushed and enclosed into a sealed stainless steel tube sample holder. The sealing was performed in argon gas. Subsequently the sample was annealed at 950 °C for 16 h and quenched into cold water after the annealing. The elemental composition of the obtained alloys was analyzed using EDX analysis. According to this analysis, the elemental composition of the alloys corresponded to the gross formula $Ti_{0.15}Zr_{0.85}La_{0.03}Ni_{1.2}Mn_{0.7}V_{0.12}Fe_{0.12}$.

X-ray diffraction (XRD) study with $CuK_{\alpha 1}$ radiation was used to identify the phase structure and composition of the alloys. The XRD data were collected using Siemens D500 BRAUN diffractometer. Powder diffraction data were analyzed by Rietveld whole-profile refinements method using the General Structure Analysis System (GSAS) software [32].

The surface morphology and phase composition of the alloys were analyzed using TESCAN VEGA II XMU Scanning Electron Microscope (SEM) with OXFORD INCA X–Sight EDX Detector. The samples were embedded into SpeciFix Resin (Struers), dried and polished. The backscattered electron (BSE) imaging mode was used to characterize the phase-structural composition and morphology of the prepared alloys at NTNU.

The isotherms of hydrogen absorption and desorption by the $Ti_{0.15}Zr_{0.85}La_{0.03}Ni_{1.2}Mn_{0.7}V_{0.12}Fe_{0.12}$ alloy were measured using a PCT setup. Annealed alloy powder was placed into a thermostated autoclave. The samples were activated in vacuum at 250 °C for 30 min. Then one cycle of full hydrogen absorption-desorption was performed. The hydrogen absorption-desorption isotherms were measured after the alloy's activation. The measurements were performed at 20, 50 and 80 °C (293, 323 and 353 K).

For the preparation of the MH electrodes, the annealed alloy was first ground and the fraction of the powder with a particle size of 40–60 μm and with average of around 50 μm was separated for the preparation of the anodes. Pellet type MH electrodes were prepared by mixing a MH alloy powder with carbonyl Ni powder having a specific surface area of ~0.7 m^2/g. The mixture contained 100 mg of the alloy and 400 mg of carbonyl Ni powder. The pellet electrodes of 10 mm in diameter with a thickness of approximately 1 mm were fabricated by cold-pressing under a pressure of 12 MPa for 5 min. Then the pellet was placed between the two Ni foam plates.

Electrochemical measurements were performed at room temperature using a three-electrode cell with a 9 M aqueous KOH electrolyte solution. Hg/HgO electrode served as a reference electrode. Sintered $Ni(OH)_2$/NiOOH plate obtained from a commercial supplier was used as a counter electrode and got a much higher capacity as compared to the working electrode. The tests were performed using a LAND CT2001A Battery Tester. Before starting the tests, MH electrode was firstly activated for 10 cycles by fully charging it at a current density of 100 mA/g for 5 h and then discharged at 100 mA/g to the cut-off voltage of 0.7 V.

Alternating Current (AC) impedance measurements were

performed for both as cast and annealed alloys. SP-300-Potentiostat from Bio-Logic Science Instruments was used during the Electrochemical Impedance Spectroscopy (EIS) characterization. Galvanostatic Electrochemical Impedance Spectroscopy (GEIS) technique was applied in a range of frequencies from 1 kHz to 0.5 mHz when using the amplitude of the current of 10 mA. Four different States of Charge (SOC) of the electrodes were selected for the studies, including SOC 0% (completely discharged anode), 30, 70, and 100% (fully charged anode).

3. Results and discussion

3.1. Phase and structural composition

Figs. 1 and 2 show the XRD patterns of the $Ti_{0.15}Zr_{0.85}La_{0.03}Ni_{1.2}Mn_{0.7}V_{0.12}Fe_{0.12}$ as-cast and annealed alloys. Table 1 summarizes the crystallographic data, including refined unit cell parameters, unit cell volumes and phase abundances. Refinements show that as-cast alloy contains three Laves phases: C15–I (61.1 wt%) and C15–II (25.7 wt%) with FCC structures as the main phase, and C14 (12.1 wt%) intermetallic with hexagonal structure as a secondary phase. Furthermore, trace amounts of LaNi orthorhombic structure phase (the most intense peak 111 is clearly seen at 31.75°) were identified. The minor phases (except of LaNi) disappear during the annealing of the alloy at 950 °C (Table 1) and only one C15 intermetallic phase remains. Refinements of the XRD data show that the experimental and calculated pattern well agree with each other (Figs. 1 and 2).

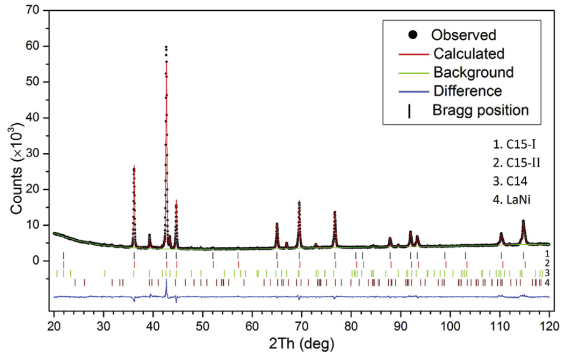

Fig. 1. XRD Rietveld refinements for the as cast alloy, $R_{wp} = 5.1\%$, $R_p = 3.8\%$, $\chi^2 = 3.5$.

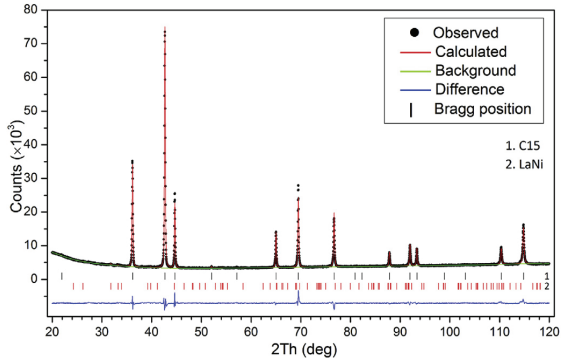

Fig. 2. XRD Rietveld refinements for the annealed alloy, $R_{wp} = 5.9\%$, $R_p = 4.2\%$, $\chi^2 = 4.3$.

Formation of three Laves phases are due to inhomogeneous distribution of the components in the alloy. Importantly, C15 phase is formed at higher Zr/Ti ratios while C14 intermetallic is formed at lower Zr/Ti ratios. A trend to form C14 phase increases with increasing Ti content. Increase of Ti content leads to a decrease in a lattice parameter of the C15 phase. Thus, Ti content in the C15–I phase should be smaller than that in the C15–II phase.

C14 phase was formed due to inhomogeneous distribution of the components in the as cast alloy. For the related $Zr_{1-x}Ti_xNi_{1.3}Mn_{0.7-y}V_y$ alloys with similar chemical composition, increase in Ti ($x > 0.2$) and vanadium ($y > 0.3$) contents leads to the formation of the C14 phase [31]. The C14 phase formation can be explained by a variation in Ti/Zr ratio between the multiphase components of the as cast alloy. Heat treatment results in a uniform distribution of the components and a formation of a pure C15 phase that is the most thermodynamically stable intermetallic for the given alloy composition.

Back-scattered electron SEM micrographs of the as-cast and annealed $Ti_{0.15}Zr_{0.85}La_{0.03}Ni_{1.2}Mn_{0.7}V_{0.12}Fe_{0.12}$ samples are presented in Fig. 3 and clearly show presence of two phases, a dark gray main phase together with light inclusions of a secondary phase. Table 2 shows the data of the elemental EDX analysis. According to the EDX analysis, the main (matrix) phase in the as-cast sample (1) is the AB_2 alloy while the secondary phase (2) is formed by lanthanum and nickel which are present in the atomic ratio La/Ni ≈ 1:1, with no contribution from the remaining elements. The content of the secondary phase is estimated as 3%. From quantitative analysis, the overall content of the elements well agrees with the gross formula of the alloy. In the annealed alloy, the fraction of the secondary phase significantly decreases, down to 1%. The reason for that could be in (a) Interaction of LaNi with metallurgical impurity of oxygen resulting in binding of O by La followed by a decrease of O content in the matrix phase; (b) Partial solubility of La in AB_2 matrix phase, probably at a trace level, but leading to a decrease on the content of LaNi secondary phase in the annealed alloy.

Even though the content of the secondary LaNi phase is rather low (1–3%) it was possible to identify it by XRD analysis. On the other hand, C14 Laves phase was also clearly identified by the XRD

Table 1
Crystallographic data for the $Ti_{0.15}Zr_{0.85}La_{0.03}Ni_{1.2}Mn_{0.7}V_{0.12}Fe_{0.12}$ as-cast and annealed alloys from Rietveld refinements of the XRD data.

Sample	Phase	Space group	Unit cell parameters, Å				Abundance, wt.%
			a	*b*	*c*	V, Å^3	
As-cast	C15–I	*Fd* $\bar{3}m$	7.0252(2)	–	–	346.718(1)	61.1(3)
	C15–II	*Fd* $\bar{3}m$	7.0125(3)	–	–	344.841(2)	25.7(2)
	C14	$P6_3/mmc$	4.9813(3)	–	8.1155(8)	174.389(2)	12.1(3)
	LaNi[a]	*Cmcm*	3.906(6)	10.77(2)	4.399(7)	185.055(4)	1.1(1)
Annealed	C15	*Fd* $\bar{3}m$	7.0235(1)	–	–	346.466(1)	99.1(1)
	LaNi	*Cmcm*	3.902(7)	10.78(2)	4.385(8)	184.449(6)	0.9(1)

[a] Rietveld refinements of LaNi phase were based on the reference data given in Ref. [33].

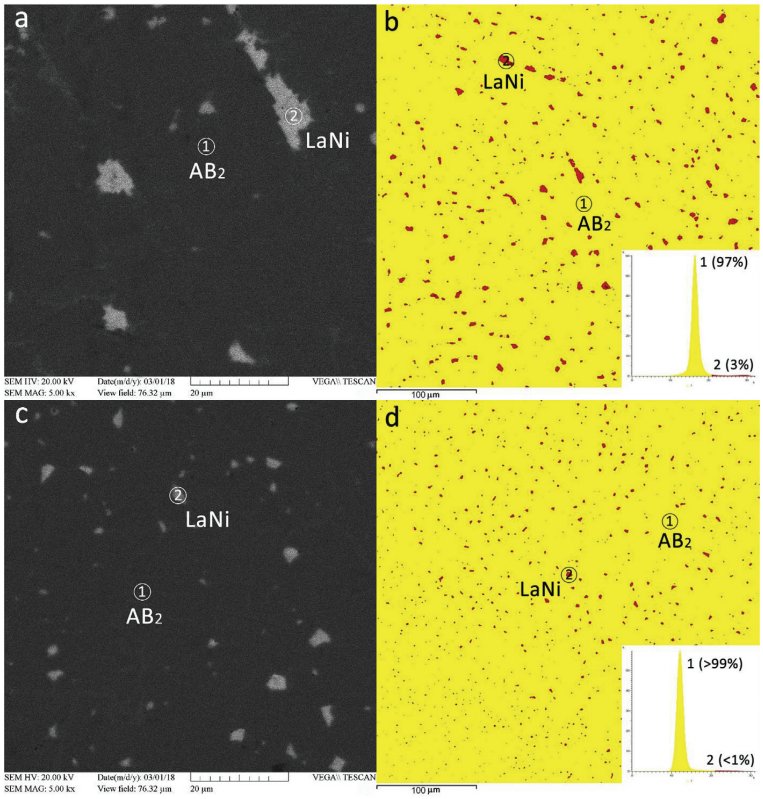

Fig. 3. SEM(BSE) (a,c) and EDX (b,d) images and abundances of the present phases, calculated from their areal in the $Ti_{0.15}Zr_{0.85}La_{0.03}Ni_{1.2}Mn_{0.7}V_{0.12}Fe_{0.12}$ as-cast (a and b) and annealed (c and d) alloys.

Table 2
Elemental compositions of $Ti_{0.15}Zr_{0.85}La_{0.03}Ni_{1.2}Mn_{0.7}V_{0.12}Fe_{0.12}$ (at.%) as cast and annealed at 950 °C alloys from EDX study.

	Region	Ti	Zr	La	Ni	Mn	V	Fe
As cast alloy	1	4.32	25.53	0.16	34.90	25.34	5.02	4.73
	2	0.15	0.33	48.54	48.58	1.43	0.97	0.00
Annealed alloy	1	5.50	26.55	0.17	37.45	21.95	4.45	3.93
	2	0.00	0.50	47.55	49.80	1.95	0.00	0.20
	Std. Dev.	0.60	0.20	0.12	0.45	0.40	0.25	0.20

study of the as cast alloy but was not distinguishable in the SEM micrographs due to an insignificant difference in its elemental composition in comparison with the main C15 phase.

From the reference publications it is known that La is poorly soluble in the Zr and Ti containing Laves phase MH alloys and thus it forms very limited solid solutions. Instead it forms a secondary LaNi phase, which is present in the microstructure as globular particles [34,35]. However, despite its very low content, the presence of the secondary LaNi phase is very important for the overall hydrogen storage performance. Indeed, LaNi absorbs a large amount of hydrogen during the initial activation forming $LaNiH_{3.6}$ [33] and contributes to an increase in the effective surface area due to the cracking and powdering of the alloy during the hydrogen absorption-desorption process. Thus, La acts as an initiator and promoter of the initial hydrogen absorption-desorption also improving the electrochemical performance at high current densities of charge and discharge.

3.2. Hydrogen absorption-desorption properties

Measured at room temperature isotherms of hydrogen absorption and desorption showed that maximum hydrogen storage capacity of the annealed $Ti_{0.15}Zr_{0.85}La_{0.03}Ni_{1.2}Mn_{0.7}V_{0.12}Fe_{0.12}$ alloy is 1.54 wt% H. At 293 K, equilibrium plateau of hydrogen desorption is close to 1 bar H_2 and shows presence of a broad and rather flat plateau (Fig. 4). It should be noted that the difference between the hydrogen absorption and desorption isotherms is rather small and the studied alloy shows a very small hysteresis. Hysteresis is an important intrinsic property of the alloy-hydrogen systems. From the PCT data, we conclude that hysteresis decreases with increasing temperature, indicating that the critical temperature in the studied system is low. Its evaluation from an intercept of the straight line dependances of lnP vs 1/T for absorption and desorption gives T_{crit} value of around 393 K. The thermodynamic parameters of interaction – enthalpy (ΔH) and entropy (ΔS) changes – during the phase transformation - were obtained from the pressure-composition isotherms measured at different temperatures using the van't Hoff equation [25]:

$$ln(P_{H_2}) = \frac{\Delta H}{RT} - \frac{\Delta S}{R} \quad (1)$$

where P_{H2} is equilibrium mid-plateau pressure in the PCT diagram and R is a universal gas constant. These values are equal to $\Delta H = -31 \pm 1$ (kJ/mol); $\Delta S = -110 \pm 5$ (J/K·mol) for the hydride

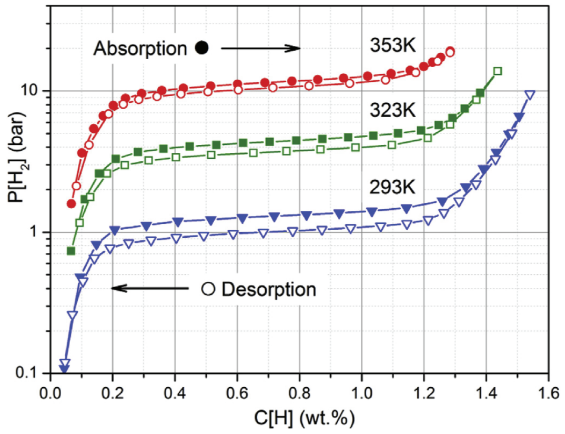

Fig. 4. PCT isotherms of hydrogen absorption-desorption for the annealed $Ti_{0.15}Zr_{0.85}La_{0.03}Ni_{1.2}Mn_{0.7}V_{0.12}Fe_{0.12}$ alloy.

formation process and $\Delta H = 34 \pm 1$ (kJ/mol); $\Delta S = 115 \pm 5$ (J/K·mol) for the hydride decomposition process (Fig. 5). Enthalpy change has a sufficiently low value, which allows a good reversibility of the system during the electrochemical charge and discharge of the battery anode when cycled in an open cell. The obtained values of ΔH and ΔS are in good agreement with the reference data for the chemically similar materials. As an example, in work [18] a similar value of $\Delta H = -33.7$ (kJ/mol) was obtained for the $Ti_{12}Zr_{21.5}V_{10}Cr_{7.5}Mn_{8.1}Co_8Ni_{32.2}Sn_{0.3}Al_{0.4}$ alloy based hydride.

Absorption/desorption hysteresis is a typical phenomenon observed in the metal-hydrogen systems. Hysteresis is related to the large volume expansion during a formation of the metal hydride, up to 25–30%. It causes stresses which appear during a growth of a hydride nucleus inside the alloy matrix having a smaller molar volume. The hysteresis decreases with increasing temperature. It should be noted that PCT plateau also become narrower with increasing temperature. Decreasing hysteresis can be explained by two factors: increased lattice mobility at a higher temperature and smaller volume change during a transition between the hydrogen solid solution and the hydride phase. Hysteresis completely disappears at critical temperature.

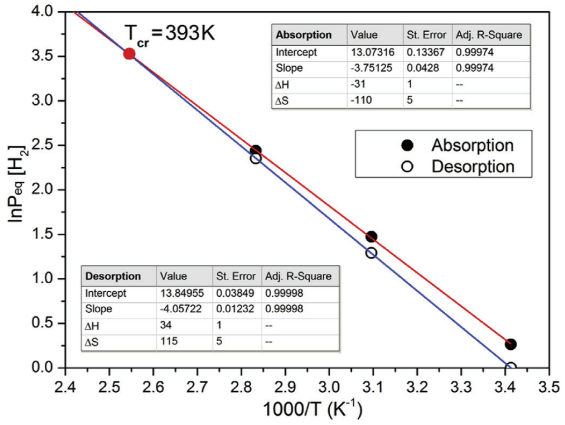

Fig. 5. Dependence between equilibrium pressure $\ln P_{eq}$ of hydrogen absorption and desorption and inverse temperature based on the PCT diagrams measured at 293, 323 and 353 K. Intersect of the straight lines for absorption and desorption gives a critical temperature T_{crit} for the $Ti_{0.15}Zr_{0.85}La_{0.03}Ni_{1.2}Mn_{0.7}V_{0.12}Fe_{0.12}$-$H_2$ system of 393 K.

Critical temperature is the temperature above which a two-phase region, corresponding to the first order transition between α-H solid solution and β-hydride phase, is replaced by a second order transition with continuous changes in H content causing continuous changes in the unit cell parameters. Two-phase region appears as a pressure plateau in the PCT curve at a specific temperature; however, this plateau disappears above the critical temperature while the α-β transition becomes continuous. From the available data we conclude that T_{crit} is rather low and equals to 393 K.

3.3. Hydrogen diffusion properties

Fig. 6 and Table 3 present the data describing a relationship between the hydrogen diffusion coefficient and state of charge (SOC) for the annealed $Ti_{0.15}Zr_{0.85}La_{0.03}Ni_{1.2}Mn_{0.7}V_{0.12}Fe_{0.12}$ alloy electrode. The measurements were carried out by potentiostatic intermittent titration technique (PITT) at low amplitude (0.02 V) current transients in the potentials range from −0.80 to −0.96 V (Fig. 6a). To calculate the effective hydrogen diffusion coefficient, we used $It^{1/2}$ vs. log t plots allowing to locate a «Cottrellian maximum» and to find the corresponding time range needed to perform the calculations. The observed maximum demonstrates pronounced deviations from a steady-state planar diffusion, as well as presence of non-diffusion type slow processes in certain time domains (including effect of Ohmic potential drop in the solution at high currents). The region of a pit in Fig. 6b is the «most Cotrellian » part of the transients. Then $1/It^{1/2}$ vs. $1/t^{1/2}$ plots were used to account for the deviations from the ideal Cottrellian dependence caused by the Ohmic losses, and to calculate D (Fig. 6c). Hydrogen diffusion coefficient was calculated according to a modified Cottrell Equation (see Refs. [36,37] for the details):

$$\frac{1}{I\sqrt{t}} = \frac{R_{\sum}}{\Delta E\sqrt{t}} + \frac{l\sqrt{\pi}}{\Delta Q\sqrt{D}} \quad (2)$$

where $R_{\Sigma} = R_{solution} + ; R_{surface\ films} + R_{charge\ transfer}$; ΔQ is the total charge of electrode at a certain potential; l is diffusion length that is equal to a half of a metal particle size (2.5×10^{-3} cm).

The obtained plots corresponding to Eq. (2) and the calculated D values are shown in Fig. 6d and in Table 3. Total resistance R_{Σ} determined from the slope of this plot equals to 2.6 Ohm. We also estimated $R_{solution} + R_{surface\ films}$ (RR) contribution independently, by interrupting polarization during the galvanostatic measurements. A sharp decrease of the potential after this interruption corresponded to 0.24 Ohm, which is by one order of magnitude smaller than RR. Even though analysis of all separate contributions is beyond the scope of this paper, we underline that the resistance caused by the charge transfer is an essential part of the overall R_{Σ} and cannot be ignored. However, for the studied experiment RR had a small value, and the deviations from Cottrell behavior were not significant. The maximum value of D (2.84×10^{-9} cm^2/s) was obtained at a minimum studied state of charge (SOC) of 2.1%. Hereinafter as the state of the charge increased, hydrogen diffusion coefficient became lower decreasing to 4.55×10^{-13} cm^2/s. Such a behavior is typical for all hydride-forming alloys [35]. Nevertheless, the obtained maximal values of D are somewhat higher as compared with the AB_3 based hydrides (for example, 2.87×10^{-11} cm^2/s for $La_{1.5}Nd_{0.5}MgNi_9$) [37] and AB_5 based hydrides (1.81×10^{-10} cm^2/s for $MmNi_{4.25}Mn_{0.25}Co_{0.45}Al_{0.3}$) [38] type alloys.

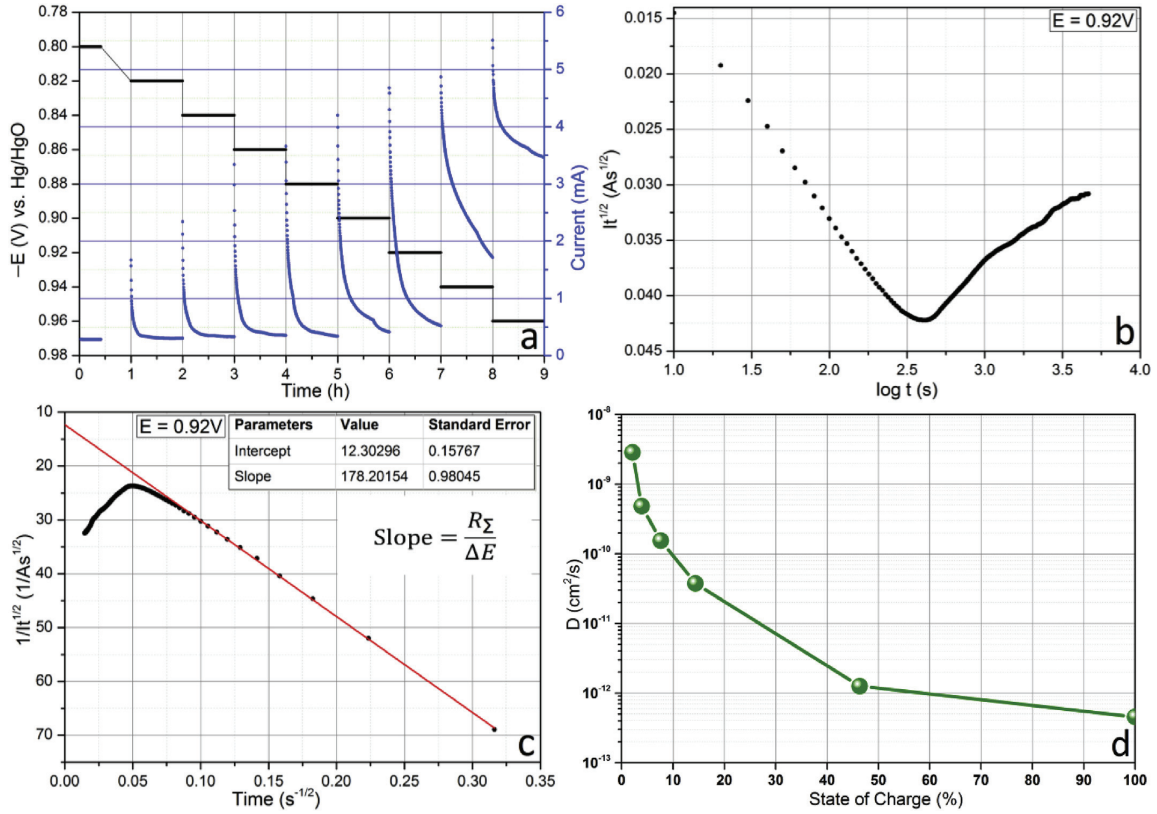

Fig. 6. Time dependence of the currents as related to the applied potential (a); «Cottrellian maximum» from graph plotted in $It^{1/2}$ vs. log t coordinates for E = −0.92 V (b); Linear fitting analysis derived from graph plotted in $1/It^{1/2}$ vs. $1/t^{1/2}$ coordinates for E = −0.92 V (c); The dependence of the effective hydrogen diffusion coefficient on the state of charge of the electrode (d).

3.4. Electrochemical properties

Lanthanum present in the alloy caused the formation of a La-rich LaNi intermetallic compound which efficiently catalyzed the process of activation of the electrodes. Both as-cast and annealed alloys approached maximum capacity during the fourth charge-discharge cycles and then showed only a slight increase in the capacities (Fig. 7). The maximum capacity during the activation of the cast alloy at a charge-discharge current density of 100 mA/g was 345 mAh/g, while for the annealed alloy it was higher reaching 370 mAh/g.

Similar studies were performed in Ref. [28] where the activation behavior of an AB_2-type $(Ti_{0.36}Zr_{0.64})(V_{0.15}Ni_{0.58}Mn_{0.20}Cr_{0.07})_2$ Laves phase alloy was investigated and lanthanum was not present in the alloy. The alloy contained C14 Laves phase as the main constituent and $(Ti_{0.5}Zr_{0.5})Ni$ intermetallic as a secondary phase. Untreated alloy initially had almost zero capacity and reached a capacity of

Table 3
Diffusion parameters as related to the state of charge for the annealed $Ti_{0.15}Zr_{0.85}La_{0.03}Ni_{1.2}Mn_{0.7}V_{0.12}Fe_{0.12}$ alloy electrode at different potentials.

Potential, V	Capacity, mAh	SOC %	$1/It^{1/2}$	Slope	D, cm^2/s
−0.80	0.02	0.1	–	–	–
−0.82	0.08	0.6	–	–	–
−0.84	0.11	1.2	–	–	–
−0.86	0.17	2.1	47.45	183.25	2.84×10^{-09}
−0.88	0.32	3.9	28.23	203.58	4.81×10^{-10}
−0.90	0.67	7.6	22.33	170.34	1.54×10^{-10}
−0.92	1.21	14.4	12.30	178.20	3.76×10^{-11}
−0.94	5.74	46.4	4.84	196.06	1.26×10^{-12}
−0.96	9.63	100	2.03	191.48	4.55×10^{-13}

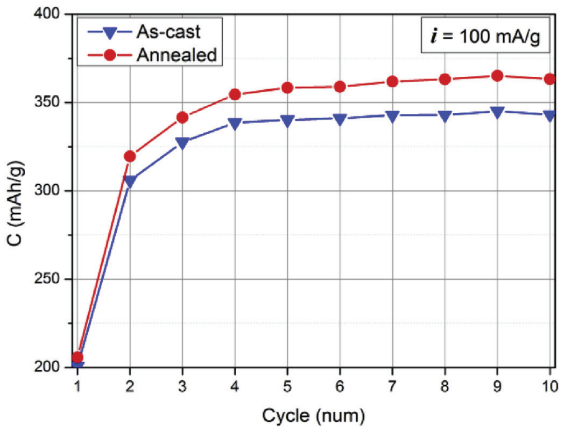

Fig. 7. Activation performance of the as-cast and annealed $Ti_{0.15}Zr_{0.85}La_{0.03}Ni_{1.2}Mn_{0.7}V_{0.12}Fe_{0.12}$ alloy electrodes.

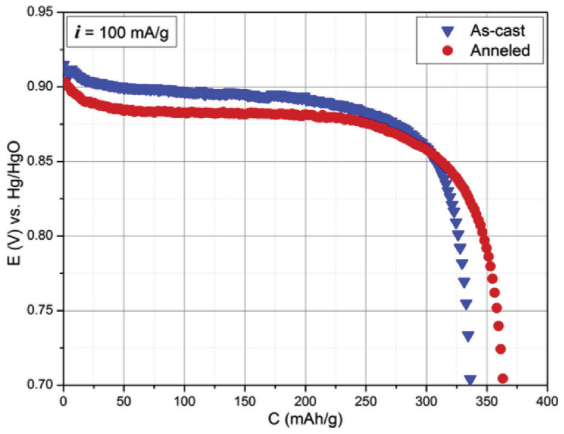

Fig. 8. Discharge capacity of the as-cast and annealed $Ti_{0.15}Zr_{0.85}La_{0.03}Ni_{1.2}Mn_{0.7}V_{0.12}Fe_{0.12}$ alloy electrodes.

220 mAh/g only after 14 cycles. A significant improvement of the activation performance of the alloy was achieved only after boiling of the alloy powder in a hot KOH solution for 80 min. After that it was possible to achieve a capacity of 390 mAh/g. In contrast, the alloys containing lanthanum which were used in Refs. [10,13], reached maximum capacity values already at the very beginning of the activation without any additional processing. In all cases, the presence of a secondary La-Ni phase was noted. From that we conclude that presence of La in the composition of the alloy is essential to reach its efficient activation performance.

It should be noted that in addition to the larger discharge capacity, the annealed alloy had a flatter and broader plateau of discharge potentials which is located between −0.85 and −0.9 V (Fig. 8). Furthermore, the plateau of potential for the annealed alloy moves to the slightly less negative values (middle of the plateau is located at −0.88 V) as compared to as-cast alloy (middle of the plateau at −0.90 V) which corresponds to a lower pressure of desorption of hydrogen from the metal hydride formed by the annealed alloy. Furthermore, the annealed alloy shows a better high rate dischargeability and a higher cyclic stability as compared to the as-cast alloy. The discharge capacity reaches 65% (246 mAh/g) at a discharge current density of 1000 mA/g (Fig. 9a and b). After 100 cycles with 100% DOD at discharge current density of 300 mA/g (1C), the discharge capacity for the annealed alloy equaled to 90% of the initial capacity which is 10% higher as compared to the as-cast alloy (Fig. 10). Improved performance of the annealed alloy appears to be related to its more homogeneous composition resulting from the annealing process.

The improvement of HRD performance after the annealing well correlates with increased hydrogen diffusion coefficient in the annealed alloy as compared to that of the as-cast alloy. Such improvements can be related to the changes in the structure as the annealed alloy contains only C15 intermetallic and this phase is known to be superior for the high-power batteries and is superior to the hexagonal C14 alloy which transforms into a homogeneous C15 type alloy after the annealing. Furthermore, the microstructure of the alloy changes after the annealing treatment. As can be seen from the micrographs (Fig. 3), after the annealing LaNi phase becomes uniformly and finely dispersed in the alloy matrix and shows presence of very small particles. The amount of LaNi visibly decreases based on the area occupied by LaNi in the SEM image but also decreases, even though less significantly, based on the analysis

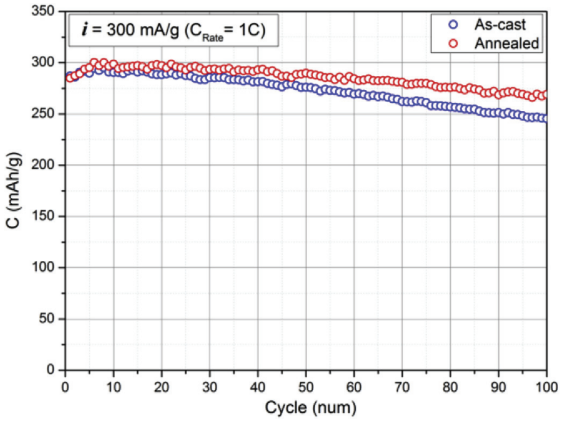

Fig. 10. Cyclic stability of the as-cast and annealed $Ti_{0.15}Zr_{0.85}La_{0.03}Ni_{1.2}Mn_{0.7}V_{0.12}Fe_{0.12}$ alloy electrodes.

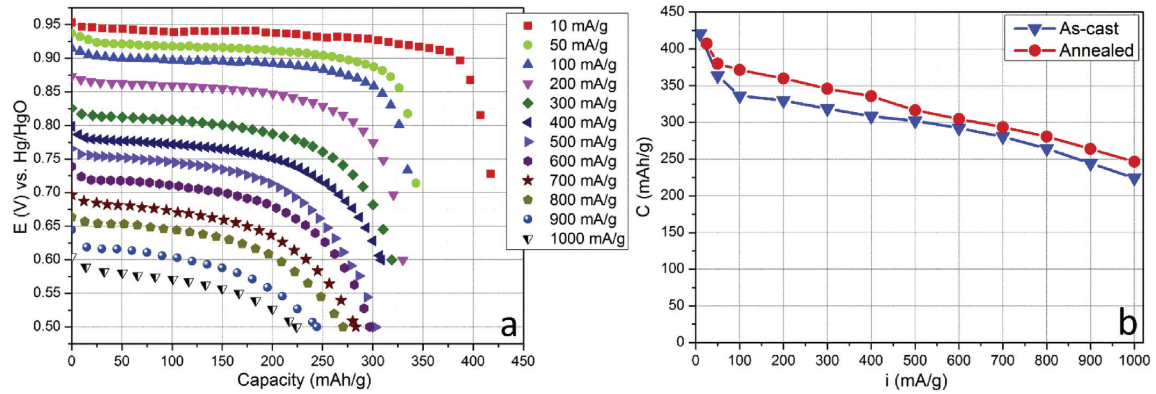

Fig. 9. The capacity of the as-cast $Ti_{0.15}Zr_{0.85}La_{0.03}Ni_{1.2}Mn_{0.7}V_{0.12}Fe_{0.12}$ alloy electrode at different current densities and cut-off potentials (a); High-rate dischargeability of the as-cast and annealed alloy electrodes (b).

of the XRD data. This could be associated with the fact that La from LaNi can raffinate the alloy from the metallurgical oxygen thus purifying the grain boundaries by removing the Ti/Zr-containing oxides because of the formation of the clusters of La_2O_3. Because of that the activity of these alloys in the hydrogenation process becomes higher. Finally, the reason for such a change could be in partial solubility of La in AB_2 matrix phase, probably at a trace level, leading to a decrease of LaNi content in the alloy.

The annealing treatment leads to the homogenization of the alloy composition and formation of a pure C15 Laves phase intermetallic. This results in a higher reversible H storage capacity of the alloy. In addition, LaNi phase (which acts as a catalyst of hydrogen absorption) becomes finely and uniformly dispersed in the alloy. This results in an increased hydrogen diffusion coefficient and improved high rate dischargeability of the annealed alloy. An improvement in the electrochemical characteristics after the annealing was observed by us earlier when studying AB_3 and A_2B_7 type alloys, and the values of specific capacitance, HRD, and cyclic stability obtained in this study are quite comparable with the data for the La-Mg-Ni alloys [39–44]. Further studies of the effect of the rare earth metals on the improved electrochemical performance of the Zr-based Laves type alloys are required to better understand the mechanism governing catalytic interaction between the main phase and the rare earth containing secondary phases, to systematically extend observations available for the multiphase Zr-based alloys doped by La, Ce, Pr or Nd [45] or Zr-based C15 type Laves phase alloys doped by 3 wt% La [46].

3.5. Electrochemical Impedance Spectroscopy (EIS) characterization

Electrochemical impedance spectroscopy (EIS) was applied to characterize the kinetics of surface electrochemical reactions occurring in the studied electrode [47]. This technique is very sensitive and is very useful; however, it meets the challenges in the evaluation of the data due to a multiparameter dependence of the results from the various processes taking place in the studied samples. The objective of the current study was in evaluating how State of Charge and homogeneity of the samples affects their impedance/resistivity and rates of hydrogen diffusion in the electrode.

The most commonly used to model the Nyquist impedance dependencies contain a hemicycle and a straight-line part which can be modeled by a Randles equivalent circuit consisting of a charge transfer resistance (R_{ct}) connected in series with a Warburg impedance (Z_w) and in parallel with a double-layer capacitance (C_{dl}) (Fig. 11a). It appears that the original Randles circuit is not suitable to fit the experimentally measured in present work Nyquist plot because of a more complex shape of the latter plot indicating that several processes are contributing to the collected data. To fit a more complex experimentally measured data than described by a classical Nyquist plot (Fig. 11b), Randles equivalent circuit has been modified by including a Constant Phase Element (CPE), which is connected in parallel while the individual Warburg impedance is in a series connection. Capacitance was replaced by CPE to describe the depressed hemicycle shape of the Nyquist plot which can originate from the surface inhomogeneity of the electrodes. A CPE is introduced because the semicircles in the Nyquist plots are depressed due to heterogeneity of the surface/surface roughness, or other effects that cause uneven current distributions at the electrode surface [48]. By replacing the capacitance C with CPE in the equivalent circuit, a much better fit of the EIS was achieved. Furthermore, in the present study, an additional parallel circuit element consisting of R and CPE in series was added to achieve a more accurate modeling of the studied electrode.

The circuit element capacitance, C, has an impedance of:

$$Z_C = \frac{1}{j\omega C} \tag{3}$$

while the impedance for CPE is:

$$Z_{CPE} = \frac{1}{Y_0(j\omega)^n} \tag{4}$$

where, Y_0 is the admittance of an ideal capacitance and n is an empirical constant, ranging from 0 to 1. We note that when $n = 1$, the CPE behaves as a pure capacitor $C = Y_0$, while when $n = 0$, the CPE behaves a pure resistor $R = Y_0^{-1}$. Furthermore, when $n = 0.5$, the CPE is an equivalent of the Warburg element.

To fit the Nyquist impedance, the observed impedance dependence was assumed to consist of two individual hemicycles as shown in Fig. 12. These two hemicycles are related to the selected circuits as depicted in the lower part of Fig. 12. The first arc in the higher frequency range represents the electrolyte resistance shown by intersection of the smallest arc with the real axis of impedance (Z_{real}), and the contact resistance and capacitance between the

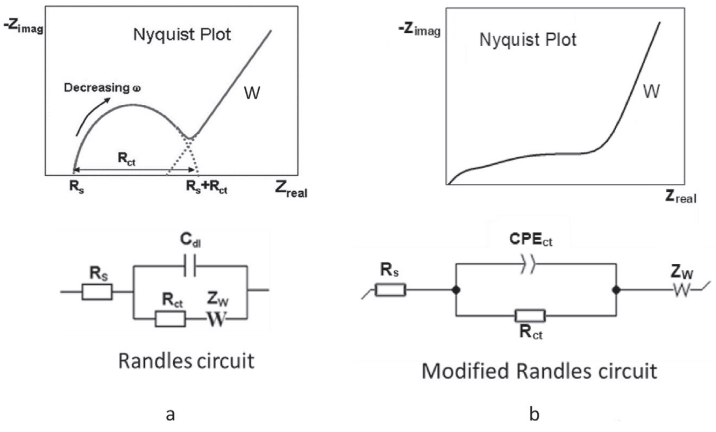

Fig. 11. Original (a) and modified (b) of Nyquist plots containing charge transfer resistance and Warburg element (W).

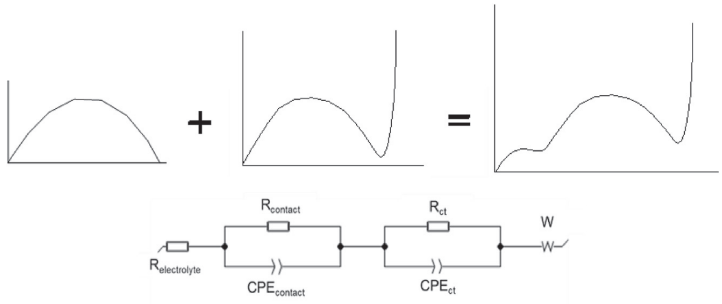

Fig. 12. Equivalent circuit well describing the Nyquist impedance plot.

current collector and the alloy particles ($R_{contact}$), while the second arc is related to the charge transfer resistance (R_{ct}) and the capacitance of the electrode surface containing the Warburg element (W).

Following the circuits model described above, the EIS experimental data for each studied sample was fitted and deconvoluted to determine the values of individual circuit components. The deconvolution has been done by setting two initial semicircles and a linear part to represent the assumed circuit model. Typical deconvolution procedure results in obtaining EIS parameters for the individual deconvoluted parts which overlap with each other resulting in the overall EIS shown in Fig. 13.

From the fitting process on the EC-Lab, 8 different parameters describing the properties of the studied system were obtained, including $R_{electrolyte}$, $R_{contact}$, $CPE_{contact}$, n_1, $R_{charge\ transfer}$, $CPE_{charge\ transfer}$, n_2, and σ. The fitting values of these parameters for as-cast and annealed alloys are shown in Table 4, while the plots presenting experimental data and modeling results as related to the SOC of the anodes are given in Supplementary Information, Fig. S1 (for as cast alloy) and Fig. S2 (annealed alloy). Excellent fit of the experimental data has been achieved by using such modeling. Quality of the fit can be evaluated by calculating the Goodness of fit (χ^2) values and Coefficient of determination (R^2).

When comparing the data of numerical fitting, we can easily conclude that fitting of two hemispherical parts shows their very

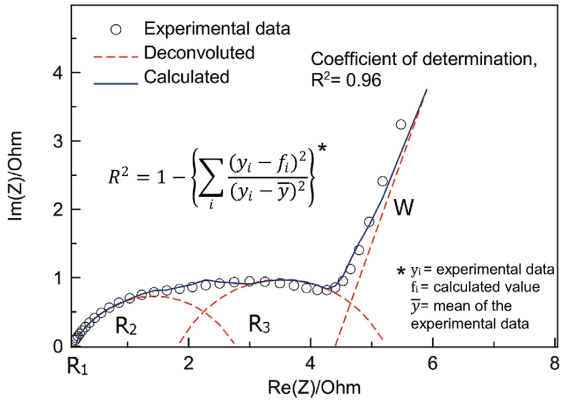

Fig. 13. Deconvolution of Nyquist impedance plot for 0% SOC of as cast alloy achieved by using a superposition of equivalent circuits, where $R_1 = R_{electrolyte}$, $R_2 = R_{contact}$, $R_3 = R_{ct}$, and W = Warburg element. As the value of R2 is rather close to 1, this shows that the proposed fit well described the data.

different properties. By applying annealing of the alloy, almost all parameters including electrolyte resistance, contact resistance, and Warburg element decreased, showing that the annealing generally reduces the total resistance. Furthermore, the hydrogen transport in the annealed alloy is faster than in the as-cast alloy. In addition, the fitted value of CPE for contact and charge transfer impedance and the empirical constant for CPE for the as-cast alloy are larger than for the annealed alloy. The reason for that is in a fact that the annealing improves the homogeneity of the alloy and enlarges the surface area of the alloy. We note that increasing of R_{ct} for some SOC due to the annealing process gives a smaller effect on hydrogen diffusion as compared to the decrease of the value of the Warburg element. This happens because H diffusion coefficient is proportional to an inverse square of Warburg element, as it follows from a simplified equation of Fick's diffusion in a metal hydride.

The following equation has been utilized to determine the diffusion coefficient D_H [49]:

$$D_H = \frac{R^2T^2}{2A^2n^4F^4C^2\sigma^2} \quad (5)$$

where D_H – diffusion coefficient of hydrogen; R – ideal gas constant; T – absolute temperature; A – electroactive surface area per unit volume of electrode; n – number of electrons transferred; C – concentration of hydrogen ions; σ – Warburg impedance coefficient.

The electroactive surface area, A, was estimated assuming that the spherical alloy particles in the studied electrode all have the same size and their entire surface is exposed to the electrolyte, being described by the following expression [50]:

$$A = \frac{3(1-\in)}{r} \quad (6)$$

where $\in$ = electrode porosity, assumed to be 0.3 [51]; r = radius of spherical particle (active alloy), an average value was chosen as 25 μm (as mentioned in the experimental part).

From the fitting results, it is easy to conclude that annealing increases the rate of hydrogen diffusion as compared to the as-cast alloy. In line with these observations, the fitting of the EIS data showed differences appearing between the as cast and annealed samples. In particular, it could be noted that the annealed alloy shows a smaller Nyquist impedance resistance as compared to the as cast one. This could be related to the increased homogeneity of the annealed alloy which contains 99.4 wt% of the C15 phase. For the as cast alloy content of C15 phase was smaller, 94.5 wt%.

As expected, impedance spectrum is strongly dependent upon state of charge of the electrodes. The refined values of the hydrogen diffusion coefficient are significantly lower for the samples of the

Table 4
Fitted parameters of EIS spectra for the as-cast and annealed $Ti_{0.15}Zr_{0.85}La_{0.03}Ni_{1.2}Mn_{0.7}V_{0.12}Fe_{0.12}$ alloy.

Parameters	0% SOC		30% SOC		70% SOC		100% SOC	
	As-cast	Annealed	As-cast	Annealed	As-cast	Annealed	As-cast	Annealed
$R_{electrolyte}$, Ohm	0.1247	0.08927	0.1350	0.07515	0.1360	0.06093	0.1574	0.07609
$R_{contact}$, Ohm	2.1670	1.306	1.8570	1.812	2.133	1.128	2.3660	1.964
$CPE_{contact}$, $F.s^{\alpha-1}$	0.5213	0.6748	0.3652	0.3129	0.2648	0.456	0.2880	0.3152
n_1	0.7592	0.905	0.9039	0.8893	0.7858	0.9918	0.7864	0.7532
R_{ct}, Ohm	1.9990	2.219	3.054	2.686	2.751	2.987	2.730	2.331
CPE_{ct}, $F.s^{\alpha-1}$	0.05219	0.05697	0.03525	0.04039	0.03679	0.04328	0.03559	0.04313
n_2	0.6459	0.6569	0.6750	0.6741	0.662	0.6647	0.6781	0.6662
σ, $Ohm.s^{1/2}$	0.2366	0.2040	0.02547	0.02199	0.02727	0.0250	0.02802	0.02700
Goodness of fit, χ^2[a]	0.05429	0.1855	0.07281	0.1159	0.09871	0.3070	0.04163	0.1610
D_H, $cm^2.s^{-1}$	$3.59e^{-12}$	$4.82e^{-12}$	$3.09e^{-10}$	$4.15e^{-10}$	$2.70e^{-10}$	$3.21e^{-10}$	$2.56e^{-10}$	$2.75e^{-10}$

[a] $\chi^2 = \sum_{i=1}^{n} \frac{|Z_{meas}(i) - Z_{model}(f_i, param)|^2}{\sigma_i^2}$

where,
Z_{meas} (i) = measured impedance at f_i frequency
Z_{model} (fi, param) = calculated impedance, based on a selected model
f_i = frequency
param = model parameters (R1, R2, C1, Q1)
σ_i = standard deviation

initial intermetallic alloy with 0% SOC, both for the as-cast and the annealed alloy. With further saturation of the alloy by hydrogen when a transformation from α-solid solution to the β-hydride phase takes place, the hydrogen diffusion in bulk of the alloy increases sharply and then decreases as extent of the alloy's transformation into the hydride progresses from 30 to 100% SOC (Fig. 14).

From the data collected at different SOC, it can be clearly seen that annealed alloy has lower contact resistances and lower Warburg element values as compared to the as cast alloy. The annealing improves the homogeneity of the phase structure where C15 is the dominant phase, which results in a to decreased resistance between the alloys particles and between the alloy and the current collector. However, a larger total area of the C15 phase contributes to the larger CPE_{ct} values and makes the charge transfer process becoming more difficult to accomplish, therefore the R_{ct} should be higher in the annealed alloy in comparison with that for the as cast alloy.

When comparing the data of the PITT and EIS experiments, we should stress that investigating the hydrogen diffusion using PITT measurements neglects the interfacial resistance and assumes that the system is diffusion-controlled. This can result in smaller D_H values than these values when using the EIS technique [52]. The diffusion coefficient derived from PITT measurements is calculated based on Cottrell equation, which is directly related to the time and concentration of the species undergoing a transient diffusion. The Ohmic potential drops, interfacial kinetics, double-layer charging and phase transitions in the bulk of host materials are neglected in this approach. This is very much different from the EIS techniques, where the diffusion process is assessed for a steady state diffusion mode. Furthermore, in the real conditions, the diffusion is the rate limiting step of the mass transport being independent of time. In the Cottrell domain, there are two diffusion control paths, a semi-infinite diffusion in a short-time domain and the finite-space diffusion in a long-time domain [53]. The semi-infinite diffusion in the short-time domain was considered during evaluation of the EIS data to obtain the diffusion coefficient of hydrogen, which is thus very much dependent of the time-dependent changes of hydrogen concentration during the short-time diffusion.

To conclude, none of the above methods (PITT and EIS) gives an unambiguous absolute value of the diffusion coefficient of hydrogen and can be used for a rough estimation of the D_H only. Nevertheless, the data obtained by using these two methods well correlate with each other, and the obtained values of D_H are mutually consistent and well agree with the reference data.

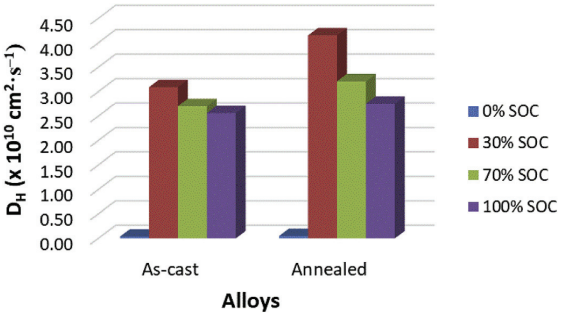

Fig. 14. Hydrogen diffusion coefficient for the as-cast and annealed alloys as related to SOC of the electrodes. The blue bars in Fig. 14 show the smallest values of hydrogen diffusion coefficient observed at 0% SOC. (For interpretation of the references to colour in this figure legend, the reader is referred to the Web version of this article.)

4. Conclusions

The AB_2-type $Ti_{0.15}Zr_{0.85}La_{0.03}Ni_{1.2}Mn_{0.7}V_{0.12}Fe_{0.12}$ alloy was prepared by arc melting and annealing. Rietveld refinements of the XRD data show that the as-cast alloy contains three Laves phases: FCC C15–I (61.1 wt%) and C15–II (25.7 wt%) intermetallics as the main component, and C14 (12.1 wt%) type hexagonal alloy as a secondary phase, together with trace amounts (appr. 1 wt%) of orthorhombic LaNi intermetallic which was however clearly identified in the XRD and SEM data. The homogenization by annealing at 950 °C results in disappearance of the secondary C14 phase (while the amount of LaNi slightly decreases).

At room temperature, the annealed alloy has a low, close to 1 bar H_2 ($\Delta H_{des} = 34 \pm 1$ (kJ/mol); $\Delta S_{des} = 115 \pm 5$ (J/K·mol); critical temperature 393 K), plateau of hydrogen absorption-desorption and shows a very small hysteresis, flat equilibrium plateaux and H storage capacity of 1.54 wt% H.

Both as-cast and annealed alloys reach maximum H storage capacity already in the fourth activation cycle. The maximum

capacity is higher for the annealed alloy reaching 370 mAh/g (345 mAh/g for the as cast material). The annealed alloy shows higher values of HRD capacity and a better cyclic stability as compared to the as-cast alloy. After 100 cycles with 100% DOD at discharge current density of 300 mA/g (1C), the discharge capacity for annealed alloy amounted 90% of the initial capacity.

The phase-structural composition affects the EIS behavior and the alloy with the highest content of C15 Laves phase present in the annealed alloy shows the fastest hydrogen diffusion. SOC of the electrode has a direct influence on the rates of hydrogen diffusion which reaches maximum values for the electrodes with smallest SOC of 2%.

The electrochemical behavior of the alloy is significantly affected by the secondary LaNi phase which acts as a catalyst of hydrogen sorption-desorption processes, both during the alloy-H_2 gas interactions and during the electrochemical tests in aqueous electrolyte.

Acknowledgements

This work was supported by the Norwegian Research Council (project “High Power Batteries Probed by Neutron Scattering”, program SYNKNØYT; RCN project 234246), IEA Task 32 project Hydrogen Based Energy Storage (RCN project 285146) and Norwegian Research Center on Zero Emission Energy Systems for Transport – FME MoZEES.

Alexei A. Volodin acknowledges the support from the Russian Science Foundation (PRJ No. 17-79-20413).

C.B. Wan acknowledges the support from the China National Natural Science Foundation (Grant No. 11605007).

Boris P. Tarasov acknowledges support from the Ministry of Science and Higher Education at the studies metal hydride materials microstructures (PRJ UI RFMEFI61318X0087).

Appendix A. Supplementary data

Supplementary data to this article can be found online at https://doi.org/10.1016/j.jallcom.2019.03.134.

References

[1] K. Young, J. Nei, The current status of hydrogen storage alloy development for electrochemical applications, Materials 6 (2013) 4574.
[2] K. Young, J. Nei, C. Wan, R.V. Denys, V.A. Yartys, Comparison of C14-and C15-predomiated AB_2 metal hydride alloys for electrochemical applications, Batteries 3 (2017) 22.
[3] K. Young, J.M. Koch, C. Wan, R.V. Denys, V.A. Yartys, Cell performance comparison between C14-and C15-predomiated AB_2 metal hydride alloys, Batteries 3 (2017) 29.
[4] K. Young, T. Ouchi, J. Koch, M.A. Fetcenko, Compositional optimization of V-free hypo-stoichiometric AB_2 metal hydride alloy for Ni/MH battery application, J. Alloys Compd. 510 (2012) 97–106.
[5] Y. Zhang, J. Li, T. Zhang, T. Wu, H. Kou, X. Xue, Hydrogenation thermokinetics and activation behavior of non-stoichiometric Zr-based Laves alloys with enhanced hydrogen storage capacity, J. Alloys Compd. 694 (2017) 300–308.
[6] M. Tliha, C. Khaldi, S. Boussami, N. Fenineche, O. El-Kedim, H. Mathlouthi, J. Lamloumi, Kinetic and thermodynamic studies of hydrogen storage alloys as negative electrode materials for Ni/MH batteries: a review, J. Solid State Electrochem. 18 (2014) 577–593.
[7] Y. Zhang, J. Li, T. Zhang, H. Kou, R. Hu, X. Xue, Hydrogen storage properties of non-stoichiometric $Zr_{0.9}Ti_xV_2$ melt-spun ribbons, Energy 114 (2016) 1147–1154.
[8] A. Matsuyama, H. Mizutani, T. Kozuka, H. Inoue, Effect of Ti substitution on electrochemical properties of ZrNi alloy electrode for use in nickel-metal hydride batteries, Int. J. Hydrogen Energy 42 (2017) 22622–22627.
[9] L. Kong, X. Li, K. Young, J. Nei, X. Liao, W. Li, Effects of rare-earth element additions to Laves phase-related body-centered-cubic solid solution metal hydride alloys: thermodynamic and electrochemical properties, J. Alloys Compd. 737 (2018) 174–183.
[10] Y. Zhang, W. Zhang, Z. Yuan, H. Shang, Y. Li, S. Guo, Structures and electrochemical hydrogen storage properties of melt-spun RE-Mg–Ni–Co–Al alloys, Int. J. Hydrogen Energy 42 (2017) 14227–14245.
[11] Y. Zhang, S. Cui, Y. Li, H. Shang, Y. Qi, D. Zhao, Structures and electrochemical performances of as-spun RE-Mg-Ni-Co-Al alloys applied to Ni-MH battery, J. Mater. Sci. Technol. 34 (2018) 370–378.
[12] S. Yasuoka, J. Ishida, K. Kishida, H. Inui, Effects of cerium on the hydrogen absorption-desorption properties of rare earth-Mg-Ni hydrogen-absorbing alloys, J. Power Sources 346 (2017) 56–62.
[13] T. Zhai, T. Yang, Z. Yuan, Y. Zhang, An investigation on electrochemical and gaseous hydrogen storage performances of as-cast $La_{1-x}Pr_xMgNi_{3.6}Co_{0.4}$ (x=0–0.4) alloys, Int. J. Hydrogen Energy 39 (2014) 14282–14287.
[14] D.F. Wong, K. Young, J. Nei, L. Wang, K.Y.S. Ng, Effects of Nd-addition on the structural, hydrogen storage, and electrochemical properties of C14 metal hydride alloys, J. Alloys Compd. 647 (2015) 507–518.
[15] K. Young, T. Ouchi, J. Nei, T. Meng, Effects of Cr, Zr, V, Mn, Fe, and Co to the hydride properties of Laves phase-related body-centered-cubic solid solution alloys, J. Power Sources 281 (2015) 164–172.
[16] E. Teliz, J. Diez, R. Faccio, F. Ruiz, F. Zinola, V. Díaz, Molybdenum incorporation on AB_2 alloys-part I metallurgical and electrochemical characterization: electrocatalytic behavior, J. Alloys Compd. 744 (2018) 583–590.
[17] E. Teliz, J. Diez, R. Faccio, E. German, F. Zinola, V. Díaz, Molybdenum incorporation on AB_2 alloys-Part II. On the synergetic effects of Laves and non-Laves phases, J. Alloys Compd. 737 (2018) 530–535.
[18] K. Young, T. Ouchi, X. Lin, B. Reichman, Effects of Zn-addition to C14 metal hydride alloys and comparisons to Si, Fe, Cu, Y, and Mo-additives, J. Alloys Compd. 655 (2016) 50–59.
[19] Z. Li, H. Wang, L. Ouyang, J. Liu, M. Zhu, Reversible hydriding in $YFe_{2-x}Al_x$ (x= 0.3, 0.5, 0.7) intermetallic compounds, J. Alloys Compd. 689 (2016) 843–848.
[20] K. Young, B. Chao, L. Bendersky, K. Wang, $Ti_{12.5}Zr_{21}V_{10}Cr_{8.5}Mn_xCo_{1.5}Ni_{46.5-x}$ AB_2-type metal hydride alloys for electrochemical storage application: Part 2. Hydrogen storage and electrochemical properties, J. Power Sources 218 (2012) 487–494.
[21] K. Young, D. Wong, S. Yasuoka, J. Ishida, J. Nei, J. Koch, Different failure modes for V-containing and V-free AB_2 metal hydride alloys, J. Power Sources 251 (2014) 170–177.
[22] S. Khajavi, M. Rajabi, J. Huot, Crystal structure of as-cast and heat-treated $Ti_{0.5}Zr_{0.5}(Mn_{1-x}Fe_x)Cr_1$, x=0, 0.2, 0.4, J. Alloys Compd. 767 (2018) 432–438.
[23] B. Hosni, C. Khaldi, O. ElKedim, N. Fenineche, J. Lamloumi, Structure and electrochemical hydrogen storage properties of Ti-Fe-Mn alloys for Ni-MH accumulator applications, J. Alloys Compd. 781 (2019) 1159–1168.
[24] Y. Yan, Y. Chen, H. Liang, C. Wu, M. Tao, The effect of Si on $V_{30}Ti_{35}Cr_{25}Fe_{10}$ BCC hydrogen storage alloy, J. Alloys Compd. 441 (2007) 297–300.
[25] L. Ouyang, J. Huang, H. Wang, J. Liu, M. Zhu, Progress of hydrogen storage alloys for Ni-MH rechargeable power batteries in electric vehicles: a review, Mater. Chem. Phys. 200 (2017) 164–178.
[26] K. Young, J. Nei, D. Wong, L. Wang, Structural, hydrogen storage, and electrochemical properties of Laves phase-related body-centered-cubic solid solution metal hydride alloys, Int. J. Hydrogen Energy 39 (2014) 21489–21499.
[27] L. Wang, K. Young, J. Nei, D. Pawlik, K. Ng, Hydrogenation of AB_5 and AB_2 metal hydride alloys studied by in situ X-ray diffraction, J. Alloys Compd. 616 (2014) 300–305.
[28] S. Tan, Y. Shen, E. Onur Şahin, D. Noréus, T. Öztürk, Activation behavior of an AB_2 type metal hydride alloy for NiMH batteries, Int. J. Hydrogen Energy 41 (2016) 9948–9953.
[29] Y. Zhang, J. Li, T. Zhang, H. Kou, X. Xue, Hydrogen absorption properties of a non-stoichiometric Zr-based Laves alloy against gaseous impurities, Int. J. Hydrogen Energy 42 (2017) 10109–10116.
[30] K. Young, B. Reichman, M. Fetcenko, Electrochemical performance of AB_2 metal hydride alloys measured at– 40 °C, J. Alloys Compd. 580 (2013) S349–S352.
[31] M. Yoshida, E. Akiba, Hydrogen absorbing-desorbing properties and crystal structure the Zr-Ti-Ni-Mn-V AB_2 Laves phase alloys, J. Alloys Compd. 224 (1995) 121–126.
[32] A.C. Larson, R.B.V. Dreele, Los Alamos National Laboratory Report LANR, 2004, p. 86.
[33] V.V. Burnasheva, V.A. Yartys, N.V. Fadeeva, S.P. Solov'ev, K.N. Semenenko, Neutron diffraction investigation of the $LaNiD_{3.7}$ deuteride, Russ. J. Inorg. Chem. 27 (1982) 1112–1116.
[34] K. Young, D.F. Wong, T. Ouchi, B. Huang, B. Reichman, Effects of La-addition to the structure, hydrogen storage, and electrochemical properties of C14 metal hydride alloys, Electrochim. Acta 174 (2015) 815–825.
[35] K. Young, B. Chao, D. Pawlik, H. Shen, Transmission electron microscope studies in the surface oxide on the La-containing AB_2 metal hydride alloy, J. Alloys Compd. 672 (2016) 356–365.
[36] A.A. Volodin, R. Denys, G. Tsirlina, B. Tarasov, M. Fichtner, V. Yartys, Hydrogen diffusion in $La_{1.5}Nd_{0.5}MgNi_9$ alloy electrodes of the Ni/MH battery, J. Alloys Compd. 645 (2015) S288–S291.
[37] A.A. Volodin, C. Wan, R.V. Denys, G.A. Tsirlina, B.P. Tarasov, M. Fichtner, U. Ulmer, Y. Yu, C.C. Nwakwuo, V.A. Yartys, Phase-structural transformations in a metal hydride battery anode $La_{1.5}Nd_{0.5}MgNi_9$ alloy and its electrochemical performance, Int. J. Hydrogen Energy 41 (2016) 9954–9967.
[38] S. Yang, S. Han, Y. Li, J. Liu, Study on the microstructure and electrochemical kinetic properties of $MmNi_{4.50-x}Mn_xCo_{0.45}Al_{0.30}$ ($0.25 \leq x \leq 0.45$) hydrogen storage alloys, Mater. Sci. Eng. B 178 (2013) 39–44.
[39] W. Hu, R.V. Denys, C. Nwakwuo, T. Holm, J.P. Maehlen, J.K. Solberg, V.A. Yartys, Annealing effect on phase composition and electrochemical properties of the Co-free La_2MgNi_9 anode for Ni-Metal Hydride batteries, Electrochim. Acta 96

(2013) 27–33.
[40] M. Latroche, F. Cuevas, W. Hu, D. Sheptyakov, R.V. Denys, V.A. Yartys, Mechanistic and kinetic study of the electrochemical charge and discharge of La_2MgNi_9 by in situ powder neutron diffraction, J. Phys. Chem. C 118 (2014) 12162–12169.
[41] I.E. Gabis, E.A. Evard, A.P. Voyt, V.G. Kuznetsov, B.P. Tarasov, J.-C. Crivello, M. Latroche, R.V. Denys, W. Hu, V.A. Yartys, Modeling of metal hydride battery anodes at high discharge current densities, Electrochim. Acta 147 (2014) 73–81.
[42] V. Yartys, D. Noreus, M. Latroche, Metal hydrides as negative electrode for Ni-MH batteries, Appl. Phys. A 122 (2016) 43.
[43] C. Wan, R.V. Denys, V.A. Yartys, In situ neutron powder diffraction study of phase-structural transformations in La-Mg-Ni battery anode alloy, J. Alloys Compd. 670 (2016) 210–216.
[44] N.S. Nazer, R.V. Denys, V.A. Yartys, W. Hu, M. Latroche, F. Cuevas, B.C. Hauback, P.F. Henry, L. Arnberg, In operando neutron diffraction study of LaNd-$MgNi_9H_{13}$ as a metal hydride battery anode, J. Power Sources 343 (2017) 502–512.
[45] K. Young, T. Ouchi, J. Nei, D. Moghe, The importance of rare-earth additions in Zr-based AB_2 metal hydride alloys, Batteries 2 (2016) 25.
[46] C. Wan, R. Denys, M. Lelis, D. Milčius, V. Yartys, Electrochemical studies and phase-structural characterization of a high-capacity La-doped AB_2 Laves type alloy and its hydride, J. Power Sources 418 (2019) 193–201.
[47] X. Li, H. Dong, A. Zhang, Y. Wei, Electrochemical impedance and cyclic voltammetry characterization of a metal hydride electrode in alkaline electrolytes, J. Alloys Compd. 426 (2006) 93–96.
[48] G.H. Ağaoğlu, G. Orhan, Elaboration and electrochemical characterization of Mg–Ni hydrogen storage alloy electrodes for Ni/MH batteries, Int. J. Hydrogen Energy 42 (2017) 8098–8108.
[49] X. Yuan, N. Xu, Determination of hydrogen diffusion coefficient in metal hydride electrode by modified Warburg impedance, J. Alloys Compd. 329 (2001) 115–120.
[50] S. Malifarge, B. Delobel, C. Delacourt, Determination of tortuosity using impedance spectra analysis of symmetric cell, J. Electrochem. Soc. 164 (2017) E3329–E3334.
[51] P. De Vidts, J. Delgado, R.E. White, Mathematical modeling for the discharge of a metal hydride electrode, J. Electrochem. Soc. 142 (1995) 4006–4013.
[52] J. Backholm, P. Georén, G.A. Niklasson, Determination of solid phase chemical diffusion coefficient and density of states by electrochemical methods: application to iridium oxide-based thin films, J. Appl. Phys. 103 (2008), 023702.
[53] M.D. Levi, C. Wang, D. Aurbach, Two parallel diffusion paths model for interpretation of PITT and EIS responses from non-uniform intercalation electrodes, J. Electroanal. Chem. 561 (2004) 1–11.

Supplementary information to the paper

STUDY OF HYDROGEN STORAGE AND ELECTROCHEMICAL PROPERTIES OF THE AB_2-TYPE $Ti_{0.15}Zr_{0.85}La_{0.03}Ni_{1.2}Mn_{0.7}V_{0.12}Fe_{0.12}$ ALLOY

by

Alexei A. Volodin[1,2], Roman V. Denys [2,3], ChuBin Wan[2,4],

Ika Dewi Wijayanti[2,5,6], Suwarno[6], Boris P. Tarasov[1], Vladimir E. Antonov[7] and Volodymyr A. Yartys[2, 5] ✉☎

[1] Institute of Problems of Chemical Physics RAS, Chernogolovka, 142432, Russia
[2] Institute for Energy Technology, P.O. Box 40, Kjeller NO-2027, Norway
[3] HYSTORSYS AS, P.O. Box 45, Kjeller NO-2027, Norway
[4] University of Science and Technology Beijing, 100083, China
[5] Norwegian University of Science and Technology, Trondheim, Norway
[6] Department of Mechanical Engineering, Sepuluh Nopember Institute of Technology (ITS), Surabaya, Indonesia
[7] Institute of Solid State Physics RAS, Chernogolovka, 142432, Russia

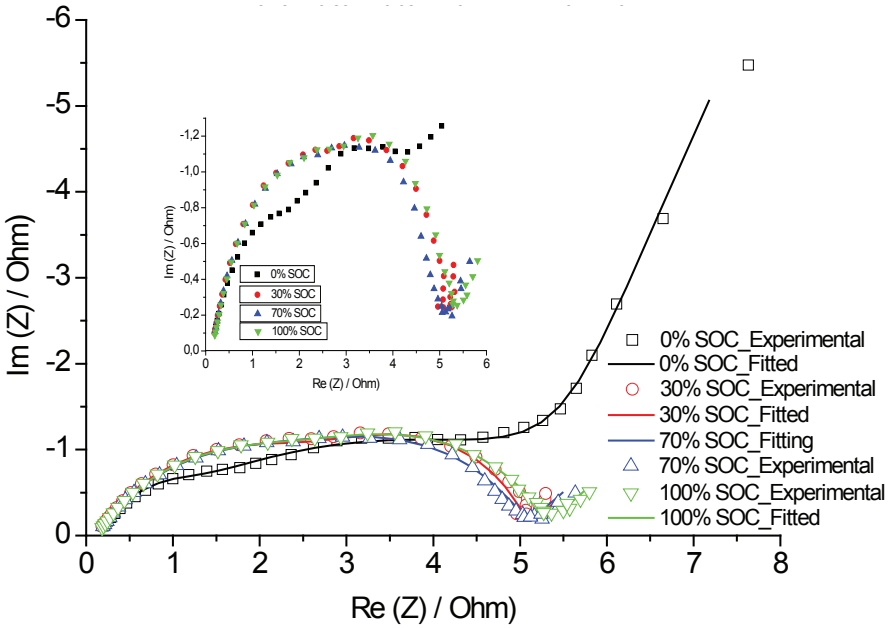

Fig. S1. Nyquist plot of EIS spectra experimental and fitted data of as cast $Ti_{0.15}Zr_{0.85}La_{0.03}Ni_{1.2}Mn_{0.7}V_{0.12}Fe_{0.12}$ alloy.

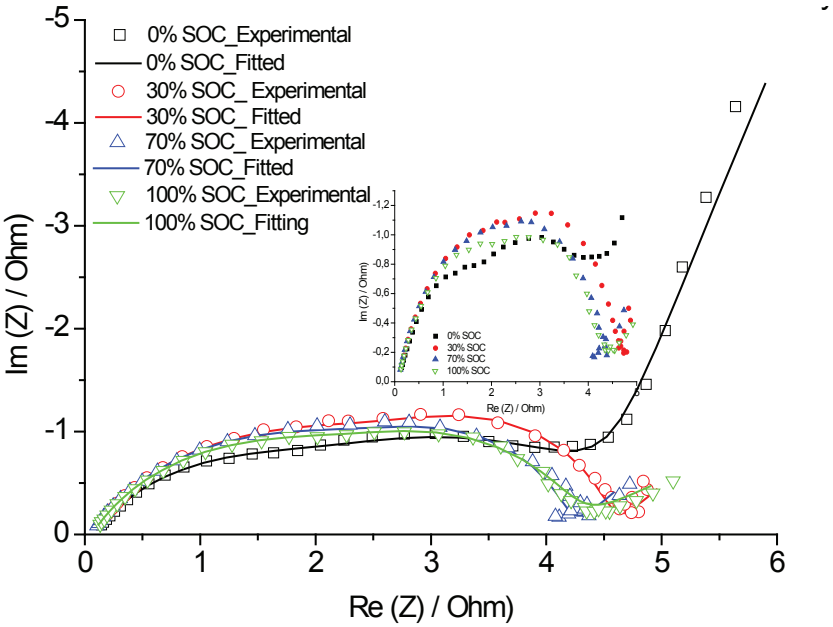

Fig. S2. Nyquist plot of EIS spectra experimental and fitted data of annealed $Ti_{0.15}Zr_{0.85}La_{0.03}Ni_{1.2}Mn_{0.7}V_{0.12}Fe_{0.12}$ alloy.

PAPER II

PAPER II

The electrochemical performance of melt-spun C14-Laves type TiZr-based alloy

I.D. Wijayanti, L. Mølmen, R.V. Denys, J. Nei, S. Gorsse, K. Young, M.N. Guzik, V. Yartys

International Journal of Hydrogen Energy, 45 (2020) 1297-1303.

INTERNATIONAL JOURNAL OF HYDROGEN ENERGY 45 (2020) 1297–1303

Available online at www.sciencedirect.com

ScienceDirect

journal homepage: www.elsevier.com/locate/he

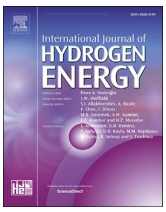

The electrochemical performance of melt-spun C14-Laves type Ti–Zr-based alloy

Ika Dewi Wijayanti [a,b,c], *Live Mølmen* [b], *Roman V. Denys* [a], *Jean Nei* [d], *Stéphane Gorsse* [e,f], *Kwo Young* [d], *Matylda N. Guzik* [g], *Volodymyr Yartys* [a,b,*]

[a] *Department of Battery Technology, Institute for Energy Technology (IFE), Kjeller, Norway*
[b] *Department of Materials Science and Engineering, NTNU, Trondheim, Norway*
[c] *Department of Mechanical Engineering, Sepuluh Nopember Institute of Technology (ITS), Surabaya, Indonesia*
[d] *BASF/Battery Materials–Ovonic, Rochester Hills, USA*
[e] *CNRS, ICMCB, University of Bordeaux, UMR 5026, Pessac F-33600, France*
[f] *Bordeaux INP, ENSCBP, Pessac F-33600, France*
[g] *Department of Physics, University of Oslo, Blindern, Oslo, Norway*

ARTICLE INFO

Article history:
Received 9 November 2018
Received in revised form
9 February 2019
Accepted 12 February 2019
Available online 8 March 2019

Keywords:
Ti–Zr based alloy
Metal hydride battery
Rapid solidification
Electrochemical performance

ABSTRACT

The main objective of the present work is to study the effect of rapid solidification on the electrochemical performance of Zr-based Laves type alloy with a nominal composition $Ti_{12}Zr_{21.5}V_{10}Cr_{7.5}Mn_{8.1}Co_8Ni_{32.2}Al_{0.4}Sn_{0.3}$. The samples were prepared from the as-cast arc melted buttons by melt spinning at different copper wheel rotation speeds of 5, 16.5, 33, and 100 Hz, which are equivalent to linear speeds of 6.3, 21, 41, and 62.8 m s^{-1} respectively using a cooling wheel with a diameter of 20 cm. The phase composition and morphology of the ribbons were analyzed by X-Ray diffraction (XRD) and scanning electron microscopy (SEM). The microstructural changes of the ribbons induced by the variations in the wheel rotation speed were found to be closely related to the electrochemical performances. High discharge capacities exceeding 400 mAh·g^{-1} were achieved for the melt spun samples during the measurements at low current densities. Furthermore, melt spun casting performed at the highest wheel rotation speed of 100 Hz resulted in the best rate performance of the alloy. As this alloy has the smallest crystallite size, this resulted in the shortest H atoms diffusion distances, and thus increased the efficient H diffusion rate and improved the electrochemical performance.

Introduction

Zr-based Laves alloys have become the most promising candidates between the metal hydride (MH) alloys used as negative active electrode materials in the Nickel/Metal Hydride batteries due to their high capacities in storing hydrogen by forming AB_2H_{3-4} hydrides [1–5]. However, poor activation performance of AB_2 MH alloys in comparison with that of the commercial AB_5 MH compositions motivated intensive studies to improve their electrochemical performance [6–8]. Rapid solidification (RS)/rapid quenching is one of the materials processing techniques which produces nanostructured alloys by applying cooling rates exceeding 10^4 K·s^{-1} to the molten metal, thus affecting both the phase composition and microstructure of the alloys [9–13]. Both the morphology and

* *Corresponding author*. Department of Battery Technology, Institute for Energy Technology (IFE), Kjeller, Norway.
E-mail addresses: Ika.Dewi.Wijayanti@ife.no (I.D. Wijayanti), Volodymyr.Yartys@ife.no (V. Yartys).
https://doi.org/10.1016/j.ijhydene.2019.02.093

phase composition resulting from the rapid quenching process can cause variations in the electrochemical performance [14–16]. Particularly, the kinetics of the processes occurring at the metal–electrolyte interface and the rate of hydrogen diffusion within the bulk alloy are changed [17,18]. Therefore, in order to improve the electrochemical performance, the optimized phase structures with fine morphology and an appropriate composition are highly desirable.

In the present study, RS process was performed on the $Ti_{12}Zr_{21.5}V_{10}Cr_{7.5}Mn_{8.1}Co_8Ni_{32.2}Al_{0.4}Sn_{0.3}$ alloy using different wheel rotation speed rates of 5, 16.5, 33, and 100 Hz. Additions of Cu [19], Fe [20], Zn [21], Si [22], Mo [23], B [24], and Pd [25] to this alloy were studied by BASF group in order to achieve improvements of the high rate dischargeability (HRD) performances. These studies showed that HRD performance improved by adding 2 wt% Pd. By applying the rapid solidification process, thus by achieving its nanostructuring [26,27], we aim at improving the HRD performance of the alloy. Furthermore, the interrelation between the melt-spinning rotation speed and the electrochemical properties of multi-component Zr-based Laves alloys and the corresponding charge-discharge mechanism will be presented in this paper. The effects of the variation of the different cooling rates on the crystal structure, microstructure, phase abundance, and electrochemical properties of the rapidly solidified alloys will be reported.

Experimental methods

Alloy with the composition of $Ti_{12}Zr_{21.5}V_{10}Cr_{7.5}Mn_{8.1}Co_{8}Ni_{32.2}Al_{0.4}Sn_{0.3}$ was prepared by induction melting under a protective atmosphere of helium gas by heating up the mixture of the raw materials placed into an Al_2O_3 crucible and holding the formed melt at 1500 °C for 5 min. The composition of the alloy was chosen because of its balanced performances in capacity, high-rate dischargeability (HRD), charge retention, and cycle stability, and was previously used as the base material in other studies performed at BASF [24]. The as-cast alloy was then used for the castings performed using a SC Edmund Buehler melt spinner accommodated at CNRS/University of Bordeaux (France) at wheel rotation speeds of 5, 16.5, 33, or 100 Hz.

The as-cast alloy and four types of melt-spun ribbons were mechanically crushed and ground to powder sizes of below 40 μm and 40–60 μm for the X-Ray diffraction (XRD) and electrochemical measurements, respectively. XRD analysis was performed on a Bruker D8 Focus diffractometer using Cu-K_α radiation in the 2θ angle range of 10–90° and with a step size of 0.00157° using a 1 mm slit. Rietveld refinements for the XRD pattern were carried out using the GSAS suite of programs [28] with the EXPGUI interface. A JEOL JSM6320F scanning electron microscope (SEM, Tokyo, Japan) equipped with energy dispersive spectroscopy (EDS) analysis was used to study the phases distribution and their composition.

MH pellet electrodes were prepared by first thoroughly mixing the alloy powder having a particle size of 40–60 μm with carbonyl Ni powder with a specific surface area of ~0.7 $m^2\ g^{-1}$ in the weight ratio of 1:4, which was then cold-pressed under a pressure of 12 MPa into a 10 mm diameter pellet which was then sandwiched between two Ni foams.

Electrochemical performance was measured using a CT 2001 Land Battery Tester with the three-electrode system consisting of a MH alloy working electrode, a sintered $Ni(OH)_2$/NiOOH counter electrode, and a Hg/HgO reference electrode using a 9 M KOH aqueous solution as the electrolyte. Galvanostatic method was used to measure the activation and rate performance of MH electrode. MH electrode was charged at a current density of 100 $mA\cdot g^{-1}$ for 5 h followed by a 30 min rest and then discharged at a current density of 100 $mA\cdot g^{-1}$ to a voltage cut–off of −0.7 V against the Hg/HgO reference electrode. After the MH electrode was fully activated, it was charged at a current density of 100 $mA\cdot g^{-1}$ followed by a 30 min rest and discharged at different current densities (0.1–1 C rate) to a voltage cut–off of −0.6 V against the Hg/HgO reference electrode (see Table 1 presenting the details of the electrochemical characterisation experiments performed during the half-cell measurements). The discharge rate performances of each sample are shown by calculating the ratio the discharge capacity at the highest current density to the capacity at the lowest current density [29].

Results and discussion

Ribbon structure

Morphologies of the ribbons appear to be directly related to the conditions of the Rapid Solidification performed at the University of Bordeaux/CNRS Bordeaux. With increasing wheel rotation speed, RS results in regular changes in width, length and thickness of the produced ribbons (see Fig. 1). Indeed, all dimensions of the ribbons gradually decrease when rotation frequency goes up from 5 to 100 Hz. This is expected as thinner, shorter, and narrower ribbons are anticipated to be produced at higher rotation speeds. Dimensional parameters of the ribbons produced by melt spinning are shown in Table 2.

Table 1 – Summary of the electrochemical characterisation experiments performed during the half-cell measurements.

Cycle number	Charge current ($mA\cdot g^{-1}$)	Charge time (h)	Discharge current ($mA\cdot g^{-1}$)	Discharge cut –off voltage (V)
1–33	100	5	100	−0.7
34	100	5	10	−0.6
35	100	5	34	−0.6
36	100	5	68	−0.6
37	100	5	100	−0.6
38	100	5	136	−0.6
39	100	5	169	−0.6
40	100	5	200	−0.6
41	100	5	237	−0.6
42	100	5	271	−0.6
43	100	5	305	−0.6

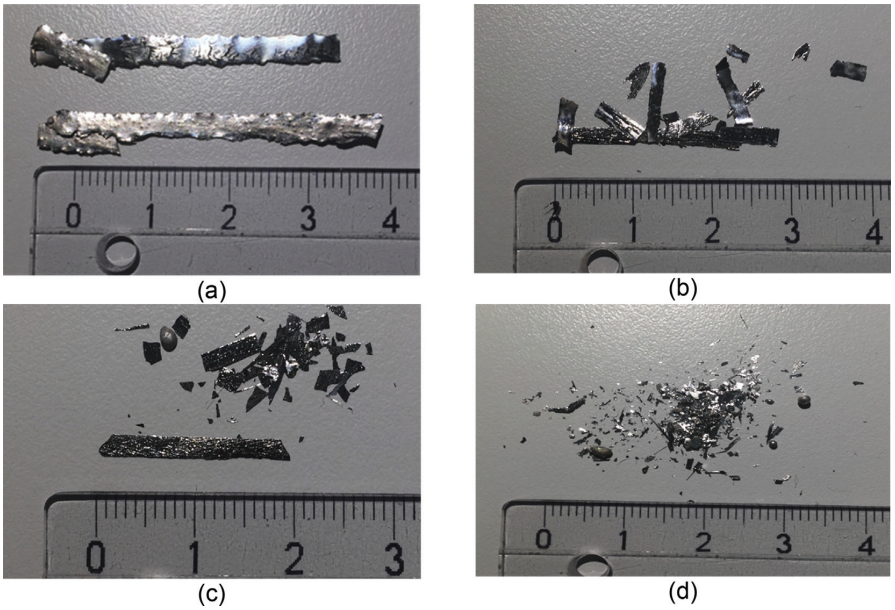

Fig. 1 – Ribbons produced using melt spinning at different wheel rotation speeds of 5 (a), 16.5 (b), 33 (c), and 100 (d) Hz. Higher solidification rates cause regular changes in width, length, and thickness of the produced ribbons which all gradually decreased when rotation frequency went up from 5 to 100 Hz. Their values change from 0.5, 4.4, and 0.213 mm to 0.1, 0.5, and 0.043 mm, respectively (see Table 2 for the details).

XRD analysis

XRD patterns of five studied alloys are shown in Fig. 2. All peaks can be fitted to a hexagonal Laves type C14 and a face-centered cubic C15 Laves type structures. However, as the C14 phase is the main component with its abundancy exceeding 83 wt% for every studied material, in analysis of the crystallite size in GSAS refinements we only considered the related data as contributed by the main C14 phase only.

A typical Rietveld GSAS refinement plot for the as-cast sample is presented in Fig. 3, while the data on the unit cell parameters, volumes of the unit cells, crystallite sizes, and phase abundances for the studied samples are given in Table 3. Two conclusions can be made when analyzing the data presented in this Table.

(a) As the wheel rotation speed increases, the abundance of the C14 phase becomes higher, suggesting that the C14 phase is more likely to form at higher solidification rates as compared to the C15 phase. This is in agreement with an earlier report [30].

(b) For the C14 intermetallic the crystallite sizes gradually decrease from the initial 104 nm for the as cast alloy to 21 nm for the sample received by the melt spinning at 100 Hz.

Table 2 – Characteristics of the ribbons produced by melt spinning.

Sample	Width (mm)	Length (mm)	Thickness (mm)
As cast	–	–	–
5 Hz	0.5	4.4	0.213
16.5 Hz	0.3	2.9	0.125
33 Hz	0.2	2.0	0.057
100 Hz	0.1	0.1	0.043

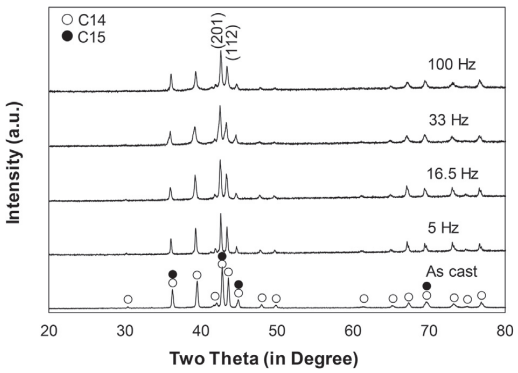

Fig. 2 – XRD patterns collected using Cu-K_α radiation for the as-cast and melt-spun samples with composition $Ti_{0.20}Zr_{0.80}La_{0.01}Ni_{1.2}Mn_{0.70}V_{0.12}Fe_{0.12}$ obtained at different wheel rotation speeds of 5, 16.5, 33, and 100 Hz. Two Laves phase intermetallics, C14 (major phase; 83.5 wt%) and C15 (minor phase; 16.5 wt%), were quantitatively identified.

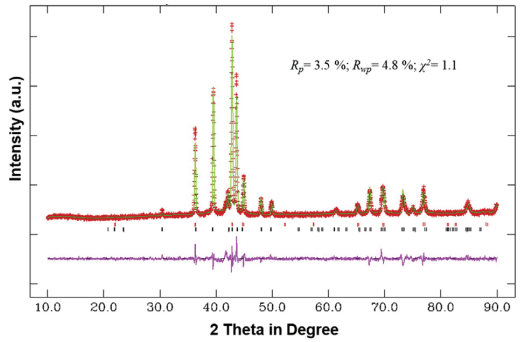

Fig. 3 – Observed (+), calculated (upper line), and difference (lower line) Rietveld GSAS refinement plots of the XRD pattern of the as-cast sample. The XRD data shows presence of two phases, C14 (83.5 wt%; bottom ticks) and C15 (16.5 wt %; top ticks) intermetallics. Reliability factors are: Rp = 3.5%; Rwp = 4.8%; and χ^2 = 1.1.

As mentioned earlier, due to the small abundance of C15 phase, crystallite size for C15 phases has not been refined.

At the same time, unit cell parameters, c/a ratios and volumes of the unit cells show only slight variations (1.3% in maximum for the volumes of the C14 Laves phase and 0.6% for the volumes of the C15 phase). These variations are probably related to the small changes in the stoichiometry of the alloys introduced during the melt casting process.

SEM/EDS analysis

Microstructures of the alloys were studied by SEM, and their images collected in the backscattered electron (BSE) mode are presented in Fig. 4.

As-cast sample shows a formation of the two-phase microstructure containing C14 Laves type intermetallic as the main constituent and a secondary C15 intermetallic, with the main phase having a grain size with a length of appr. 15 μm and a width of appr. 3–5 μm (see Fig. 4).

Casting by rapid solidification significantly and regularly changes the phase composition and morphology of the constituents because of the increasing solidification rate being proportional to the increasing wheel rotation speed.

Rapid solidification causes the following changes

(a) Grain size significantly and gradually decreases with increasing the wheel rotation speed. Indeed, already at a rotation speed of 5 Hz the grain size drops from the initial 15 μm to just approximately 2 μm at 5 Hz and further down to 900 nm at 100 Hz.
(b) Increased rate of RS causes formation of a dendrite microstructure. Dendrites appear in the samples casted at 16.5 Hz and at 33 Hz. The size (3 → 2 μm) and arm spacing (250 → 200 nm) of the dendritic structure decreases with increasing solidification rate (16.5 → 33 Hz).
(c) Finally, at 100 Hz rotation speed, the morphology becomes more uniform with a matrix C14 phase composing a core and a secondary C15 phase forming a shell. Large number of nuclei of the main C14 phase is formed in the RS samples due to the higher melting temperature of this intermetallic. When the rotation speed increases, these nuclei do not have enough time to grow and these limitations in the kinetics of growth result is a smaller dendrite sizes and arm spacings. When reaching the highest solidification rate, the matrix and secondary phase compete with each other to firstly nucleate while not always having a sufficient time to grow. By increasing the rotation speed to 100 Hz, a homogeneous structure with a more even distribution of secondary phase in the structure is formed while the dendrite structure is no longer observed.

Electrochemical measurements

As shown in Fig. 5, the as-cast alloy has the best activation performance among all studied alloys, requiring approximately 10 activation cycles to reach the discharge capacity of close to 280 mA·g^{-1}. All melt-spun alloys need more than 15 cycles to be activated, even up to 17 to 20 cycles for a 16.5 Hz speed (Fig. 5 (a)). We assume that the RS process increased the thickness of the native oxide on the MH alloy surface which required extra cycles of charge-discharge to be removed. The increase in the C14 phase abundance and a larger amount of the surface oxides in the starting 5 Hz RS alloy caused a more difficult activation of the sample. Similar difficulties in activation were observed for other RS materials. Thirty-three cycles were performed for all the melt-spun alloys to ensure that the MH electrodes were fully activated and ready for the discharge rate measurements. Among all the melt-spun alloys, 100 Hz melt-spun alloy showed the fastest activation and

Table 3 – Crystallographic data, crystallite size and phase abundances for the as-cast and melt-spun samples from the Rietveld GSAS refinements.

C14							C15		
Alloy	*a*, Å	*c*, Å	*c*/*a*	V, Å^3	Crystallite size, nm	Abundance, wt.%	*a*, Å	V, Å^3	Abundance wt.%
As cast	4.9662 (1)	8.0935 (2)	1.6297	172.9 (1)	104	83.5 (4)	7.0037 (3)	343.5 (4)	16.5 (1)
5 Hz	4.9454 (2)	8.0587 (3)	1.6295	170.7 (1)	29	89.3 (4)	6.9888 (1)	341.3 (2)	10.7 (4)
16.5 Hz	4.9594 (2)	8.0800 (5)	1.6292	172.1 (2)	26	94.3 (3)	7.0106 (6)	344.6 (9)	5.7 (3)
33 Hz	4.9563 (4)	8.0761 (8)	1.6294	171.8 (4)	21	84.6 (8)	6.9945 (6)	342.2 (9)	15.4 (2)
100 Hz	4.9660 (4)	8.0906 (8)	1.6291	172.8 (4)	21	83.8 (1)	7.0173 (6)	345.5 (9)	16.2 (3)

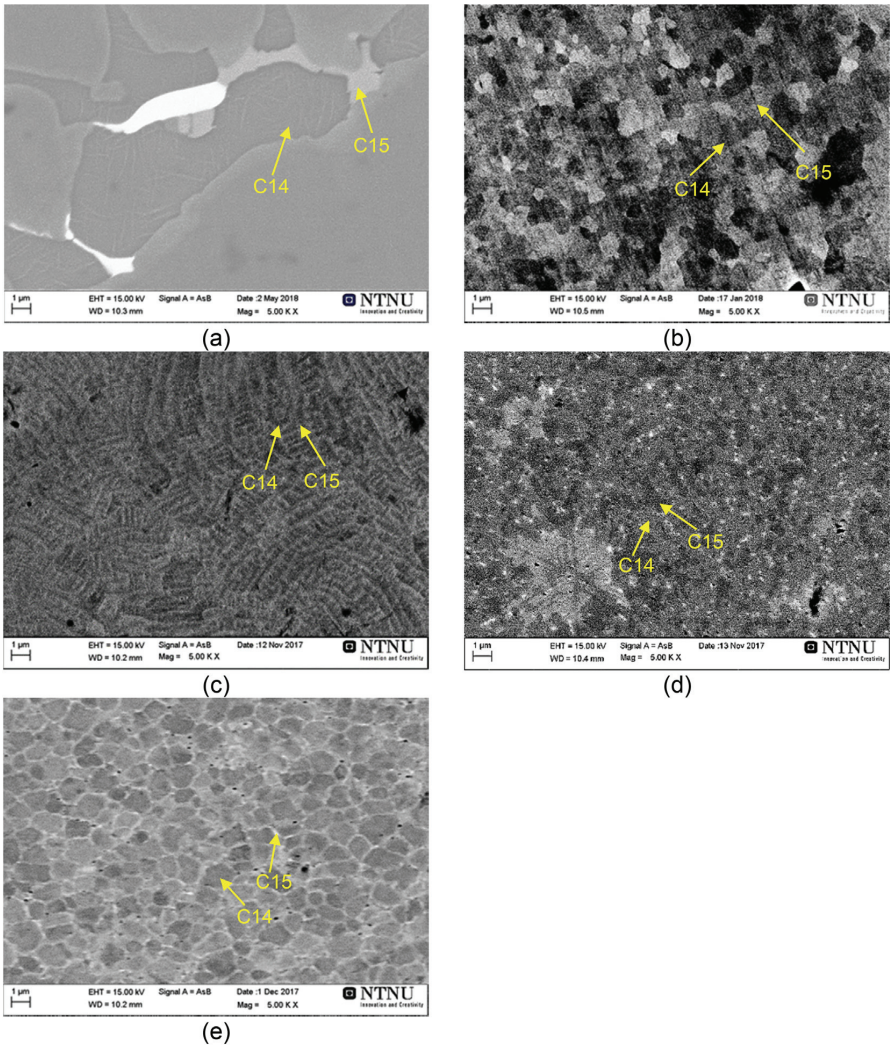

Fig. 4 – BSE SEM micrographs of as-cast (a) and melt-spun samples produced at different rotation speeds of 5 Hz (b), 16.5 Hz (c), 33 Hz (d), and 100 Hz (e).

the highest discharge capacity (after 33 charge-discharge cycles) of 237 mAh·g^{-1}. This can be due to its optimized microstructure showing a significant refinement, and a rather limited phase segregation as compared to the other melt spun samples.

The discharge rate performances of each sample are presented in Fig. 5 (b). These rate performances were evaluated by calculating high rate dischargeability (HRD) given in Table 4, which presents the ratio of the discharge capacity available at the highest current density of 304 mA g^{-1} to the electrochemical capacity at the lowest current density at 10 mA g^{-1}. The as-cast alloy shows the highest discharge capacity at most applied discharge current densities. The highest discharge capacity at the lowest current density measurement is observed for the melt spun 16.5 Hz sample. This capacity drops faster during the initial increase in current densities, but the decrease in capacity slows down as the current density increases further indicating that the RS process effectively improves the rate performance at higher current densities. Gradual capacity decrease for the studied alloys with increasing current densities can be observed clearer by analyzing the data of the Table 4. The largest decrease in HRD is found to happen for a 16.5 Hz sample, then followed by 33 Hz and 5 Hz samples. However, this rapid decrease only takes place at lower current densities. As-cast sample shows the smallest decrease in the capacity at the beginning, but it becomes more pronounced when the current density increases.

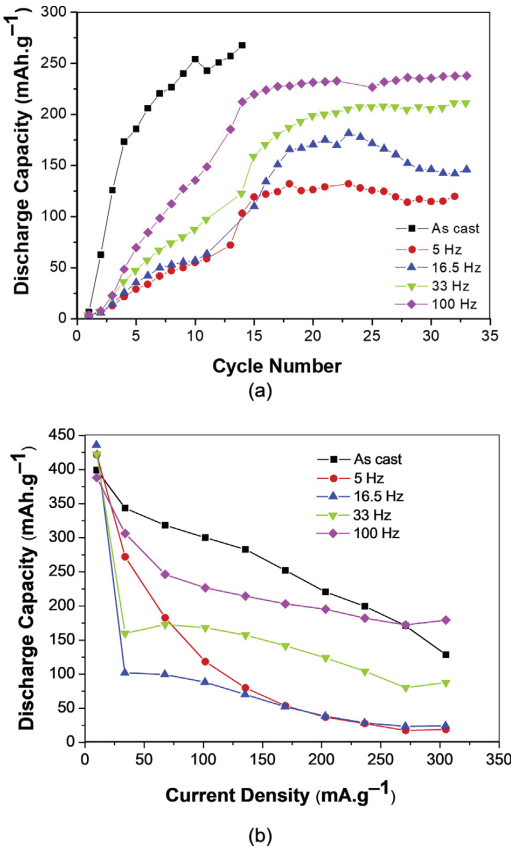

Fig. 5 – Electrochemical activation on cycling (a) and rate dependence of discharge capacity (b) of the alloys studied in this work. The activation becomes more difficult for the melt-spun samples; however, the best rate performance is achieved at the highest rotation speed of 100 Hz, as can be concluded from its lowest slope.

We observe evidences that different quenching rates achieved due to the variation of the wheel rotation speed of the melt-spinner result in microstructural changes in the alloy which significantly affect the electrochemical performance. Further to the microstructural modifications, the abundance of the C14 and C15 phases also changes as a result of rapid solidification. The ratio C14/C15 plays an important role in electrode performance as C14 phase is favourable for achieving high electrochemical capacity while C15 phase causes high rate performance of the electrode. With increasing the rotation speed, the higher solidification rates are achieved which results in reduced grain sizes of the processed alloy. Lower solidification rates resulting from application of lower wheel rotation speeds (16.5 and 33 Hz) cause formation of dendritic structures and such morphology slows down hydrogen diffusion thus causing inferior rate performance of the battery anodes. Not only slowing down of the hydrogen diffusivity but also a decrease in the surface exchange currents for the dendritic structures were reported earlier in the reference data [31] and were linked to the inferior rate performance of the metal hydride anodes. Thus, forming a homogeneous nanostructured metal hydride anode with an optimised ratio C14/C15 which was achieved for the highest applied solidification rate will allow reaching the best electrochemical performance.

The best HRD performance is observed for the 100 Hz sample which is showing only a small drop in the discharge capacity at each step of ramping up of the applied current density during the HRD experiments. This is probably caused by the smallest crystallite sizes observed for this sample resulting in the fastest hydrogen diffusion in the bulk material.

The slight compositional variations and phase-structural changes induced by RS process affect the activation and rate performances. The most abundant C14 phase which is less prone to pulverization with smaller amount of the C15 phase present in the melt-spun alloy (which undergoes hydride decrepitation faster and more easily) correlates with the poorer activation performance of the C14-predominant alloys. The surface of these alloys should be activated to reach their maximum electrochemical capacity, and a treatment in hot (80 °C) KOH solution is one of the possible options to try. On the other hand, the optimized structure obtained by reaching an appropriate ratio between C14 and C15 phases provides a synergetic effect and improves the rate performance. Moreover, RS process proved to cause a pronounced refinement of the microstructures thus reducing the distance for the hydrogen diffusion and creating a faster hydrogen diffusion paths through the alloy.

Table 4 – HRD characteristics of the as-cast and melt-spun samples (%).

Current density ($mA \cdot g^{-1}$)	As-cast	5 Hz	16.5 Hz	33 Hz	100 Hz
10	100	100	100	100	100
34	86	64	23	38	79
68	80	43	23	41	63
100	75	28	20	40	58
136	71	19	16	37	55
169	63	13	12	33	52
200	55	9	9	29	50
237	50	6	7	25	47
271	43	4	5	19	44
304	32	4	6	21	46

Conclusions

The effect of cooling rate variation during the melt casting of the $Ti_{12}Zr_{21.5}V_{10}Cr_{7.5}Mn_{8.1}Co_8Ni_{32.2}Al_{0.4}Sn_{0.3}$ alloy has been studied. All melt-spun samples showed a predominant formation of the C14 Laves type intermetallic phase. Rapid solidification process significantly affects the morphology and microstructure of the alloys. Equiaxed grain structure is formed at a lower rotation speed, while the dendritic structures solidify at higher rotation speeds, and finally the dendritic structure vanished and equiaxed grains with the phase segregation at the grain boundaries are observed at the highest rotation speed. The discharge rate performances improved with the rapid solidification process and were the best at the highest applied

cooling rate achieved at 100 Hz. This phenomenon is believed to be due to the optimized structure obtained by reaching an appropriate ratio between C14 and C15 phases providing a synergetic effect and improving the rate performance.

Acknowledgement

This work was supported by Norwegian Research Center on Zero Emission Energy Systems for Transport (MoZEES). We thank CNRS/University of Bordeaux and Prof. Jean-Louis Bobet for the availability of the laboratory facilities for the rapid solidification process, and BASF-Ovonic Rochester Hills, USA for the access to their research laboratories during the work on this project. Ika Dewi Wijayanti received a fellowship from Indonesia Endowment fund for Education (LPDP) to perform a PhD research project at NTNU/IFE in Norway.

REFERENCES

[1] Yartys V, Noreus D, Latroche M. Metal hydrides as negative electrode materials for NiMH batteries. Appl Phys A 2016;122:43.
[2] Young K-H, Nei J, Wan C, Denys R, Yartys V. Comparison of C14- and C15-predomiated AB_2 metal hydride alloys for electrochemical applications. Batteries 2017;3:22.
[3] Young K-H, Koch JM, Wan C, Denys RV, Yartys VA. Cell performance comparison between C14-and C15-predomiated AB_2 metal hydride alloys. Batteries 2017;3:29.
[4] Young K-H, Nei J. The current status of hydrogen storage alloy development for electrochemical applications. Materials 2013;6:4574–608.
[5] Fetcenko MA, Ovshinsky SR, Reichman B, Young K, Fierro C, Koch J, et al. Recent advances in NiMH battery technology. J Power Sources 2007;165:544–51.
[6] Tan S, Shen Y, Onur Şahin E, Noréus D, Öztürk T. Activation behavior of an AB_2 type metal hydride alloy for NiMH batteries. Int J Hydrog Energy 2016;41:9948–53.
[7] Miao H, Gao M, Liu Y, Lin Y, Wang J, Pan H. Microstructure and electrochemical properties of Ti–V-based multiphase hydrogen storage electrode alloys $Ti_{0.8}Zr_{0.2}V_{2.7}Mn_{0.5}Cr_{0.8-x}Ni_{1.25}Fe_x$ (x=0.0–0.8). Int J Hydrog Energy 2007;32:3947–53.
[8] Liu Y, Pan H, Gao M, Wang Q. Advanced hydrogen storage alloys for Ni/MH rechargeable batteries. J Mater Chem 2011;21:4743–55.
[9] Suwarno S, Solberg JK, Maehlen JP, Krogh B, Børresen BT, Ochoa-Fernandez E, et al. Microstructure and hydrogen storage properties of as-cast and rapidly solidified Ti-rich Ti–V alloys. Trans Nonferrous Metals Soc China 2012;22:1831–8.
[10] Wu Y, Lototsky MV, Solberg JK, Yartys VA. Microstructural evolution and improved hydrogenation–dehydrogenation kinetics of nanostructured melt-spun Mg–Ni–Mm alloys. J Alloy Comp 2011;509:S640–5.
[11] Wu Y, Han W, Zhou SX, Lototsky MV, Solberg JK, Yartys VA. Microstructure and hydrogenation behavior of ball-milled and melt-spun Mg–10Ni–2Mm alloys. J Alloy Comp 2008;466:176–81.
[12] Wu Y, Solberg JK, Yartys VA. The effect of solidification rate on microstructural evolution of a melt-spun Mg–20Ni–8Mm hydrogen storage alloy. J Alloy Comp 2007;446–447:178–82.
[13] Nwakwuo CC, Holm T, Denys RV, Hu W, Maehlen JP, Solberg JK, et al. Effect of magnesium content and quenching rate on the phase structure and composition of rapidly solidified La_2MgNi_9 metal hydride battery electrode alloy. J Alloy Comp 2013;555:201–8.
[14] Zhang Y, Shang H, Li Y, Hou Z, Qi Y, Guo S. Structure and electrochemical hydrogen storage behaviors of RE-Mg-Ni-Co-Al-based AB_2-type alloys prepared by melt spinning. J Alloy Comp 2017;699:378–85.
[15] Zhang Y, Ren H, Li B, Guo S, Pang Z, Wang X. Electrochemical hydrogen storage characteristics of nanocrystalline and amorphous $Mg_{20}Ni_{10-x}Co_x$ (x=0–4) alloys prepared by melt spinning. Int J Hydrog Energy 2009;34:8144–51.
[16] Zhang Y, Cai Y, Zhao C, Zhai T, Zhang G, Zhao D. Electrochemical performances of the as-melt $La_{0.75-x}M_xMg_{0.25}Ni_{3.2}Co_{0.2}Al_{0.1}$ (M=Pr, Zr; x=0, 0.2) alloys applied to Ni/metal hydride (MH) battery. Int J Hydrog Energy 2012;37:14590–7.
[17] Zhang SK, Shu KY, Lei YQ, Lü GL, Wang QD. Effect of solidification rate on the phase structure and electrochemical properties of alloy $Zr_{0.7}Ti_{0.3}(MnVNi)_2$. J Alloy Comp 2003;352:158–62.
[18] Zhang Y, Li B, Ren H, Wu Z, Dong X, Wang X. Investigation on structures and electrochemical characteristics of the as-cast and quenched $La_{0.5}Ce_{0.2}Mg_{0.3}Co_{0.4}Ni_{2.6-x}Mn_x$ (x=0–0.4) electrode alloys. J Alloy Comp 2008;461:591–7.
[19] Young K-H, Ouchi T, Huang B, Reichman B, Fetcenko MA. Studies of copper as a modifier in C14-predominant AB_2 metal hydride alloys. J Power Sources 2012;204:205–12.
[20] Young K-H, Ouchi T, Huang B, Reichman B, Fetcenko MA. The structure, hydrogen storage, and electrochemical properties of Fe-doped C14-predominating AB_2 metal hydride alloys. Int J Hydrog Energy 2011;36:12296–304.
[21] Young K, Ouchi T, Lin X, Reichman B. Effects of Zn-addition to C14 metal hydride alloys and comparisons to Si, Fe, Cu, Y, and Mo-additives. J Alloy Comp 2016;655:50–9.
[22] Young K-H, Ouchi T, Huang B, Reichman B, Blankenship R. Improvement in– 40 C electrochemical properties of AB_2 metal hydride alloy by silicon incorporation. J Alloy Comp 2013;575:65–72.
[23] Young K-H, Ouchi T, Huang B, Reichman B, Fetcenko MA. Effect of molybdenum content on structural, gaseous storage, and electrochemical properties of C14-predominant AB_2 metal hydride alloys. J Power Sources 2011;196:8815–21.
[24] Chang S, Young K-H, Ouchi T, Nei J, Wu X. Effects of Boron-incorporation in a V-containing Zr-based AB_2 metal hydride alloy. Batteries 2017;3:36.
[25] Young K-H, Ouchi T, Nei J, Chang S. Increase in the surface catalytic ability by addition of Palladium in C14 metal hydride alloy. Batteries 2017;3:26.
[26] Zhang Y, Zhao C, Yang T, Shang H, Xu C, Zhao D. Comparative study of electrochemical performances of the as-melt $Mg_{20}Ni_{10-x}M_x$ (M=None, Cu, Co, Mn; x=0, 4) alloys applied to Ni/metal hydride (MH) battery. J Alloy Comp 2013;555:131–7.
[27] Zhang Y, Liu Z, Li B, Ma Z, Guo S, Wang X. Structure and electrochemical performances of $Mg_2Ni_{1-x}Mn_x$ (x=0–0.4) electrode alloys prepared by melt spinning. Electrochim Acta 2010;56:427–34.
[28] Larson AC, Von Dreele RB. General structure analysis system (GSAS), Los Alamos national laboratory report LAUR 86-748. 2004.
[29] Young K, Ouchi T, Liu Y, Reichman B, Mays W, Fetcenko M. Structural and electrochemical properties of $Ti_xZr_{7-x}Ni_{10}$. J Alloy Comp 2009;480:521–8.
[30] Stein F, Palm M, Sauthoff G. Structure and stability of Laves phases part II—structure type variations in binary and ternary systems. Intermetallics 2005;13:1056–74.
[31] Young K, Young M, Ouchi T, Reichman B, Fetcenko MA. Improvement in high-rate dischargeability, activation, and low-temperature performance in multi-phase AB_2 alloys by partial substitution of Zr with Y. J Power Sources 2012;215:279–87.

PAPER III

PAPER III

Studies of Zr-based C15 type metal hydride battery anode alloys prepared by rapid solidification

I.D. Wijayanti, L. Mølmen, R.V. Denys, J. Nei, S. Gorsse, M.N. Guzik, K. Young, V. Yartys

Journal of Alloys and Compounds, 804 (2019) 527-537.

Journal of Alloys and Compounds 804 (2019) 527–537

Contents lists available at ScienceDirect

Journal of Alloys and Compounds

journal homepage: http://www.elsevier.com/locate/jalcom

Studies of Zr-based C15 type metal hydride battery anode alloys prepared by rapid solidification

Ika Dewi Wijayanti [a, b, c, **], Live Mølmen [b], Roman V. Denys [a], Jean Nei [d], Stéphane Gorsse [e], Matylda N. Guzik [f], Kwo Young [d], Volodymyr Yartys [a, b, *]

[a] Department of Battery Technology, Institute for Energy Technology (IFE), Kjeller, Norway
[b] Department of Materials Science and Engineering, NTNU, Trondheim, Norway
[c] Department of Mechanical Engineering, ITS, Surabaya, Indonesia
[d] BASF/Battery Materials-Ovonic, Rochester Hills, USA
[e] Univ. Bordeaux, CNRS, Bordeaux INP, ICMCB, UMR 5026, Pessac F, 33600, France
[f] Department of Physics, University of Oslo, Blindern, Oslo, Norway

ARTICLE INFO

Article history:
Received 6 May 2019
Received in revised form
25 June 2019
Accepted 26 June 2019
Available online 27 June 2019

Keywords:
Ti-Zr alloys
Laves phase intermetallic
Rapid solidification
Metal hydride electrode
Electrochemical performance
EIS characterization

ABSTRACT

The objective of the present work was to study an interrelation between the conditions of the rapid solidification casting and electrochemical properties of a C15 Laves-type Zr-based metal hydride battery anode alloy. A 7-component overstoichiometric with B/A>2 alloy (Ni + Mn + V + Fe/Zr + Ti + La = 2.078) was Zr- and Ni-rich. Melt spinning was performed using as cast mother ingot at different rotation speeds of 5, 16.5, and 33 Hz with a 20-cm diameter Cu cooling wheel. The phase composition and morphology of the ribbons were analyzed by X-ray diffraction (XRD) and scanning electron microscopy (SEM) along with X-ray energy dispersive spectroscopy (EDS). Partial Mn vaporization took place during the melt spinning and became more pronounced with the increase in the quenching rate at higher wheel rotation speeds. The SEM study showed a successful refinement and a more homogeneous distribution of La in the melt-spun alloys. However, the alloys demonstrated a more difficult activation performance as compared to the as-cast sample which was associated with introduction of Zr into the composition of the secondary La-and Ni-rich phase when quenching the melt. Presence of Zr in the secondary phase results in inferior rate of its hydrogenation. The formed during the rapid solidification (La,Zr) (Ni,Mn) secondary phase also contained a significant amount of oxygen additionally worsening the activation performance. The grain size gradually decreased from 3.5 μm in the as-cast alloy to approximately 250 nm for the melt spun sample obtained at the highest cooling rate. The two-phase alloys contained a mixture of two Laves type intermetallics, C15 and C14 ones. The abundance of the secondary C14 phase decreased with increase of the cooling rate as compared to the as-cast sample. The electrochemical performance was significantly affected by the compositional and microstructural changes associated with the variation in the cooling rate. The highest electrochemical discharge capacity of 414 mAh/g was obtained for the 16.5 Hz melt spun rate because of an optimized composition of the Laves phase. Furthermore, the diffusion coefficient of hydrogen in this alloy was the highest in a full state of charge, which indicates that faster hydrogen diffusion and shorter hydrogen diffusion paths were achieved via an application of the rapid solidification process. An optimization of the rapid solidification conditions is required to improve an activation behavior of the studied Laves types metal hydride anode alloys.

1. Introduction

Intermetallic compounds which contain hydride-forming and transition metals can reversibly absorb large amounts of hydrogen to form intermetallic hydrides. The very first examples of such hydrides - rather stable ZrNiH and $ZrNiH_3$ formed by ZrNi

* Corresponding author. Institute for Energy Technology (IFE), Kjeller, Norway.
** Corresponding author. Institute for Energy Technology (IFE), Kjeller, Norway.
E-mail addresses: Ika.Dewi.Wijayanti@ife.no (I.D. Wijayanti), Volodymyr.Yartys@ife.no (V. Yartys).

https://doi.org/10.1016/j.jallcom.2019.06.324

intermetallic compound - have been reported already in the 1950s [1]. Increased relative amount of transition metal as in $LaNi_5$, destabilizes corresponding $LaNi_5H_{6.7}$ hydride (P_{abs}/P_{des} @20 °C of 1.83/1.36 atm H_2) [2]. As its equilibrium hydrogen pressure becomes close to 1 bar, this allows to synthesize it both by a reaction of intermetallic alloy with hydrogen gas but also electrochemically using the alloys as an anode electrode of the metal hydride battery. In spite of a high theoretical electrochemical capacity of 400 mAh/g, the instability of $LaNi_5$-based hydride at normal conditions results in its much lower capacity of around 250 mAh/g as compared to the theoretical limit [3]. Substitution of a part of Ni by Cr or Mn in $LaNi_{4.5}(Cr/Mn)_{0.5}$ increased reversible capacity by 10% to the values 275–285 mAh/g as the formed hydrides have dissociation pressures below 1 bar H_2. In practical applications a severe corrosion of $LaNi_5$ in the aqueous KOH electrolyte has been observed and this issue should be conteracted by modifying the alloy to make it suitable for applications in rechargeable batteries.

Optimum performance of the Nickel Metal Hydride (NiMH) batteries can be achieved by optimizing microstructure, type of intermetallic compound, constituting elements type and content, by changing the composition of hydrogen storage alloy (multicomponent alloy) or by adding electrocatalytic materials for facilitating the hydrogen evolution reaction [4]. As an example, excellent stability was achieved with a very small capacity loss of only 30% over one thousand cycles for $La_{0.8}Nd_{0.2}Ni_{2.5}Co_{2.4}Si_{0.1}$ alloy synthesized via a modification of $LaNi_5$. However, the high cost of rare-earth metals becomes the big challenge to utilize such type of alloys.

The discharge process of the metal hydride battery consisting of nickel hydroxide as a cathode, $LaNi_5$ as anode and aqueous solution of KOH as an electrolyte, has been successfully modelled by considering the electrochemical processes in porous electrodes with hydrogen diffusion coefficient in the $LaNi_5$ electrode being close to 5×10^{-11} cm^2/s [5]. This allowed to assess operating characteristics of the cell, while an optimization of the electrode thickness and the porosity was performed by considering the specific energy and power of the cell.

In order to improve the discharge efficiency and electrochemical properties, multicomponent AB_2 Laves phase alloys become the preference anode materials in the NiMH batteries as they exhibit higher discharge capacities than AB_5-type alloys, further to the Mg-containing $A_{3-x}Mg_xNi_9$ and $A_{2-x}Mg_xNi_7$ compositions [4,6]. Anani and his coworkers [7] reported that a multiphase $Ti_{0.51}Zr_{0.49}V_{0.76}Ni_{1.18}Cr_{0.21}$ alloy with a plateau pressure of 0.83 bar H_2 at ambient conditions, achieved a discharge capacity of 350 mAh/g, which was superior to the electrochemical performance of $LaNi_5$. Similar values of the capacity (350 mAh/g discharge capacity at 50 mA/g current density) were also reported for a multiphase $Zr_{0.8}Ti_{0.2}V_{0.6}Mn_{0.3}Ni_{0.9}Fe_{0.2}$ alloy [4].

The used Laves type intermetallic alloys belong to the largest group of the hydride-forming intermetallics and are utilized for storage of gaseous hydrogen and for the electrochemical storage in the metal hydride batteries. The structures of Laves phases contain a stacking of the layers with compositions A_2B, AB_2 and B_3. Variation of their stacking order results in the formation of different types of the Laves type intermetallics. The most promising Laves phase alloys that absorb hydrogen to form hydrides crystallize with hexagonal $MgZn_2$ (C14), cubic $MgCu_2$ (C15), and di-hexagonal $MgNi_2$ (C36) type structures [8]. For the metal hydride-based hydrogen storage applications, the most frequently utilized are the alloys with C14 and C15 types [9].

Hydrogen storage performance including hydrogen storage capacity, stability of the hydrides, kinetics of hydrogen absorption, and cycling performance are highly dependent on the type of Laves phase present in the alloys [10]. C15 type alloys exhibit excellent high-rate dischargeability (HRD) and are easier to activate than C14 type alloys [8,10,11]. To optimize and to improve the performance of the C15 predominate alloy, one approach is to perform substitutions in the parent alloy containing the transition elements [12,13]. Synthesis of non-stoichiometric alloys with $B/A \neq 2$ is frequently used to modify the properties via a multi-component alloying [14]. By combining certain elements (A = Ti, Zr, V; B= Mn, V, Ni, and Fe) to move the stoichiometry off with B/A becoming higher than 2, higher storage capacities, improved cycle life, and easier activation can be achieved [15]. Various participating elements have their own role in influencing the H storage performance. Hydride-forming A elements include Ti, Zr and V, while transition elements B have several functions, including increased catalytic activity in reduction-oxidation of hydrogen (Ni), improved surface activity to achieve fast hydrogen reduction or oxidation (Mn), and increased corrosion resistance (Fe). In addition to this conventional alloying strategy, it is worth to note that the present alloy satisfies the high entropy alloys definition [16–18], which consists in an entropy stabilization when mixing several kinds of atoms on the same sublattice.

Our earlier work revealed that annealing treatment increased the maximum discharge capacity of the multicomponent AB_2-type $Ti_{0.15}Zr_{0.85}La_{0.03}Ni_{1.2}Mn_{0.7}V_{0.12}Fe_{0.12}$ [19] and $Ti_{0.2}Zr_{0.8}La_xNi_{1.2}Mn_{0.7}V_{0.12}Fe_{0.12}$ (x = 0.01–0.05) alloys [20]. Additions of La (optimum content 3 wt% La) to both alloys improved their activation performance. Furthermore, higher discharge capacities were also achieved. However, the discharge capacity of the alloys decreases significantly when the current density increases. To achieve progress towards high power MH batteries development, it has been suggested that a nanocrystalline microstructure can improve the hydrogen storage performance by minimizing the amount of the secondary phases that do not contribute to the storage capacity and may allow to increase the diffusion rates of hydrogen in the alloys by having an increased amount of grain boundaries where the mobility of hydrogen is higher thus achieving advanced performance at high rates of charge and discharge of the Ni-MH batteries [21,22]. Furthermore, more homogeneous and refined phase distribution was achieved for the alloys by applying a Rapid Solidification process [23–25] which is also beneficial for their use as metal hydride anodes.

In the present study, Rapid Solidification technique was applied to the $Ti_{0.15}Zr_{0.85}La_{0.03}Ni_{1.2}Mn_{0.7}V_{0.12}Fe_{0.12}$ alloy to improve the rate performance of the anode electrode by producing nanostructured alloys [26,27]. The effect of variation of the wheel rotation speed on the crystal structure, morphology of the alloys' microstructures, phases abundance, electrochemical performance, and hydrogen diffusion properties of the non-stoichiometric C15 predominated alloys will be reported. In our earlier work [25], C14 predominated alloy with hexagonal structure prepared by rapid solidification was studied, and the obtained data will also be reviewed as a reference point in order to compare the electrochemical performances of the C15 and C14 types rapidly solidified alloys.

2. Experimental methods

The composition of the studied alloy was chosen as $Ti_{0.15}Zr_{0.85}La_{0.03}V_{0.12}Mn_{0.7}Fe_{0.12}Ni_{1.2}$ and contained a 10% excess of Mn as compared to the listed stoichiometry to compensate for a high rate of evaporation of Mn during the melting and casting. The alloy was prepared by arc melting of the alloying elements with a purity higher than 99.7% on a water-cooled copper hearth under argon atmosphere and re-melted three times to improve its homogeneity. The as-cast samples were then used for the rapid solidification casting performed in a SC Edmund Buehler melt spinner accommodated at Institut de Chimie de la Matière Condensée de Bordeaux (ICMCB, France) using the wheel rotation speeds of 5,

16.5, and 33 Hz. Parts of the as-cast alloy and the ribbon samples were crushed and mechanically ground, before separating a 40–60 μm fraction of the powder using a sieve. The fine powder with a size of less than 40 μm was used for the X-ray powder diffraction (XRD) measurements, which were performed by with a CuK_α radiation (λ = 1.5418 Å) by using a Rigaku MiniFlex 600 BenchTop X-Ray diffractometer having a flat plate geometry, with the measurements covering a range from 20° to 80° and with a step size of 0.01°. The experimental XRD data was processed by using Rietveld refinements and GSAS software [28].

The 40–60 μm powder which was used in the electrochemical measurements was mixed with a Carbonyl Nickel in a weight ratio of 1:4. This mixture was cold-pressed under a pressure of 12 MPa into a 10 mm pellet which was sandwiched between two nickel foams. The electrolyte used for the testing was a 9 M aqueous KOH solution. A half-cell was constructed using a MH alloy powder electrode as a working electrode, a platinum wire as a counter electrode and a mercury/mercury oxide (Hg/HgO) as a reference electrode. The metal hydride anode tests were performed at room temperature using a LAND CT2001A Battery Tester in an open-to-air flooded cell configuration against a partially pre-charged sintered $Ni(OH)_2$ counter electrode. 100 mA/g current density was applied to charge the electrodes for 5 h, then the same rate was applied to discharge the electrodes until a cut-off voltage of −0.7 V was reached.

For the microstructure characterization, bulk alloy and ribbon type samples were embedded in epoxy resin. The microstructures and the compositions of the samples were studied by LV-FE scanning electron microscopy (SEM) of the Zeiss Supra 55VP type.

To determine the hydrogen diffusion coefficient in the studied samples, Electrochemical Impedance Spectroscopy (EIS) characterization was performed [29] by using SP-300-Potentiostat from Bio-Logic Science Instruments. Galvanostatic Electrochemical Impedance Spectroscopy (GEIS) technique was applied in a range of frequencies from 1 kHz–0.5 mHz when using the current amplitude of 10 mA. Four different States of Charge (SoC) of the electrodes were selected for the studies, including SOC 0 (completely discharged anode), 30, 70, and 100 (fully charged anode) (%).

By assuming that the diffusion process is concentration independent, Fick's equation can be applied to calculate the hydrogen diffusion coefficient in the alloys which has an inverse square relation to the Warburg element [30]:

$$D_H = \frac{R^2T^2}{2A^2n^4F^4C^2\sigma^2}$$

where

D_H - diffusion coefficient of hydrogen
R - ideal gas constant
T - absolute temperature
A - electroactive surface area per unit volume of electrode
n - number of electrons transferred
C - concentration of hydrogen ions
σ - Warburg impedance coefficient.

The electrodes are considered as containing spherical particles which have a uniform size and are entirely exposed to the electrolyte. Thus, the electroactive surface area, A, can be determined using the equation [31]:

$$A = \frac{3(1-\in)}{r}$$

where

$\in$ = electrode porosity assumed to be 0.3 [32].
r = radius of spherical particles, an average value was 25 μm (see Experimental part).

3. Results and discussion

3.1. XRD analysis

The XRD patterns of four studied materials (as cast and melt-spun samples at 5, 16.5 and 33 Hz samples) are shown in Fig. 1 (a). Both as-cast and melt-spun samples consist of a cubic C15 type Laves phase as the main constituent and C14 phase as a minor phase. Rietveld refinements showed that the abundance of the C15 phase is higher than 70 wt% for every studied material.

Clearly distinguishable peaks (103) and (112) of the hexagonal C14 phase disappeared after applying the rapid solidification at a rate of 5 Hz indicating that the abundance of the C14 phase significantly decreased.

A typical plot of Rietveld refinements performed using GSAS software for the sample solidified at 16.5 Hz is shown in Fig. 1 (b). The refinements yielded the abundances of C15 and C14 phases, unit cell volumes of the C15 and C14 phases, and the crystallite sizes of C15 phase which are given in Table 1. We note that the crystallite size for the minority C14 phase was not determined because of its low abundance.

From the presented in Table 1 data, we conclude that:

(a) The crystallographic data of as-cast and melt-spun samples well agree with the results of our earlier publication [19]. Addition of 10 wt% Mn to the alloy causes an increase of the unit cell volume for the C15 phase [33]. This is as expected, as Mn has a larger atomic radius (1.264 Å) than Ni (1.246 Å); thus, a partial replacement of Ni will cause enlargement of the lattice parameter of the alloy. We furthermore note that the alloy with the higher content of Ti studied in Ref. [20] shows the smallest unit cell volume of the C15 intermetallic as compared to the results of the present study. The cell parameters of the C15 Laves phases decrease as the amount of Ti increases due to the fact that a smaller in size Ti atom (1.462 Å) substitutes for a larger Zr atom (1.602 Å) in the crystal structures of the alloys [34]. In addition, we also observe that C14 phase identified as the main component of the $Ti_{12}Zr_{21.5}V_{10}Cr_{7.5}Mn_{8.1}Co_8Ni_{32.2}Al_{0.4}Sn_{0.3}$ alloy studied in our earlier work also showed a smaller unit cell volume as compared to the current study showing the effect of increased Mn content in the present work.
(b) The crystallite size of the C15 phase (around 80 nm in average) remained unchanged during the rapid solidification process.
(c) When rapid solidification was applied at 5 Hz rotation speed, the abundance of the C15 phase became higher. As the rotation speed increases further to 16.5 and 33 Hz, the abundance of C15 phase becomes lower than at 5 Hz speed indicating that the C15 phase is more likely to form at lower solidification rates as compared to the C14 phase. This phenomenon was also observed in an earlier report [35].
(d) At 16.5 Hz rotation speed, the melt-spun sample shows the largest unit cell volume for both C15 and C14 phases, while for the 33 Hz melt-spun alloy an opposite trend is observed.

In contrast, the rapid solidification process performed on C14 predominated alloy [25] produced a different outcome. As the wheel rotation speed increased, the abundance of the C14 phase became higher, indicating that the C14 phase is preferably formed

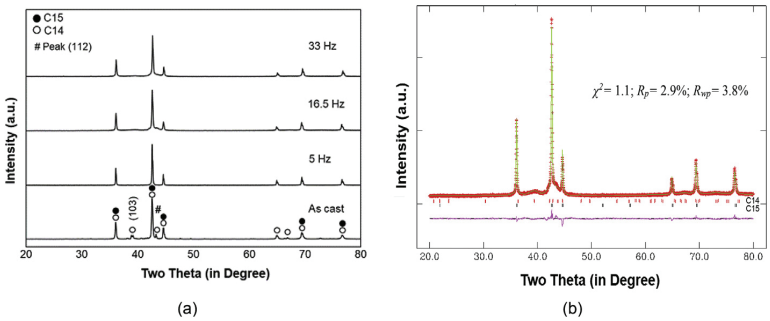

Fig. 1. XRD patterns (Cu-K_α) for as-cast and melt-spun samples of the alloy $Ti_{0.15}Zr_{0.85}La_{0.03}Ni_{1.2}Mn_{0.70}V_{0.12}Fe_{0.12}$ prepared at different wheel rotation speeds of 5, 16.5, and 33 Hz. Two Laves phases (C15 and C14) can be identified (a). Observed (+), calculated (upper line), and difference (lower line) Rietveld GSAS refinement plots of the XRD pattern of the 16.5 Hz melt-spun sample are shown as an example. The refined abundances of the intermetallics are: C15 (80 wt%) and C14 (20 wt %) (b).

Table 1
Phase abundances and crystallographic data for the C15 and C14 Laves type intermetallics.

Alloy	C15					C14				
	a, Å	V, Å^3	Crystallite size, nm	Abundance, wt.%	Reference data a (Å), V (Å^3)	a, Å	c, Å	V, Å^3	Abundance, wt.%	Reference data a, c (Å), V (Å^3)
As cast	7.0236(1)	346.5(2)	42	76.7(4)	7.0235(1) 346.47(1) [19]	4.9848(3)	8.1516(9)	175.4(2)	23.3(2)	4.9662(1)
5 Hz	7.0289(4)	347.3(7)	49	100		–				8.0935(2)
16.5 Hz	7.0391(8)	348.8(1)	41	80.0(3)	7.0163(1)	4.9645(1)	8.1600(5)	174.2(2)	20.0(2)	172.9(1) [25]
33 Hz	7.0156(8)	345.3(1)	42	78.7(3)	345.40(1) [20]	4.9481(1)	8.1486(3)	172.8(1)	21.3(3)	

at higher solidification rates compared to the C15 phase. The crystallite size for the C14 phase significantly decreased from the initial 104 nm for the as-cast alloy to 21 nm for the melt-spun sample at 100 Hz. The smallest crystallite size sample produced at the highest rotation wheel speed resulted in the best electrochemical performance by allowing the shortest H atoms diffusion distances.

3.2. SEM/ EDS analysis

Microstructures of as-cast and melt-spun samples were studied using SEM in a back-scattered electron (BSE) mode and are presented in Fig. 2.

Changing the wheel rotation speed which proportionally changed the solidification rate, modified the phase-structural composition, morphology and microstructure of the alloys. The alloys contained 3 different phases including C15, C14, and La-rich phase. The grain size of each phase depends on a wheel rotation speed. With an increase in the wheel rotation speed, the grain size decreases. The as-cast sample contained a three-phase microstructure with the main C15 Laves type intermetallic having a grain size of approximately 3.5 μm. The grain size was slightly lower, 2 μm, for the secondary C14 intermetallic phase, while for the La-rich phase it got a size of 2.9 μm (see Fig. 2).

Applying rapid solidification yielded the following results:

(a) Refinement of the microstructures took place. When the higher rotation speeds are applied, a decrease in the grain size was observed. At a 5 Hz rotation speed the grain size of C15 phase dramatically drops from the initial 3.5 μm to just approximately 500 nm and further down to 300 nm at 33 Hz.
(b) An increase in the rotation speed causes formation of more homogeneous and refined microstructures. La-rich phase seen as white globular particles became smaller and more evenly distributed in the 5 Hz melt-spun sample as compared to the as-cast sample, with the grain size of approximately 375 nm. Formation of La-rich globular particles have also been reported for the similar alloy compositions in reference publications [36,37]. C14 intermetallic phase has a decreased grain size of 200 nm.
(c) At 16.5 Hz, smaller grain sizes of C15 phase, 300 nm, and C14 phase, 175 nm, were formed, and La-rich white globular structures with just 250 nm in grain size became more evenly and regularly distributed as compared to the 5 Hz melt-spun sample.
(d) The smallest grain size for the main C15 phase of 250 nm, 100 nm for the secondary C14 phase, and 70 nm of the La-rich phase appeared when applying 33 Hz rotation speed. The dendritic structures were formed by applying this casting speed. C15 phase forms more homogeneous structures [38] which create less nuclei sites required for the solidification. Because of that, a homogeneous nucleation is taking place. When the solidification rate increases, a supercooled liquid of C15 phase forms which then solidifies and produces dendritic microstructures [39].

Similar phenomena were also observed in rapidly solidified C14-predominated alloys [25]. Here also more uniform and refined microstructures were produced during the rapid solidification process. However, significant morphology variations of the melt-spun samples were found in C14 predominated alloys. Increased rate of rapid solidification caused formation of a dendritic microstructures at 16.5 Hz and at 33 Hz. In contrast, at the highest rotation speed of 100 Hz, the morphology becomes more uniform with a matrix C14 phase composing a core and a secondary C15 phase forming a shell. Furthermore, the dendrite structure was no longer observed.

This paper contains the Supplementary Materials data which includes 3 Figures (Figs. S1, S2, and S3) and 3 Tables (Tables S1, S2, and S3). The EDS/ SEM micrographs for as-cast, and rapidly

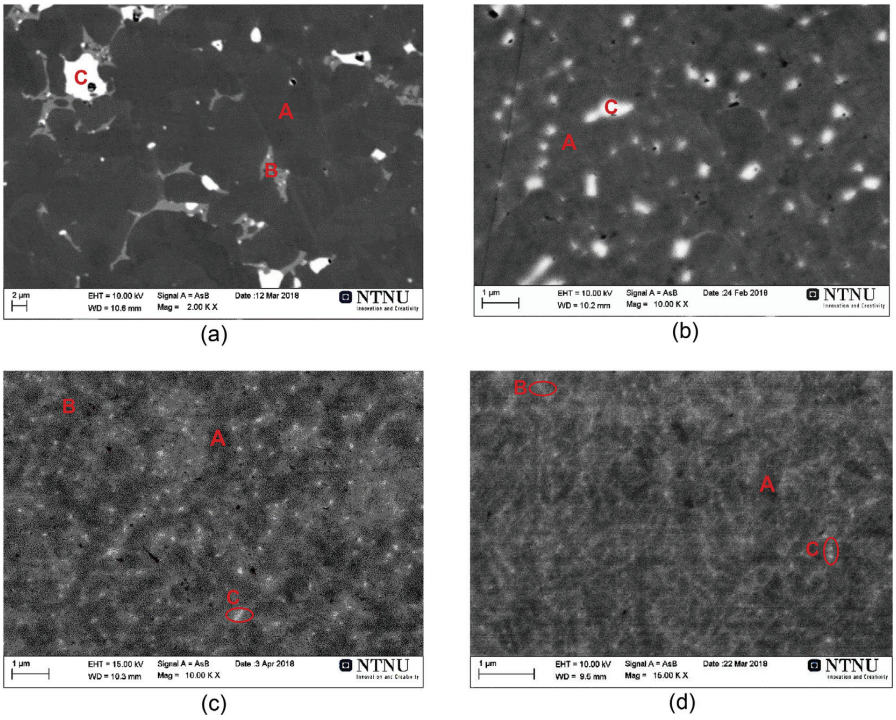

Fig. 2. SEM BSE images of as-cast (a) and melt-spun samples obtained at variable rotation speeds of 5 Hz (b), 16.5 Hz (c), 33 Hz (d). The sample contains 3 different phases, A: matrix phase (C15), B: secondary phase (C14), and C: La-rich phase. Decreasing grain size of matrix phase from 3.5 μm for the as-cast down to 250 nm achieved during the Rapid Solidification can be noticed.

solidified at 5, and 16.5 Hz samples are shown in Fig. S1, while the EDS analysis results for as-cast, 5, and 16.5 Hz melt-spun samples are given in Table S1. The darker area of EDS images (see Fig. S1) represents the matrix phase, while the lighter area (grey) shows the secondary phase, and the white globular area located on the secondary phase is La-rich phase.

33 Hz melt-spun sample has been characterized by Auger electron spectroscopy (AES) to determine the surface compositions by analyzing the electronic state energies of the constituent elements (see Fig. 3). The data showing the mapping of the elemental distribution is shown in Fig. 3. We conclude that La-rich phase formed as a secondary phase which dissolved another A-element, Zr, but also it contained less Ni as compared to the reference LaNi secondary intermetallic [19,20]. These changes affected the hydrogenation performance of the La-rich phase.

From the data presented in Tables S1 and S2 we can draw the following conclusions.

(a) The data of EDS and Auger spectroscopy measurements shows a very uniform homogeneous distribution of constituent elements in the studied samples. Indeed, only slight variations of elementary content were observed during the parallel measurements (see Table S1 and Table S2). Matrix phase contains Zr and Ti as A components, with almost no La present. The B component mixture is dominated by Ni and Mn, with a significantly smaller contributions from V and Fe (see Fig. S2). The matrix phase also contained oxygen, but its amount is reasonably modest. The compositional change for the matrix phase takes place during the Rapid Solidification, particularly for the Mn and Ni amount. A gradual decrease in the content of Mn is taking place from as-cast to 33 Hz sample (by appr. 32%) indicating that Mn is subjected to a profound evaporation during the rapid solidification process. Furthermore, the amount of Ni increases from as-cast to 33 Hz sample suggesting that enrichment by Ni takes place for the matrix phase because of a decay in Mn content.

(b) The La-rich secondary phase studied in Refs. [19,20] and acting as a catalyzer of the hydrogenation of the matrix phase was La-rich and contained a LaNi intermetallic. It appears that rapid solidification caused the change in the composition of this phase, and further to La and Ni, it also included Zr and Mn. This brings us to a conclusion that rapid solidification causes a significant solubility of Zr in the LaNi-based secondary phase which also dissolves Mn.

Furthermore, the secondary phase contains a significant amount of oxygen as its level is 3 times higher than O content in the matrix Laves phase. Because of a significant amount of zirconium and oxygen present, the secondary phase becomes unable to act as a catalyst of hydrogenation causing a very slow and difficult activation of the alloys. Probably the conditions of rapid solidifications need to be changed to benefit from an easy activation behavior of the LaNi intermetallic as observed in Refs. [19,20].

There are two reasons for the observed difficulties in the hydrogenation and in electrochemical charging performance of the anode electrode alloy.

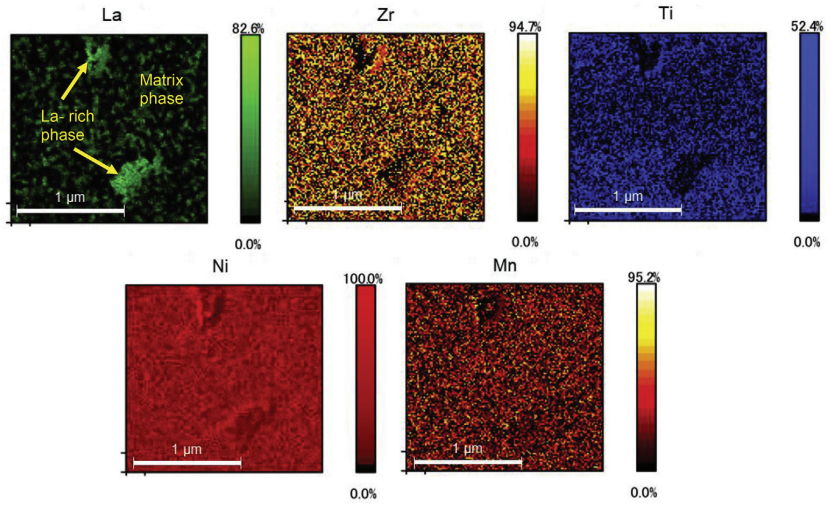

Fig. 3. The elemental mapping obtained by using the data of Auger analysis of the 33 Hz melt-spun sample shows presence of two phases – a matrix phase and a secondary La-rich phase, even though the XRD analysis of the sample confirmed presence of two Laves phases, C15 intermetallic (78.7%) and C14 phase (21.3%). However, because of a very similar chemical composition, these phases are indistinguishable in the Auger spectroscopy data. We also note a homogeneous distribution of Zr, Ti, Ni and Mn in the matric phase.

(a) During the solidification of the initial as cast alloy, LaNi intermetallic compound is formed which is known to actively form the hydride phase $LaNiH_{3.6}$. The annealing does not change the fact that the microstructure of the alloy shows presence of the Laves type intermetallic together with a secondary LaNi-based phase compound. However, during the rapid solidification the composition of the LaNi alloy becomes modified by a partial replacement of La by a smaller in size Zr. (La,Zr)Ni intermetallic has a lower affinity to hydrogen and is not able to quickly and actively form a hydride phase. Thus, a catalytic influence of (La,Zr)Ni intermetallic does not appear to be present anymore and thus activation performance worsens.

(b) Furthermore, as zirconium has a strong affinity to oxygen, as it easily oxidizes. Such oxidation is mostly limited to the surface layers because of the presence of trace amounts of oxygen in argon gas during the rapid solidification. The formation of the surface oxides creates a barrier for hydrogen atoms for their diffusion into the bulk and thus decreases the catalytic activity of the alloy to absorb hydrogen and to form a metal hydride.

Further to the elemental mapping using Auger analysis, by analyzing the areas occupied by the secondary phase (see Fig. 3 and Table S3), we conclude that the secondary phase is enriched with La and contains significant amounts of Zr. This is opposite to the situation in the as cast alloy where LaNi intermetallic is formed instead, with no Zr solubility observed.

3.3. Electrochemical measurements

The activation performances of as-cast and melt-spun alloys are presented in Fig. 4 (a). Metal hydride anodes were charged at a current density of 100 mA/g for 5 h followed by a 30 min rest and then discharged at a current density of 100 mA/g to a voltage cut–off of −0.7 V against the Hg/HgO reference electrode. After the anodes were fully activated, they were charged at a current density of 100 mA/g followed by a 30 min rest and discharged at different current densities (10–500 mA/g) to a voltage cut-off of −0.6 V against the Hg/HgO reference electrode.

It appeared that the melt-spun samples required a longer cycling to reach a complete activation as compared to the as-cast alloy. It is likely that rapid solidification process increased the content of oxides in the surface layer of the melt-spun samples and because of that they required a higher number of the charge-discharge cycles to remove the oxide barriers and to allow a fast charge-discharge process. In addition, a more increased Zr content in the secondary phase due to the rapid solidification process causes a worse activation performance. The secondary phase does not act any more as a catalyst capable of accelerating the hydrogenation of the matrix phase.

For the as-cast alloy its maximum capacity was achieved already in the fourth cycle, while for the 5 Hz sample 7 cycles were needed to activate it, and 33 Hz sample needed 6 cycles to get fully activated. The most difficult activation performance was observed for the 16.5 Hz sample. Even 11 cycles were not sufficient to activate the sample. However, the full activation capacity of this sample results in the same capacity as for the 5 Hz alloy, 306 mAh/g. We note that the activation capacity of the 5 Hz samples is 50% higher than for the 33 Hz, 306 mAh/g and 181 mAh/g, respectively. Higher activation capacity achieved for the 5 Hz sample could be due to the optimized microstructure of the sample that shows a significant refinement as compared to the other samples. To conclude, rapid solidification process improved the maximum discharge capacity of as-cast alloy which was limited to 273 mAh/g only (this is smaller than in our earlier publication due to the excess of Mn added to the presently studied alloy [19]), while a greater number of cycles was required to activate the alloys.

Fig. 7 (b) shows discharge capacity vs. discharge potentials for as-cast and melt-spun alloys measured at 100 mA/g current density. It can be noted that together with a larger discharge capacity, 5 and 16.5 Hz, melt-spun alloys also show longer and flatter plateau of discharge potentials which are located between −0.85 and −0.9 V indicating that these samples achieve more stable and better performance as compared to the other samples.

In the case of rapidly solidified C14 predominated alloys [16],

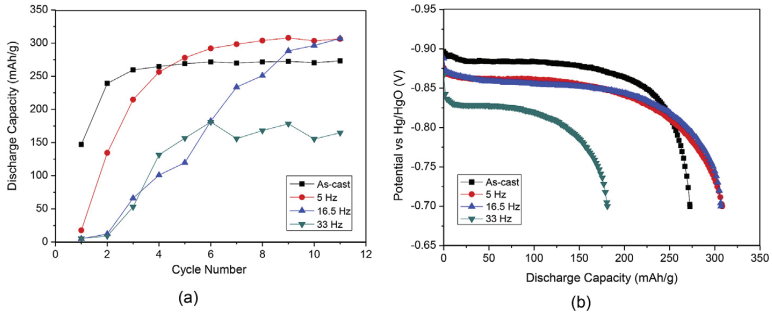

Fig. 4. Activation performance (a), discharge capacity vs potential (b), of the as-cast and melt-spun alloys at 100 mA/g discharge current density.

melt-spun alloys also showed a poorer activation performance as compared to the as-cast alloy. Indeed, more than 15 cycles were not enough to activate the as-cast alloy giving an indication that C14 predominated alloy is more difficult to activate than C15 alloy. Inferior activation performance of the samples obtained by rapid solidification process is likely to be caused by the presence of a thicker oxide layer on their surface.

Furthermore, by varying the wheel rotation speed, morphology of the microstructures significantly changes, thus affecting the electrochemical properties of the melt-spun samples. The best rate performance is achieved for a 16.5 Hz melt-spun sample which reached 414 mAh/g discharge capacity at 10 mA/g current density, followed by 5 Hz, as-cast, and 33 Hz samples (see Fig. 5 (b)). The discharge capacities vs. discharge potentials for 16.5 Hz sample measured at different current densities are shown in Fig. 5 (a). We note that an excellent rate performance was achieved for this sample at high current densities. Thus, the formation of the optimized refined microstructure results in the best rate performance.

For the HRD performance (the ratio between the capacities obtained at the highest current density of 450 mA/g to the lowest current density of 10 mA/g), 16.5 Hz sample shows the best HRD performance by showing the smallest decrease in the capacity at increasing current densities (see Fig. 5 (c)). At the same time, 33 Hz sample shows a rapid decrease in the capacity at a current density

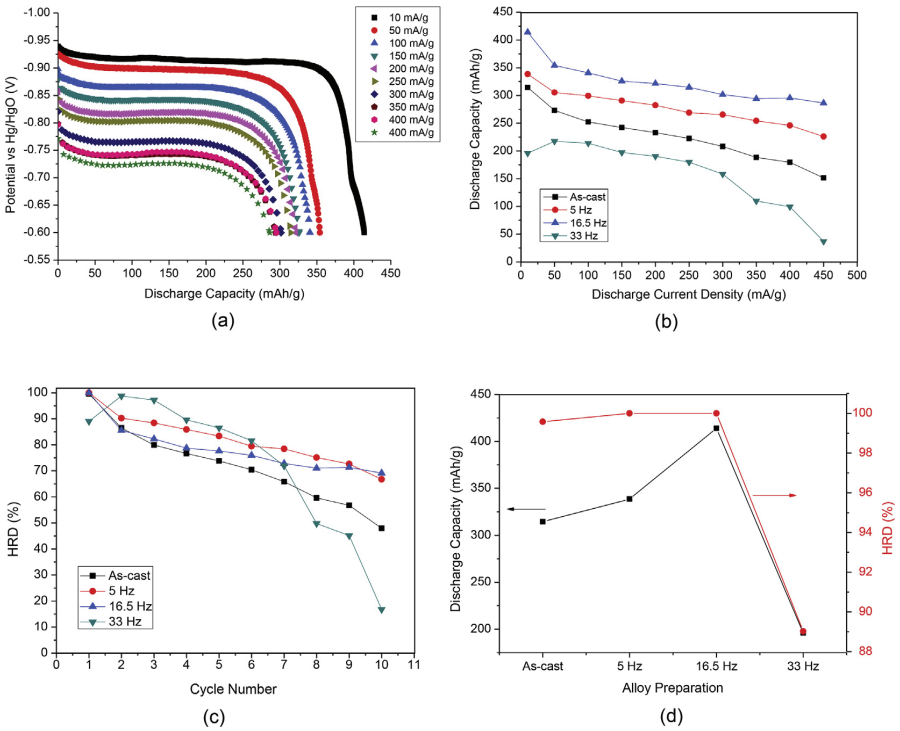

Fig. 5. The capacity of the melt-spun 16.5 Hz alloy electrode at variable discharge current densities and cut-off potentials (a); rate performance of the as-cast and melt-spun alloys (b); HRD performance (c); comparison of the performance of the samples as related to the conditions of alloys preparation (d).

exceeding 100 mA/g. After reaching a current density of 100 mA/g, capacity markedly dropped. The dendritic microstructure is considered as a reason for this decline in the performance.

Rapid solidification significantly changes the phase-structural composition of the alloys and because of that it affects the activation behavior and HRD performance. The C15 Laves phase predominant samples show a more developed pulverization and form more homogeneous microstructures with less C14 phase present in the melt-spun alloy which correlates with their better activation performance. On the other hand, the optimized microstructure which is formed by reaching an appropriate ratio between C15 and C14 phases benefits from a synergetic effect of C15 intermetallic with high hydrogen diffusivity and C14 intermetallic with H storage capacity resulting in improved rate performance of the metal hydride anode electrodes. Importantly, rapid solidification process proved to significantly refine the microstructure thus reducing the distances of hydrogen atoms diffusion and creating a faster hydrogen diffusion paths through the structure (see Fig. 5 (d)). We note that the improvement of the rate performance of the melt-spun alloys was achieved at 16.5 Hz melt-spun sample.

In the case of rapidly solidified C14-predominant alloy, it was observed that the rapid solidification improves the HRD performance of the melt-spun sample at the highest wheel rotation speed [16]. Thus, producing a homogeneous refined microstructure of the metal hydride anode materials with an optimized ratio C14/C15 which was achieved for the highest applied solidification rate will result in the best electrochemical performance. This is associated with the smallest crystallite sizes observed for such an alloy resulting in the fastest hydrogen diffusion in the material.

These studies showed that phase-structural composition and electrochemical performance of these alloys can be modified by selecting and optimizing conditions of rapid solidification, allowing to tailor their properties. As examples, (a) for A_2B_7 alloys melt spinning resulted in an increased abundance of the AB_5 phase acting as a catalyst activating the (La, Mg)$_2$Ni$_7$ phase [40]; (b) for La_2MgNi_9 alloy, appropriate conditions of its rapid solidification and adjustment of Mg content in the initial material resulted in increased content of La_2MgNi_9 with increase of the electrochemical capacity [41]; (c) Optimization of the rate of the wheel rotation speed allowed to reach maximum discharge capacity of 323 mAh/g for the Mm(NiCoMnAlV)$_5$ alloy [42]. However, in case of the AB_2 alloy, even though a maximum discharge capacity of 385 mAh/g was achieved for the melt-spun $Zr_{0.7}Ti_{0.3}Mn_{0.4}V_{0.4}Ni_{1.2}$ alloy electrode, however a large number - approximately 25 cycles - were needed to reach the maximum activation capacity [43]. Thus, activation of the melt-spun processed $Zr_{0.7}Ti_{0.3}Mn_{0.4}V_{0.4}Ni_{1.2}$ alloy required improvements – similar to the results of the present study for the $Ti_{0.15}Zr_{0.85}La_{0.03}V_{0.12}Mn_{0.7}Fe_{0.12}Ni_{1.2}$ alloy after the rapid solidification.

The $Ti_{0.15}Zr_{0.85}La_{0.03}V_{0.12}Mn_{0.7}Fe_{0.12}Ni_{1.2}$ alloy prepared in the current study using melt-spinning at 16.5 Hz wheel rotation speed showed a superior compared to the reference data discharge capacity of 414 mAh/g. The tailoring of the chemical composition achieved due to the rapid solidification led to the improved electrochemical performance of the electrode. However, increased amount of oxygen present in the alloy after the rapid solidification and introduction of Zr into the composition of La-rich phase caused difficulties in its activation. Therefore, controlling the content of oxygen and conditions of rapid solidification are the most important factors to achieve the improved electrode performance. Controlled addition La to the alloy is one of the alternatives to reduce the amount of oxygen as lanthanum is capable in refining the alloys from O thus making the surface of the alloy cleaner because of the reduced content of oxide at the surface. Furthermore, optimum conditions of rapid solidification need to be selected to achieve improved electrochemical behaviours of the metal hydride anode electrodes.

3.4. Electrochemical Impedance Spectroscopy (EIS) characterization

To determine the hydrogen diffusion coefficient in the studied materials, EIS studied were performed for the selected samples, including as-cast alloy, 16.5 Hz, and 33 Hz materials. The EIS data show a clear interrelation between the conditions of the rapid solidification and the hydrogen diffusion characteristics.

Two series of equivalent circuits were used to fit the Nyquist impedance plots (see Fig. 6). Constant Phase Elements (CPE) were used as pseudo-capacitance to describe the depressed semicircle shape of Nyquist impedance plot indicating the surface inhomogeneity/ surface roughness or other effects that possibly cause uneven current distributions at the electrode surface [23]. By using pseudo-capacitance CPE in the equivalent circuit, a much better fit of the EIS was achieved. Furthermore, in the present study, two parallel circuits were connected in series to achieve a more accurate modelling of the studied electrode. These models were successfully utilized to fit the experimental Nyquist impedance plots.

The equivalent circuit elements shown in Fig. 6 include R_{el} (electrolyte resistance), $R_{contact}$ (contact resistance between alloy particles and current collector), $R_{charge\ transfer}$ (charge transfer resistance on the interface between electrode and electrolyte), and Warburg element (capacitance of the electrode surface exhibiting the mass transport limitation related to hydrogen diffusion).

Nyquist impedance plots, the experimental and fitted ones, for the selected samples including as-cast, 16.5 Hz, and 33 Hz are shown in Fig. 7. It could be noted that the melt-spun alloys show significantly different EIS plots as compared to the as-cast sample. The data for the as-cast sample contains only one large semicircle, with a very small Warburg element in its low frequency region for all SOC, while EIS data for the 16.5 and 33 Hz samples show presence of two semicircles and a developed Warburg element at all SOC. To account for the insufficiently developed Warburg component for the as-cast sample, a parallel Randles circuit was used to fit the Nyquist impedance plot. For both melt-spun samples it was necessary to use 2 equivalent circuits connected in series and this allowed to achieve an appropriate fitting (Fig. 7).

The numerical fitting results of two main semicircles parts with one tail of Warburg element show quite a significant difference in properties. After applying the rapid solidification to the alloy, Warburg element becomes more pronounced while the Nyquist impedance plot becomes split showing a different shape, which indicates the changes of contact and charge transfer resistances. Furthermore, almost all the fitting parameters including CPE charge transfer, contact resistance of the alloy particle and current collector, and Warburg element decreased, indicating that the rapid solidification reduced the total resistance of the alloy electrodes (see Fig. 7 b and c). 16.5 Hz sample shows the smallest total resistance, while 33 Hz sample shows an opposite behavior. Thus, 16.5 Hz appears to be the optimized wheel rotation speed which

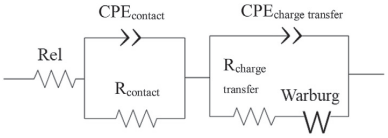

Fig. 6. Modified equivalent circuit which contains two parallel circuits, R-CPE and Randles circuits, to fit the Nyquist impedance plot.

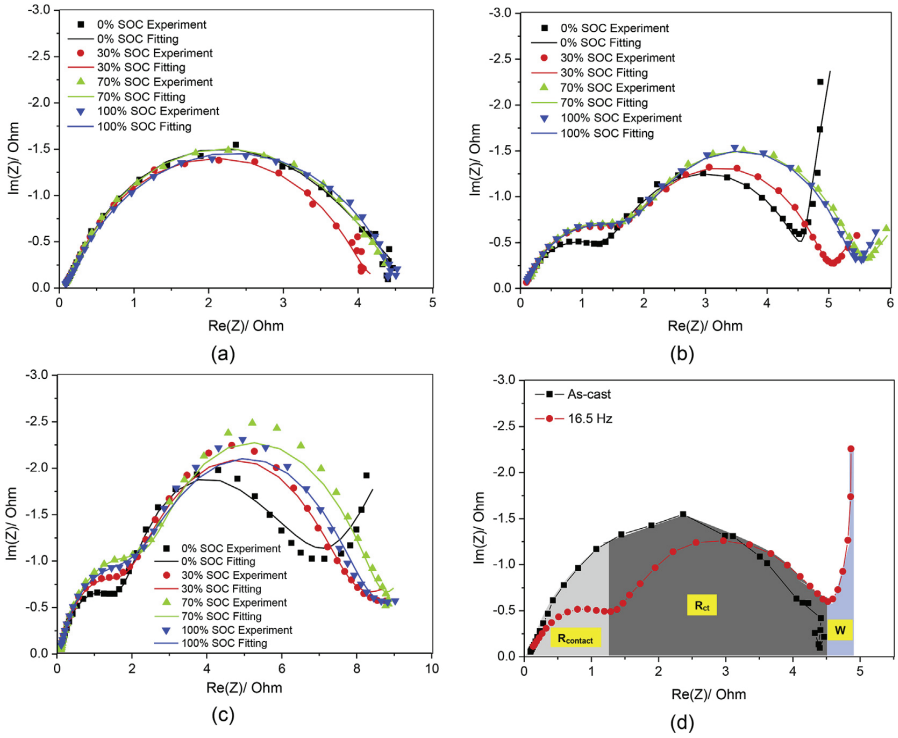

Fig. 7. Nyquist impedance plots, including the experimental and the fitted data for the 0, 30, 70, and 100% SOC electrodes measured for the as-cast (a), 16.5 Hz (b), and 33 Hz (c) alloys. Two modified equivalent circuits (see Fig. 6) were used to fit the EIS spectra. Split of one semicircle for as-cast sample into two semicircles for the melt-spun samples indicates a significant change in their electrochemical behavior (d). Rapid solidification enhances the contact resistance (R_{ct}) and Warburg element (W) of the samples.

produces the best discharge capacity by achieving the smallest total resistance and by having the highest hydrogen diffusion coefficient (see Table 2). The grain refinement which was caused by applying rapid solidification decreased the contact resistance between the refined alloy particles and the current collector. Indeed, the decreasing CPE for charge transfer in the melt-spun samples can originate from the improvement of the surface homogeneity of the alloy and the enlargement of the surface-active area of the alloy. However, charge transfer resistance of the as-cast is smaller than the values for the melt-spun samples. Interestingly, increasing of Rct for all SOC in the melt-spun samples gives a less pronounced effect on the hydrogen diffusion as compared to the decreased value of the Warburg element.

The diffusion coefficient of hydrogen appears to be significantly

Table 2
Fitted parameters of EIS spectra for the as-cast and melt-spun samples.

Parameters	0% SOC			30% SOC			70% SOC			100% SOC		
	As-cast	16.5 Hz	33 Hz	As-cast	16.5 Hz	33 Hz	As-cast	16.5 Hz	33 Hz	As-cast	16.5 Hz	33 Hz
$R_{electrolyte}$, Ohm	0.02504	0.09234	0.1164	0.01644	0.08047	0.09197	0.01678	0.08823	0.09024	0.0116	0.07254	0.09727
$CPE_{contact}$, $F.s^{\alpha-1}$	0.02303	0.03028	0.02002	0.02866	0.02766	0.02105	0.02769	0.02539	0.02276	0.03533	0.02893	0.02243
n_1	0.8618	0.7313	0.8139	0.808	0.7154	0.7762	0.7879	0.7407	0.7607	0.7491	0.706	0.7733
$R_{contact}$, Ohm	3.008	1.391	1.442	3.52	1.799	1.805	4.043	1.745	2.297	4.252	1.858	1.951
CPE_{ct}, $F.s^{\alpha-1}$	0.5512	0.4212	0.3034	1.622	0.2772	0.2235	2.749	0.2645	0.2193	3.893	0.3098	0.2144
n_2	0.1891	0.8854	0.7779	0.1186	0.8646	0.794	0.06414	0.8555	0.8133	0.046	0.872	0.773
R_{ct}, Ohm	0.05817	2.771	5.167	0.06902	3.01	5.558	0.08032	3.361	5.864	0.09654	3.019	5.924
σ, $Ohm.s^{1/2}$	3.628	0.07426	0.1017	3.379	0.02881	0.0982	3.192	0.02659	0.0908	2.869	0.02501	0.05906
Goodness of fit, χ^{2*}	0.2236	0.07066	0.4276	0.05787	0.02054	0.2197	0.01655	0.02072	0.5088	0.01626	0.02741	0.2029
D_H, $cm^2.s^{-1}$	8.21E-14	1.96E-10	1.05E-10	9.47E-14	1.30E-09	1.12E-10	1.06E-13	1.53E-09	1.31E-10	1.31E-13	1.73E-09	3.10E-10

$^*\chi^2 = \sum_{i=1}^{n} \frac{\left|Z_{means(i)} - Z_{model}(f_i, param)\right|^2}{SD_i^2}$.

where

Z_{meas} (i) = measured impedance at f_i frequency

Z_{model} (f_i, param) = function of chosen model

f_i = frequency

param = model parameters: $R_{electrolyte}$, $R_{contact}$, $CPE_{contact}$, CPE_{ct}

SD_i = standard deviation

affected by Warburg element as an inverse square of Warburg element is proportional to the H diffusion coefficient, according to a simplified equation of Fick's diffusion (see the experimental part). It appears that for the studied materials Warburg element becomes the most pronounced in the case of 0% SOC. The decrease of Warburg element indicates an increase in hydrogen diffusion coefficient, with 16.5 Hz having the larger reduction of Warburg element as compared to the 33 Hz alloy. Thus, 16.5 Hz alloy has the largest hydrogen diffusion coefficient among the studied materials.

In our earlier publication [25] we observed that the best electrochemical discharge for the alloy with the smallest size of the crystallites which was obtained at the highest wheel rotation speed. Similarly, the 16.5 Hz melt-spun sample showed the presence of the smallest crystallites and a larger unit cell volume among other studied materials thus allowing the fastest diffusion of H atoms with the largest hydrogen diffusion coefficient and the shortest H diffusion distances. The smallest crystallite size allowed to get the lowest contact resistance which was beneficial when SoC of the samples increased. Further to this, the optimized ratio between C15 and C14 phases contributed to assist the faster hydrogen diffusion in the multiphase alloy.

For all studied materials at 0% SOC the hydrogen diffusion coefficient appears to be significantly lower. By increasing SOC during a transformation from α-solid solution to the hydride phase, the hydrogen diffusion dramatically increases following an extent a transformation into the hydride ranging from 30 to 100% SOC (Fig. 8). Transforming the α-solid solution into the hydride phase changes intrinsic properties of the hydrogen-containing materials, with higher diffusion rates observed for the hydride thus leading to the increase of D.

4. Conclusions

- Rapid solidification of a Laves type C15 predominated $Ti_{0.15}Zr_{0.85}La_{0.03}V_{0.12}Mn_{0.7}Fe_{0.12}Ni_{1.2}$ alloy has been performed at 5, 16.5, and 33 Hz of wheel rotation speeds and resulted in changes which strongly affected alloys performance as anode materials of the Ni-MH battery, including
  (a) changes in a ratio between the main C15 and the secondary C14 phases;
  (b) a gradual decrease in the grain size from the initial 3.5 μm size down to 250 nm;
  (c) modification of the morphology of the microstructures;
  (d) changes in the discharge capacity, activation properties, and high rate discharge performance as related to the metallurgical and phase-structural state of the alloys.
- The melt-spun alloys show a more difficult activation performance as compared to the as-cast sample. These changes are associated with introduction of Zr into the composition of the secondary La-and Ni-rich phase during the melt casting at high speeds and rapid cooling/quenching of the alloy. Presence of Zr causes a worsening of the hydrogenation rates as compared to LaNi itself as in Refs. [19,20]. In present study, rapid solidification resulted in the formation of (La,Zr) (Ni,Mn) secondary phase appearing in the melt-spun samples while the La-rich intermetallic also contained a significant amount of oxygen. Thus, La-rich secondary phase was not acting as a catalyzer of hydrogenation anymore and because of that the activation performance significantly worsened. Optimization of the rapid solidification conditions is required to achieve a quick activation behavior of the Laves type metal hydride anode alloys.
- 16.5 Hz alloy provided the best rate performance because of an optimum two-phase microstructure containing C15 and C14 phases.
- Diffusion coefficient of hydrogen shows a close interrelation with SOC of the electrode and increases for all materials reaching the highest value for the completely charged electrodes with the smallest values observed for the completely discharged anodes.
- As the present alloy satisfies the high entropy alloys definition, the HEA concept may contribute to the design of new functional materials for battery anodes.

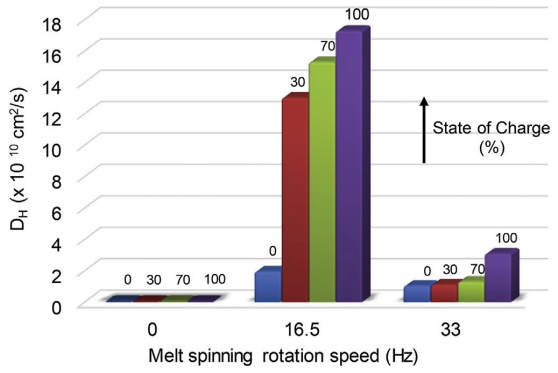

Fig. 8. Hydrogen diffusion coefficient (D_H) for as-cast and melt-spun alloys as related to SOC of the electrodes. The blue bars in the Figure show much smaller values of hydrogen diffusion coefficient observed at 0% SOC as compared to the coefficients at higher values of SOC with the highest values of D_H observed for the completely charged electrodes. (For interpretation of the references to colour in this figure legend, the reader is referred to the Web version of this article.)

Acknowledgements

This work was supported by Indonesia Endowment fund for Education (LPDP) and a PhD research project at Norwegian Research Center on Zero Emission Energy Systems for Transport (MoZEES). We thank CNRS Bordeaux and NTNU for the availability of the laboratory facilities for the rapid solidification process, and BASF-Ovonic Rochester Hills, USA for the access to their research laboratories.

Appendix A. Supplementary data

Supplementary data to this article can be found online at https://doi.org/10.1016/j.jallcom.2019.06.324.

References

[1] G.G. Libowitz, H.F. Hayes, T.R.P. Gibb, The system zirconium–nickel and hydrogen, J. Phys. Chem. 62 (1958) 76–79.
[2] T. Sakai, K. Oguro, H. Miyamura, N. Kuriyama, A. Kato, H. Ishikawa, C. Iwakura, Some factors affecting the cycle lives of $LaNi_5$-based alloy electrodes of hydrogen batteries, J. Less Common Met. 161 (1990) 193–202.
[3] J. Willems, K. Buschow, From permanent magnets to rechargeable hydride electrodes, J. Less Common Met. 129 (1987) 13–30.
[4] F. Feng, M. Geng, D.O. Northwood, Electrochemical behaviour of intermetallic-based metal hydrides used in Ni/metal hydride (MH) batteries: a review, Int. J. Hydrogen Energy 26 (2001) 725–734.
[5] B. Paxton, J. Newman, Modeling of nickel/metal hydride batteries, J. Electrochem. Soc. 144 (1997) 3818–3831.
[6] V. Yartys, D. Noreus, M. Latroche, Metal hydrides as negative electrode materials for Ni–MH batteries, Appl. Phys. A 122 (2016) 43.
[7] A. Anani, A. Visintin, K. Petrov, S. Srinivasan, J.J. Reilly, J.R. Johnson, R.B. Schwarz, P.B. Desch, Alloys for hydrogen storage in nickel/hydrogen and nickel/metal hydride batteries, J. Power Sources 47 (1994) 261–275.
[8] K.-H. Young, J. Nei, C. Wan, R. Denys, V. Yartys, Comparison of C14- and C15-predomiated AB_2 metal hydride alloys for electrochemical applications,

Batteries 3 (2017) 22.
[9] Y. Liu, H. Pan, M. Gao, Q. Wang, Advanced hydrogen storage alloys for Ni/MH rechargeable batteries, J. Mater. Chem. 21 (2011) 4743–4755.
[10] K.-H. Young, J.M. Koch, C. Wan, R.V. Denys, V.A. Yartys, Cell performance comparison between C14-and C15-predomiated AB_2 metal hydride alloys, Batteries 3 (2017) 29.
[11] K.-H. Young, S. Chang, X. Lin, C14 Laves phase metal hydride alloys for Ni/MH batteries applications, Batteries 3 (2017) 27.
[12] D.-M. Kim, K.-J. Jang, J.-Y. Lee, A review on the development of AB_2-type Zr-based Laves phase hydrogen storage alloys for Ni–MH rechargeable batteries in the Korea Advanced Institute of Science and Technology, J. Alloy. Comp. 293 (1999) 583–592.
[13] F. Cuevas, J.-M. Joubert, M. Latroche, A. Percheron-Guégan, Intermetallic compounds as negative electrodes of Ni/MH batteries, Appl. Phys. A 72 (2001) 225–238.
[14] Y. Zhang, J. Li, T. Zhang, H. Kou, R. Hu, X. Xue, Hydrogen storage properties of non-stoichiometric $Zr_{0.9}Ti_xV_2$ melt-spun ribbons, Energy 114 (2016) 1147–1154.
[15] K. Young, T. Ouchi, J. Yang, M.A. Fetcenko, Studies of off-stoichiometric AB_2 metal hydride alloy: Part 1. Structural characteristics, Int. J. Hydrogen Energy 36 (2011) 11137–11145.
[16] S. Gorsse, D.B. Miracle, O.N. Senkov, Mapping the world of complex concentrated alloys, Acta Mater. 135 (2017) 177–187.
[17] S. Gorsse, F. Tancret, Current and emerging practices of CALPHAD toward the development of high entropy alloys and complex concentrated alloys, J. Mater. Res. 33 (2018) 2899–2923.
[18] M.C. Gao, D.B. Miracle, D. Maurice, X. Yan, Y. Zhang, J.A. Hawk, High-entropy functional materials, J. Mater. Res. 33 (2018) 3138–3155.
[19] A.A. Volodin, R.V. Denys, C. Wan, I.D. Wijayanti, B.P. Tarasov, V.E. Antonov, V.A. Yartys, Study of hydrogen storage and electrochemical properties of AB_2-type $Ti_{0.15}Zr_{0.85}La_{0.03}Ni_{1.2}Mn_{0.7}V_{0.12}Fe_{0.12}$ alloy, J. Alloy. Comp. 793 (2019) 564–575.
[20] C. Wan, R. Denys, M. Lelis, D. Milčius, V. Yartys, Electrochemical studies and phase-structural characterization of a high-capacity La-doped AB_2 Laves type alloy and its hydride, J. Power Sources 418 (2019) 193–201.
[21] M. Fichtner, Properties of nanoscale metal hydrides, Nanotechnology 20 (2009) 204009.
[22] C. Liu, F. Li, L.-P. Ma, H.-M. Cheng, Advanced materials for energy storage, Adv. Mater. 22 (2010) E28–E62.
[23] S. Suwarno, J.K. Solberg, J.P. Maehlen, B. Krogh, B.T. BØRresen, E. Ochoa-Fernandez, E. Rytter, M. Williams, R. Denys, V.A. Yartys, Microstructure and hydrogen storage properties of as-cast and rapidly solidified Ti-rich Ti–V alloys, Trans. Nonferrous Metals Soc. China 22 (2012) 1831–1838.
[24] S. Suwarno, J.K. Solberg, V.A. Yartys, B. Krogh, Hydrogenation and microstructural study of melt-spun $Ti_{0.8}V_{0.2}$, J. Alloy. Comp. 509 (2011) S775–S778.
[25] I.D. Wijayanti, L. Mølmen, R.V. Denys, J. Nei, S. Gorsse, K. Young, M.N. Guzik, V. Yartys, The electrochemical performance of melt-spun C14-Laves type TiZr-based alloy, Int. J. Hydrogen Energy (2019). https://doi.org/10.1016/j.ijhydene.2019.02.093.
[26] S.K. Zhang, K.Y. Shu, Y.Q. Lei, G.L. Lü, Q.D. Wang, Effect of solidification rate on the phase structure and electrochemical properties of alloy $Zr_{0.7}Ti_{0.3}(MnVNi)_2$, J. Alloy. Comp. 352 (2003) 158–162.
[27] Y. Wu, M.V. Lototskyy, J.K. Solberg, V.A. Yartys, Effect of microstructure on the phase composition and hydrogen absorption-desorption behaviour of melt-spun Mg-20Ni-8Mm alloys, Int. J. Hydrogen Energy 37 (2012) 1495–1508.
[28] A.C. Larson, R. Von Dreele, General Structure Analysis System (GSAS)(Report LAUR 86-748), Los Alamos, New Mexico, Los Alamos National Laboratory, 2004.
[29] X. Yuan, N. Xu, Comparative study on electrochemical techniques for determination of hydrogen diffusion coefficients in metal hydride electrodes, J. Appl. Electrochem. 31 (2001) 1033–1039.
[30] X. Yuan, N. Xu, Determination of hydrogen diffusion coefficient in metal hydride electrode by modified Warburg impedance, J. Alloy. Comp. 329 (2001) 115–120.
[31] S. Malifarge, B. Delobel, C. Delacourt, Determination of tortuosity using impedance spectra analysis of symmetric cell, J. Electrochem. Soc. 164 (2017) E3329–E3334.
[32] P. De Vidts, J. Delgado, R.E. White, Mathematical modeling for the discharge of a metal hydride electrode, J. Electrochem. Soc. 142 (1995) 4006–4013.
[33] K. Young, T. Ouchi, J. Koch, M.A. Fetcenko, The role of Mn in C14 Laves phase multi-component alloys for NiMH battery application, J. Alloy. Comp. 477 (2009) 749–758.
[34] K. Shu, S. Zhang, Y. Lei, G. Lü, Q. Wang, Effect of Ti on the structure and electrochemical performance of Zr-based AB_2 alloys for nickel–metal rechargeable batteries, J. Alloy. Comp. 349 (2003) 237–241.
[35] F. Stein, M. Palm, G. Sauthoff, Structure and stability of Laves phases part II—structure type variations in binary and ternary systems, Intermetallics 13 (2005) 1056–1074.
[36] K. Young, D.F. Wong, T. Ouchi, B. Huang, B. Reichman, Effects of La-addition to the structure, hydrogen storage, and electrochemical properties of C14 metal hydride alloys, Electrochim. Acta 174 (2015) 815–825.
[37] K. Young, B. Chao, D. Pawlik, H. Shen, Transmission electron microscope studies in the surface oxide on the La-containing AB_2 metal hydride alloy, J. Alloy. Comp. 672 (2016) 356–365.
[38] S. Kanazawa, Y. Kaneno, H. Inoue, W.Y. Kim, T. Takasugi, Microstructures and defect structures in $ZrCr_2$ Laves phase based intermetallic compounds, Intermetallics 10 (2002) 783–792.
[39] Y. Liu, K.-H. Young, Microstructure investigation on metal hydride alloys by electron backscatter diffraction technique, Batteries 2 (2016) 26.
[40] W. Lv, Y. Wu, Effect of melt spinning on the structural and low temperature electrochemical characteristics of La-Mg-Ni based $La_{0.65}Ce_{0.1}Mg_{0.25}Ni_3Co_{0.5}$ hydrogen storage alloy, J. Alloy. Comp. 789 (2019) 547–557.
[41] C.C. Nwakwuo, T. Holm, R.V. Denys, W. Hu, J.P. Maehlen, J.K. Solberg, V.A. Yartys, Effect of magnesium content and quenching rate on the phase structure and composition of rapidly solidified La_2MgNi_9 metal hydride battery electrode alloy, J. Alloy. Comp. 555 (2013) 201–208.
[42] R. Li, J. Wu, H. Su, S. Zhou, Microstructure and electrochemical performance of vanadium-containing AB_5-type low-Co intermetallic hydrides, J. Alloy. Comp. 421 (2006) 258–267.
[43] S.K. Zhang, Q.D. Wang, Y.Q. Lei, G.L. Lü, L.X. Chen, F. Wu, The phase structure and electrochemical properties of the melt-spun alloy $Zr_{0.7}Ti_{0.3}Mn_{0.4}V_{0.4}Ni_{1.2}$, J. Alloy. Comp. 330 (2002) 855–860.

Supplementary Material

Studies of Zr-based C15 type metal hydride battery anode alloy prepared by rapid solidification

Ika Dewi Wijayanti[a,b,c], Live Mølmen[b], Roman V. Denys[a], Jean Nei[d], Stéphane Gorsse[e], Matylda N. Guzik[f], Kwo Young[d], Volodymyr Yartys[a,b]

[a] *Department of Battery Technology, Institute for Energy Technology (IFE), Kjeller, Norway*

[b] *Department of Materials Science and Engineering, NTNU, Trondheim, Norway*

[c] *Department of Mechanical Engineering, ITS, Surabaya, Indonesia*

[d] *BASF/Battery Materials-Ovonic, Rochester Hills, USA*

[e] *University of Bordeaux, CNRS, Bordeaux INP, ICMCB, UMR 5026, Pessac F-33600, France*

[f] *Department of Physics, University of Oslo, Blindern, Oslo, Norway*

Emails: Ika.Dewi.Wijayanti@ife.no; Volodymyr.Yartys@ife.no

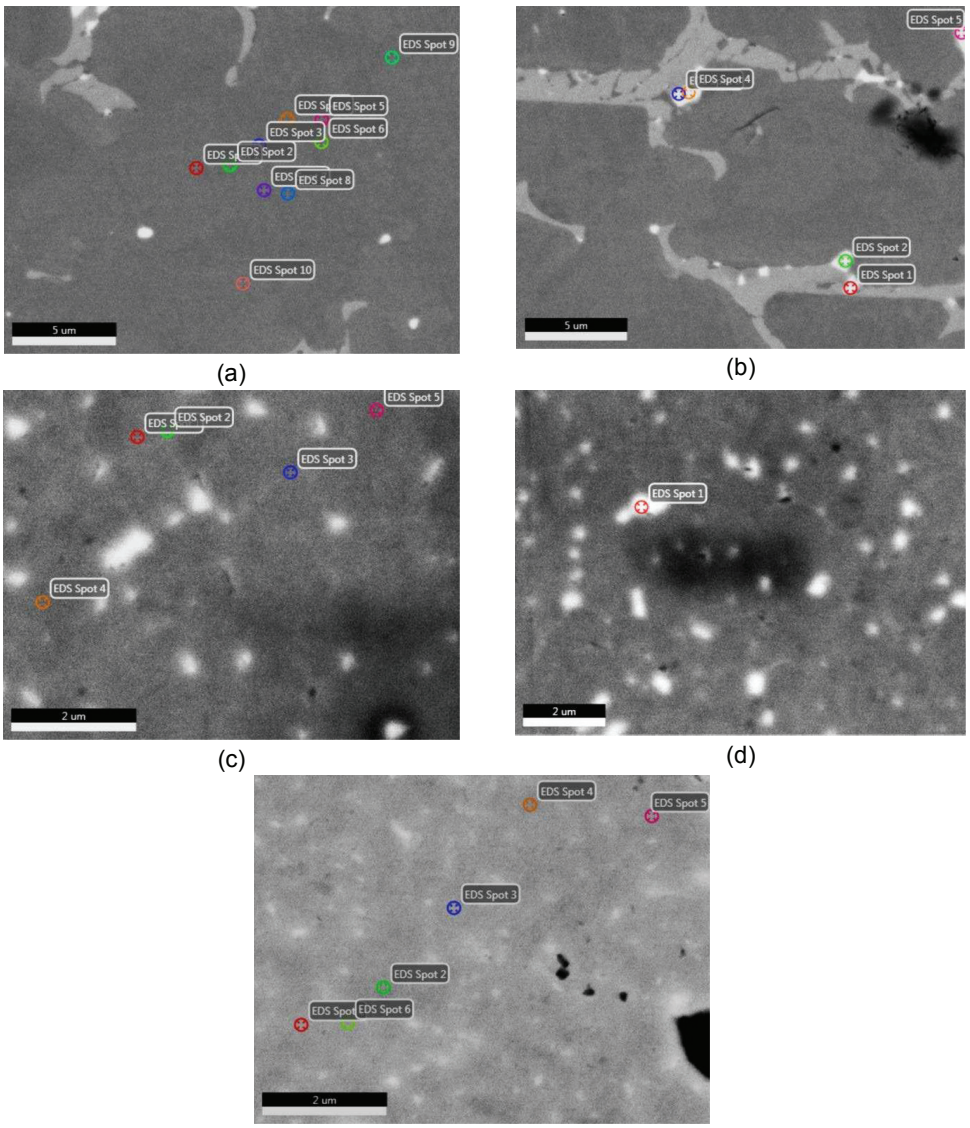

Fig. S1.

SEM images of the matrix phase (a) and secondary phase (b) in the as-cast sample; matrix phase (c) and secondary phase (d) in the 5 Hz melt-spun sample, and matrix phase (e) in the 16.5 Hz melt-spun sample. The compositions of both matrix and secondary phase regions for each sample were averaged from parallel measurements.

Table S1.

EDS statistically averaged compositions of as-cast, 5, and 16.5 Hz melt-spun samples

Sample	Region	Points measured	La	Ti	Zr	V	Mn	Fe	Ni
As-cast	Matrix	1	0.21	4.00	25.21	6.78	36.05	3.3	24.45
		2	0.31	3.94	25.39	6.70	35.84	3.3	24.53
		3	0.29	4.03	25.26	6.76	35.82	3.34	24.49
		4	0.33	4.01	25.29	6.67	35.66	3.27	24.78
		5	0.29	4.00	25.24	6.79	35.59	3.35	24.75
		6	0.28	3.84	25.29	6.67	35.47	3.34	25.11
		7	0.33	4.58	24.96	5.21	32.29	2.53	30.10
		8	0.22	4.59	25.07	5.11	31.55	2.44	31.01
		9	0.26	3.76	25.32	6.73	35.99	3.32	24.62
		10	0.27	4.66	25.16	4.74	31.65	2.37	31.14
		Average	0.27	4.14	25.2	6.21	34.59	3.05	26.49
	Secondary	1	61.95	2.29	7.05	1.09	4.76	1.83	21.04
		2	56.73	3.21	8.54	0.85	3.67	1.50	25.49
		4	62.74	2.64	7.46	0.77	4.32	2.69	19.38
		5	68.36	1.93	5.05	0.92	5.19	1.98	16.58
		Average	62.45	2.52	7.03	0.91	4.49	2.00	20.62
5 Hz	Matrix	1	0.67	4.83	24.84	4.29	28.41	2.03	34.93
		2	0.22	4.51	25.78	4.39	28.50	2.12	34.47
		3	0.71	5.12	25.23	4.01	26.76	1.8	36.37
		4	0.62	4.91	24.80	4.55	28.56	2.08	34.48
		5	0.33	4.85	25.32	4.11	28.23	1.93	35.23
		Average	0.51	4.85	25.19	4.27	28.09	1.99	35.10
16.5 Hz	Matrix	1	0.88	4.86	23.85	4.02	23.15	3.32	39.90
		2	2.30	4.71	23.35	3.58	22.62	3.16	40.28
		3	1.23	4.79	23.77	3.80	23.13	3.17	40.10
		4	1.58	4.65	23.22	4.17	24.31	3.35	38.70
		5	0.67	4.89	23.84	4.09	23.51	3.29	39.71
		6	0.87	4.85	23.94	4.03	23.24	3.21	39.88
		Average	1.26	4.79	23.66	3.95	23.33	3.25	39.76

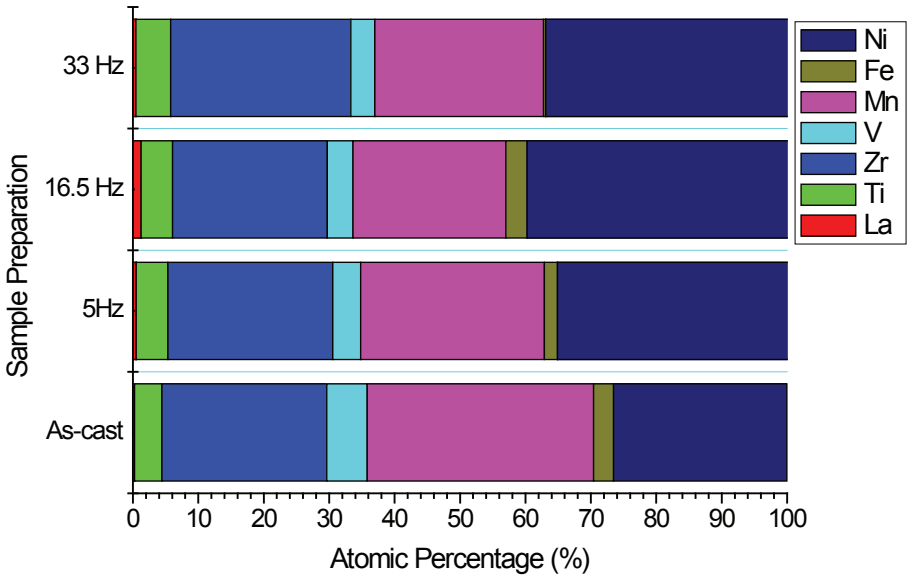

Fig. S2. EDS data for the chemical composition of the matrix phase in the as-cast, 5, 16.5, and 33 Hz alloys. Note that 33 Hz composition results was taken from Auger spectroscopy data with oxygen content not accounted.

Table S2.

Auger spectroscopy analysis data for the 33 Hz melt-spun sample

Region		La	Ti	Zr	V	Mn	Fe	Ni	O
Matrix phase	Average	0.46(1)	5.08(11)	26.35(4)	3.53(6)	24.71(17)	0.33(11)	35.31(14)	4.15(6)
	O is not accounted	0.48	5.30	27.51	3.69	25.80	0.34	36.87	-
Secondary	Average	48.23(10)	1.01(8)	9.34(7)	1.2(5)	10.7(2)	0.06(7)	15.61(1)	13.9(3)
	O is not accounted	56.00	1.17	10.85	1.39	12.39	0.07	18.13	-

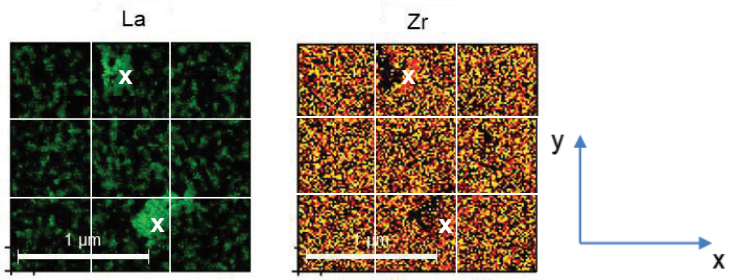

Fig. S3. Two points marked by white crosses showing increased content of La and Zr in the area of a secondary (La,Zr)(Ni,Mn) intermetallic phase. These have the same coordinates indicated in Table S3 thus confirming a solubility of Zr in the La-rich phase.

Table S3

The points of Auger elemental mapping belonging to the secondary (La,Zr)(Ni,Mn) phase

Components	Top		Bottom	
	x	y	x	y
La	0.85	1.5	1.175	0.35
Zr	0.85	1.5	1.175	0.35

PAPER IV

PAPER IV

Hydrides of Laves type Ti-Zr alloys with enhanced H storage capacity as advanced metal hydride battery anodes

I.D. Wijayanti, R.V. Denys, S. Suwarno, A.A. Volodin, M.V. Lototsky, M.N. Guzik, J. Nei, K. Young, Hans J. Roven, V. Yartys

Journal of Alloys and Compounds, 828 (2020) 154354.

Journal of Alloys and Compounds 828 (2020) 154354

Contents lists available at ScienceDirect

Journal of Alloys and Compounds

journal homepage: http://www.elsevier.com/locate/jalcom

Hydrides of Laves type Ti–Zr alloys with enhanced H storage capacity as advanced metal hydride battery anodes

Ika Dewi Wijayanti [a, b, c, **], Roman Denys [a], Suwarno [c], Alexey A. Volodin [d], M.V. Lototskyy [e], Matylda N. Guzik [f], Jean Nei [g], Kwo Young [g], Hans Jørgen Roven [b], Volodymyr Yartys [a, *]

[a] Institute for Energy Technology, Kjeller, Norway
[b] Norwegian University of Science and Technology, Trondheim, Norway
[c] Department of Mechanical Engineering, ITS, Surabaya, Indonesia
[d] Institute of Problems of Chemical Physics RAS, Chernogolovka, 142432, Russia
[e] University of the Western Cape, South Africa
[f] University of Oslo, Blindern, Oslo, Norway
[g] BASF/Battery Materials-Ovonic, Rochester Hills, USA

ARTICLE INFO

Article history:
Received 21 November 2019
Received in revised form
9 February 2020
Accepted 13 February 2020
Available online 15 February 2020

Keywords:
Metal hydrides battery anode
Hydrogen storage materials
AB_2 Laves type intermetallics
Hydrogen diffusion
EIS characterization

ABSTRACT

The present work was focused on the studies of the effect of variation of stoichiometric composition of Ti–Zr based $AB_{2\pm x}$ Laves phase alloys by changing the ratio between A (Ti + Zr) and B (Mn + V + Fe + Ni) components belonging to both hypo-stoichiometric ($AB_{1.90}$, $AB_{1.95}$) and over-stoichiometric ($AB_{2.08}$) alloys further to the stoichiometric $AB_{2.0}$ composition to optimize their hydrogen storage behaviours and performances as the alloy anodes of nickel metal hydride batteries.

$AB_{2-x}La_{0.03}$ Laves type alloys ($A = Ti_{0.15}Zr_{0.85}$; $B = Mn_{0.64-0.69}V_{0.11-0.119}Fe_{0.11-0.119}Ni_{1.097-1.184}$; x = 0, 0.05 and 0.1) were arc melted and then homogenized by annealing.

The studies involved probing of the phase-structural composition by X-Ray diffraction (XRD), together with studies of the microstructural state, hydrogen absorption–desorption and thermodynamic characteristics of gas–solid reactions and electrochemical charge-discharge performance, further to the impedance spectroscopy characterization. The alloys were probed using scanning electron microscopy (SEM), energy dispersive spectroscopy (EDS), and XRD.

These studies concluded that the alloys contained the main C15 FCC Laves type AB_2 intermetallic co-existing with a secondary C14 hexagonal Laves phase and a small amount of LaNi intermetallic. The gaseous H storage capacity and electrochemical performances were found to be closely dependent on the stoichiometric compositions of the alloys. High discharge capacities approaching 500 mAh/g were achieved for the $AB_{1.95}$ alloy. At 500 mA/g current density, the discharge capacity was maintained as high as 80%, with very low capacity retention after 500 cycles. The alloy which had the highest capacity retention after 500 cycles was found to be $AB_{2.0}$ alloy. Furthermore, $AB_{2.0}$ alloy showed an excellent cyclic stability together with a high hydrogen diffusion coefficient. Studies of hydrogen diffusion coefficients showed that annealing enhanced the H diffusion rates allowing advanced performance at high discharge current densities. This has been related to a higher content of C15 Laves compound which allows to reach a higher H mobility in contrast with higher storage capacity observed for the C14 Laves type polymorph.

1. Introduction

Nickel metal hydride (Ni-MH) batteries are considered as safe and robust batteries with low manufacturing costs, high energy efficiency and environmental friendliness [1–3]. Zr-based AB_2 Laves phase type hydrogen storage alloys are promising materials as negative electrodes in metal hydride batteries that show high

* Corresponding author.
** Corresponding author. Institute for Energy Technology, Kjeller, Norway.
E-mail addresses: Ika.Dewi.Wijayanti@ife.no (I.D. Wijayanti), Volodymyr.Yartys@ife.no (V. Yartys).

https://doi.org/10.1016/j.jallcom.2020.154354

storage capacities and a long cycle life [4]. On the other hand, these alloys are inferior in their activation performance, high-rate dischargeability (HRD), and cycle durability [5–7].

Laves type intermetallic compounds are used not only as anode electrodes of the metal hydride batteries but also form the largest group of hydrides used for the storage of hydrogen gas. Hexagonal C14 ($MgZn_2$ type) and cubic C15 ($MgCu_2$ type) are the most frequently used types of Laves phases which are suitable for the H storage and for the electrochemical applications. The electrochemical performance of the battery anodes when applied in the Ni-MH battery is closely related to the type of their crystal structure. C15 type alloys show an excellent HRD performance and are superior in this aspect as compared to the C14 type alloys [8,9]. However, further improvements should be achieved to advance the discharge capacity of the C15 type intermetallics, and optimization of the composition of the alloys is an important tool allowing to reach such a goal [10,11].

The stoichiometry plays an important role in designing multiphase C15 type AB_2 based alloys in order to achieve improved performance [12,13]. Variation of the stoichiometry in the C15 type AB_2 based alloys composition was found to have a very significant effect on the phase structural and electrochemical properties [14–16]. Hypo-stoichiometric Zr-based AB_{2-x} alloys with excess of the elements on the A-side and B/A ratio <2.0, were reported to show improved hydrogenation kinetics, higher hydrogen storage capacities, and lower plateau pressures than the stoichiometric and over-stoichiometric AB_{2+x} ones [17]. As an example, in Ref. [18] it has been shown that an excess of Mn in the composition of the $ZrMn_{2+x}$ alloy system with x = 0.6, 0.8, and 1.8 substantially reduced the stabilities of the hydrides and raised the equilibrium hydrogen pressures. This has been linked to the replacement of large Zr atoms (atomic radius 1.602 Å) by small Mn atoms (atomic radius 1.264 Å) in the lattice causing a significant decrease of the lattice parameters and "shrinking" of the unit cells.

Studies of the hydrogen storage capacity, equilibrium hydrogen pressure, and the stability of hydrides of the $Zr_{0.7}Ti_{0.3}MnFe$ alloy showed that they all significantly change as compared to the $Zr_{0.8}Ti_{0.2}MnFe$ alloy [19] having a higher Zr/Ti ratio. In particular, the replacement of Zr by Ti decreased the unit cell parameters which caused the reduction of the stability of the hydrides. The work [20] also showed that the hydrogen storage capacity gradually decreased when x > 1 in the $Zr_{0.9}Ti_{0.1}(Mn_{0.6}V_{0.2}Co_{0.1}Ni_{1.1})_x$ alloys. Furthermore, the increase of the stoichiometric ratio (x > 1) led to an increase of the equilibrium pressure (to the values exceeding 1 bar) creating the conditions when the reversible electrochemical capacity would be difficult to achieve. At the same time, two over-stoichiometric alloys showed a smaller hysteresis than the other alloys.

15 alloys with three different B/A element combinations with various ratios for 5 different $AB_{2\pm x}$ stoichiometries (1.8, 1.9, 2.0, 2.1, and 2.2) were studied in Ref. [21]. It has been found that the maximum capacities were obtained for the $AB_{1.9}$ alloys. For the alloys with over-stoichiometric composition (B/A > 2.0), the hydrogen storage capacities decreased.

Three hypo-stoichiometric alloys, including $Zr_{0.7}Ti_{0.3}(Mn_{0.2}V_{0.2}Cr_{0.15}Ni_{0.45})_{1.8}$, $Zr_{0.65}Ti_{0.35}(Mn_{0.3}V_{0.14}Cr_{0.11}Ni_{0.65})_{1.76}$, and $Zr(Mn_{0.2}V_{0.2}Ni_{0.6})_{1.6}$ alloys, were studied in Ref. [22]. Excellent hydrogen storage capacities were achieved, together with improved cycle life and higher electrochemical discharge capacities.

Our earlier publications related to the topic studied in the current work were focused on the effect of rapid solidification process of $Ti_{12}Zr_{21.5}V_{10}Cr_{7.5}Mn_{8.1}Co_8Ni_{32.2}Al_{0.4}Sn_{0.3}$ as C14 [23] and $Ti_{0.15}Zr_{0.85}La_{0.03}Ni_{1.2}Mn_{0.70}V_{0.12}Fe_{0.12}$ as C15 [24] predominated alloys aimed to improve the performance of the AB_2 based Laves type alloys as battery anode materials. After the rapid solidification both alloys achieved a significant improvement in their discharge capacities and rate performances. However, the activation performance of the alloys became inferior. The worsening of the activation performances occurred for the melt-spun alloys due to the formation of the thicker oxide layers and the changes in chemical composition of the LaNi-based secondary phase which was no longer acting as a catalyser to speed up the hydrogenation during the activation.

Annealing treatment was applied to the two C15 predominated alloys including $Ti_{0.15}Zr_{0.85}La_{0.03}Ni_{1.2}Mn_{0.7}V_{0.12}Fe_{0.12}$ [25] and $Ti_{0.2}Zr_{0.8}La_xNi_{1.2}Mn_{0.7}V_{0.12}Fe_{0.12}$ (x = 0.01–0.05) [26] and resulted in achieving excellent discharge capacity performance including high reversible storage capacity, together with easy activation, fast kinetics of charge, and low hysteresis observed in the isotherms of hydrogen absorption-desorption. Both alloys achieved high discharge capacities, 410 mAh/g and 420 mAh/g, respectively. 3 wt% of La was added to both alloys causing an easier activation and an increased capacity.

However, the improvements of the performance for the anode materials are still in need aimed to achieve higher discharge capacities and better rate performances.

In the present study, to satisfy the demands for developing the advanced Ni-MH battery with improved performance and enhanced hydrogen storage capacity, the alloys with the hypo-stoichiometric Laves type composition $AB_{2-x}La_{0.03}$ (A = $Ti_{0.15}Zr_{0.85}$; B=$Mn_{0.64-0.69}V_{0.11-0.119}Fe_{0.11-0.119}Ni_{1.097-1.184}$; x = 0, 0.05 and 0.1) were prepared by arc melting and annealing. Our goal was to study the effect of changing the ratio between A (Ti, Zr) and B (Mn, V, Fe, Ni) components in the annealed alloys including their phase-structural composition and microstructure, gaseous hydrogen absorption-desorption and electrochemical properties, together with Alternating Current (AC) impedance characterization to probe the rates of hydrogen diffusion in the alloys.

2. Experimental methods

Approximately 10 g alloys with the composition of $AB_{2-x}La_{0.03}$ (A = $Ti_{0.15}Zr_{0.85}$; B=$Mn_{0.64-0.69}V_{0.11-0.119}Fe_{0.11-0.119}Ni_{1.097-1.184}$; x = 0, 0.05 and 0.1) (see Table 1) were prepared by arc melting on a water-cooled copper hearth under argon atmosphere and re-melted three times to improve their homogeneity. The purity of each element constituent was not less than 99.7%. The variation of chemical composition of the alloys for the B components (transition metals) was intended at the preparation of the hypo-stoichiometric compositions $AB_{1.9}$, $AB_{1.95}$, and $AB_{2.0}$ (see Table 1). In order to compensate for the partial evaporation at high melting temperatures, 3 wt% of excess of Mn was added to the mixture of the components prepared for the arc melting preparation as compared to the aimed stoichiometric composition.

After the melting, the as-cast alloy ingots were sealed into stainless-steel tube sample holders filled with Ar and then transferred into an annealing furnace. These alloys were then annealed at 950 °C for 24 h and then quenched into cold water (4 °C) resulting in their homogenization.

Table 1
Chemical composition of the annealed alloys $AB_{2-x}La_{0.03}$ (in atoms/$AB_{2-x}La_{0.03}$).

Alloys	Ti	Zr	La	Ni	Mn	V	Fe	B/A
$AB_{1.9}$	0.15	0.85	0.03	1.097	0.64	0.11	0.11	1.90
$AB_{1.95}$	0.15	0.85	0.03	1.126	0.657	0.113	0.113	1.95
$AB_{2.0}$	0.15	0.85	0.03	1.155	0.674	0.116	0.116	2.0

The annealed alloys were characterized using the following techniques:

2.1. Structural characterization

XRD measurements were performed on the powders of less than 40 μm in size by using a monochromator-equipped Bruker D8 diffractometer (λ = 1.5418 Å ($CuK_{\alpha 1}$), step-size: 0.01975° 2θ, Bragg-Brentano geometry), with a 2 theta measurements range of 10°−120°. The experimental data was processed using Rietveld refinements and GSAS software [27]. A HITACHI FlexSEM 1000 VP-SEM equipped with EDS analysis was used to study the microstructures, distribution of phases, and the local composition of the phases in the samples.

2.2. Characterization of alloys interaction with hydrogen using alloy-H_2 gas and electrochemical techniques

The powdered samples, about 0.5−1 g in mass, were inserted into a stainless-steel sample cell placed into a thermostated autoclave and activated in vacuum at 250 °C for 30 min. The hydrogen absorption-desorption isotherms were measured at 20, 50 and 80 °C (293, 323 and 353 K), after a completion of the alloy's activation. Several hydrogen absorption-desorption cycles were performed before measuring equilibrium P−C-T diagrams.

The powders of 40−60 μm were mixed with carbonyl Ni powder in a weight ratio of 1:4, respectively. The mixture (appr. mass 500 mg) was then cold-pressed under a 12 MPa pressure to prepare the pellets with a diameter of 10 mm. The final step to make the anodes was to place the pellet in between two Ni foams and to prepare a compacted sandwich type electrode. Electrochemical performance was characterized using a CT 2001 Land Battery Tester and three-electrode system measurements.

2.3. EIS characterization

Electrochemical Impedance Spectroscopy (EIS) characterization was performed using SP-300-Potentiostat from Bio-Logic Science Instruments. Galvanostatic Electrochemical Impedance Spectroscopy (GEIS) technique was applied by performing the measurements at 0.1 kHz−0.5 mHz frequencies with the 10-mA current amplitude. Hydrogen diffusion coefficients in the electrodes were calculated using Fick's equation, for more details please consult our earlier publication [24].

2.4. Studies of the metal - hydrogen gas interactions

The experimental study of metal - hydrogen gas interaction was carried out using in-house made Sieverts-type installation, in the range of temperatures 20−80 °C at hydrogen pressures from 0.1 to 25 bar absolute. The accuracy of the measurements was ±0.02 bar for H_2 pressure and ±0.3 Ncm^3/g for the hydrogen concentration in the solid.

The PCT data was further processed by:

(a) Plotting experimental data in van't Hoff coordinates $Ln(P_{eq})$ versus 1/T to yield apparent values for the entropy (ΔS) and entropy (ΔH) changes during hydrogenation and dehydrogenation. The experimental values of the equilibrium pressures, P_{eq}, were taken for the plateau midpoint at hydrogen concentration, C_H, of 0.7 wt %, separately for H absorption and desorption.
(b) Fitting of the whole PCT datasets using a semi-empirical model of phase equilibria in the metal - hydrogen systems [30]. The fitting of the experimental data allowed to further refine the ΔS and ΔH values for the desorption (commonly considered as representing a "true" equilibrium), as well as to further analyze PCT diagrams to derive maximum H storage capacity, critical temperature, hysteresis energy loss, plateau slope (see Supplementary information for the details).

3. Results and discussion

3.1. Phase-structural characterization by XRD

Measured XRD patterns and Rietveld refinements of the XRD data for three studied alloys are shown in Fig. 1 and in a Supplementary Information file (Figure S1, a and b). The annealing improved the homogeneity of the alloys, as compared with the as cast alloys. The refinements showed that C15 phase is a predominant constituent (>95 wt %) in all studied annealed alloys. Further to the main cubic C15 phase the homogenized alloys also contained two secondary phases, a C14 Laves phase intermetallic and a LaNi intermetallic compound.

The crystallographic data and abundances of the phase constituents are listed in Table 2.

Refinements of the XRD data show that the experimental and calculated pattern well agree with each other. $AB_{1.95}$ alloy has the highest abundance of C15 phase (98.3 wt%), followed by $AB_{2.0}$ (97.2 wt%), and $AB_{1.9}$ (95.2 wt%). In turn, $AB_{1.9}$ alloy has the highest abundance of C14 phase (4.6 wt%), followed by $AB_{2.0}$ (2.7 wt%), and $AB_{1.95}$ (1.5 wt%). For LaNi phase, its abundance is small, 0.8 wt% in maximum for the $AB_{1.95}$ alloy. Nevertheless, despite of the small abundance, LaNi phase has an important role in the activation of the hydrogenation process by the alloys.

From Table 2 we conclude that:

(a) The XRD refined crystal structure data for the annealed alloys well agree with the results of our previous publications [25,26]. With increasing B/A stoichiometry in the alloys, the lattice constants and the unit cell volumes decrease. The atomic radii of the A site elements are normally larger than that for the B elements. With increasing B/A stoichiometry, the excessive elements in B site occupy A sites which causes shrinking of the unit cells [28].
(b) The alloy with higher content of Ti [26] shows the smallest unit cell volume of C15 phase as compared to the results of the present study and previous alloy with less content of Ti. The substitution of Zr atoms (1.602 Å) by Ti atoms which have the smaller radii (1.462 Å) caused shrinkage of unit cells [29].
(c) When changing the stoichiometry (from $AB_{1.9}$ to $AB_{2.08}$), the abundance of C15 phase increases and the abundance of the C14 phase decreases. Thus, increasing the B/A stoichiometric ratio causes a better homogeneity of the alloys.

3.2. Microstructural analysis

Microstructures of as-cast and annealed $AB_{1.95}$ alloys characterized using SEM in a back-scattered electron (BSE) mode and are presented in Fig. 2 as a typical example.

The microstructure of the as cast alloy shows presence of three phase constituents which based on the data of the XRD study were identified as a C15 type matrix phase (dark grey grains in Fig. 2a) and two minor in abundances phase constituents, including a light grain C14 phase formed in between the grain boundaries of the C15 intermetallic, and a white globular grains of the LaNi intermetallic.

Annealing of the alloy resulted in its homogenization

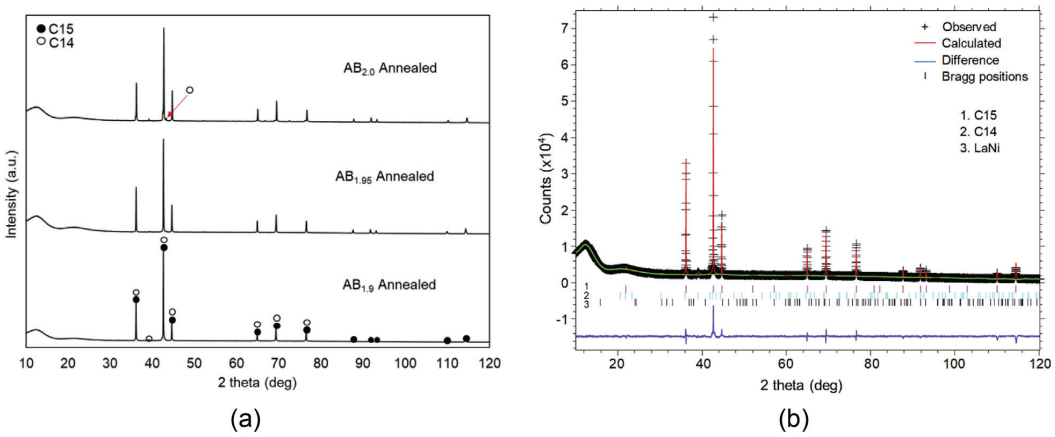

Fig. 1. XRD patterns (Cu-$K_{\alpha 1}$) for the studied alloys (a) and typical Rietveld refinement for the $AB_{1.9}$ annealed alloy shown as an example (b). Two Laves phase type intermetallics (C15 and C14) are present. Content of C15 phase exceeds 95 wt % for all studied alloys, see Table 1.

manifested by a decreased content of the C14 phase in the annealed alloy, as is clearly seen from a comparison of the micrographs shown in Fig. 2a–d. The annealing also results in a growth of the size of the LaNi grains as is clearly seen from a comparison of the Fig. 2a and c.

Table S1 shows that the annealing leading to the homogenization of the alloy does not change the overall stoichiometry of the alloy which remains very close to the composition of the as-cast alloy.

3.3. Hydrogenation properties of the $AB_{1.90}$, $AB_{1.95}$ and $AB_{2.0}$ alloys

After the activation by heating in vacuum for 30 min at 300 °C all studied $AB_{1.90}$, $AB_{1.95}$ and $AB_{2.0}$ alloys show a fast kinetics of hydrogen absorption and in just a few minutes form saturated hydrides when hydrogenated at hydrogen pressure of 20 bar H_2. After the synthesis of the saturated hydrides these hydrides of the AB_{2-x} alloys with stoichiometric B/A ratios of 1.90, 1.95 and 2.0 were used to study Pressure-Composition-Temperature (PCT) isotherms of hydrogen absorption and desorption. Studies of the PCT shown in Fig. 3 were performed at 20, 50, and 80 °C.

Increase in B/A leads to a decrease in the H storage capacity, from appr. 1.72–1.75 wt % H for $AB_{1.9}$ and $AB_{1.95}$ alloys to 1.55 wt% for the $AB_{2.0}$-based hydride. Increasing the temperature of the P–C measurements leads to the narrowing of the plateau range for of each of the studied alloys indicating increased homogeneity range for both α-solid solution and for the β-hydride phase. It is easy to note that the hysteresis between the hydrogen absorption and desorption plateau decreases with increasing temperature of the measurements and is the smallest at 80 °C. This indicates that the critical temperature of the studied metal-hydrogen systems should be slightly above 80 °C.

By using van't Hoff equation and PCT modelling approach [30], the thermodynamic parameters of the hydride formation-decomposition were obtained. These parameters for the AB_{2-x}-based hydrides are listed in Table 3. As can be seen from the Table 3, $AB_{1.9}$ alloy has the lowest ΔH and ΔS formation of 33.98 kJ/mol H_2 and 107.67 J/mol H_2 followed by the $AB_{1.95}$ and $AB_{2.0}$ alloys. The

Table 2
Crystallographic data and phase abundances for the annealed $AB_{2-x}La_{0.03}$ Laves type alloys from the Rietveld GSAS refinements.

Alloys	Phase	Space group	Unit cell parameters, Å				Abundance (wt.%)
			a	b	c	V, Å^3	
$AB_{1.9}$	C15	$Fd\bar{3}m$	7.0374(6)	–	–	348.532(1)	95.2(1)
	C14	$P6_3/mmc$	4.9969(1)	–	8.1817(5)	176.920 (1)	4.3(1)
	LaNi[a]	$Cmcm$	3.902(7)	10.78(2)	4.385(8)	184.449(6)	0.5(6)
$AB_{1.95}$	C15	$Fd\bar{3}m$	7.0338(6)	–	–	348.004(9)	98.3(4)
	C14	$P6_3/mmc$	4.9834(4)	–	8.1053(1)	174.325(2)	0.9(1)
	LaNi	$Cmcm$	3.902(7)	10.78(2)	4.385(8)	184.449(6)	0.8(5)
$AB_{2.0}$	C15	$Fd\bar{3}m$	7.0235(7)	–	–	346.468(1)	97.2(1)
	C14	$P6_3/mmc$	4.9941(3)	–	8.1533(8)	176.111(2)	2.7(7)
	LaNi	$Cmcm$	3.902(7)	10.78(2)	4.385(8)	184.449(6)	0.1(5)
Reference data for $Ti_{0.15}Zr_{0.85}La_{0.03}Ni_{1.2}Mn_{0.7}V_{0.12}Fe_{0.12}$ alloy [25]							
$AB_{2.08}$	C15	***$Fd\bar{3}m$***	7.0235(1)	–	–	346.466(1)	99.1(1)
	LaNi	$Cmcm$	3.902(7)	10.78(2)	4.385(8)	184.449(6)	0.9(1)
Reference data for $Ti_{0.2}Zr_{0.8}La_{0.03}Ni_{1.2}Mn_{0.7}V_{0.12}Fe_{0.12}$ alloy [26]							
$AB_{2.08}$	C15	***$Fd\bar{3}m$***	7.0163(1)	–	–	345.41(1)	100

[a] Rietveld refinements of LaNi phase were performed by using the reference data from Ref. [25].

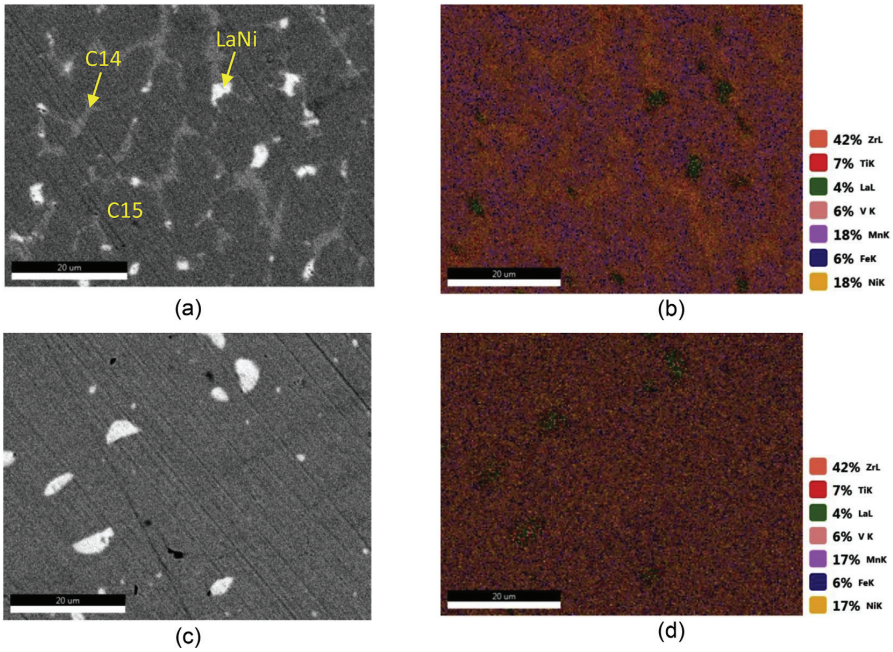

Fig. 2. SEM images of $AB_{1.95}$ as-cast (a) and its elemental mapping (b), annealed (c) and its elemental mapping (d). Different color on the images indicates different element composition. (For interpretation of the references to color in this figure legend, the reader is referred to the Web version of this article.)

data presented in Table 3 are in good agreement with our earlier publication on the properties of the hydride of the $AB_{2.08}$ alloy [25].

In addition to Table 3, we can see that the critical temperatures have rather low values, around 100 °C, with a trend of decrease in their values following an increase in B/A ratio and the lowest value of 366 K (93 °C) observed for $AB_{2.0}$ alloy.

3.4. PCT modelling results

The experimental PCT data (both H_2 absorption and desorption in one dataset) were fitted by the developed by the authors semi-empirical model [30] assuming that the metal hydride formed is described by a core model of van der Waals lattice gas with one plateau segment present at the Pressure-Composition isotherms.

All model parameters except of slope factors (fixed values were used) were refined. Refinement of the slope factors which has the range between 0 and 0.1 was required only in the cases when the isotherms showed a combination of flat plateaux and smooth transitions from the α- and β-solid solution regions into two-phase (α+β) region.

As can be seen from the results presented in Supplementary Material (Tables S3–S5), in all cases the fitting was reasonably good, with the goodness of fit R-factors below 0.15% for $AB_{2.0}$ and below 0.3% for the alloys with B/A < 2.0.

According to the modelling procedure [30], the accuracies of the refinements of the fitting parameters (values in brackets in Table 3; column "Error" in Table S4) were estimated as their variances which resulted in the increase of the total squared deviation of the experimental points from the calculated isotherms by 1%.

From Fig. 3 (f) and Tables S3–S5 we can conclude that enthalpy of formation remains practically unchanged, -(34–35) kJ/mol H_2 and is independent of the composition for the $AB_{1.90}$, $AB_{1.95}$ and $AB_{2.0}$ alloys. Thus, an obvious decrease in the stability of the hydrides manifested by a significant increase of equilibrium dissociation pressure, from 0.4 to 0.85 bar H_2, is caused by the changes in entropy of phase transformation, from −108 to − 118 J/(mol H_2 K).

All the alloys are characterized by rather low (below 366–386 K) critical temperatures of α–β transformation (T_C; minimum value was observed for the stoichiometric alloy) and low (below 1 kJ/mol) hysteresis energy losses (ΔG_h). At the same time (see Fig. 3 (g)), the increase of B/A from 1.9 to 2.0 results in a doubling of ΔG_h and a significant increase of hysteresis.

The pressure – composition isotherms for all the alloys were characterized by moderately sloping plateaux (distribution width parameter shows width of hydrogen absorption-desorption plateau, w~0.15 which is obtained by PCT modelling, see Tables S3–S5) but quite high contributions of Lorentz profile shows the shape profile of the plateau PCT, η (which is obtained by PCT modelling, in most cases, higher than 0.5, see Tables S3–S5) that indicates a low PCI curvatures in the transient regions between plateau and α- or β-solid solutions. As it was noted in Ref. [31], such a feature (sloping of $P(C)$ dependence at the initial and final stages of hydride formation/decomposition) is associated with stress effects accompanying the hydride phase formation.

3.5. Electrochemical characterization

The activation performances of studied alloys at 100 mA/g current density are shown in Fig. 4 (a). As mentioned earlier, the aim of adding Lanthanum was to improve the activation performance of the alloys. 3 wt% La is the optimized and effective amount resulting in the most efficient activation of the Zr based AB_2 alloys. This is in agreement with our earlier publications [25,26]. Indeed, the alloys studied our earlier publications which were activated in the fourth cycle with a maximum capacity of 370 mAh/g [25] and 360 mAh/g

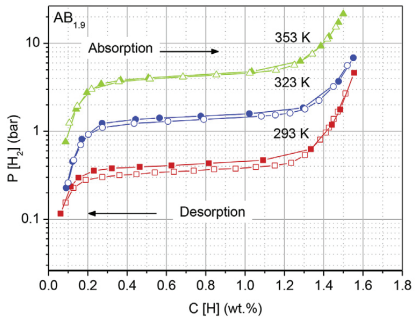
AB1.9
Absorption
353 K
323 K
293 K
Desorption
P [H2] (bar)
C [H] (wt.%)

(a)

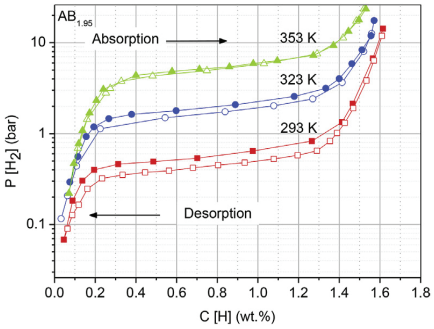
AB1.95
Absorption
353 K
323 K
293 K
Desorption
P [H2] (bar)
C [H] (wt.%)

(b)

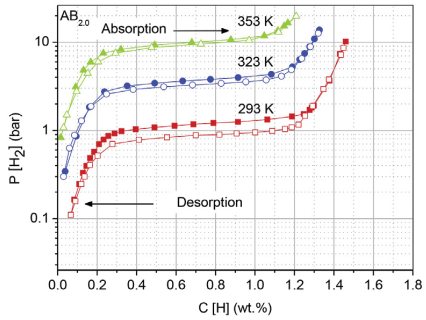
AB2.0
Absorption
353 K
323 K
293 K
Desorption
P [H2] (bar)
C [H] (wt.%)

(c)

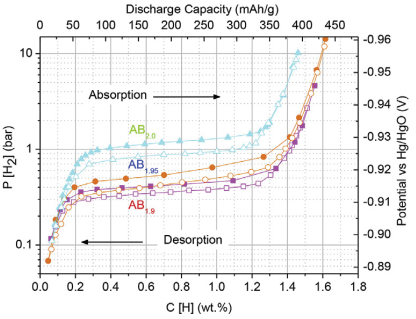
Discharge Capacity (mAh/g)
Absorption
AB2.0
AB1.95
AB1.9
Desorption
P [H2] (bar)
C [H] (wt.%)
Potential vs Hg/HgO (V)

(d)

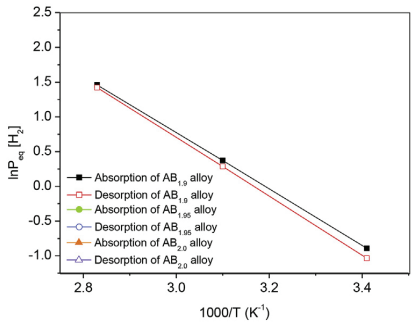
Absorption of AB1.9 alloy
Desorption of AB1.9 alloy
Absorption of AB1.95 alloy
Desorption of AB1.95 alloy
Absorption of AB2.0 alloy
Desorption of AB2.0 alloy
1000/T (K-1)

(e)

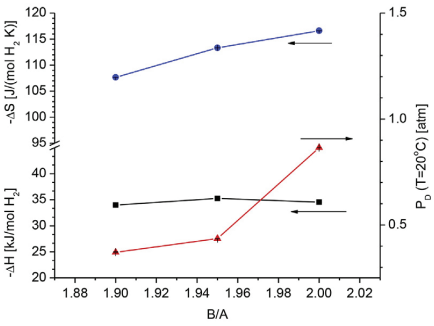
-ΔS [J/(mol H2 K)]
-ΔH [kJ/mol H2]
PD (T=20°C) [atm]
B/A

(f)

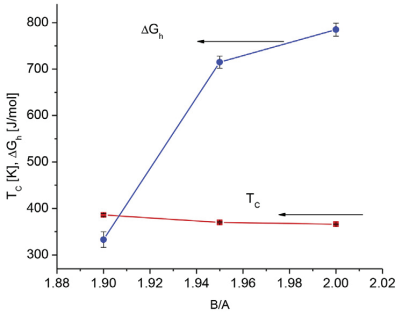
ΔGh
Tc
Tc, ΔGh [J/mol]
B/A

(g)

Table 3
Thermodynamic properties of AB_x hydrides (taken from the PCT modelling data).

Samples	Fitting parameters					Calculated H content (P = 100 bar, T = 298 K)	
	Plateau parameters (H_2 desorption)		Hysteresis energy loss	Critical temperature	Asymptotic H concentration		
	$-\Delta H$, kJ/mol H_2	$-\Delta S$, J/mol H_2 K	ΔG_{h_2}, J/mol H_2	T_C, K	C_{max}, Ncm^3/g wt.% H	C_H, Ncm^3/g wt.% H	C_H, mAh/g
$AB_{1.9}$ (annealed)	33.98(2)	107.67(1)	333(17)	386(3)	231.1(6) 2.077	192 1.725	462.3
$AB_{1.95}$ (annealed)	35.25(1)	113.33(3)	715(13)	370(1)	236(2) 2.121	195 1.753	469.8
$AB_{2.0}$ (annealed)	34.54(1)	116.61(1)	785(14)	366(1)	210.9(5) 1.896	173 1.555	416.8

[26], while the presently studied hypo-stoichiometric alloys became activated in the fifth cycle with maximum capacity of 390 mAh/g reached for the $AB_{1.95}$ alloy. $AB_{2.0}$ alloy shows a slightly lower activation capacity, 370 mAh/g.

Fig. 4 (b) presents discharge capacity of $AB_{1.90}$, $AB_{1.95}$, and $AB_{2.0}$ alloys performed at 100 mA/g current density. As can be seen, all studied alloys show close values of the plateaux of discharge potentials, which became longer, flatter, and were located between −0.875 and −0.915 V $AB_{1.95}$ shows the longest and flattest plateau of discharge potentials and the best performance among the studied alloys.

As shown in Fig. 4 (d), $AB_{1.95}$ alloy achieved the best HRD performance among the other alloys by showing the smallest decrease in the discharge capacity at increasing current densities (see Fig. 4 (c) and (e)).

HRD performance can be characterized as the ratio between the capacities shown at the highest current density of 500 mA/g as compared to the capacity at the lowest current density of 10 mA/g. The $AB_{1.9}$ alloy with the largest unit cell showed the best discharge capacity as shown in Fig. 4 (d).

Cyclic performance of the alloys studied at charge-discharge current density of 300 mA/g is shown in Fig. 4 (g). With increasing the number of cycles, we observe that the alloys show a decreased linear slope. Indeed $AB_{2.0}$ alloy shows the best capacity retention among other alloys, followed by $AB_{1.9}$, and $AB_{1.95}$ alloy. The better mechanical stability in $AB_{2.0}$ alloy causes its smaller surface area thus further pulverization can be hindered resulting in its better cyclic stability [20]. Further to this, the higher content of Ni in $AB_{2.0}$ contributed to lower a corrosion rate of the alloy which resulted in the best capacity retention during the cycling.

With changing the stoichiometry of the alloy to $AB_{2.08}$ [25,26], the capacity retention shows even higher values than that for the $AB_{2.0}$ stoichiometry alloy. This is caused by a decreased pulverization due to a better mechanical stability during the cycling of the hyper-stoichiometric alloys.

3.6. H storage capacity during studies of the metal-gas interactions vs. electrochemical performance

Even though hydrogen storage capacity of the metal hydride forming alloy should provide converging data, however differences normally are observed since PCT diagrams are measured in equilibrium conditions while electrochemical characteristics are obtained dynamically during discharge in the open cells. Thus, many features can diverge, including (a) H storage capacity; (b) slope of the PCT curves or slope of the capacity-voltage dependence; (c) hysteresis or overpotential; (d) homogeneity ranges for the α-solid solution and β-hydride phase.

Thus, it is interesting to compare the data of the metal-gas interactions vs. electrochemical performance as related to the chemical composition/ratio between B and A components in the $AB_{1.90}$, $AB_{1.95}$ and $AB_{2.0}$ alloys.

Fig. 5 and Fig. S3 show the gaseous H capacity vs. electrochemical capacity of the anode electrode for the studied $AB_{2.0}$ alloy. The data in Fig. S3 also show a similar comparison for $AB_{1.9}$ and $AB_{1.95}$ alloys. Gaseous capacity is smaller than the electrochemical capacity indicating that metal hydride reaches a deeper saturation during the electrochemical environment. Furthermore, we note that the plateau of gaseous H capacity in the PCT diagrams is shorter and flatter than in for the voltage plateau of electrochemical capacity plot. $AB_{1.9}$ alloy showed the best agreement between the experimentally measured gaseous and electrochemical capacities probably because it forms the most stable hydride ($P_{eq.}H_2$ is 0.3 bar @ 293 K) thus preventing uncontrollable loss of hydrogen gas because of the desorption from the anode electrode during the electrochemical experiments in an open cell.

The hysteresis of hydrogen absorption-desorption/overpotential for the electrochemical charge-discharge process for the studied alloys shows a clear trend with increasing B/A stoichiometric ratio. The smallest hysteresis was observed for the alloy with the lowest B content, $AB_{1.9}$. However, for the alloys with B content higher than 1.9 the hysteresis increases and becomes independent of the B/A ratio. This finding is in agreement with the results of our earlier publication [25] for the hyper-stoichiometric $AB_{2.08}$ alloy, which shows a similar hysteresis with the presently studied $AB_{1.95}$ and $AB_{2.0}$ alloys.

Furthermore, the changes in the plateaux of electrode potentials show similar trends as variations of ΔG for the studied hydrides. Indeed, the changes in discharge potential, −0.9385 V for $AB_{1.9}$, −0.9505 V for $AB_{1.95}$, and −0.9652 V for $AB_{2.0}$ (middle points of the plateaux in each case), correlate with the changes in ΔG, $AB_{1.9}$: 333; $AB_{1.95}$: 715: $AB_{2.0}$: 785 J/(mol H_2) showing an interrelation between the values of the overpotential and hysteresis following an increase in the B/A ratio.

When comparing interrelation between the gaseous and electrochemical H storage capacity, one should account that the open-to-air configuration might cause loss of hydrogen from the formed hydride during the electrochemical process leading to the smaller H content in the studied metal hydride. On the other hand, it is well known that electrochemical charging can cause an opposite

Fig. 3. PCT isotherms of hydrogen absorption and desorption for $AB_{1.9}$ (a), $AB_{1.95}$ (b), $AB_{2.0}$ (c) alloys, gaseous H_2 vs. electrochemical capacity of the studied alloys at 293 K (d), van't Hoff plots showing dependence of equilibrium pressure (ln P_{eq}) of hydrogen absorption and desorption based on the PCT diagrams measured at 293, 323 and 353 K from 1/T, (e), dependencies of changes in hydrogenation entropy and enthalpy (left Y-axes) and desorption plateau pressures at T = 20 °C (right Y-axis) (f), and dependencies of hysteresis energy loss and critical temperature of α−β transformation on the stoichiometry of the $AB_{2-x}La_{0.03}$ alloys (g). The plateau pressure for absorption is shown by filled symbols while open symbols are used for the desorption in each data set.

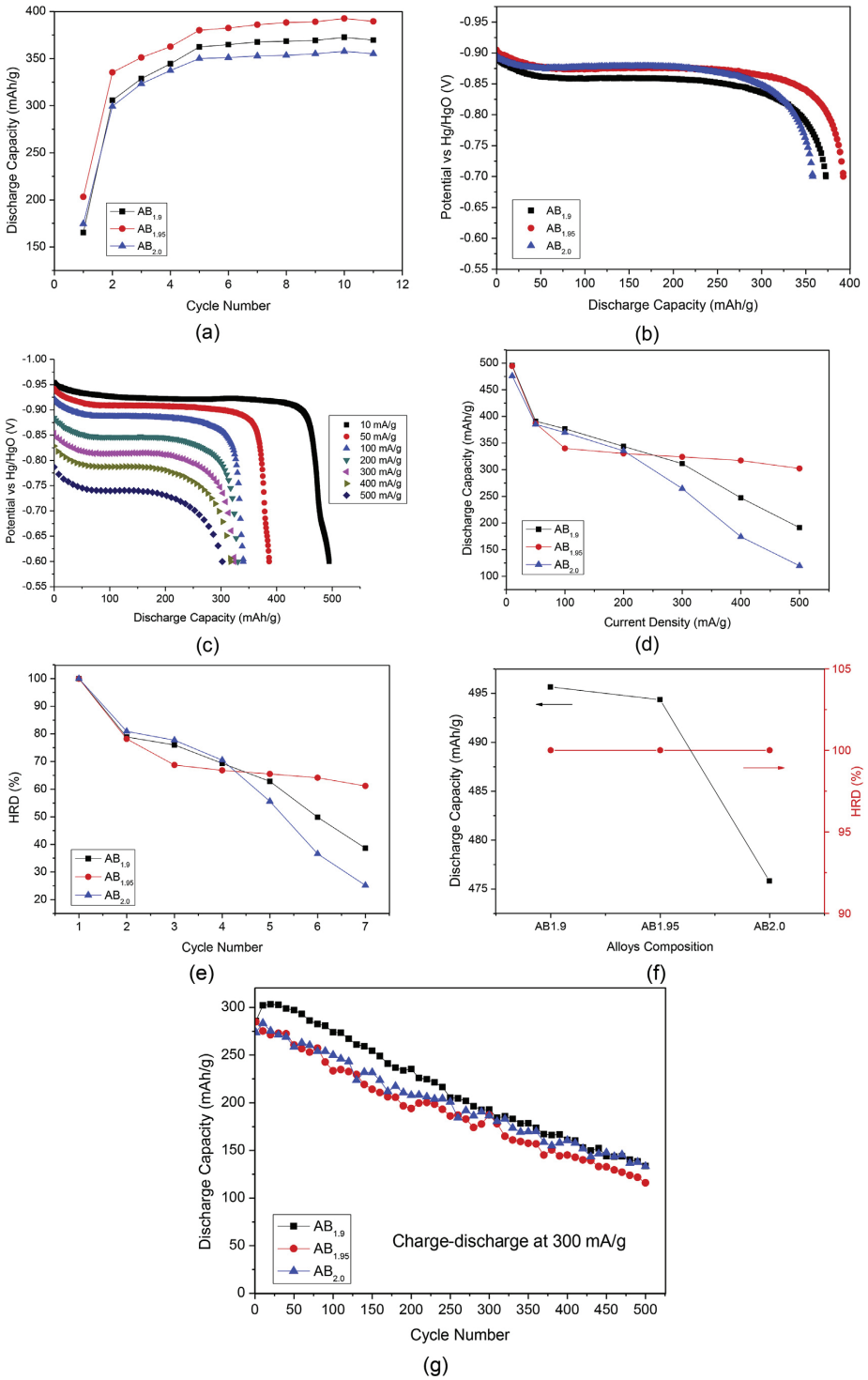
Discharge Capacity (mAh/g)
Cycle Number
AB1.9
AB1.95
AB2.0
(a)
Potential vs Hg/HgO (V)
Discharge Capacity (mAh/g)
(b)
10 mA/g
50 mA/g
100 mA/g
200 mA/g
300 mA/g
400 mA/g
500 mA/g
(c)
Current Density (mA/g)
(d)
HRD (%)
(e)
AB1.9
AB1.95
AB2.0
Alloys Composition
(f)
Charge-discharge at 300 mA/g
(g)

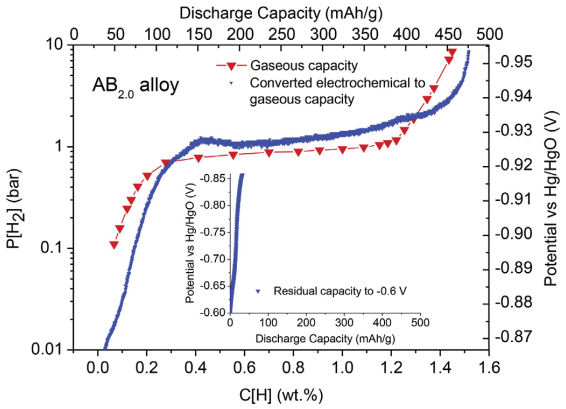

Fig. 5. Gaseous capacity vs. electrochemical capacity for $AB_{2.0}$ alloy. The inserts of the graphs show the tails of the curves measured from −0.85 to −0.6 V (cut-off voltage applied during the measurements of the discharge electrochemical capacity).

behaviour when electrochemical charging allows even at ambient conditions using a promotor of the hydrogenation to synthesize hydrides requiring application of high pressures of hydrogen gas (example: Ni hydride NiH which has been synthesized electrochemically [32] while in the nickel-hydrogen system equilibrium pressure of hydrogen desorption was measured as being around 4 kBar H_2 at room temperature [33]. Thus, measurements in the close electrochemical cells allowing to control H_2 pressure and to use overpressures could be valuable in the future work.

3.7. EIS studies

EIS characterization was performed for the studied alloys to assess characteristics of hydrogen diffusion. 50% State of Charge (SoC) samples were used to measure the EIS spectra after performing different number of cycles, 10, 100, 200, 300, 400, and 500.

EIS spectra of the studied alloy electrodes at 50% SoC and different number of performed cycles are shown at Fig. S4. We note that all the alloys show an unusual depressed semicircles shape of EIS spectra. Such a behaviour was also observed in our earlier study [25], were we used an equivalent circuit containing the Constant Phase Element (CPE) instead of a commonly used capacitance. Surface inhomogeneity/surface roughness is expected to cause such an uncommon shape of the EIS spectra. Therefore, in order to achieve a better fit of the EIS data, CPE was used to replace capacitance to properly describe the depressed semicircle shape of Nyquist plot. In addition to the equivalent circuit, a series of modified Randles circuits with added CPE and parallel circuit elements consisting of R and CPE was applied to fit the EIS spectra to achieve more accurate fitting results (Fig. 6 (a)).

As shown in Fig. S4, the alloys show a similar shape of the EIS spectra for the cycled sample by containing a Warburg element in the low frequency region related to the hydrogen transport in the studied alloys. It appears that the slope and the length of Warburg elements are different for each measurement. For longer cycled samples, the contact resistances, charge transfer resistances, and Warburg elements were all decreased, showing that the cycling performance generally results in a better hydrogen transport in the

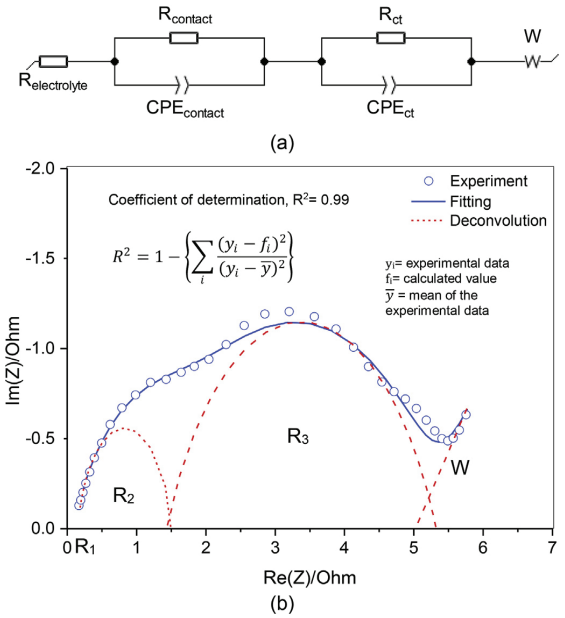

Fig. 6. Modified equivalent circuit used to fit the EIS experimental data (a), and deconvolution of Nyquist impedance plot for 50% SoC of $AB_{1.9}$ annealed alloy achieved by using a superposition of equivalent circuits, where $R_1 = R_{electrolyte}$, $R_2 = R_{contact}$, $R_3 = R_{ct}$, and W = Warburg element (b). Successful deconvolution result was shown by the coefficient of determination (R^2) value of 0.99, or close to 1.

electrodes.

The EIS spectra resulted from the measurements were fitted by using the modified equivalent circuit shown in Fig. 6 (a) - to determine the values of parameters in equivalent circuit. Further to the fitting, the deconvolution has also been done by configuring and by superimposing two semicircles and a straight-line dependence to represent the equivalent circuit model. The EIS parameters values resulting from the deconvolution (see Fig. 6 (b)) were then compared with the results from the fitting. 8 different parameters describing the physical properties of the studied alloy electrodes were obtained by the fitting, including $R_{electrolyte}$, $R_{contact}$, $CPE_{contact}$, n_1, $R_{charge\ transfer}$, $CPE_{charge\ transfer}$, n_2, and σ. The values of these parameters for the studied alloys as related to the number of the applied cycles are shown in Tables S6–S12. Further to these results, in order to determine the quality of the fit and deconvolution, the Goodness of fit (χ^2) and Coefficient of determination (R^2) values were used. As the values for χ^2 obtained from the EIS spectra fitting were less than 0.9, this indicated that the applied equivalent circuit model produces an excellent fitting. Thus, suggested deconvolution resulted in the excellent agreement with experimental data as R^2 values were close to 1.

To summarize, the EIS spectra for each studied alloy at 50% SoC and subjected to a different number of cycles were shown in Fig. S4. After the activation, all alloys show a larger total resistance, while after 500 cycles the results show that the total resistance decreased. We also can see that the length and the angle of Warburg impedance decreased during the cycling which means the that the

Fig. 4. Activation performance (a); discharge capacity (b) for the studied alloys at 100 mA/g current density; the capacity of the studied alloys at variable discharge current densities and cut-off potentials (c); rate performance (d); HRD performances (e); comparison of the performance of the studied samples as related to composition of the studied alloys (f); cycling performances of studied alloys measured at 300 mA/g with the capacity retention of $AB_{1.9}$ = 46.7%, $AB_{1.95}$ = 40.7%, and $AB_{2.0}$ = 48.7% (g).

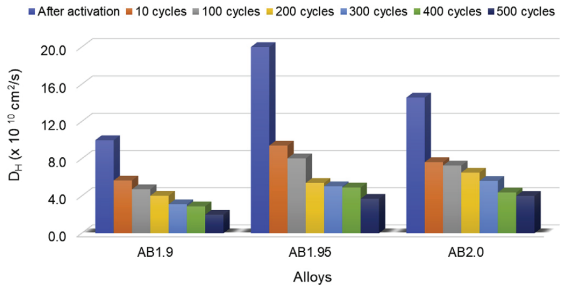

Fig. 7. Hydrogen diffusion coefficient (D_H) for the studied alloys as related to the cycles number at 50% SoC. The smallest decrease of hydrogen diffusion coefficient vs. cycle number is observed for $AB_{2.0}$ alloy.

hydrogen diffusion was significantly facilitated by the cycling. Probably this can be associated with a gradual cracking of the alloy powder particles resulting in a faster charge and discharge of the smaller particles.

We observe that the contact resistance of the studied alloy electrodes decreased with repeated cycling indicating that corrosion of the alloys surface has not been extensive and did not produce the oxide/hydroxide layer on the surface, while the reduction of the resistance could be related to a gradual decrease of the particle size during expansion and contraction followed by the cracking taking place during the cycling of hydrogen uptake and release.

Fig. 7 shows the hydrogen diffusion coefficient (D_H) for the studied alloys as related to the number of applied cycles for the electrodes with 50% SoC. We observed a large difference between the hydrogen diffusion coefficient value after activation and during the cycling. After activation, $AB_{1.95}$ shows the largest hydrogen diffusion coefficient which is almost 2×10^{-9} cm^2/s, followed by $AB_{2.0}$ 1.5×10^{-9} cm^2/s and $AB_{1.9}$ alloys 1.0×10^{-9} cm^2/s. Furthermore, we note that stoichiometric $AB_{2.0}$ alloy shows an excellent cyclic stability and shows a fast H diffusion even after 500 cycles (see Fig. 7).

4. Discussion

PCT isotherms of hydrogen absorption and desorption for all studied alloys were measured at 20, 50, and 80 °C. These isotherms are presented in Fig. 3 and show that they all form stable at ambient conditions hydrides with dissociation pressures 0.4–0.8 bar H_2. Increasing B/A results in a gradual decrease in the H storage capacity. Fitting of the PCT data for the studied alloys shows that for the hypo-stoichiometric alloys their H storage capacity is around 2.1 wt % H, while the capacity drops to 1.9 wt% H for the hydride formed by a stoichiometric $AB_{2.00}$ alloy. Indeed, $AB_{1.95}$ alloy has the highest capacity among other alloys with the similar Zr-based AB_2 Laves phase alloys, which are $Zr_{0.9}Ti_{0.1}V_{1.9}$ alloy with the capacity 1.1 wt% of hydrogen [17], $ZrMn_{2.8}$ and $ZrMn_{3.8}$ alloys with the capacity 1.44 and 1.14 wt% of hydrogen respectively [18], and $AB_{1.9}$ produced by Young with having capacity of 1.4 wt% of hydrogen [21]. This concludes that the studied alloy shows an excellent hydrogen storage capacity.

Increasing temperature leads to a narrowing down the plateaux indicating that the H capacity is the highest at room temperature. Interestingly, the hysteresis at higher temperatures becomes smaller confirming that the loss in the efficiency of the material due to its deformation during absorption-desorption of hydrogen becomes less pronounced at higher temperatures. In addition to this, plateaux become narrower, and equilibrium pressures increase (see Fig. 3 (d)). It appears that the hysteresis in the alloy hydrides shows an opposite trend with increasing stoichiometry. The smallest hysteresis was observed for the alloy with the lowest B/A stoichiometry, $AB_{1.9}$. However, the alloys with a higher than 1.9 B/A stoichiometry show a similar behaviour concluding that varying the stoichiometry in Ti–Zr AB_2 based Laves alloys has a modest effect on the hysteresis. Indeed hyper-stoichiometric $AB_{2.08}$ alloy studied in our previous work [25] got a similar value of hysteresis as presently studied $AB_{1.95}$ and $AB_{2.0}$ alloys.

Using van't Hoff relation and a modelling approach [30], the thermodynamic parameters of the interaction in the studied systems were obtained and these are listed in Table 3. We can see in the Table 3, $AB_{1.9}$ alloy has the lowest ΔH and ΔS formation 33.98 kJ/mol H_2 and 107.67 J/mol H_2 which are in good agreement with our previous publication $AB_{2.08}$ alloy [25], followed by $AB_{2.0}$, and $AB_{1.95}$ alloys. From the Table 3, enthalpy of desorption has similar values for all studied hydrides, being a range 34.0–35.3 kJ/mol H_2. However, significant differences in the stabilities of the hydrides were observed with equilibrium pressure of H_2 desorption @ 293 K changing from 0.4 to 0.85 bar H_2 following increase in B/A ratio from 1.90 to 2.00. Thus, changes in their stability are related to the gradual increase in changes in entropy as related to the hydrogenation, from 107.7 to 116.5 J/mol H_2 K. We note that critical temperature gradually decreases following an increase of B/A.

Furthermore, the change of electrode potential has the similar values changing between with −0.9385 V for $AB_{1.9}$, −0.9505 V for $AB_{1.95}$, and −0.9652 V for $AB_{2.0}$.

When converted to the electrochemical capacity, this results in the capacities approaching 500 mAh/g for all three alloys. However, since the measurements of the capacity were performed using the open cells, the measured capacity were limited to the values corresponding to hydrogen pressures in gaseous phase of 1 bar H_2, even though in the close cells one can expect to achieve electrochemical capacities exceeding 500 mAh/g, depending on the applied hydrogen pressure.

In case of electrochemical capacity conversion, increasing the stoichiometry, capacity decreases from 568.5 mAh/g for $AB_{1.95}$ alloy, followed by 556.6 mAh/g for $AB_{1.9}$ alloy, and 508.1 mAh/g for $AB_{2.0}$ alloy (see Table 3, the data are taken from PCT modelling). It appeared that $AB_{1.95}$ alloy achieved the highest capacity among others which might be caused by the optimizing phase composition and structures obtained during annealing.

With regards to the interrelation between the gaseous and electrochemical capacities of the alloys, we note a good agreement between these two sets of the data. However, there are also some differences as the higher driving force causing the hydrogenation of the alloy during the electrochemical charging leads a higher absorption capacity of the metal hydride anode as compared to the experiments during studied of the metal-hydrogen gas interactions. Thus, the electrochemical capacity is slightly higher than the gaseous capacity. Furthermore, the potential plateau slope in electrochemical discharge curves is flatter and the plateau is longer as compared with the corresponding PCT diagrams while in addition α- and β-phases have longer homogeneity ranges in studied of the electrochemical characteristics.

5. Conclusions

- Annealed hypo-stoichiometric and stoichiometric $AB_{2-x}La_{0.03}$ Laves type alloys (A = $Ti_{0.15}Zr_{0.85}$; B= $Mn_{0.64-0.69}V_{0.11-0.119}Fe_{0.11-0.119}Ni_{1.097-1.184}$; x = 0, 0.05 and 0.1) were studied as materials for the metal hydride battery anodes. Their performance was characterized by metal-H_2 gas and electrochemically as metal hydride battery anodes;

- A significant increase of discharge capacity of AB_{2-x} with A = Zr, Ti, La, B= Ni, Fe, Mn, V and x = 0; 0.05 and 0.10, Laves type alloys was achieved by shifting alloys composition from hyper-stoichiometric $AB_{2.08}$ (420 mAh/g; reference data) [25,26] to hypo-stoichiometric $AB_{1.90}$ and $AB_{1.95}$ alloys (495 mAh/g; present study).
- Increasing B/A ratio (1.9, 1.95, and 2.0) significantly increases equilibrium pressure of hydrogen desorption, from 0.3 to 0.4 and 0.8 bar H_2 @ 293 K, while this change in composition of the alloys only slightly affects the enthalpy of hydrogen desorption, with all values being within a narrow interval between 34.0 and 35.2 kJ/mol H_2. Thus, decreasing of the stability of the hydrides is associated with a significant increase in the entropy change during the phase transformation which changes from 107.67 to 113.33 and 116.61 J/mol H_2 K, respectively. Furthermore, the critical temperature also continuously decreases from 386 to 370 and 366 K, while the hysteresis energy losses are increasing from 333 to 715 and 785 J/mol, respectively.
- $AB_{1.95}$ alloy showed the best activation performance with the best rate performance between all studied materials when high, 80% of the maximum, discharge capacity maintained at 500 mA/g (1 C) of applied current density.
- The stoichiometric $AB_{2.0}$ alloy showed an excellent cyclic stability associated with efficient hydrogen diffusion process which maintained practically unchanged after 500 cycles. During the cycling, hydrogen diffusion coefficients of the alloys show only marginal changes indicating that they maintain stable hydrogen transport characteristics.
- Some differences in hydrogen storage performance characterized by metal-H_2 gas interactions and electrochemically can be associated with reaching thermodynamic equilibrium during the PCT studies of the metal-H_2 systems in contrast to the dynamic process of hydrogen change and discharge in open cells applied during electrochemical characterization of the metal hydride anodes.

Declaration of competing interest

The authors declare that they have no known competing financial interests or personal relationships that could have appeared to influence the work reported in this paper.

CRediT authorship contribution statement

Ika Dewi Wijayanti: Writing - original draft, Writing - review & editing. **Roman Denys:** Writing - original draft. **Suwarno:** Writing - original draft. **Alexey A. Volodin:** Writing - original draft. **M.V. Lototskyy:** Formal analysis, Writing - original draft, Writing - review & editing. **Matylda N. Guzik:** Writing - original draft. **Jean Nei:** Writing - original draft. **Kwo Young:** Writing - original draft. **Hans Jørgen Roven:** Writing - original draft. **Volodymyr Yartys:** Writing - original draft, Writing - review & editing, Supervision, Formal analysis.

Acknowledgements

This work has received support from EU HORIZON2020 project HYDRIDE4MOBILITY (S.S, R.D., M.L., V.A.Y.). IDW thanks for the support from Indonesia Endowment fund for Education (LPDP) and via a PhD research project at Norwegian University of Science and Technology and at Institute for Energy Technology. Alexey A. Volodin acknowledges financial support from the Ministry of Science and Higher Education of the Russian Federation (AGT: 14.613.21.0087; UI: RFMEFI61318X0087). We thank Department of Mechanical Engineering of ITS, Surabaya for the availability of the laboratory facilities for the SEM and EDS characterizations.

Appendix A. Supplementary data

Supplementary data to this article can be found online at https://doi.org/10.1016/j.jallcom.2020.154354.

References

[1] V. Yartys, D. Noreus, M. Latroche, Metal hydrides as negative electrode materials for Ni–MH batteries, Appl. Phys. A 122 (2016) 43.
[2] N. Furukawa, Development and commercialization of nickel-metal hydride secondary batteries, J. Power Sources 51 (1994) 45–59.
[3] M.L. Soria, J.n. Chacón, J.C. Hernández, D. Moreno, A. Ojeda, Nickel metal hydride batteries for high power applications, J. Power Sources 96 (2001) 68–75.
[4] M.A. Fetcenko, S.R. Ovshinsky, B. Reichman, K. Young, C. Fierro, J. Koch, A. Zallen, W. Mays, T. Ouchi, Recent advances in NiMH battery technology, J. Power Sources 165 (2007) 544–551.
[5] S. Tan, Y. Shen, E. Onur Şahin, D. Noréus, T. Öztürk, Activation behavior of an AB_2 type metal hydride alloy for NiMH batteries, Int. J. Hydrogen Energy 41 (2016) 9948–9953.
[6] K. Young, D.F. Wong, T. Ouchi, B. Huang, B. Reichman, Effects of La-addition to the structure, hydrogen storage, and electrochemical properties of C14 metal hydride alloys, Electrochim. Acta 174 (2015) 815–825.
[7] Y. Liu, H. Pan, M. Gao, Q. Wang, Advanced hydrogen storage alloys for Ni/MH rechargeable batteries, J. Mater. Chem. 21 (2011) 4743–4755.
[8] K.-H. Young, J. Nei, C. Wan, R. Denys, V. Yartys, Comparison of C14- and C15-predomiated AB2 metal hydride alloys for electrochemical applications, Batteries 3 (2017) 22.
[9] K.-H. Young, J.M. Koch, C. Wan, R.V. Denys, V.A. Yartys, Cell performance comparison between C14-and C15-predomiated AB_2 metal hydride alloys, Batteries 3 (2017) 29.
[10] D.-M. Kim, K.-J. Jang, J.-Y. Lee, A review on the development of AB_2-type Zr-based Laves phase hydrogen storage alloys for Ni–MH rechargeable batteries in the Korea Advanced Institute of Science and Technology, J. Alloys Compd. 293 (1999) 583–592.
[11] F. Cuevas, J.-M. Joubert, M. Latroche, A. Percheron-Guégan, Intermetallic compounds as negative electrodes of Ni/MH batteries, Appl. Phys. A 72 (2001) 225–238.
[12] H. Taizhong, W. Zhu, X. Baojia, X. Naixin, Effect of stoichiometry on hydrogen storage performance of Ti–Cr–VFe based alloys, Intermetallics 13 (2005) 1075–1078.
[13] T.A. Zotov, R.B. Sivov, E.A. Movlaev, S.V. Mitrokhin, V.N. Verbetsky, IMC hydrides with high hydrogen dissociation pressure, J. Alloys Compd. 509 (2011) S839–S843.
[14] S.R. Ovshinsky, M.A. Fetcenko, Development of high catalytic activity disordered hydrogen-storage alloys for electrochemical application in nickel–metal hydride batterie, Appl. Phys. A 72 (2001) 239–244.
[15] Y. Zhu, H. Pan, M. Gao, Y. Liu, Q. Wang, A study on improving the cycling stability of $(Ti_{0.8}Zr_{0.2})(V_{0.533}Mn_{0.107}Cr_{0.16}Ni_{0.2})_4$ hydrogen storage electrode alloy by means of annealing treatment: II. Effects on the electrochemical properties, J. Alloys Compd. 348 (2003) 301–308.
[16] J. Nei, K. Young, R. Regmi, G. Lawes, S.O. Salley, K.Y.S. Ng, Gaseous phase hydrogen storage and electrochemical properties of Zr_8Ni_{21}, Zr_7Ni_{10}, Zr_9Ni_{11}, and ZrNi metal hydride alloys, Int. J. Hydrogen Energy 37 (2012) 16042–16055.
[17] Y.L. Zhang, J.S. Li, T.B. Zhang, R. Hu, X.Y. Xue, Microstructure and hydrogen storage properties of non-stoichiometric Zr–Ti–V Laves phase alloys, Int. J. Hydrogen Energy 38 (2013) 14675–14684.
[18] F. Pourarian, H. Fujii, W. Wallace, V. Sinha, H.K. Smith, Stability and magnetism of hydrides of nonstoichiometric $ZrMn_2$, J. Phys. Chem. 85 (1981) 3105–3111.
[19] V.K. Sinha, F. Pourarian, W.E. Wallace, Hydrogenation characteristics of $Zr_{1-x}Ti_xMnFe$ alloys, J. Less Common Met. 87 (1982) 283–296.
[20] B.H. Liu, Z.P. Li, S. Suda, Electrochemical cycle life of Zr-based Laves phase alloys influenced by alloy stoichiometry and composition, J. Electrochem. Soc. 149 (2002) A537–A542.
[21] K. Young, J. Nei, B. Huang, M. Fetcenko, Studies of off-stoichiometric AB_2 metal hydride alloy: Part 2. Hydrogen storage and electrochemical properties, Int. J. Hydrogen Energy 36 (2011) 11146–11154.
[22] S.-M. Lee, H. Lee, J.-H. Kim, P.S. Lee, J.-Y. Lee, A study on the development of hypo-stoichiometric Zr-based hydrogen storage alloys with ultra-high capacity for anode material of Ni/MH secondary battery, J. Alloys Compd. 308 (2000) 259–268.
[23] I.D. Wijayanti, L. Mølmen, R.V. Denys, J. Nei, S. Gorsse, K. Young, M.N. Guzik, V. Yartys, The electrochemical performance of melt-spun C14-Laves type TiZr-based alloy, Int. J. Hydrogen Energy 45 (2020) 1297–1303.
[24] I.D. Wijayanti, L. Mølmen, R.V. Denys, J. Nei, S. Gorsse, M.N. Guzik, K. Young, V. Yartys, Studies of Zr-based C15 type metal hydride battery anode alloys prepared by rapid solidification, J. Alloys Compd. 804 (2019) 527–537.
[25] A.A. Volodin, R.V. Denys, C. Wan, I.D. Wijayanti, B.P. Tarasov, V.E. Antonov,

V.A. Yartys, Study of hydrogen storage and electrochemical properties of AB_2-type $Ti_{0.15}Zr_{0.85}La_{0.03}Ni_{1.2}Mn_{0.7}V_{0.12}Fe_{0.12}$ alloy, J. Alloys Compd. 793 (2019) 564–575.
[26] C. Wan, R. Denys, M. Lelis, D. Milčius, V. Yartys, Electrochemical studies and phase-structural characterization of a high-capacity La-doped AB_2 Laves type alloy and its hydride, J. Power Sources 418 (2019) 193–201.
[27] A.C. Larson, R. Von Dreele, General Structure Analysis System (GSAS)(Report LAUR 86-748), Los Alamos National Laboratory, Los Alamos, New Mexico, 2004.
[28] Y.L. Du, G. Chen, G.L. Chen, Optimization of Zr-based hydrogen storage alloys for nickel-hydride batteries, Intermetallics 13 (2005) 399–402.
[29] K. Shu, S. Zhang, Y. Lei, G. Lü, Q. Wang, Effect of Ti on the structure and electrochemical performance of Zr-based AB_2 alloys for nickel–metal rechargeable batteries, J. Alloys Compd. 349 (2003) 237–241.
[30] M. Lototskyy, New model of phase equilibria in metal–hydrogen systems: features and software, Int. J. Hydrogen Energy 41 (2016) 2739–2761.
[31] C.-N. Park, S. Luo, T.B. Flanagan, Analysis of sloping plateaux in alloys and intermetallic hydrides: I. Diagnostic features, J. Alloys Compd. 384 (2004) 203–207.
[32] Z. Szklarska-Smialowska, M. Smialowski, Electrochemical study of the nickel-hydrogen system, J. Electrochem. Soc. 110 (1963) 444–448.
[33] E.G. Ponyatovsky, V.E. Antonov, I.T. Belash, in: A.M. Prokhorov, A.S. Prokhorov (Eds.), High Hydrogen Pressures, Synthesis and Properties of New Hydrides, Problems in Solid State Physics, Mir Publ, Moscow, 1984, pp. 109–171.

Supplementary Material

Hydrides of Laves type Ti-Zr alloys with enhanced H storage capacity as advanced metal hydride battery anodes

Ika Dewi Wijayanti[a,b,c], Roman Denys[a], Suwarno[c], Alexey A. Volodin[d], M.V. Lototskyy[e], Matylda N. Guzik[f], Jean Nei[g], Kwo Young[g], Volodymyr Yartys[a]

[a]*Institute for Energy Technology, Kjeller, Norway*
[b]*Norwegian University of Science and Technology, Trondheim, Norway*
[c]*Department of Mechanical Engineering, ITS, Surabaya, Indonesia*
[d]*Institute of Problems of Chemical Physics RAS, Chernogolovka, 142432, Russia*
[e]*University of the Western Cape, South Africa*
[f]*Department of Physics, University of Oslo, Blindern, Oslo, Norway*
[g] *BASF/Battery Materials-Ovonic, Rochester Hills, USA*

Email: Ika.Dewi.Wijayanti@ife.no; Volodymyr.Yartys@ife.no

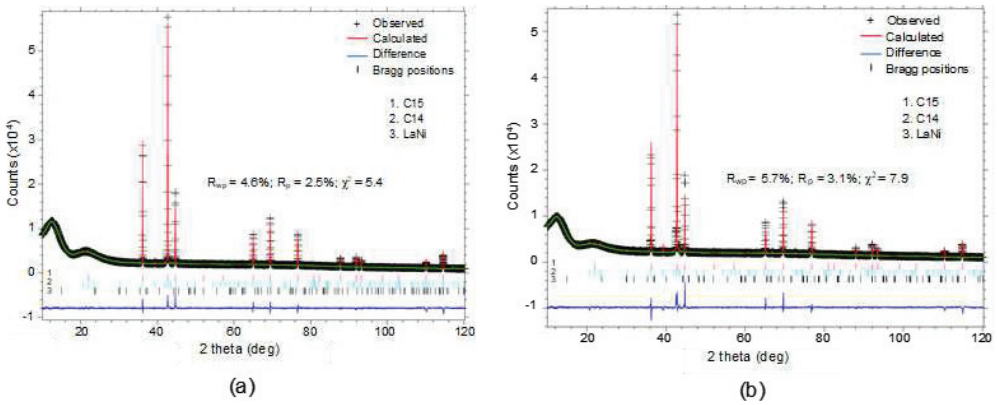

Fig. S1.

XRD patterns (Cu-$K_{\alpha 1}$) for the studied alloys

Rietveld refinements for annealed $AB_{1.95}$ alloy (a) and annealed $AB_{2.0}$ alloy (b).

Table S1.

The change in elementary composition (wt.%) of the $AB_{1.95}$ alloy as related to the preparation conditions

Type	**Ti**	**Zr**	**La**	**Ni**	**Mn**	**V**	**Fe**
Design	4	39	2	19	31	3	3
As-cast	7	42	4	18	18	6	6
Annealed	7	42	4	17	17	6	6

Table S2.

Refined model parameters used to fit the PCT data.

Group	Notation	Description [units]	Equations	General constrains	Number (for k plateau segments)
General	C_{max}	Maximum hydrogen concentration [(1)]	6, 7, 48	$C_{max}>0$	1
	W_i	Segment weight [-]	48	$W_i \geq 0; \sum_{i=1}^{k} W_i = 1$	k–1(2)
Core function	T_C	Critical temperature [K]	20	$T_C>0$	k
	ΔS^o_i	Hydrogenation entropy [J / (mol H_2 K)]	14	$\Delta S^o<0$	k
	ΔH^o_i	Hydrogenation enthalpy [J / mol H_2]	14	$\Delta H^o<0$	k
Distribution (absorption)	$\Delta G_{h(A,i)}$	Hysteresis energy loss [J / mol H]	34, 43	$\Delta G_h \geq 0$	k
	$w_{0(A,i)}$	Width parameter, 1/2 FWHM at X=0 (f=f_0) [-]	36, 39, 41	$w_0 \geq 0$	k
	$\eta_{(A,i)}$	Contribution of Lorentz profile [-]	40	$0 \leq \eta \leq 1$	k
	$A_{(A,i)}$	Asymmetry [-]	41	–	k
	$s_{(A,i)}$	Slope factor [-]	42	$0 \leq s \leq 1$	k
Distribution (desorption)	$w_{0(D,i)}$	Width parameter (1/2 FWHM at X=0 (f=f_0) [-]	36, 39, 41	$w_0 \geq 0$	k
	$\eta_{(D,i)}$	Contribution of Lorentz profile [-]	40	$0 \leq \eta \leq 1$	k
	$A_{(D,i)}$	Asymmetry [-]	41	–	k
	$s_{(D,i)}$	Slope factor [-]	42	$0 \leq s \leq 1$	k
Distributions temperature dependence	$T_{0(i)}$	Characteristic temperature related to the minimum plateau slope [K]	45	$T_0>0$	k
	$\rho_{SH(i)}$	Pearson correlation coefficient between ΔS^o and ΔH^o [-]	45	$0 \leq \rho_{SH} \leq 1$	k
	M_i	Mixing coefficient [-]	46, 47	$M \geq 0$	k
TOTAL					16 k

Notes: (1) – Units proportional to H/M atomic ratio, NL/kg in this work
(2) – For k=1 W_1=1 (fixed).

According to the modelling algorithm [1], errors of the refined fitting parameters were assumed to be equal to their increments or decrements at the end of the fitting refinements resulting in ~1% increase of the sum of squared distances of the experimental points from the calculated curves plotted in C/C_{max} – ln P coordinates. The experimental temperatures were taken as averages of the values of observed reactor temperatures in the raw data. The pressures units were atmospheres.

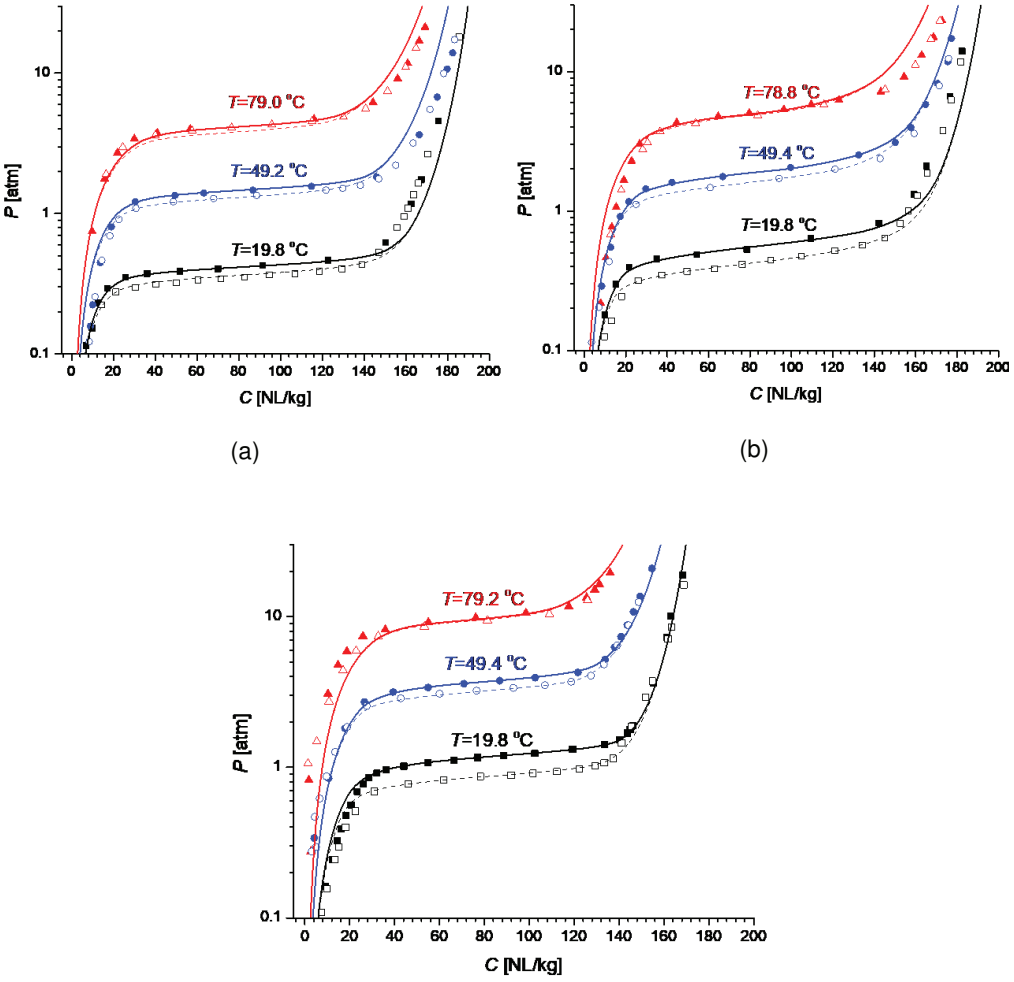

Fig S2.

Experimental and fitted using the model PCT data for $AB_{1.9}$ (a), $AB_{1.95}$ (b), $AB_{2.0}$ (c) alloys; (absorption – filled symbols / solid lines; desorption – empty symbols, dashed lines). Symbols – experimental data; lines – fitting results when using parameters listed in Table 3.

Table S3.

Fitting parameters to fit the PCT diagrams for H – $AB_{1.9}$ system.

Parameter [units]		**Value**	**Error**
Asymptotic H concentration, C_{max} [NL/kg]		231.1	0.6
Critical temperature, T_C [K]		386	3
Entropy change for the hydride formation, ΔS [J/(mol H_2 K)]		-107.67	0.01
Enthalpy change for the hydride formation, ΔH [kJ/mol H_2]		-33.98	0.02
Hysteresis energy loss, ΔG_h [J/mol]		333	17
Distribution parameters: H desorption	Width parameter, w_D [-]	0.13	0.05
	Contribution of Lorentz profile, η_D [-]	0.60	0.02
	Asymmetry, A_D [-]	-1.2	0.6
	Slope factor, s_D [-][1]	1	-
Distribution parameters: H absorption	Width parameter, w_A [-]	0.11	0.01
	Contribution of Lorentz profile, η_A [-]	0.61	0.05
	Asymmetry, A_A [-]	-1	1
	Slope factor, s_A [-] (not refined)	1	-
Temperature dependence of the distribution parameters	Mixing coefficient, M [-]	3	3
	Temperature corresponding to the minimum plateau slope, T_0 [K]	522	26
	Pearson correlation coefficient, ρ_{SH} [-]	0.95	0.02
Goodness of the fit	$\Delta C/C_{max}$	0.0008	-
	$R_l(C,\ln(P))$=	0.0026	-

Table S4.

Fitting parameters to fit the PCT diagrams for H – $AB_{1.95}$ system.

Parameter [units]		**Value**	**Error**
Asymptotic H concentration, C_{max} [NL/kg]		236	2
Critical temperature, T_C [K]		370	1
Entropy change for the hydride formation, ΔS [J/(mol H_2 K)]		-113.33	0.03
Enthalpy change for the hydride formation, ΔH [kJ/mol H_2]		-35.25	0.01
Hysteresis energy loss, ΔG_h [J/mol]		715	13
Distribution parameters: H desorption	Width parameter, w_D [-]	0.17	0.02
	Contribution of Lorentz profile, η_D [-]	0.46	0.07
	Asymmetry, A_D [-]	-1.4	0.4
	Slope factor, s_D [-]	1	-
Distribution parameters: H absorption	Width parameter, w_A [-]	0.15	0.02
	Contribution of Lorentz profile, η_A [-]	0.4	0.2
	Asymmetry, A_A [-]	-1.3	0.4
	Slope factor, s_A [-] (not refined)	1	-
Temperature dependence of the distribution parameters	Mixing coefficient, M [-]	0.5	0.5
	Temperature corresponding to the minimum plateau slope, T_0 [K]	759	38
	Pearson correlation coefficient, ρ_{SH} [-]	0.75	0.04
Goodness of the fit	$\Delta C/C_{max}$	0.0005	-
	$R_I(C,\ln(P))$=	0.0021	-

Table S5.

Fitting parameters to fit the PCT diagrams for H – AB_2 system.

Parameter [units]		**Value**	**Error**
Asymptotic H concentration, C_{max} [NL/kg]		210.9	0.5
Critical temperature, T_C [K]		366.1	0.9
Entropy change for the hydride formation, ΔS [J/(mol H_2 K)]		-116.61	0.01
Enthalpy change for the hydride formation, ΔH [kJ/mol H_2]		-34.538	0.004
Hysteresis energy loss, ΔG_h [J/mol]		785	14
Distribution parameters: H desorption	Width parameter, w_D [-]	0.12	0.02
	Contribution of Lorentz profile, η_D [-]	0.463	0.004
	Asymmetry, A_D [-]	2	3
	Slope factor, s_D [-] (not refined)	1	-
Distribution parameters: H absorption	Width parameter, w_A [-]	0.123	0.006
	Contribution of Lorentz profile, η_A [-]	0.57	0.06
	Asymmetry, A_A [-]	2	1
	Slope factor, s_A [-] (not refined)	1	-
Temperature dependence of the distribution parameters	Mixing coefficient, M [-]	0.23	0.08
	Temperature corresponding to the minimum plateau slope, T_0 [K]	620	11
	Pearson correlation coefficient, ρ_{SH} [-]	0.98	0.02
Goodness of the fit	$\Delta C/C_{max}$	0.0003	-
	$R_f(C,\ln(P))$=	0.0012	-

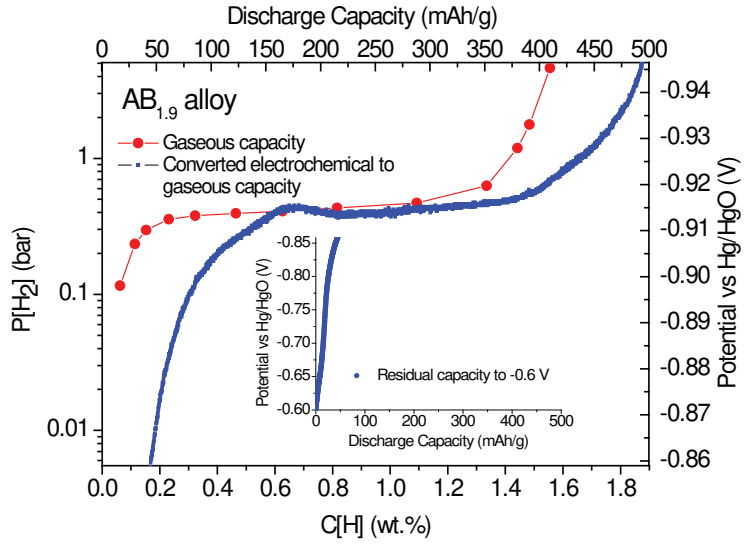

(a)

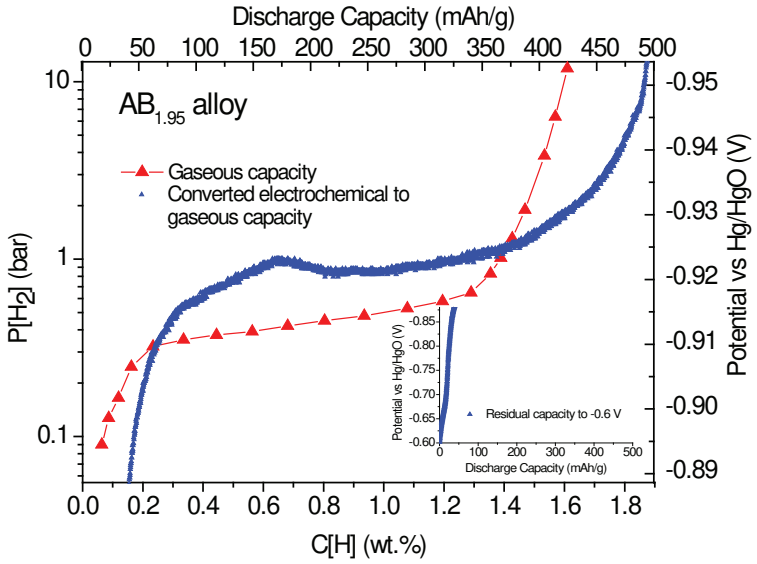

(b)

Fig. S3.

Hydrogen desorption PCT curves and discharge curves measured for electrochemical capacity for $AB_{1.9}$ (a) and $AB_{1.95}$ (b) alloys.

The inserts of the graphs show the tails of the curves measured from -0.85 to -0.6 V (cut-off voltage applied during the measurements of the discharge electrochemical capacity).

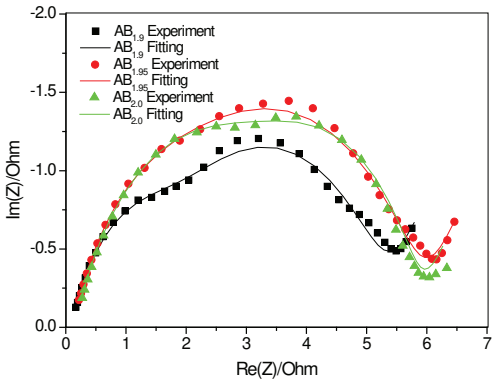

(a)

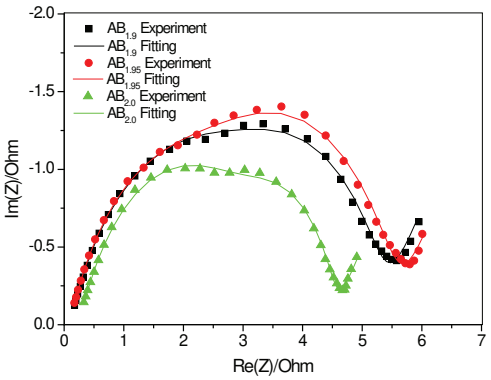

(b)

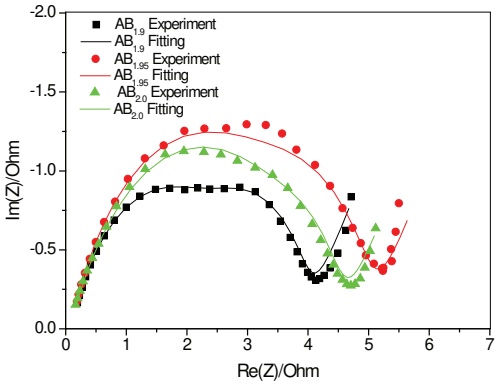

(c)

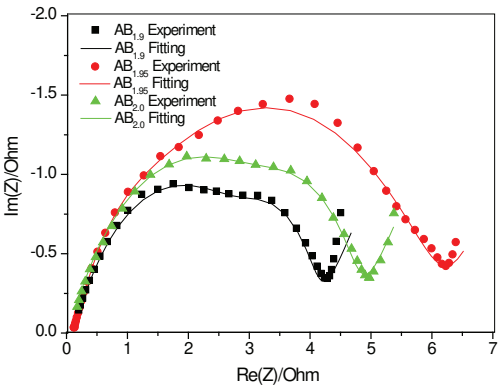

(d)

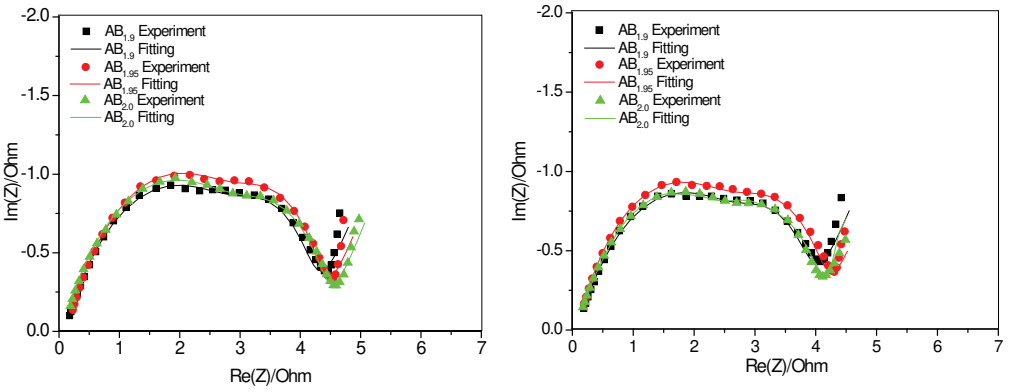

(e) (f)

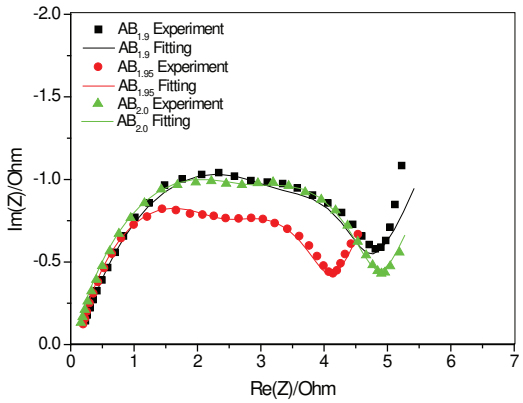

(g)

Fig S4.

EIS spectra measured after activation at 100 mA/g discharge current density (a), after 10 cycles (b), after 100 cycles (c), after 200 cycles (d), after 300 cycles (e), after 400 cycles (f), after 500 cycles (g) all measured at 50% SOC.

Table S6.

Fitting parameters to describe EIS data for the alloys after activation.

Parameters	$AB_{1.9}$ Annealed	$AB_{1.95}$ Annealed	$AB_{2.0}$ Annealed
	50% SOC	50% SOC	50% SOC
$R_{electrolyte}$, Ohm	0.1008	0.08592	0.1567
$R_{contact}$, Ohm	1.667	5.585	3.007
$CPE_{contact}$, $F.s^{\alpha-1}$	0.05681	0.11	0.03993
n_1	0.71	0.5721	0.6816
R_{ct}, Ohm	2.219	0.4225	2.787
CPE_{ct}, $F.s^{\alpha-1}$	0.3484	0.07973	0.2853
n_2	0.6637	0.9586	0.712
σ, $Ohm.s.^{1/2}$	0.03288	0.02325	0.02724
Goodness of fit, χ^2	0.07597	0.09156	0.1699
D_H, $cm^2.s^{-1}$	1.00E-09	2.00E-09	1.46E-09

Table S7.

Fitting parameters to describe EIS data for the alloys after 10 cycles.

Parameters	$AB_{1.9}$ Annealed	$AB_{1.95}$ Annealed	$AB_{2.0}$ Annealed
	50% SOC	50% SOC	50% SOC
$R_{electrolyte}$, Ohm	0.09854	0.1039	0.2559
$R_{contact}$, Ohm	3.319	2.447	3.235
$CPE_{contact}$, $F.s^{\alpha-1}$	0.05273	0.05405	0.04293
n_1	0.6579	0.6932	0.6691
R_{ct}, Ohm	1.887	2.997	0.9517
CPE_{ct}, $F.s^{\alpha-1}$	0.5045	0.2843	0.8373
n_2	0.8184	0.7551	0.9927
σ, $Ohm.s.^{1/2}$	0.04366	0.03389	0.03764
Goodness of fit, χ^2	0.02652	0.03711	0.0969
D_H, $cm^2.s^{-1}$	5.67E-10	9.41E-10	7.63E-10

Table S8.

Fitting parameters to describe EIS data for the alloys after 100 cycles.

Parameters	$AB_{1.9}$ Annealed	$AB_{1.95}$ Annealed	$AB_{2.0}$ Annealed
	50% SOC	50% SOC	50% SOC
$R_{electrolyte}$, Ohm	0.08829	0.08448	0.06859
$R_{contact}$, Ohm	1.495	2.953	0.5546
$CPE_{contact}$, $F.s^{\alpha-1}$	0.493	0.04329	1.803
n_1	0.7855	0.6909	0.827 6
R_{ct}, Ohm	2.47	2.14	3.996
CPE_{ct}, $F.s^{\alpha-1}$	0.04365	0.3203	0.04884
n_2	0.6752	0.6888	0.6292
σ, $Ohm.s.^{1/2}$	0.04785	0.03666	0.03857
Goodness of fit, χ^2	0.1103	0.1245	0.0607
D_H, $cm^2.s^{-1}$	4.72E-10	8.04E-10	7.27E-10

Table S9.

Fitting parameters to describe EIS data for the alloys after 200 cycles.

Parameters	$AB_{1.9}$ Annealed	$AB_{1.95}$ Annealed	$AB_{2.0}$ Annealed
	50% SOC	50% SOC	50% SOC
$R_{electrolyte}$, Ohm	0.1053	0.07947	0.0548
$R_{contact}$, Ohm	3.162	3.059	3.625
$CPE_{contact}$, $F.s^{\alpha-1}$	0.0519	0.05282	0.0453
n_1	0.634	0.6716	0.6288
R_{ct}, Ohm	0.7875	0.9491	1.166
CPE_{ct}, $F.s^{\alpha-1}$	1.279	0.9933	0.7977
n_2	0.9799	0.9799	0.8596
σ, $Ohm.s.^{1/2}$	0.05185	0.04474	0.04074
Goodness of fit, χ^2	0.08149	0.03668	0.0276
D_H, $cm^2.s^{-1}$	4.02E-10	5.40E-10	6.51E-10

Table S10.

Fitting parameters to describe EIS data for the alloys after 300 cycles.

Parameters	$AB_{1.9}$ Annealed	$AB_{1.95}$ Annealed	$AB_{2.0}$ Annealed
	50% SOC	50% SOC	50% SOC
$R_{electrolyte}$, Ohm	0.1097	0.1345	0.07082
$R_{contact}$, Ohm	3.163	3.28	3.312
$CPE_{contact}$, $F.s^{\alpha-1}$	0.06454	0.05812	0.04375
n_1	0.6186	0.6533	0.6294
R_{ct}, Ohm	0.9073	0.8925	0.9913
CPE_{ct}, $F.s^{\alpha-1}$	1.49	1.416	1.095
n_2	0.9038	0.998	0.9256
σ, $Ohm.s.^{1/2}$	0.059	0.04632	0.04384
Goodness of fit, χ^2	0.04746	0.05953	0.03398
D_H, $cm^2.s^{-1}$	3.11E-10	5.04E-10	5.62E-10

Table S11.

Fitting parameters to describe EIS data for the alloys after 400 cycles.

Parameters	$AB_{1.9}$ Annealed	$AB_{1.95}$ Annealed	$AB_{2.0}$ Annealed
	50% SOC	50% SOC	50% SOC
$R_{electrolyte}$, Ohm	0.08197	0.08346	0.08382
$R_{contact}$, Ohm	3.138	2.962	0.784
$CPE_{contact}$, $F.s^{\alpha-1}$	0.07891	0.06087	1.7
n_1	0.6056	0.6626	0.9922
R_{ct}, Ohm	0.6365	1.012	3.07
CPE_{ct}, $F.s^{\alpha-1}$	2.913	1.486	0.05774
n_2	0.9986	0.939	0.6182
σ, $Ohm.s.^{1/2}$	0.06118	0.04691	0.04969
Goodness of fit, χ^2	0.02949	0.04948	0.04389
D_H, $cm^2.s^{-1}$	2.89E-10	4.91E-10	4.38E-10

Table S12.

Fitting parameters to describe EIS data for the alloys after 500 cycles.

Parameters	$AB_{1.9}$ Annealed	$AB_{1.95}$ Annealed	$AB_{2.0}$ Annealed
	50% SOC	50% SOC	50% SOC
$R_{electrolyte}$, Ohm	0.119	0.1059	0.06689
$R_{contact}$, Ohm	0.5784	1.141	1.378
$CPE_{contact}$, $F.s^{\alpha-1}$	4.309	1.576	1.11
n_1	1	0.8766	0.8503
R_{ct}, Ohm	3.868	2.595	3.25
CPE_{ct}, $F.s^{\alpha-1}$	0.0817	0.06089	0.05516
n_2	0.5928	0.666	0.6315
σ, $Ohm.s.^{1/2}$	0.07366	0.05405	0.05197
Goodness of fit, χ^2	0.1036	0.06905	0.01581
D_H, $cm^2.s^{-1}$	1.99E-10	3.70E-10	4.00E-10

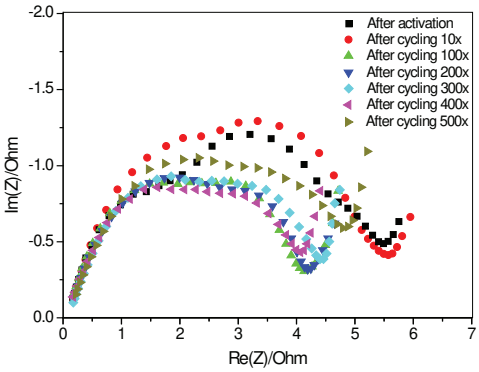

(a)

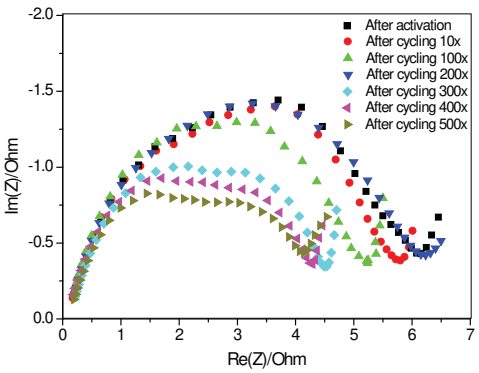

(b)

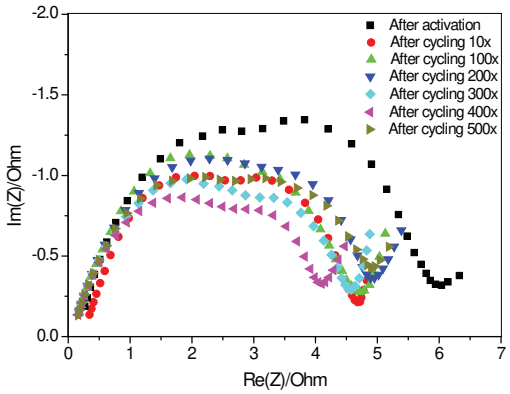

(c)

Fig S5.
EIS spectra for the studied alloys at variable measurements conditions; $AB_{1.9}$ (a), $AB_{1.95}$ (b), and $AB_{2.0}$ (c).

Table S13.

ESI parameters for the annealed $AB_{1.9}$ alloy

Measurements	**$R_{electrolyte}$ (Ohm)**	**$R_{contact}$ (Ohm)**	**$R_{charge\ transfer}$ (Ohm)**	**D_H, $cm^2.s^{-1}$**
After activation	0.1008	1.667	2.219	1.0E-09
After cycling 10x	0.09854	3.319	1.887	5.7E-10
After cycling 100x	0.08829	1.495	2.47	4.7E-10
After cycling 200x	0.1053	3.162	0.7875	4.0E-10
After cycling 300x	0.1097	3.163	0.9073	3.1E-10
After cycling 400x	0.08197	3.138	0.6365	2.9E-10
After cycling 500x	0.119	0.5784	3.868	2.0E-10

Table S14.

ESI parameters for the annealed $AB_{1.95}$ alloy.

Measurements	**$R_{electrolyte}$ (Ohm)**	**$R_{contact}$ (Ohm)**	**$R_{charge\ transfer}$ (Ohm)**	**D_H, $cm^2.s^{-1}$**
After activation	0.08592	5.585	0.4225	2.0E-09
After cycling 10x	0.1039	2.447	2.997	9.4E-10
After cycling 100x	0.08448	2.953	2.14	8.0E-10
After cycling 200x	0.07947	3.059	0.9491	5.4E-10
After cycling 300x	0.1345	3.28	0.8925	5.0E-10
After cycling 400x	0.08346	2.962	1.012	4.9E-10
After cycling 500x	0.1059	1.141	2.595	3.7E-10

Table S15.

ESI parameters for the annealed $AB_{2.0}$ alloy.

Measurements	**$R_{electrolyte}$ (Ohm)**	**$R_{contact}$ (Ohm)**	**$R_{charge\ transfer}$ (Ohm)**	**D_H, $cm^2.s^{-1}$**
After activation	0.1567	3.007	2.787	1.5E-09
After cycling 10x	0.2559	3.235	0.9517	7.6E-10
After cycling 100x	0.06859	0.5546	3.996	7.3E-10
After cycling 200x	0.0548	3.625	1.166	6.5E-10
After cycling 300x	0.07082	3.312	0.9913	5.6E-10
After cycling 400x	0.08382	0.784	3.07	4.4E-10
After cycling 500x	0.06689	1.378	3.25	4.0E-10

REFERENCES

[1] M. Lototskyy, New model of phase equilibria in metal–hydrogen systems: Features and software, international journal of hydrogen energy, 41 (2016) 2739-2761.